ENVIRONMENTAL INFLUENCES ON CROSSFLOW INSTABILITY

A Dissertation

by

ROBERT STUART DOWNS III

Submitted to the Office of Graduate Studies of
Texas A&M University
in partial fulfillment of the requirements for the degree of

DOCTOR OF PHILOSOPHY

Approved by:

Chair of Committee,	Edward White
Committee Members,	Rodney Bowersox
	Andrew Duggleby
	William Saric
Head of Department,	Dimitris Lagoudas

December 2012

Major Subject: Aerospace Engineering

ABSTRACT

The laminar-to-turbulent transition process in swept-wing boundary layers is often dominated by an inflectional instability arising from crossflow. It is now known that freestream turbulence and surface roughness are two of the key disturbance sources in the crossflow instability problem. Recent experimental findings have suggested that freestream turbulence of low intensity (less than 0.2%) may have a larger influence on crossflow instability than was previously thought. The present work involves experimental measurement of stationary and traveling crossflow mode amplitudes in freestream turbulence levels between 0.02% and 0.2%. A 1.83 m chord, 45-degree swept-wing model is used in the Klebanoff–Saric Wind Tunnel to perform these experiments. The turbulence intensity and length scales are documented. Although a significant amount of research on the role of turbulence has been completed at higher turbulence levels, comparatively little has been done at the low levels of the present experiments, which more closely reflect the flight environment. It is found that growth of the traveling crossflow mode is highly dependent on small changes to the freestream turbulence. Additionally, previously studied attenuation of saturated stationary disturbance amplitudes is observed at these low turbulence levels. The extent of laminar flow is also observed to decrease in moderate freestream turbulence.

ACKNOWLEDGMENTS

A great debt of thanks is owed to committee chair and academic advisor, Professor Edward White, for several years of instruction and support. Thanks are also due to the dissertation committee (Professor William Saric, Professor Rodney Bowersox and Professor Andrew Duggleby) for their helpful comments, suggestions and guidance. The author also thanks Dr. Lauren Hunt and Professor William Saric for the use of their swept-wing setup and for guidance. Linear stability calculations provided by Matt Tufts and Professor Helen Reed were of great utility throughout the experimental campaign.

The experiments completed in support of this research required several hundred hours of wind tunnel testing. This would not have been possible without the assistance of students at the Klebanoff–Saric Wind Tunnel and Texas A&M University Flight Research Laboratory including, in particular, Erica Lovig, David West, Doug Kutz and Matt Kuester. The technical support of Cecil Rhodes and the staff of the Oran W. Nicks Low Speed Wind Tunnel is greatly appreciated. Administrative support by Colleen Leatherman and Rebecca Marianno is also appreciated. This work is supported by the U.S. Air Force Office of Scientific Research under grants FA9550-08-1-0093 and FA9550-09-1-0341.

NOMENCLATURE

To stay consistent with relevant literature, symbols are occasionally used to represent more than one quantity. For example, in the boundary-layer stability community, k is used to denote surface roughness height. However, the yaw coefficient for a hot-wire probe is also commonly referred to as k. The meaning of such homonymous nomenclature is discernible from the context and clarifying text is added to dispel ambiguity as necessary.

A	Stationary disturbance amplitude
a, a_{rms}	Unsteady disturbance amplitude
A, B, n	Hot-wire probe calibration constants
c	Airfoil chord length, normal to leading edge
c_l	Lift coefficient
C	Swept-wing model chord length in global coordinates, 1.83 m
$C_{p,2}$	Coefficient of pressure in model-fixed coordinate system
$C_{p,3}$	Coefficient of pressure in global coordinate system
C_T	Thermal compensation coefficient
d	Roughness diameter, wire diameter
e	Leading-edge ellipse ratio
E	Hot-wire probe voltage, disturbance energy
E_h, E_l	Probe voltages measured at high and low temperatures
E_{comp}	Temperature-compensated hot-wire probe voltage
$f(r)$	Streamwise autocorrelation function

H_k	FFT coefficients
h	Convective heat transfer coefficient
I	Hot-wire probe current
k	Roughness height, thermal conductivity, X-wire yaw coefficient
m	Hot-wire thermal voltage drift
N	Amplification factor
N_0	Number of time-record zero crossings per unit time
Nu	Nusselt number, hd/k
PSD	Power spectral density
p	Static pressure
q	Dynamic pressure, $\rho U_\infty^2/2$
q	Variable name for u, v, w, p
r	Leading-edge radius, spatial autocorrelation lag
R	Hot-wire probe resistance
$\overline{R}$	Attachment-line Reynolds number
Re_c	Chord-based Reynolds number, UC/ν (swept)
Re_k	Roughness-height-based Reynolds number
$Re_{x,tr}$	Streamwise Reynolds number at transition location
T	Temperature
T_a	Ambient temperature
T_{comp}	Compensation temperature
T_h, T_l	High and low temperatures
T_w	Hot-wire temperature

Tu	Freestream turbulence intensity
u', v', w'	Fluctuating components of velocity
u'_{rms}, v'_{rms}, w'_{rms}	Temporal root-mean-square of u', v', w'
u, v, w	Velocity components in the global coordinate system
u_n, v_n, w_n	Velocity components in the model-fixed coordinate system
u_t, v_t, w_t	Velocity components in the streamline-fixed coordinate system
U	Mean boundary-layer velocity
U_e	Boundary-layer edge velocity, U/U_{fs}
U_n, U_t	Normal and tangential velocity in a wire-fixed system
U_∞	Freestream velocity
$\overline{U}$	Mean boundary-layer profile
U'	Steady disturbance velocity
U'_{rms}	Spanwise rms of the U' profiles
V_e	Effective cooling velocity
W_{ss}	FFT window function, squared and summed
x, y, z	Model-fixed coordinate axes
x_t, y_t, z_t	Streamline-fixed coordinate axes
X, Y, Z	Global (test section fixed) coordinate axes
x/c_{tr}	Transition location as a fraction of chord length
Y_{wall}	Wall location in traverse coordinates
α	Model angle of attack, X-wire probe yaw angle
α, β	Streamwise and spanwise wavenumbers
β	Probe rotation angle about Z axis

β	Mesh porosity; open-area ratio
δ^*	Boundary-layer displacement thickness
$\delta_{99.9}$	Boundary-layer thickness at which $U/U_e = 0.999$
λ	Spanwise wavelength
λ_{cr}	Spanwise crossflow wavelength
λ_{crit}	Wavelength of the most unstable disturbance
λ_k	Spanwise roughness spacing
λ_x	Streamwise dissipation microscale
Λ	Sweep angle, integral length scale
ν	Kinematic viscosity
ρ	Density
σ	Mesh solidity, $1 - \beta$
τ	Temporal autocorrelation lag
τ_w	Surface shear stress
χ^2	Sum of the squares of the residuals
ω	Angular frequency
$[k\|\lambda\|d]$	Roughness array: k in μm, λ and d in mm

TABLE OF CONTENTS

LIST OF FIGURES

FIGURE Page

FIGURE Page

FIGURE Page

FIGURE Page

LIST OF TABLES

CHAPTER I

INTRODUCTION

Though the concept of using swept wings to lower the drag of high-speed aircraft was introduced by Adolf Busemann at the fifth Volta conference in 1935, it was not a commonly accepted design feature until late in the next decade. Research in this area was classified by the Luftwaffe in 1936 and the Allied technical teams that entered the German aeronautics research laboratories in May of 1945 uncovered wind tunnel models and experimental data that confirmed the utility of this concept (Anderson, 1998). However, the American aerodynamicist Robert T. Jones independently recognized the benefit of using swept wings and shared his theories with the management at the NACA Langley research laboratories. Subsequent experiments confirmed this theory and the results were presented to the United States Army in a classified memorandum in June, 1945. These findings were later published openly in NACA technical report 863 (Jones, 1945). As such, the concept of the swept wing is credited to both Busemann and Jones by Anderson (1998), who describes the history of the swept wing in detail.

This concept rests on the idea that the pressure distribution over an airfoil is determined by the velocity component normal to the leading edge. By introducing a sweep angle, this velocity component is reduced. For subsonic aircraft traveling near the speed of sound, this reduced velocity effectively raises the critical Mach number, allowing greater forward speed without the drag penalty imposed by shock waves forming on the wings. Another explanation is given by Anderson (2001) in the context of airfoil thickness. The thickness ratio of a swept wing is lower in the streamwise reference frame. As such, the drag divergence Mach number is higher.

With the introduction of the Boeing B-47 and the North American F-86 in 1947, the swept-wing concept became a common design element for high speed aircraft. However, the three-dimensional boundary layers that form on swept wings are susceptible to the so-called crossflow instability (in addition to the instabilities that may arise on straight wings). As reported by Gray (1952), crossflow instability can hasten transition and increase the drag on swept wings compared with their unswept counterparts. Further experimental evidence of the crossflow instability was presented by Gregory *et al.* (1955) using the flow over a rotating disk as a model problem. In the same report, Stuart provides the theoretical basis for the problem and presents disturbance equations for three-dimensional boundary layers.

The crossflow instability arises within a boundary layer due to an imbalance between streamwise pressure gradient and the centripetal acceleration that results from the curved streamlines around a swept wing. This imbalance—due to the fact that velocity decreases in the boundary layer while the pressure gradient does not—produces a secondary flow (crossflow) perpendicular to the local stream direction resulting in a three-dimensional boundary layer. The no-slip condition requires that the crossflow velocity goes to zero on the wing surface while in the freestream, the definition of crossflow as perpendicular to the streamwise direction requires zero crossflow velocity there as well (Saric *et al.*, 2003). Thus, for any non-trivial crossflow velocity profile, an inflection point must exist somewhere within the boundary layer. This inflection point is the source of an inviscid instability: Rayleigh's stability criterion states that a sign change in $U''(y)$ is a necessary condition for instability (Drazin, 2002).

In addition to crossflow instability, there are other types of flow instability that may arise within a swept-wing boundary layer and produce disturbance growth leading to transition. A summary of these instabilities and strategies for laminar flow control (LFC) are given in a recent review by Saric *et al.* (2011). Viscous effects pro-

duce a streamwise instability commonly known as Tollmien–Schlichting (T–S) waves. Among several possible methods for stabilizing T–S waves the most common is tailoring of the pressure gradient. In fact, the design principle behind natural laminar flow (NLF) airfoils includes maintaining a favorable pressure gradient over large portions of the airfoil surface. A centrifugal instability may arise in boundary layers over a concave surface. This so-called Görtler instability can be controlled passively by avoiding concave airfoil sections (Saric, 1994). Another potential source of turbulent flow is contamination of the attachment-line flow from the fuselage boundary layer. This problem may be managed by designing swept wings with suitably small leading-edge radii to maintain attachment-line Reynolds numbers (Saric *et al.*, 2011) below the critical value of 250. This point is discussed further in Chapter II in the context of the model used in the present experiments. The crossflow instability, however, has resisted efforts to develop a robust, passive means of control. This is complicated in part by the fact that the favorable pressure gradients imposed to stabilize T–S waves will destabilize the crossflow instability. Though reducing the sweep angle may attenuate the growth of this instability, the cost is a lower critical Mach number. As such, the study of crossflow instability has been an active area of research since Gray's initial work in 1952.

In a recent review of LFC technology, Joslin (1998) notes that skin friction drag represents on the order of 50% of the total drag budget for a modern transport aircraft. Increasing the extent of laminar flow on such aircraft can potentially result in significant fuel savings, increased range and more environmentally responsible aircraft. In evaluating the possibilities for performance improvement in future aircraft, Green (2008) examines the theoretical and practical limitations on aerodynamic efficiency, propulsion efficiency and aircraft weight. Though there are gains to be had from further research into these and other areas, Green concludes that largest potential for

fuel-efficient aircraft is in continuing to develop LFC. Given the prevalence of swept wings in modern transport aircraft and the fact that crossflow instability is currently the largest obstacle in swept-wing laminar flow control (SWLFC), research in this area is of paramount importance in the ongoing effort to produce efficient aircraft.

A. Transition in Swept-Wing Flows

The study of laminar-to-turbulent transition is concerned with the processes by which small (often immeasurably so) disturbances provide the initial conditions for instability growth leading to breakdown. Though many scenarios are possible, the current understanding of the transition process may be summarized using the transition road map, the origin of which lies with Morkovin, Reshotko & Herbert (1994). The transition road map is also available as Fig. 1 in Saric *et al.* (2002). The first step toward transition is receptivity, or the process by which environmental disturbances produce disturbances in the flow (Morkovin, 1969). There are many things that may be classified as environmental disturbances: freestream turbulence, sound, surface roughness (either two or three-dimensional, isolated or distributed), surface non-uniformities (curvature discontinuities, for example) or other non-uniformities in the freestream quantities.

Early research on crossflow instability in different facilities produced results that varied in character. In a review by Reed & Saric (1989), it was concluded that the initial conditions provided by environmental disturbances played a large role in shaping the transition process for three-dimensional boundary layers. Significant effort has been expended in the intervening years on the receptivity problem and an improved understanding now exists. However, as will be argued following a review of relevant results in following sections, work still remains to be done in this area.

Following receptivity, the primary instability mode is physically manifested as a spanwise array of co-rotating vortices. In the context of a normal mode solution (Eq. 1.1),

$$q'(x,y,z,t) = q(y)e^{i(\alpha x+\beta z-\omega t)} + \text{complex conjugate} \tag{1.1}$$

linear stability theory demonstrates that these disturbances may be either stationary ($\omega = 0$) or traveling ($\omega \neq 0$). In practice, transition is dominated by either stationary or traveling waves (not both) and their respective initial amplitudes are set by the environmental conditions. Early experiments using a swept flat plate (Saric & Yeates, 1985) (with a contoured body on the opposing wall to generate the requisite streamwise pressure gradient) observed stationary crossflow waves whose spanwise wavelength was measured using hot-wire anemometry and flow visualization. These experiments were used to investigate the linear stability theory for the crossflow problem and found that crossflow wavelengths and disturbance growth rates were in reasonable agreement with the predicted values.

Crossflow waves have the effect of transferring streamwise momentum within the boundary layer, producing large mean flow distortions. The mean flow profiles become modulated in the spanwise direction: inflection points in the streamwise velocity profiles appear and are subject to a secondary instability. Kohama *et al.* (1991) observed this high-frequency instability upstream of the breakdown region in a swept-wing boundary layer. More recent experiments by White & Saric (2005) demonstrated that as many as five instability modes in the kilohertz range may coexist. Additionally, the rapid onset of transition was noted: the first observation of secondary instability was always followed by local breakdown within a few percent chord. A direct numerical simulation (DNS) of the primary and secondary crossflow instabilities was performed by Wassermann & Kloker (2002). In addition, these efforts

showed that the secondary instability is convective rather than fixed in space.

The traveling mode is also an important facet of the crossflow problem. Though (as will be shown) the stationary mode is more relevant to the flight environment, study of traveling waves has produced useful results. In one experiment by Takagi & Itoh (1994), the traveling waves were measured in the boundary layer of a yawed cylinder. The waves propagated in a direction opposite to the crossflow, which is perpendicular to the freestream flow. Deyhle *et al.* (1993) used a flush-mounted array of hot-film sensors to measure the phase speed and wavelength of traveling waves by rotating the sensor through several angles. It was found in this case that linear stability theory correctly predicts the velocity and wavelength of the traveling crossflow mode.

The present work is concerned primarily with the receptivity of swept-wing boundary layers to three-dimensional surface roughness and freestream turbulence, as well as the subsequent primary mode growth. Detailed discussion here is restricted to recent results concerning these aspects of the swept-wing transition process. A recent review by Saric *et al.* (2003) provides further discussion of the secondary instability, among other topics. In contrast to two-dimensional boundary layers, it has been demonstrated that three-dimensional boundary layers are insensitive to both sound and two-dimensional roughness. In their swept flat plate experiments, Deyhle & Bippes (1996) applied a two-dimensional strip near the neutral stability point and observed little change to the amplitude of traveling and stationary crossflow disturbances. In fact, the only spanwise region where these amplitudes are affected corresponds to the end of the two-dimensional roughness strip (which is itself a three-dimensional surface feature).

The receptivity of a swept-wing boundary layer to sound was tested by Radeztsky *et al.* (1999). Broad-band sound up to 95 dB produced no measurable change to the

transition location. Other frequencies (in the T–S unstable band, the most unstable traveling wave frequency and a secondary instability frequency) were tested with similar results. These results were confirmed by the experiments of Deyhle & Bippes (1996), who introduced 103-dB sound at the frequency of the most amplified traveling wave. Though the hot-wire measurements clearly showed the effectiveness of acoustic forcing in the freestream, the (much larger) traveling wave amplitudes in the boundary layer were unchanged and no change in transition location was observed. These observations led Deyhle and Bippes to conclude that the crossflow instability is most sensitive to the perturbations in streamwise vorticity provided by three-dimensional roughness and freestream turbulence.

1. Receptivity to Surface Roughness

The crossflow instability is largely insensitive to the spanwise vorticity created by two-dimensional roughness of modest height. However, a wide body of research exists demonstrating that the initial conditions produced by three-dimensional roughness can markedly alter the character of the resulting crossflow waves. One of the early key results comes from the experiments of Müller & Bippes (1989). In this swept flat plate experiment, crossflow waves are measured at a constant height above the plate surface across seven wavelengths. By translating the plate in the spanwise direction and repeating the measurements, it is determined that the crossflow waves must be initiated by surface roughness as the measured crossflow pattern moves with the plate. In a concurrent experiment, Dagenhart *et al.* (1989) examined the role of surface roughness in crossflow-induced transition in a swept-wing boundary layer. This experiment, which served as the foundation for many subsequent crossflow experiments, used a 45-degree swept wing with contoured wall liners designed to simulate an infinite-span swept-wing flow. It was found that transition was dominated by

stationary crossflow waves and occurred in a distinctive saw-tooth pattern. Changes to the incoming flow (achieved by changing the order of the wind tunnel screens, removing screens and cleaning the screens) did not change the transition pattern, nor did shifting the position of the model within the test section. It was concluded that minute variations in the surface roughness produced different initial disturbances across the span which in turn led to the model-fixed saw-tooth transition pattern.

Later experiments by Radeztsky *et al.* (1994) utilized spanwise arrays of discrete micron-sized roughness elements near the leading edge of the swept-wing model to produce uniform stationary crossflow vortices. Comparisons of the experimental data with linear stability theory produced good agreement for the stationary crossflow wavelengths and mode shapes. However, the disturbance growth rates are not well-described by linear stability theory and it was concluded that further calculations retaining the nonlinear terms were necessary. Continuing this work, Radeztsky *et al.* (1999) also made several important observations regarding distributed surface roughness. Measurements of transition location were made using naphthalene flow visualization for three levels of surface finish. Starting with a painted model (whose surface finish was characterized by peak-to-peak roughness of approximately 9 μm) and progressively polishing the surface to a root-mean-square (rms) roughness level of 0.25 μm, the transition location was observed to move downstream by over 30% of the chord length. This indicates the sensitivity of crossflow-induced transition to surface roughness. Using discrete roughness elements, it was also observed that the effectiveness of roughness in modifying transition is strongly related to the location of the roughness. The most effective location for the roughness is found to be within 1% chord of the first neutral stability point. The disturbance created by roughness upstream of this band decays; the disturbance created by roughness downstream of this location is too small to affect transition.

Spanwise arrays of discrete roughness elements (DREs) were a key feature in the experiments of Reibert *et al.* (1996). The roughness was applied in this case to control the initial conditions and produce a uniform series of crossflow vortices. In doing so, it was determined that roughness whose spanwise spacing, λ_k, was that of the most unstable wavelength (so-called critically-spaced roughness) was effective at inducing transition via growth of stationary crossflow vortices. The amplitude of these disturbances appeared to reach a plateau in advance of the transition location. This disturbance amplitude saturation is due to nonlinear interactions of the disturbances. In an effort to account for these nonlinear interactions, Haynes & Reed (2000) performed numerical calculations using nonlinear parabolized stability equations (NPSE). The utility of this approach is that the nonlinear terms are retained without incurring the computational expense of direct numerical simulation. Using the experimentally measured initial disturbances, the NPSE calculations correctly modeled the disturbance amplitude saturation confirming that it is due to nonlinear interactions.

Spectral analysis (in the spanwise direction) of the disturbances measured by Reibert & Saric (1997) indicates that the disturbances are composed of the roughness wavelength as well as its harmonics. By exciting longer spanwise wavelengths, interactions among the fundamental mode and its harmonics are observed. It is also noted that subharmonic disturbances are not observed. Building on this concept, Saric *et al.* (1998) used subcritically-spaced roughness (spaced at 2/3 of the most unstable wavelength, λ_{crit}) to suppress the growth of disturbances with this wavelength. This had the remarkable effect of delaying transition. Following this work, several experiments have sought to utilize these control DREs for laminar flow control. The direct numerical simulations of Wassermann & Kloker (2002) are able to provide further insight into the behavior of subcritically-spaced disturbances. The

resulting closely-spaced vortices saturate at a lower amplitude and do not deform the mean flow to the same extent as the longer-wavelength critical disturbance. These disturbances are thus not as susceptible to the secondary instability that brings about transition.

To test the effectiveness of subcritically-spaced roughness at higher Reynolds numbers in flight conditions, flight test experiments were performed by Saric *et al.* (2011). Using a 30-degree swept-wing model flown at a chord-based Reynolds number of $Re_c = 7.5 \times 10^6$, baseline tests demonstrated that natural transition occurred at approximately $x/c = 0.80$ when the leading edge is polished to an rms surface finish of 0.3 μm. However, a realistic wing would have a painted leading edge (and there is little improvement to be had with 80% laminar flow). When the model's leading edge is painted, the rms surface finish is 1 μm and transition is observed at approximately $x/c = 0.30$. As the flight environment is characterized by low freestream turbulence ($u'_{\text{rms}}/U_\infty \approx 0.05\%$ in this experiment), these results indicate the extreme sensitivity of the crossflow-induced transition to surface roughness in the absence of other significant sources of streamwise vorticity. When 12-μm-high control roughness elements (with $\lambda_k = \lambda_{\text{crit}}/2 = 2.25$ mm) are applied near the leading edge, the transition location is moved back to approximately $x/c = 0.60$.

These flight experiments also tested the effect of critically-spaced roughness on crossflow growth and transition (Carpenter *et al.*, 2010). The role of roughness height, k, on transition is not clear. Increasing k for critically-spaced roughness does not appear to have an effect below a critical value (24 μm) at which point transition moved from $x/c = 0.80$ to 0.15. Using pneumatic, variable-height roughness produced similar results. However, for the latter experiments, the stationary crossflow waves are measured using an array of surface-mounted hot-film sensors. These measurements confirmed that the roughness was exciting crossflow waves of the expected wave-

length. Further flight experiments are in progress (see Woodruff *et al.* (2011) for current results). The flow studied in these flight experiments is simulated in the direct numerical simulations of Rizzetta *et al.* (2010). In the vicinity of the leading-edge roughness, DNS is used to solve for the flow field and these results are used as an input to NPSE calculations. These computations are able to reproduce the experimental results (transition) to within about 10% chord. The computations investigated the disturbance growth produced by cylindrical, square and parabolic-bump roughness elements and found qualitatively similar behavior (on a logarithmic scale) for roughness elements of similar volume.

Recent wind tunnel experiments by Hunt & Saric (2011) sought to measure the initial disturbance amplitudes created by roughness at various heights. The goal of this work is to expand the database of receptivity measurements for use with computational tools (NPSE and DNS) for validation of these models. It was observed that the initial disturbance amplitudes increased linearly with k for measurements made upstream of $x/c = 0.20$. In this region, the disturbance amplitudes are small enough that the growth is well-described by linear stability theory. However, these experiments also uncovered new questions regarding receptivity to freestream turbulence.

2. Receptivity to Freestream Turbulence

As earlier experiments have shown, the crossflow instability is highly sensitive to streamwise vorticity. As is the case of three-dimensional roughness, freestream turbulence is an important source of this vortical disturbance for the crossflow problem. Early experiments concerning freestream turbulence and crossflow instability by Bippes (1990) used the same model in different wind tunnels. These facilities produce different levels of fluctuation in the freestream and comparison of the results indicated that the traveling mode appeared to be initiated by freestream turbulence.

It was observed that the traveling modes became the dominant instability in the higher-turbulence facility and that the stationary mode was attenuated.

These experiments are continued by Deyhle & Bippes (1996). Three different wind tunnel facilities (each characterized by different levels of turbulence) are used and the stationary and traveling mode amplitudes are measured in a swept flat plate boundary layer. A key result from this effort is that the traveling mode is the dominant instability for a freestream turbulence intensity $Tu > 0.2\%$, where Tu is defined by Eq. 1.2.

$$Tu = \frac{1}{U_\infty}\sqrt{\frac{1}{3}\left(u'^2_{\mathrm{rms}} + v'^2_{\mathrm{rms}} + w'^2_{\mathrm{rms}}\right)} \tag{1.2}$$

Similarly, it is observed that decreasing the level of freestream turbulence increases the saturation level of the stationary mode. This observation explains the remarkable result that modest increases to the freestream turbulence delays transition by reducing the growth rate of the stationary mode. However, this effect is transient and increasing the freestream turbulence intensity further moved transition forward. Bippes & Lerche (1997) conclude that the initial amplitude of the stationary mode is set by surface roughness whereas the initial amplitudes of the traveling modes are set by freestream turbulence. Thus, the traveling modes become the dominant instability in higher turbulence environments due to their higher initial amplitudes. They further conclude that growth of traveling modes is of low relative importance in low turbulence environments. In a review by Bippes (1999), these conclusions are confirmed. It is noted that although the steady disturbances are primarily excited by surface roughness, they depend on other environmental conditions in an as-yet not understood manner.

However, traveling waves may also be present in low-turbulence environments. Dagenhart & Saric (1999) measured traveling wave amplitudes up to 0.7% of the

local freestream velocity, but noted that the stationary mode amplitudes were always an order of magnitude larger. These observations were made in the Arizona State University Unsteady Wind Tunnel (ASU UWT) using a 45-degree swept-wing model, with Tu approximately 0.04% of the test speed. In an experiment designed to test the effect of boundary-layer suction on crossflow instability, traveling waves with amplitudes as high as 1% of the freestream speed are observed by Eppink & Wlezien (2011). The streamwise component of the turbulence intensity in this facility (NASA Langley Transonic Pressure Tunnel) is $u'_{\mathrm{rms}}/U_\infty = 0.02\%$ (Wlezien *et al.*, 1994) at the test speed; the transverse fluctuation intensities are not reported. The freestream u' spectra for the facilities used in these two experiments are compared by Wlezien *et al.* (1994). With the exception of a higher level of low-frequency oscillation (below 8 Hz) in the UWT, the spectra are similar. However, the larger contraction ratio in the TPT (20:1, compared with approximately 6.5:1 when swept-wing wall liners are installed in the UWT) may result in higher v' and w' components in the TPT experiments.

3. Combined Receptivity

Theoretical studies of the receptivity of a three-dimensional boundary layer to surface roughness, acoustic modes and freestream turbulence were undertaken by Crouch (1994). Traveling waves are excited by a combination of freestream turbulence and surface roughness. Crouch states that the freestream turbulence provides a temporal dependence to the steady disturbances created by surface roughness. This process sets the initial conditions for traveling mode growth. In an experiment designed to test the receptivity of a swept-wing boundary layer to both roughness and turbulence, Gladden (2001) and White *et al.* (2001) studied crossflow-induced transition in both low and high-turbulence environments. To do so, a turbulence-generating

grid was placed upstream of the model to raise the turbulence level to 0.25% (above the criterion given by Deyhle and Bippes for traveling wave dominance). When critically-spaced roughness is applied to the model, stationary-wave-dominated transition is observed as evidenced by the characteristic saw-tooth transition pattern. However, in the presence of increased freestream turbulence, the transition front moves forward and takes on a more uniform spanwise distribution, indicating that the traveling mode is the dominant instability. In the absence of artificial roughness, the transition appears to dominated by stationary waves in the presence of higher turbulence. However, when subcritically-spaced roughness is applied (using pneumatic variable-height roughness), the transition front becomes more uniform and moves forward. This indicates that in the presence of high turbulence, the control roughness actually enhances the traveling wave mode growth and brings about earlier transition (Saric *et al.*, 2003). These results serve as notice that the selection of traveling or stationary modes involves both surface roughness and freestream disturbances.

Direct numerical simulations of receptivity of a swept flat plate boundary layer to surface roughness and freestream turbulence are performed in the work of Schrader *et al.* (2009). Surface roughness is found to excite stationary crossflow modes, in general agreement with previous experiments. Additionally, freestream turbulence is found to excite traveling modes and this effect is more prominent at lower Reynolds numbers. When the two disturbances are considered in concert, roughness with $k/\delta^* = 0.025$ provides for stationary mode dominance in turbulence intensities up to 0.5%. This exceeds the Deyhle and Bippes criterion, indicating that surface roughness and freestream turbulence interact in an unknown manner to set the initial conditions. Tempelmann (2011) performed DNS of a swept-wing boundary layer to study the receptivity to surface roughness and freestream turbulence. The simulations are modeled using the experimental conditions of Reibert (1996). The receptivity prob-

lem is addressed by solving the adjoint of the linearized Navier–Stokes equations and freestream turbulence is modeled using inhomogeneous flow at the inlet boundary. Discrete roughness is modeled and the results are used to validate the computational technique. Although it is noted that the freestream disturbance environment may be prescribed, these simulations focus on optimal disturbances instead: those that produce the maximum spatial growth. It is found that the optimal disturbance is physically manifested as "streamwise-tilted vortices" that "smoothly evolve into the dominant crossflow mode" (Tempelmann, 2011). It is noted that for optimal disturbances, the swept-wing boundary layer studied is more receptive to surface roughness than freestream turbulence.

Recent experiments by Kurian *et al.* (2011) utilized discrete surface roughness and freestream turbulence (albeit separately) to test the receptivity of a swept flat plate boundary layer. In one portion of the experiment, Tu is varied between 0.23% and 0.58% using a series of passive grids. For all but the lowest value, traveling waves are the dominant instability. Furthermore, it was demonstrated that the initial disturbance energy scales with Tu^2, implying linear receptivity to freestream turbulence over the range tested. When spanwise arrays of cylindrical roughness elements are applied to the model, the stationary mode is found to the dominant feature. The stationary disturbance is decomposed into the roughness wavelength and its harmonics, although only the fundamental wavelength appears to grow. In contrast with the experiments of Hunt & Saric (2011), the initial disturbance energy scales with $Re_k^{2.3}$, which is equivalent to $k^{4.6}$ for small k. This indicates that receptivity to surface roughness is nonlinear for these experiments. However, it may be argued that the swept flat plate boundary layer is less sensitive to surface roughness than a swept-wing boundary layer due to the difference in the location of the neutral stability point.

This complicated dependence on initial conditions and nonlinear interaction of

disturbances makes transition prediction difficult. The e^N method of Smith and van Ingen (2008) is the standard transition prediction tool for two-dimensional boundary layers dominated by viscous instability. In this scenario, the disturbance growth is well-described by linear stability theory. The nature of crossflow-induced transition makes this method far less effective, although it may be used to evaluate relative disturbance growth rates for mode-selection purposes. At present, an effective tool for transition prediction in swept-wing boundary layers does not exist.

B. Motivation and Objectives

These efforts to understand the interaction of surface roughness and freestream turbulence in swept-wing boundary layers have led to the conclusion that both features must be considered. Recent wind tunnel experiments by Hunt (2011) and Hunt & Saric (2011) as well as flight experiments by Carpenter *et al.* (2010) have also raised questions regarding the effect of freestream turbulence with respect to roughness receptivity and stationary mode growth. Differences among the results of some of the recent crossflow stability experiments at ASU (Reibert & Saric, 1997; Saric *et al.*, 1998) and Texas A&M University (TAMU) (Carpenter *et al.*, 2010; Hunt, 2011; Hunt & Saric, 2011) indicate that minor differences in the freestream turbulence levels in the respective facilities may be responsible. Although the wind tunnel used for the ASU experiments was a low-disturbance facility (Saric, 1992), freestream turbulence levels in the Klebanoff–Saric Wind Tunnel (KSWT) used in the TAMU experiments are slightly lower (Hunt *et al.*, 2010). Additionally, transition results and streamwise fluctuation measurements in the flight environment obtained by Carpenter *et al.* (2010) indicate that the flow quality in flight is the highest of the three experiments.

The discrepancy among these experiments may be stated as such: the effect of

regular arrays of surface roughness on crossflow instability is somewhat different in each case. With respect to the height of critically-spaced roughness, Reibert (1996) notes that increasing k from 6 μm to 48 μm produces almost no change in transition location if the disturbance amplitude is already saturated at transition. The increased roughness height does, however, increase the initial disturbance amplitude and move the saturation location forward. In the experiments of Hunt & Saric (2011), increasing the roughness height moves transition progressively forward. Experiments (Bippes, 1999) have shown that increasing the freestream turbulence decreases the stationary disturbance saturation amplitude. Using this information, Hunt (2011) concluded that the lower (compared with ASU) freestream turbulence level in the KSWT may have produced a higher disturbance amplitude saturation level to explain the different transition behavior observed in the respective experiments. However, disturbance amplitude saturation had not yet been tested in the KSWT.

In the ASU experiments (Saric *et al.*, 1998), transition delay was achieved with subcritically-spaced roughness. This technique has found some success in the flight environment (Saric *et al.*, 2011) when a painted leading edge is used. However, wind tunnel tests in the KSWT have not yet demonstrated successful transition control with subcritical roughness. As the interaction between freestream turbulence and surface roughness is now thought to be an important facet of the crossflow problem, investigation of the effectiveness of control roughness in varying levels of freestream turbulence is needed. Finally, given the difference in roughness receptivity observed by Hunt & Saric (2011) and Kurian *et al.* (2011), there is some indication that the initial disturbance amplitudes created by surface roughness may be affected to some degree by the freestream turbulence environment.

Because other studies in elevated turbulence have focused on relatively high levels ($\geq$ 0.15%), the data that exist for Tu below this level are somewhat limited.

Turbulence intensity is an important characteristic for transition experiments, and it is now known that the length scales of the turbulence may also play a role (Kurian & Fransson, 2009). These scales are not always reported, making a careful comparison of experimental conditions impossible. This research will explore the effect of moderate freestream turbulence (0.02%–0.20%) on crossflow instability, particularly with respect to the initial disturbance amplitudes created by surface roughness, the disturbance amplitude saturation levels and transition location. The intensity and scale of the turbulence are documented to facilitate comparison with similar experiments and simulations. The goal of this research is to test the hypothesis that varying the turbulence intensity will affect transition location via modified initial disturbance amplitudes and saturation levels. In doing so, this research seeks to reconcile the differences among the aforementioned wind tunnel and flight test results.

C. Outline

This document describes a series of crossflow stability experiments in which the interaction between surface roughness and freestream turbulence as initial disturbance sources is investigated. Chapter I provides the background information necessary to motivate the present experiments. A review of relevant literature is given to provide context for these experiments and to describe the intended contribution of this work to the field of boundary-layer stability. These experiments are the first to test disturbance amplitude saturation levels in the KSWT. The effect of moderate changes to the freestream turbulence is quantified in the context of stationary and traveling mode growth to give a better understanding of their interaction. Finally, initial disturbance amplitudes are measured over a wider range of conditions for further validation of computational tools.

A detailed description of the experimental facility and wind tunnel model is given in Chapter II. The KSWT is the product of recent reconstruction, modification and renaming. The history of this unique facility is described and the flow-quality measurement campaign undertaken upon completion demonstrates the success of these efforts. The swept-wing model used for this research has been utilized by past cross-flow stability experiments. The product of lessons learned from similar experiments, this model is designed specifically for this class of experiment. Operational details concerning the model preparation and generation of controlled surface roughness are given.

Chapter III is a survey of the experimental techniques used in the course of this work. Flow visualization using a subliming surface coating (naphthalene) is described and the rationale and justification for this choice are given. Constant temperature anemometry is applied for flow measurement; hot-wire probes of several types are used to quantify streamwise and transverse components of turbulence intensity and turbulence length scales. A software filtering technique is used to separate these measurements into the acoustic and vortical contributions. The probe traversing system is also described as well as the methods of measuring the mean and fluctuating components of the boundary-layer velocity.

As generating turbulence of specific intensity is a large part of this work, Chapter IV is devoted to this effort. Briefly, a review of active and passive techniques for turbulence generation is given. The set of passive grids used for these experiments are cataloged. Measurement of the freestream turbulence is described and the intensity, spectral content and length scales are given.

Chapter V describes a series of test points intended to serve as baseline receptivity measurements for varying freestream turbulence. In these tests, no artificial roughness is applied to the model. Rather, the turbulence intensity is increased while the

initial disturbance amplitudes and transition locations are measured. This allows for more meaningful interpretation of the results when roughness and turbulence level are varied together. The interaction between artificial arrays of roughness and increased freestream turbulence forms the basis of Chapter VI. As before, initial disturbance amplitudes and transition are measured; the streamwise evolution of the resulting disturbances is used to draw conclusions regarding the effect of moderate levels of freestream turbulence on stationary disturbance amplitude saturation. Subcritically-spaced roughness is applied for notional control purposes and tested in an elevated level of freestream turbulence. The effects of roughness height and freestream turbulence on transition location are tested. Critically-spaced roughness is used to set the initial stationary disturbance and produce a uniform series of crossflow vortices for more effective study. Initial disturbance amplitudes are also measured to expand the database of these values and to give insight into the nature of the disturbances created by this roughness. Prospects for swept-wing laminar flow control given these latest results are also discussed.

The seventh and final chapter brings the results of these tests together to form a larger picture of the role of freestream turbulence and crossflow instability. Results are discussed in the context of previous work (primarily Deyhle & Bippes (1996) and Hunt & Saric (2011)). It is found that freestream turbulence plays an important role in crossflow instability mode growth, particularly in the growth of unsteady fluctuations in the boundary layer. Increasing freestream turbulence even slightly in a low-disturbance facility produces measurable losses of laminar flow on the test article. These results indicate the importance of the disturbance environment in which a crossflow experiment is conducted. Recommendations are made for future experiments.

CHAPTER II

EXPERIMENTAL SETUP

The sensitive nature of a stability experiment requires careful control of many factors. In their landmark experimental investigation on the origins of turbulence in a flat plate boundary layer, Schubauer & Skramstad (1947) observed that decreasing the level of freestream turbulence increased the extent of laminar flow. By installing turbulence-damping screens in the wind tunnel facility, the fluctuation levels were reduced from $Tu = 0.35\%$ to 0.03% and consequently, the Reynolds number at transition was raised from $Re_{x,tr} = 1.5 \times 10^6$ to approximately 2.8×10^6. This early stability experiment demonstrated the importance of having a low-level disturbance environment in which to conduct such research. This is particularly true for the present experiments, in which the role of freestream turbulence is of explicit interest.

In response to unexplained discrepancies in boundary-layer transition results among early stability experiments, the NASA transition study group was founded in 1970 (Reshotko, 1975). A set of guidelines was developed with the intent of fostering high-quality experimental results to help resolve these discrepancies. The guidelines stressed that the disturbance environment (as well as other facility characteristics) must be documented; disturbances introduced by the models themselves (via surface roughness, for example) must also be reduced if possible and documented. The basic rules for a successful stability experiment are given in detail by Saric (2007).

A. Wind Tunnel Facility

The present experiments are carried out in the Klebanoff–Saric Wind Tunnel at Texas A&M University. This unique facility has a long history of successful boundary-

layer stability experiments. The lineage of the wind tunnel starts with the Unsteady Wind Tunnel (UWT) that was built and operated by Phillip Klebanoff at the National Bureau of Standards. The wind tunnel had an unusual design feature: a secondary duct through which the test-section flow could be diverted to produce gusts and lulls. Following his retirement, the wind tunnel was moved to Arizona State University (ASU) in 1984 by Professor William Saric. During the reconstruction, several modifications were made to the wind tunnel with the intent of lowering the turbulence levels for the purpose of stability experiments. The flow quality measurements are documented by Saric (1992). Given the success of this effort, the wind tunnel became known as the ASU Transition Research Facility. The unsteady capabilities were retained and the name ASU UWT is common in the literature.

Several important experiments were completed in this facility at ASU. Some of these results are summarized in recent review articles (Saric *et al.*, 2002, 2003) concerning the stability of two- and three-dimensional boundary layers. The wind tunnel was once again moved in 2005 by Professor William Saric; this time to Texas A&M University. Based on the operational knowledge obtained during its tenure at ASU, several modifications were made to the wind tunnel to further improve the flow quality. These efforts and the results are documented by Hunt *et al.* (2010); a summary is given here. During this reconstruction, the secondary duct and related unsteady components were not installed. The immediate needs of the facility required only the steady (and low-turbulence) capability. The unsteady components remain in storage and will be installed at a future date; renewed interest in unsteady flows for applied research (micro-unmanned air vehicles and wind turbine flows, for example) will likely motivate this effort. To reflect this configuration change, the "Unsteady" modifier was dropped and the wind tunnel is currently known as the Klebanoff–Saric Wind Tunnel (KSWT).

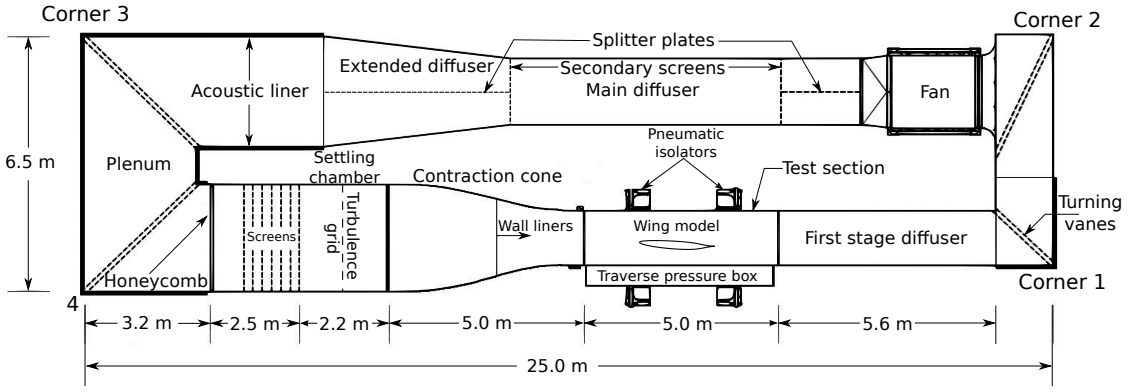

Figure 2.1: Top view of the Klebanoff–Saric wind tunnel. The flow direction is counter-clockwise. The turbulence grid, wall liners and swept-wing model reflect the setup of the present experiments.

The KSWT is a low-speed, closed-loop wind tunnel and is shown in plan view in Fig. 2.1. In its current configuration, the top speed is approximately 32 m/s. At its entrance, the test section measures 1.37-m square; the floor drops by 51 mm over the 4.88-m length to minimize the streamwise pressure gradient that would otherwise result from the increasing thickness of the wall boundary layers. The test section rests on pneumatic vibration isolation pads to attenuate the effects of environmental vibration from the motor or neighboring activity. The first-stage diffuser at the test section exit has been redesigned with a smaller diffusion angle and has a full-length splitter plate. In the ASU installation, this section was a source of flow unsteadiness caused by separation, though its effect on test section flow quality was small. The current diffuser is built in a modular fashion to accommodate installation of the shutters for the unsteady configuration. The smaller diffusion angle required a re-designed first corner along with a re-shaped contraction leading into the second corner.

The fan and motor section is also largely re-designed compared with the ASU installation. The 1.83-m-diameter fan is now externally driven by the 150-hp motor via a v-belt drive system. Previously a direct-driven system, installing the motor

outside of the tunnel airflow removed a significant source of heat and noise. The motor is housed in a ventilated enclosure that is lined with egg–crate–style acoustic foam. Though this system is more mechanically complex, it allows for longer run times at high speed. Due to frictional heating of the air, it is possible to exceed temperature limits on tunnel instrumentation (in particular, the differential pressure transducer is limited to 40°C) if the tunnel is run near its top speed for several hours on a hot day. This installation also allowed the fan nacelle to be re-designed; it now follows the shape of a fifth-order polynomial with zero slope and curvature at each end.

The main diffuser expands vertically to a rectangular duct 1.68 meters wide by 3.66 meters high. The extended diffuser expands horizontally such that the plenum section is 2.74 meters wide by 3.66 meters high. Each of these diffusers have full-length splitter plates and two secondary screens are installed in the main diffuser to address an area of flow separation observed in the extended diffuser. The constant-area plenum is lined with broadband-absorbing acoustic panels and open-celled foam to attenuate the sound from the fan and motor. In addition, the turning vanes in corners 1, 3 and 4 are filled with fiberglass insulation exposed to the airflow via slotted faces to further reduce the level of acoustic fluctuation. Though the crossflow instability is largely unaffected by sound, this facility is also used for two-dimensional boundary-layer stability experiments. It is well known (Saric *et al.*, 2002) that 2D boundary layers are receptive to sound and the excitation of T–S waves with acoustic forcing (a common experimental technique) benefits from a low level of background noise.

Following the last corner, the airflow encounters a honeycomb flow straightener. This aluminum honeycomb has 6.35-mm hexagonal cells and is 76 mm in streamwise extent. After a short settling distance (0.84 m) is a series of seven high-tension

screens, each separated by 0.23 m. These screens are woven from stainless steel wire of 0.0065-inch-diameter (0.165 mm) and evenly spaced at 30 wires per inch. This produces an open-area ratio of 65%. These dimensions follow the recommendations given by Saric & Reshotko (1998) for low-turbulence wind tunnel design.

Screens may be used to increase turbulence, but in this application the wire diameter is small enough that vortex shedding is avoided due to the low-speed flow in this area. Rather, these screen damp turbulence by improving the uniformity of the flow. The Reynolds–Orr energy equation (Eq. 2.1) describes the rate of change in the kinetic energy of a velocity perturbation u_i' (Drazin, 2002). The second term is always positive and thus contributes to perturbation energy decay; this viscous term dissipates energy. The first term represents production of perturbation kinetic energy. Increasing the flow uniformity decreases $\partial U_j/\partial x_i$ in the production term. Following the last screen is a settling chamber that is 2.19 m in streamwise length. In this section, viscous dissipation acts to remove the small-scale disturbances in the flow. Finally, a contraction section (contraction ratio of 5.33:1) completes the flow quality treatments and accelerates the flow entering the test section.

$$\frac{\mathrm{d}E}{\mathrm{d}t} = -\int_V \underbrace{\left[\frac{1}{2}\left(\frac{\partial U_i}{\partial x_j} + \frac{\partial U_j}{\partial x_i}\right) u_i' u_j'\right.}_{\text{production}} + \underbrace{\left.\frac{1}{Re}\left(\frac{\partial u_i'}{\partial x_j}\right)^2\right]}_{\text{dissipation}} \mathrm{d}V \tag{2.1}$$

The freestream speed in the test section is set using velocity feedback from a pitot-static tube mounted on the non-test side wall. This instrument provides static pressure measurement via an MKS Baratron 1000-torr absolute pressure transducer with a 270B signal conditioner. Dynamic pressure measurement is through an MKS 10-torr differential pressure transducer with a 670 signal conditioner. These transducers (type 390HA-01000SP05 and 698A11TRA, respectively) have specified accuracies of 0.05% of the reading. An Omega RTD is mounted near the pitot-static tube

to measure the freestream temperature and has a specified accuracy of 0.15°C. Using standard error propagation techniques, the relative uncertainty in the freestream speed measurement is 0.4% to 1%, depending on temperature.

The data acquisition system consists primarily of three National Instruments USB-6211 DAQ boards. This system provides up to 24 analog voltage inputs at 16 bits of resolution. Variable voltage ranges are possible, up to ±10 V. During tunnel operation, the averaged values of the freestream quantities p, T and q are used to compute the freestream speed at 1 Hz. The motor speed is adjusted using an automated routine to maintain a constant flow velocity. An additional routine is available that uses Sutherland's formula to compute viscosity and adjust the speed to maintain a constant Reynolds number (such that the speed gradually increases as temperature and viscosity increase). In the present experiments, constant Reynolds-number control is used. Motor control is accomplished with a Quantum III controller and the motor speed can be set with 0.1-rpm precision.

Constant temperature anemometry is used for boundary-layer measurements: Dantec Dynamics hot-wire probes are used in conjunction with an AA Labs AN-1003 anemometer. The probe types used in the present experiments are 1.25-mm-long single-normal (SN) wires (55P11 for freestream measurement and 55P15 for boundary-layer measurement) and 55P61 X-wires for transverse velocity measurement. The sensing elements are 5 μm in diameter. Further details concerning the use of these probes are given in Chapter III. Due to their high-frequency response rates (on the order of 150 kHz or higher) and unintrusive size, these probes are the preferred tool for making the freestream turbulence intensity measurements that are used to characterize this wind tunnel. The recommendation of Saric & Reshotko (1998) for a low turbulence tunnel is that $Tu \leq 0.05\%$.

Toward that end, a series of flow quality measurements are made and docu-

mented by Hunt *et al.* (2010). Important results are summarized here. Fluctuations in the freestream velocity are measured using constant temperature anemometry. These measurements are made in an otherwise empty test section (baseline measurements are repeated when the swept-wing model is installed). Focusing first on the streamwise component, two single-normal hot-wire probes are used to make redundant measurements. The probes are placed in a streamwise plane 0.23 m downstream of the test section entrance. Separated by 1.15 m near opposite corners of the test section (though far enough from the walls to avoid the boundary layers here), these probe measurements are used to separate the signals into acoustic and turbulent components. The fluctuating voltage signals are amplified by 30 dB and filtered using a 1 Hz to 10 kHz passband. The streamwise components of the fluctuation intensity at several speeds are given in Table 2.1.

U_∞	u'_{rms}/U_∞ (%)		
	Probe 0	Probe 1	Uncorrelated
5 m/s	0.031	0.052	0.048
10 m/s	0.051	0.059	0.041
15 m/s	0.083	0.083	0.017
20 m/s	0.102	0.098	0.022
25 m/s	0.143	0.131	0.030

Table 2.1: Streamwise component of velocity fluctuation intensity: total values and uncorrelated contributions. A 1 Hz to 10 kHz passband is used. Results are for an empty test section.

These values are as much as three times higher than the recommendation. However, when the optimal filtering technique of Naguib *et al.* (1996) is applied to these

measurements, the uncorrelated component is shown to be of acceptable magnitude. This optimal filtering technique requires that two signals are measured at locations separated by a distance greater than the largest turbulent length scale. In this case, the probes are separated by the largest practical distance possible while in the same streamwise plane. The software filter is then used to compute the correlated and uncorrelated parts of these signals. The correlated part represents pressure fluctuations that are experienced by both probes, while the uncorrelated component is attributed to the vortical component of the fluctuations. The uncorrelated component is a better measure of the streamwise turbulence intensity. The intensities of the uncorrelated components are given in Table 2.1. Across this range of speeds, these values all meet the recommended value for a low-turbulence wind tunnel.

Although the streamwise turbulence intensity is often used to represent the total turbulence level, this practice may obscure important information regarding the disturbance environment. For example, nozzles with large contraction ratios can be used to produce flows with very low levels of streamwise velocity fluctuation at the expense of high transverse fluctuations. When characterizing the flow quality, all three components of the fluctuation intensity should be measured. Toward that end, double yawed hot-wire probes of the X-wire type are used to measure v' and w'. As before, the fluctuating components of these measurements are acquired using a 30 dB gain and filtered using a passband of 1 Hz to 10 kHz. The transverse components of the fluctuation intensities are given in Table 2.2. As these components are not influenced by the streamwise pressure variations that produce high u'_{rms} values, the transverse components are a better representation of the turbulence intensity. Using Eq. 1.2, Tu is computed at each speed using the uncorrelated part of u'. These values fall well below the recommended maximum value.

Normalized rms values of turbulence intensity are a convenient measure of the

U_∞	u'_{rms}/U_∞ (%)	v'_{rms}/U_∞ (%)	w'_{rms}/U_∞ (%)	Tu (%)
5 m/s	0.048	0.015	0.013	0.030
10 m/s	0.041	0.010	0.012	0.025
15 m/s	0.017	0.011	0.016	0.015
20 m/s	0.022	0.015	0.019	0.019
25 m/s	0.030	0.019	0.023	0.024

Table 2.2: Baseline turbulence intensity measurements for an empty test section. A 1 Hz to 10 kHz passband is used and the u'_{rms} values represent the uncorrelated part of the signal.

fluctuation intensity. However, the frequency spectrum of these fluctuations provides additional information characterizing the disturbance environment. The power spectral densities (PSD) of the velocity fluctuations are plotted in Fig. 2.2. The complete u' signal is plotted along with the uncorrelated component. As the plot shows, the difference between the two is primarily due to low-frequency (10 Hz and less) oscillations that are correlated across the measurement plane. As before, these measurements are made in an empty test section. These turbulence measurements justify the use of the KSWT as a low-disturbance facility. Baseline turbulence measurements are repeated once the test model is installed. These measurements are discussed in detail in Chapter IV.

B. Swept-Wing Model

Experimental studies of crossflow instability have utilized several types of test models. The crossflow instability may exist in the boundary layers of rotating disks or bodies of revolution, yawed cylinders, swept flat plates and swept wings. Important advances in this area of research have been made using all of these types of models.

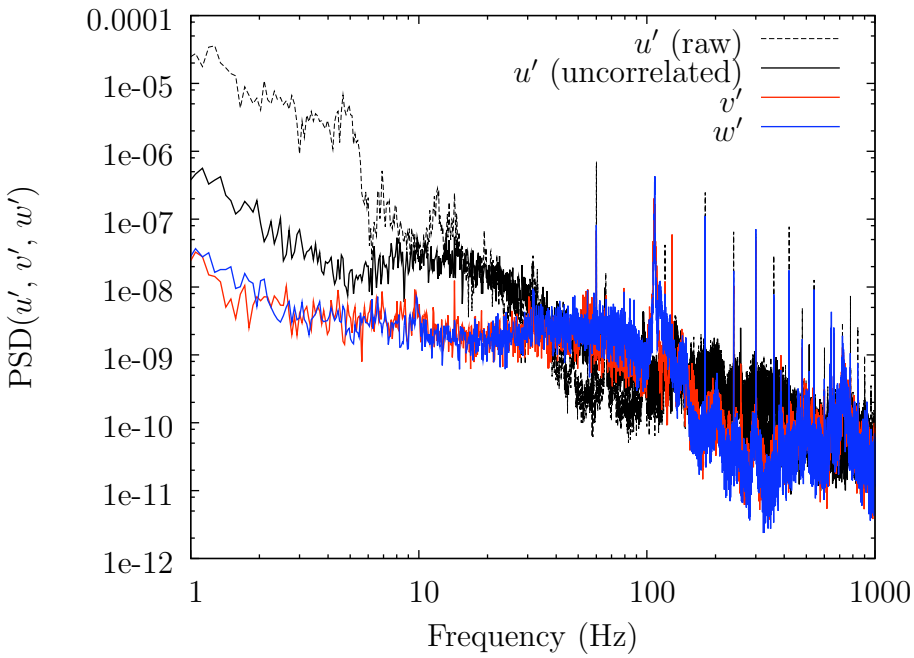

Figure 2.2: Temporal PSDs of velocity fluctuations measured at $U_\infty = 20$ m/s. These baseline measurements are made in an empty test section.

The study of crossflow instability in a swept-wing boundary layer is the most readily applicable to the field of aircraft design. Although some of the model problems have simpler experimental setups, they have some drawbacks as well. The swept flat plate boundary layer, for example, is less sensitive to surface roughness due to the position of the neutral stability point. The swept-wing model of the present experiments balances flight applicability with concessions to experimental simplicity. This model was designed by Mark Reibert at ASU and has been used in several earlier stability experiments at ASU (White & Saric, 2005; Gladden, 2001) and TAMU (Hunt & Saric, 2011).

Although the model for these experiments is based on one of the standard NACA 6-series NLF airfoils, its design is modified to enhance the growth of the crossflow instability for experimental purposes. The airfoil shape is designated as ASU(67)-

0315; since the airfoil is somewhat modified, it does not carry the NLF designation. The first digit signifies that the airfoil is from the 6-series. The second digit signifies that the location of the pressure minimum is closest to 70% x/c. The third and fourth digits indicate that low-drag is attained at a lift coefficient $c_l = 0.3$ and the last two digits give the maximum airfoil thickness as $0.15c$ (unswept).

To maximize the crossflow for experimental purposes, the pressure minimum is placed as far downstream as reasonable, as a favorable pressure gradient destabilizes the crossflow instability and inhibits the growth of T–S waves. Furthermore, concave curvature is avoided upstream of 70% chord to avoid destabilizing the Görtler instability. The airfoil is swept at $\Lambda = 45°$; larger sweep angles would enhance the crossflow instability but make experimental measurements increasingly awkward. The leading-edge radius is approximately $r = 23$ mm and the ellipse ratio is $e = 3.05$. The criterion for avoiding contamination of the attachment-line flow by the wall boundary layer is reviewed by Saric *et al.* (2011). The critical attachment-line Reynolds number, $\overline{R}_{\text{crit}}$ must be kept below 250 for stability. This form of the Reynolds number is defined in Eq. 2.2. For a test point of $Re_c = 3.6 \times 10^6$ (the highest chord-based Reynolds number attainable with this model in this facility), $\overline{R} = 88$ and attachment-line contamination is avoided. As such, this airfoil is subcritical to all but the crossflow instability.

$$\overline{R} = \left(\frac{U_\infty r \sin\Lambda \tan\Lambda}{\nu\,(1+e)} \right)^{1/2} \tag{2.2}$$

The physical realization of this swept airfoil is a 1.83-m-chord model constructed primarily of aluminum and fiberglass-covered foam. A schematic of this model is shown in Fig. 2.3. A support shaft runs through the model, parallel to the leading edge. This shaft is keyed into a test-section-mounted bearing that allows the model pitch to be adjusted. The frame and leading edge are machined from aluminum while aft sections of the model (where the quality of the surface finish is less important

for stability experiments) are constructed from fiberglass. As shown in Fig. 2.3, a modular leading-edge insert that extends to $x/c = 0.23$ forms the mid-span region of the model. The leading-edge insert used for the present experiments includes a thin roughness insert that extends from approximately 1.9% to 4.0% x/c. For the present configuration, the neutral stability point is located at 2.5% x/c. Several roughness inserts are available and a blank insert is used with appliqué-type roughness for these experiments. The roughness insert, leading-edge insert and leading 9% of the model (all exposed aluminum) are hand polished to a 0.3-μm-rms surface finish. Further details concerning the model surface preparation and installation are given by Hunt (2011).

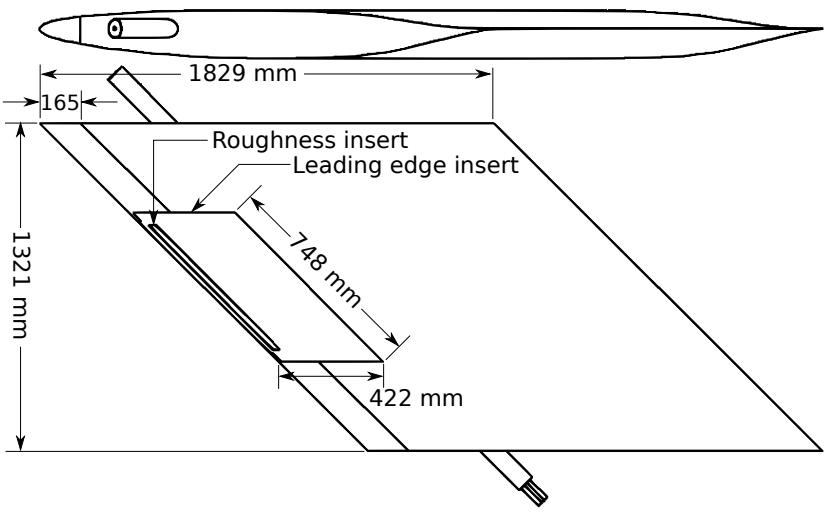

Figure 2.3: Schematic view of the ASU(67)-0315 45-degree swept-wing test model. Dimensions are in mm.

The swept-wing model is designed for zero lift at $\alpha = -3^\circ$ using the leading-edge coordinate system, or $\alpha = -2.1^\circ$ in the test-section-fixed, or global coordinate system. However, miscommunication between researchers engaged in computational and experimental efforts resulted in the zero-lift angle being interpreted as -3° in the global

coordinate system by the latter. To be clear, all angles of attack described henceforth are measured in the global coordinate system unless otherwise noted. Operational experience at ASU obtained prior to designing this model led to the conclusion that a zero-lift configuration simplifies the experimental setup while maintaining strong crossflow growth. The model is installed vertically in the test section at a realized angle $\alpha = -2.9°$ (such that the model is pitched $-0.8°$ from the true zero-lift angle). This orientation provides easier access to the test side of the model for boundary-layer measurement and decreases the amount of dust that settles on the model (such dust acts as isolated roughness elements that affect the disturbance growth). The position of the model relative to the test section is shown in Fig. 2.4, along with measured dimensions of the final model placement. The model is mounted slightly off-center to avoid the potential rotational node at that location (Saric, 2007).

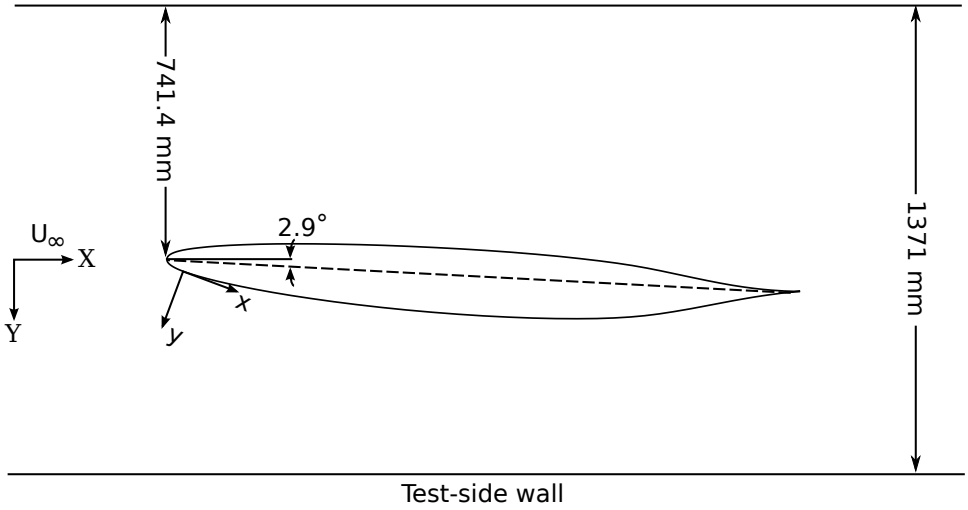

Figure 2.4: Top view of the swept-wing model location in the test section.

To simplify measurement of the basic state, additional consideration is given to setting up a spanwise-invariant mean flow. The model is designed with a constant chord length, whereas real swept wings are usually tapered. More importantly, con-

toured wall liners are built and attached to the test section floor and ceiling. The wall-liner shapes follow computational results for the streamlines around an infinite-span swept wing at $\alpha = -3^\circ$ (relative to the leading-edge coordinate system). Constructed of fiberglass-covered foam, these wall liners increase the contraction ratio from 5.33:1 to 6.9:1. The liners are the length of the test section and extend into the contraction cone to avoid forward-facing steps, as shown in Fig. 2.1.

To verify the spanwise-invariant mean flow, the pressure distribution is measured in the streamwise direction. The swept-wing model has two rows of 29 pressure ports in spanwise locations above and below the leading-edge insert. With the wall liners installed, the pressures are measured using a Pressure Systems model ESP-32HD pressure scanner, whose accuracy is 0.037 torr. The reference pressure p_∞ is acquired using the static port on the pitot-static tube. The coefficient of pressure is computed in the global coordinate system as in Eq. 2.3.

$$C_{p,3} = \frac{p - p_\infty}{\frac{1}{2}\rho U_\infty^2} \tag{2.3}$$

Computational efforts often use the leading-edge coordinate system to compute the two-dimensional coefficient of pressure, $C_{p,2}$. Here, the normalizing freestream speed is $U_\infty / \cos\Lambda$. Thus, in the present experiments, these coefficients of pressure are proportional by a constant of 0.5. The pressure distribution measured by Hunt (2011) is shown in Fig. 2.5 for a test point of $Re_c = 2.8 \times 10^6$. That these values agree within experimental uncertainty indicates that the assumption of spanwise invariance is valid. Furthermore, these data indicate that the favorable pressure gradient extends to the design-point pressure minimum near 70% x/c. Comparison with computational results in Hunt & Saric (2011) shows close agreement between the two.

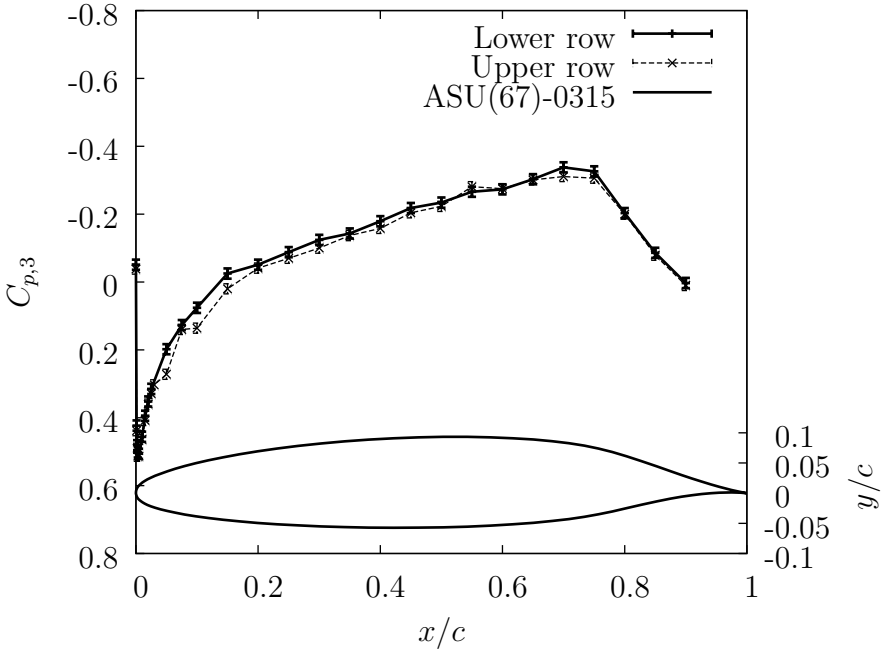

Figure 2.5: Measured values of the pressure coefficient $C_{p,3}$ at $Re_c = 2.8 \times 10^6$. Data are from Appendix B of Hunt (2011). The plotted airfoil shape is in the unswept coordinate system.

C. Artificial Surface Roughness

The experiments of Radeztsky *et al.* (1999) demonstrate that natural surface roughness can affect crossflow-instability-induced transition. Additionally, these experiments show that roughness is most effective when it is near the neutral stability point. Based on these findings, the leading edge of the model used in the present experiment is polished to a high level of surface finish. This provides a controlled environment in which the effects of artificial roughness may be studied. Spanwise arrays of roughness elements are used to control the initial conditions and produce uniform crossflow waves, as in previous experiments (Saric *et al.*, 1998). Additionally, the effect of roughness height and spacing on the receptivity of the boundary layer is of interest. To investigate this, appliqué roughness is used; this type of roughness has

been used in previous wind tunnel (Reibert & Saric, 1997; Saric *et al.*, 1998; Hunt & Saric, 2011) and flight (Saric *et al.*, 2011; Carpenter *et al.*, 2010) experiments.

The nominally-cylindrical roughness is used because of its inherent geometric simplicity and its known effectiveness. Previous experiments have shown that roughness whose diameter d is 40% to 50% of the spanwise wavelength λ is the most effective. In the present experiments, critically-spaced roughness with $d = 3$ mm and $\lambda = 12$ mm is used. Although the effect of roughness height k is not completely understood, values between 6 μm and 48 μm can excite the crossflow instability without producing a bypass-type transition. These dimensions are shown for a typical roughness array in Fig. 2.6. To maintain consistency with earlier references, the nomenclature used for a given roughness array is $[k|\lambda|d]$.

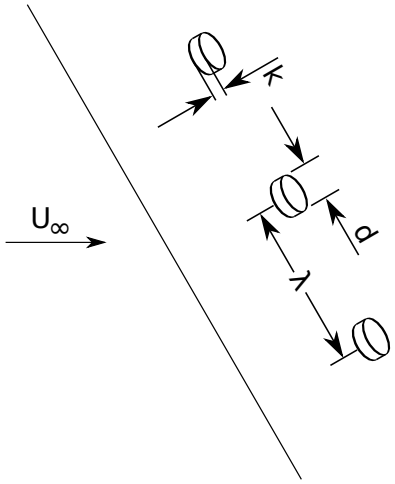

Figure 2.6: Schematic drawing of a spanwise roughness array. The roughness height k is exaggerated for display purposes.

The physical realization of this roughness is produced using a dry transfer ink common in the graphic arts community. Grids of specified roughness are purchased from REDD Europe, Ltd. and cut into single rows for application using a rub-on

technique. The roughness elements may also be stacked to increase k. Though batch-to-batch variability in k is known to exist, a typical single layer of roughness is approximately 12 μm high. Laser scanning microscopy has been used in previous experiments (Hunt & Saric, 2011) to measure the roughness height. Full-span arrays of roughness are applied to the roughness insert, centered at $x/c = 0.029$.

D. Coordinate Systems

Some consideration must be given to the coordinate systems used in this work. Three such systems will be used as appropriate, and it is important to make the distinction in order to facilitate comparison with results of computations or other experimental efforts. As depicted in Fig. 2.7 for a wing with sweep angle Λ, the three coordinate systems are streamline-oriented, model-oriented and test-section-oriented (or global). The streamline-oriented system is denoted by (x_t, y_t, z_t) and the corresponding velocity components are (u_t, v_t, z_t). This system is aligned such that the x_t axis is tangent to the local streamlines and as such, its orientation changes with location. Using a right-handed system, the positive y_t direction is generally (but not exactly, as it varies with local curvature) out of the page.

The use of a model-fixed coordinate system is convenient for computational studies. In this system, the axes are named (x, y, z) and the velocities are (u_n, v_n, w_n). The x direction is defined as normal to the leading edge and y is normal to the model surface. As before, a right-handed coordinate system is used. However, this system of coordinates is cumbersome for experimental measurements. The global coordinates defined by (X, Y, Z) in which the velocities (u, v, w) are measured form a more straightforward system for this purpose. These coordinates are fixed to the test section (and more importantly, the probe traversing mechanism). The X axis is parallel

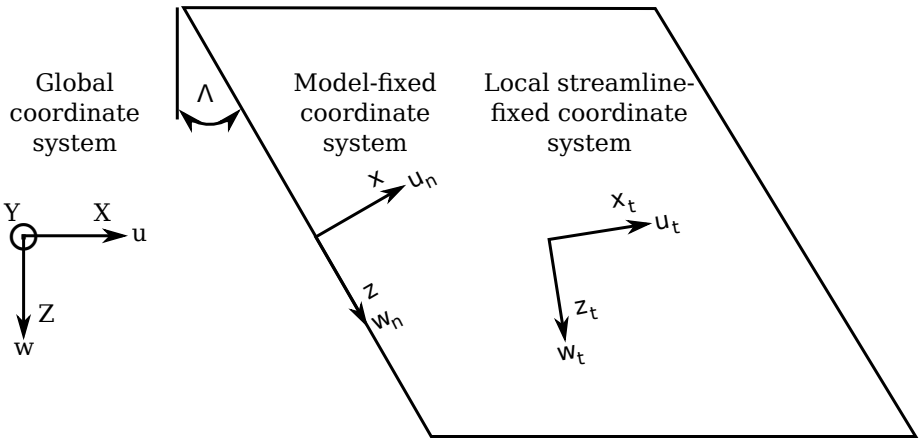

Figure 2.7: Coordinate systems and conventional swept-wing nomenclature.

to the freestream flow direction and the positive Y axis points at the test-side wall of the test section. The use of a right-handed coordinate system makes Z point down when the flow is from left to right (as in the present experiments).

For highly-resolved measurements of boundary layers, it is most convenient to work in a system defined by (x/c, Y, z). Although measuring velocity as a function of y would better facilitate comparison with computational and theoretical work, this is difficult from an operational standpoint. The y axis is defined as normal to the model surface and as such, changes with streamwise location, though this is not an insurmountable obstacle. The thin boundary layers encountered in these experiments (typically less than 5 mm) require that very small steps (on the order of 10 μm) are taken for near-wall measurements. To accomplish such a feat in the y direction, the required traverse movement would consist of steps in X and Y. The traverse resolution in the Y axis is equal to this task, but the approximately 1 μm step in the X direction is not possible with the present setup. The X range of the traverse must be on the order of the chord length of the model; micron-resolution across this range is comparatively difficult to attain. As such, boundary-layer velocity is measured

as a function of Y. Because y and Y are not separated by large angles (except in the vicinity of the leading edge) this measurement scheme is deemed an acceptable concession. The traverse mechanism (described in greater detail in Chapter III) is capable of multi-axis movements. As z is fixed by the sweep angle, measurements in a (Y, z) plane are easily accomplished.

CHAPTER III

EXPERIMENTAL METHODS

A successful experiment should include multiple forms of measurement when possible, for the sake of independent verification. In the present experiments, two types of measurement are primarily used: flow visualization using a sublimating surface coating and hot-wire anemometry. The flow visualization is used for its ability to provide a rapid measurement of the transition location. It can also be used to measure the spanwise wavelength of stationary crossflow vortices under certain circumstances. Hot-wire anemometry is used for quantifying the freestream turbulence levels and for finely-resolved measurements of the boundary-layer velocity profiles. Single-normal (SN) probes and X-wire probes provide a redundant measurement of u'_{rms}. The boundary-layer measurements can be used to verify the location of transition as determined by the flow visualization. Each of these tools are chosen because they are appropriate methods of accomplishing their respective tasks; their overlapping utility is an additional benefit.

A. Flow Visualization

There are many methods for visualizing or otherwise measuring the transition location. Since turbulent flow is characterized by higher wall shear stress τ_w, a higher rate of convective heat transfer and an increased rate of mixing when compared with laminar flow, a transition measurement scheme need only exploit one of these differences. Infrared (IR) thermography has been used successfully to measure transition by placing a model in an air stream of different temperature (as in Carpenter *et al.* (2010), for example). Arrays of surface-mounted hot-film sensors may also accomplish

this measurement; turbulent flow will appear with higher shear stress in the mean flow and increased high-frequency fluctuations in the temporal spectra. This technique has been used in a number of wind tunnel experiments (Agarwal *et al.*, 1992; White *et al.*, 2011). Other techniques include liquid crystal coatings and oil-film interferometry; these are somewhat awkward to use and introduce other problems (Saric, 2007). A thorough review of transition detection techniques for in-flight measurement is given by Mavris *et al.* (2010). A detailed feasibility study in that work concludes that IR thermography and surface-mounted thermocouples are the most attractive options for monitoring the performance of laminar flow control systems. However, both of these techniques require a modest temperature difference between the air and the wing (or test model).

Naphthalene flow visualization (NFV) is one technique that has been used in similar experiments for transition detection (Radeztsky *et al.*, 1999; Hunt & Saric, 2011). As with any chemical, the proper safety precautions *must* be observed. Solid naphthalene sublimes at a rate that increases with temperature and shear stress. As a result, when applied to an object in an airflow, naphthalene sublimes more rapidly in regions of turbulent flow. To accomplish NFV in the present experiments, naphthalene is dissolved in a solvent and sprayed onto the swept-wing model. Using a light, even spray, the solvent evaporates almost immediately leaving a thin coat of solid naphthalene on the model. The mixture is not applied to the leading 25% of the model, as the surface coating it produces has a higher level of surface roughness that may affect transition. Additionally, the mixture is only sprayed in the spanwise region between the pressure port rows: this is the usable measurement region.

Taking into account the mass of naphthalene used, its density and the approximate surface area over which it is applied, the resulting coating has an average thickness of 13 μm. The successful use of this technique has been verified by Dagen-

hart & Saric (1999), who used a shear-sensitive liquid crystal coating and hot-wire anemometry to confirm the transition location determined using NFV. Radeztsky *et al.* (1999) demonstrated that crossflow-induced transition is less sensitive to surface roughness a few percent chord aft of the neutral stability point. At $x/c = 0.25$, the boundary-layer thickness is approximately 3 mm for $Re_c = 2.8 \times 10^6$. The surface roughness created by the naphthalene does not modify the stability characteristics of the flow when it is applied this far downstream of the neutral stability point.

In addition to detecting transition, NFV may also be used to identify the wavelength of stationary crossflow vortices. These co-rotating vortices produce a surface shear stress pattern that alternates in the spanwise direction. This is shown conceptually in Fig. 3.1. Because the naphthalene sublimes more rapidly in areas of higher shear stress, streaks will form in the surface coating spaced at the crossflow vortex wavelength. This pattern is shown in the bottom of Fig. 3.1 and an experimental example of this is given in Fig. 3.2. In this photograph, the flow is from left to right and the left edge of the naphthalene coating is near $x/c = 0.30$. As the shear stress produced by the crossflow vortices is less than the turbulent shear stress, these streaks typically form well after the transition pattern has emerged.

B. Hot-Wire Anemometry

The use of hot-wire anemometry for boundary-layer stability experiments is a common choice. The probes are typically very small (thus their influence on the flow is minimal) and they have high rates of frequency response. Optical measurement techniques such as particle image velocimetry or laser Doppler velocimetry that rely on seed particles are not well-suited for this type of experiment due to the difficulty in entraining a sufficient number of particles in the boundary layer. Similarly, pressure-

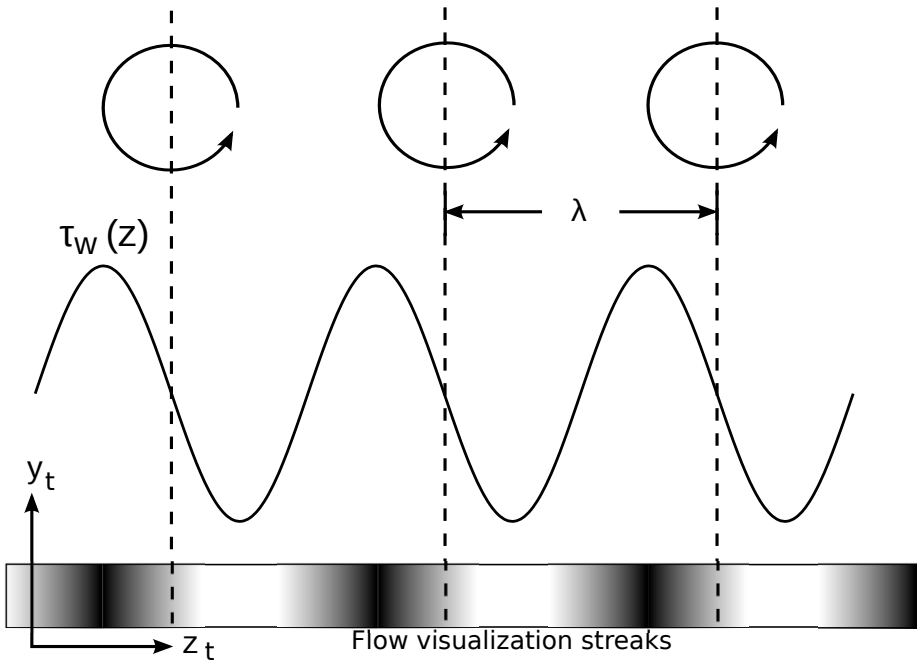

Figure 3.1: Conceptual drawing of the surface shear stress induced by stationary crossflow vortices. Adapted in part from Agarwal *et al.* (1992).

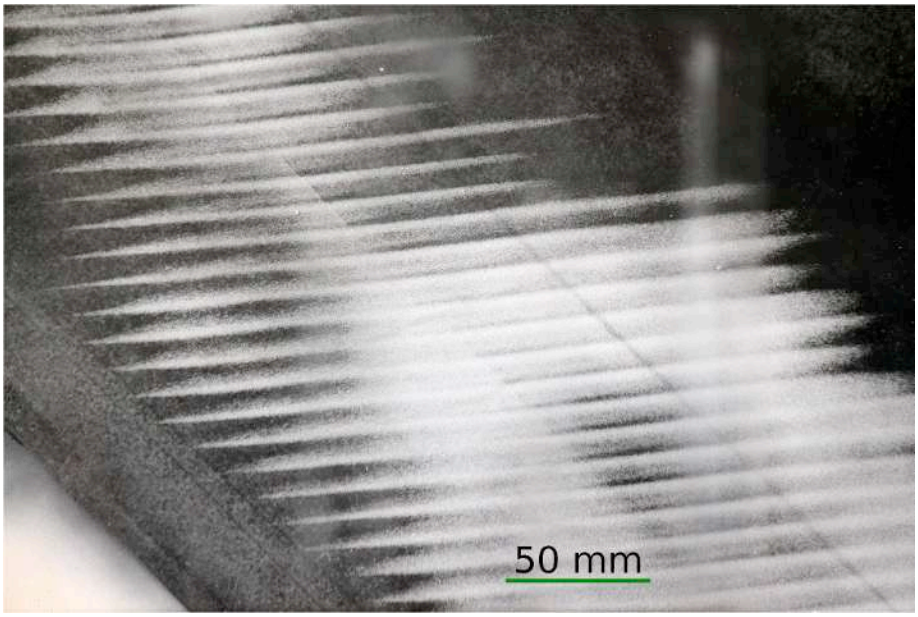

Figure 3.2: Flow visualization streaks from stationary crossflow vortices.

based measurements using boundary-layer rakes or similar devices either cannot provide the necessary spatial resolution or present too great a disturbance themselves. Miniature hot-wire probes are the best choice for taking dense grids of measurements inside millimeter-sized boundary layers.

The principle behind hot-wire anemometry is that the rate of heat transfer between a heated object and the fluid in which it is immersed is related to the fluid velocity and temperature difference (among other quantities). For a hot-wire probe of sufficient length, this relationship may be modeled as an infinite cylinder in cross-flow. The standard empirical correlation describing the heat transfer in this scenario is given by Eq. 3.1. In this expression, the Nusselt number Nu is a dimensionless ratio of the convective and conductive heat transfer coefficients, hd/k, while A and B are constants. For a long cylinder (where end effects are negligible) of resistance R that is heated electrically by a current I, the heat transfer equation is developed by Bruun (1995) and given in Eq. 3.2.

$$Nu = A + BRe^{1/2} \tag{3.1}$$

$$I^2R = \pi lk(T_w - T_a)Nu \tag{3.2}$$

For constant temperature anemometry, the wire temperature T_w is maintained by an electronic feedback circuit that keeps the wire resistance balanced. Introducing the wire voltage, $E = IR$, and re-grouping terms within the arbitrary constants of Eq. 3.1, the relationship between probe voltage and velocity is given as Eq. 3.3. Here the exponent is replaced with $1/n$ to absorb the variable properties in the Reynolds number and to provide an additional degree of freedom to the equation.

$$E^2 = (T_w - T_a)(A + BU^{1/n}) \tag{3.3}$$

If the air temperature T_a is also constant (as in actively cooled wind tunnels or open circuit tunnels in sufficiently large rooms) then the temperature difference

term may be moved into the constants. The KSWT is not temperature-controlled, and T_a may rise as much as 15°C over the course of a run. However, as discussed in the subsequent sections, the hot-wire voltage can be compensated for temperature changes. In either case, the relationship for $U(E)$ is given by Eq. 3.4.

$$U = (A + BE_{\text{comp}}^2)^n \tag{3.4}$$

1. Calibration of Single Normal Probes

A pair of single normal hot-wire probes are used for boundary-layer measurement. The sensor-element axis is normal to the X axis. The probes are mounted to a carbon composite sting attached to the traversing mechanism on the test side of the model. The freestream probe is separated from the boundary-layer probe by a distance 178 mm in the Y direction. To calibrate these probes, the test section velocity is measured using a pitot-static tube mounted upstream of the model on the non-test side of the test section. As the hot-wire probes and the location of this reference velocity measurement are separated by a large spatial distance, it is expected that a difference in velocity between these points may exist. Certainly the presence of the swept-wing model and the wall liners will influence the pressure field. Rather than calibrating the hot-wire probes in close vicinity to the pitot-static tube (this would significantly increase the complexity of the experimental setup), the probes are calibrated essentially in place. The calibration location is defined as the X location corresponding to 60% chord on the model, full retraction of the sting in the Y direction and the Z location that places the probes at mid-span. In this position, environmental influences on the freestream flow are minimal and the transverse velocities are small.

To correct for the differences in the velocity field between these points, concurrent measurements of the streamwise velocity are made using two pitot-static tubes. The first is the permanent wall-mounted tube on the non-test side and the second is mounted to the sting in place of the hot-wire probes. Repeating these measurements with the second pitot-static tube positioned at each wire location over a range of speeds, ratios describing the difference in mean velocity across these spatial points are developed. Prior to beginning boundary-layer measurements, it is found (Hunt, 2011) that the ratio of the boundary-layer probe velocity to the reference freestream speed is 1.114 ± 0.031. Likewise, the velocity ratio for the freestream hot-wire probe location is 1.069 ± 0.035. These velocity ratios are used to correct the reference freestream velocity values during hot-wire calibration.

For these boundary-layer measurements, both the mean and fluctuating components of the velocity are of interest. However, precise measurement of the mean velocity with a hot-wire probe requires additional consideration to account for temperature changes in the wind tunnel. As shown in Eq. 3.3, the measured hot-wire voltage is dependent on the temperature difference between the fluid and the wire. In the present experiments, this temperature difference changes as the wind tunnel temperature increases over the course of a series of measurements. To account for temperature change, a compensation may be applied to the hot-wire voltage. Radeztsky *et al.* (1993) measured the voltage drift as a function of temperature and applied a linear correction to compensate for temperature changes. For the present experiments, the compensation approach from White (2000) is used. To do so, a thermal compensation coefficient, C_T, is computed from hot-wire voltages measured at high and low temperatures (denoted by subscripts h and l).

$$C_T = \frac{E_h^2 - E_l^2}{T_h - T_l} \tag{3.5}$$

The compensation coefficient varies with velocity. To capture this relationship, C_T values are computed at several speeds across the range. Operationally, the wind tunnel is run at 10 to 12 speeds from 2 to 30 m/s and mean values of the velocity, temperature and voltage are recorded. To generate the so-called hot voltages, the wind tunnel is then run at a high speed (30 to 32 m/s) until a temperature increase of 6°C is attained. The wind tunnel speed is then decreased in steps (corresponding to the velocities measured during the ramp-up period) while the hot voltages are measured at each speed. The velocity dependence on the temperature compensation is then modeled by fitting these data to Eq. 3.6 using a nonlinear curve fitting routine. A typical set of these data is shown in Fig. 3.3.

$$C_T(U) = -A - BU^{1/n} \tag{3.6}$$

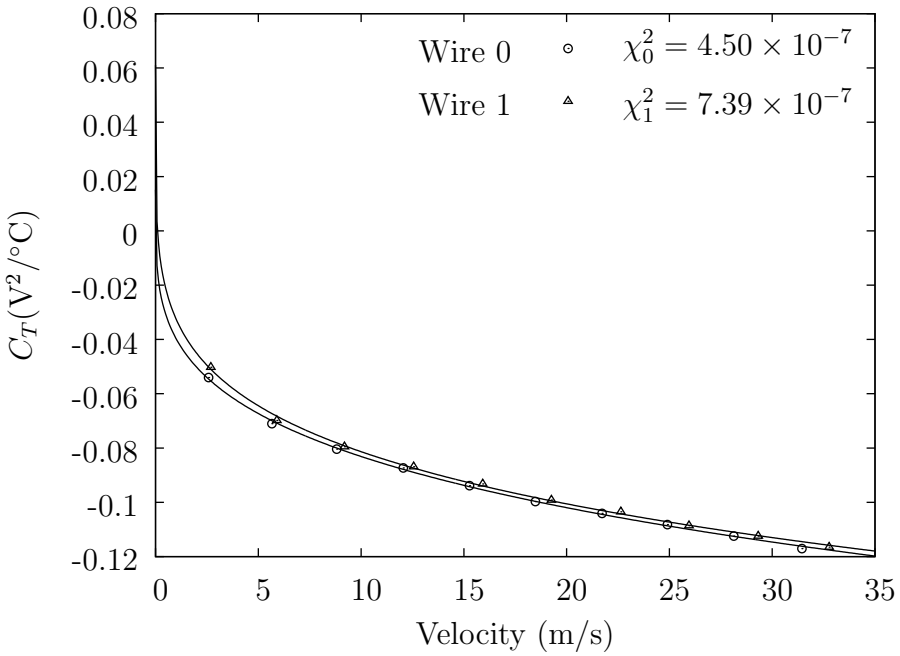

Figure 3.3: Temperature compensation curves for two SN hot-wire probes.

The compensated hot-wire voltage, E_{comp}, is determined by re-arranging Eq. 3.5 as shown in Eq. 3.7. In this expression, the compensation temperature T_{comp} is the arbitrary temperature to which all measurements are corrected. In practice, the compensation temperature is that recorded at the highest-velocity cold voltage reading, as it is a consistently mid-range value. Thus, for any given measurement, the temperature and raw hot-wire voltage are used in conjunction with the fitted parameters in Eq. 3.6 to compute the value of C_T. Moving averages of the temperature computed at 1 second intervals are used for temperature compensation. The compensated voltages are then used to perform a curve fit to the well-known velocity calibration of Eq. 3.4. A representative set of these data is shown in Fig. 3.4.

$$E_{\text{comp}}^2 = E^2 + C_T(U)(T_{\text{comp}} - T) \tag{3.7}$$

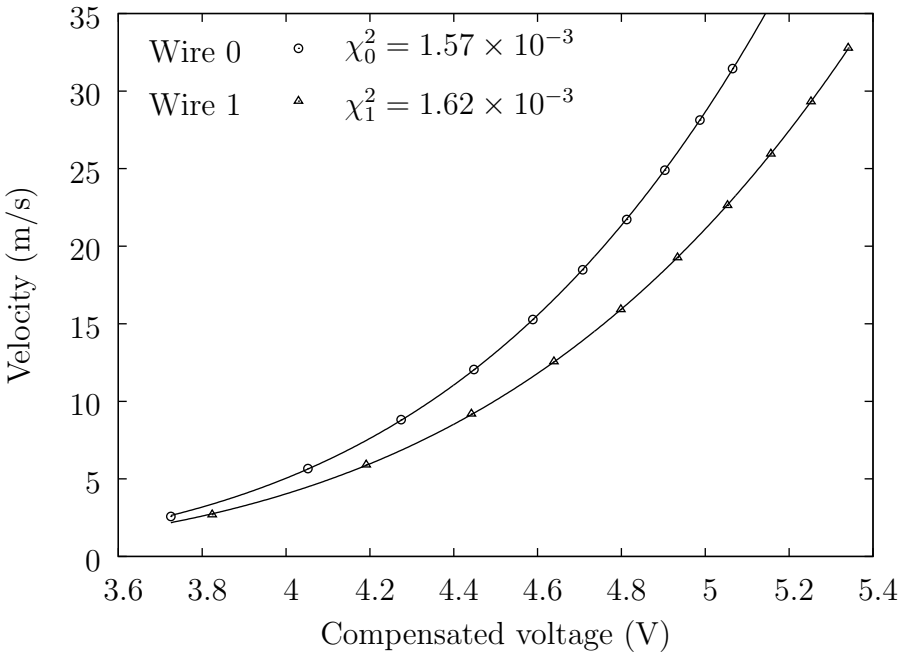

Figure 3.4: Velocity calibration curves for two temperature-compensated SN hot-wire probes.

During calibration, the velocities are given by the pitot-static tube. However, Eq. 3.4 implicitly contains the velocity via the $C_T(U)$ term in Eq. 3.7. To resolve this problem, an iterative solution approach is used for every voltage reading. An initial guess for the velocity is computed using the raw hot-wire voltage. The value of E_{comp} is then computed using Newton–Raphson iteration. In practice, this iteration converges within a small number of steps; the computational overhead is minimal. The converged value of E_{comp} is then used to compute the velocity in the usual way (Eq. 3.4).

2. Calibration of X-Wire Probes

Measurement of transverse velocity with hot-wire probes is accomplished using a pair of yawed probes. These so-called X-wire probes (Dantec 55P61) consist of two 5–μm–diameter wires separated by a small vertical distance. The wires are inclined at yaw angles $\alpha_1 = -45°$ and $\alpha_2 = 45°$ (respectively) to the streamwise direction. Each wire measures an effective cooling velocity V_e that is related to the streamwise and transverse component of the velocity. As will be shown, measurements of $V_{e,1}$ and $V_{e,2}$ can be used to to compute the velocities u and v (or w, if the probe is rotated by 90° about its longitudinal axis). The numerical subscripts refer to the wire number. Calibration of the X-wires follows the methods outlined by Bruun (1995) and Ergin & White (2005). In addition to calibrating the probes at several speeds, the sensitivity of the probes to flow angularity must be determined. In practice, this involves running the velocity calibration multiple times with the probe oriented at different angles to the flow.

To avoid introducing the additional dimension of measuring X-wire probe voltages at low and high temperatures across the speed range, a simpler temperature compensation scheme is used following the method of Radeztsky *et al.* (1993). As

the X-wires are used primarily for measurement of freestream turbulence, temperature variation due to wind tunnel heating is small compared with the much more time-consuming boundary-layer measurements. As such, a simpler (though arguably less precise) temperature compensation scheme represents an acceptable compromise. This method assumes that the voltage drift is linear with temperature change. To test this assertion, the wind tunnel is run at a speed near the top of the range (28 m/s) for 20 minutes and the X-wire voltages are measured. The measured voltages are presented as a function of temperature in Fig. 3.5. The voltage drift values, m, are determined via curve fit and then used to correct the measured voltages to an arbitrary temperature using Eq. 3.8.

$$E_{\text{comp}} = E + m(T_{\text{comp}} - T) \tag{3.8}$$

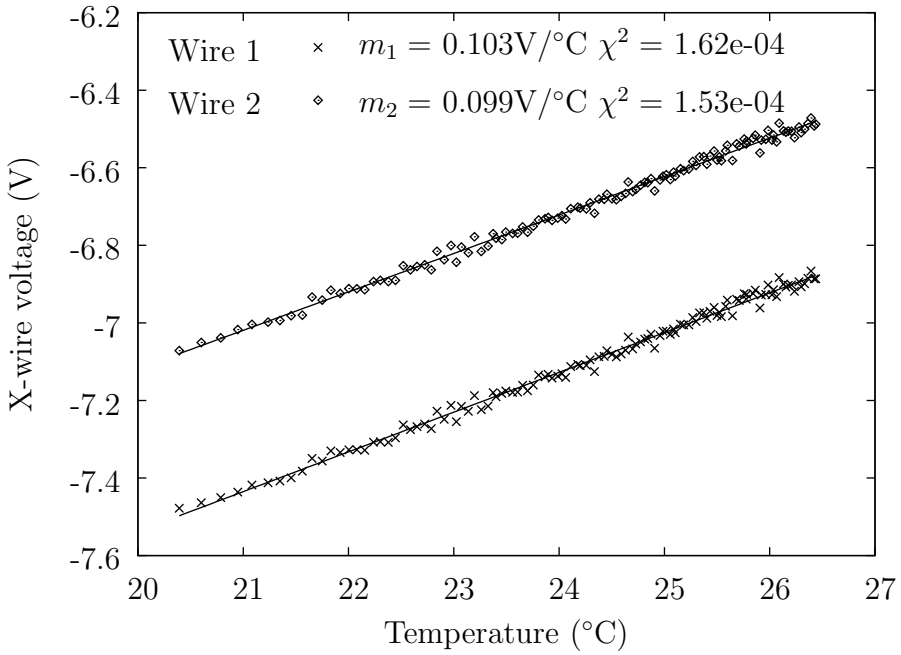

Figure 3.5: Thermal voltage drift measured for a X-wire probe.

The effective cooling velocity measured by a yawed wire is related to the free-stream speed using a yaw coefficient, k, and the yaw angle as in Hinze's formula (Eq. 3.9). Furthermore, the yaw coefficient can also be used to express V_e as a function of the velocity components normal and tangent to the yawed wire (denoted by U_n and U_t, respectively). As noted by Bruun (1995), for long wires (length-to-diameter aspect ratio of approximately 600) k may be close to zero for a wire yawed at $\alpha = 45°$. In this case, the yaw function is simply $1/\sqrt{2}$.

$$V_e = U\left(\cos^2\alpha + k^2\sin^2\alpha\right)^{1/2} = \left(U_n^2 + k^2U_t^2\right)^{1/2} \tag{3.9}$$

The procedure for determining the value of k requires velocity calibrations at multiple yaw angles. To do so, a wall-mounted probe stand is designed such that the probe can be rotated about its yaw axis using an externally-mounted rotation stage (whose precision is 0.2°). Because these probes are used to measure freestream turbulence intensity (where the transverse components are expected to be small compared with the streamwise flow), velocity calibration measurements are performed at the angles $\alpha \pm 5°$. Although the measurements are made together, calibration for each wire is treated independently. Equation 3.9 is then used to produce two sets of V_e data for each wire. Using an assumed value of k to compute V_e, these data are interleaved and a fifth-order polynomial is fitted to the resulting $V_e(E_{\text{comp}})$ data. The value of k is then determined by iteratively changing the assumed value of k and recomputing the $V_e(E_{\text{comp}})$ curve fit. The value of k that minimizes χ^2 of the curve fit is taken as the proper value.

A representative set of calibration data for a X-wire is shown in Fig. 3.6. Each wire has its own calibration constants (k, and the six polynomial constants used to fit $V_e(E_{\text{comp}})$). As this plot shows, the optimized values of k accurately produce the correct yaw sensitivity for each wire. That the probe voltage decreases

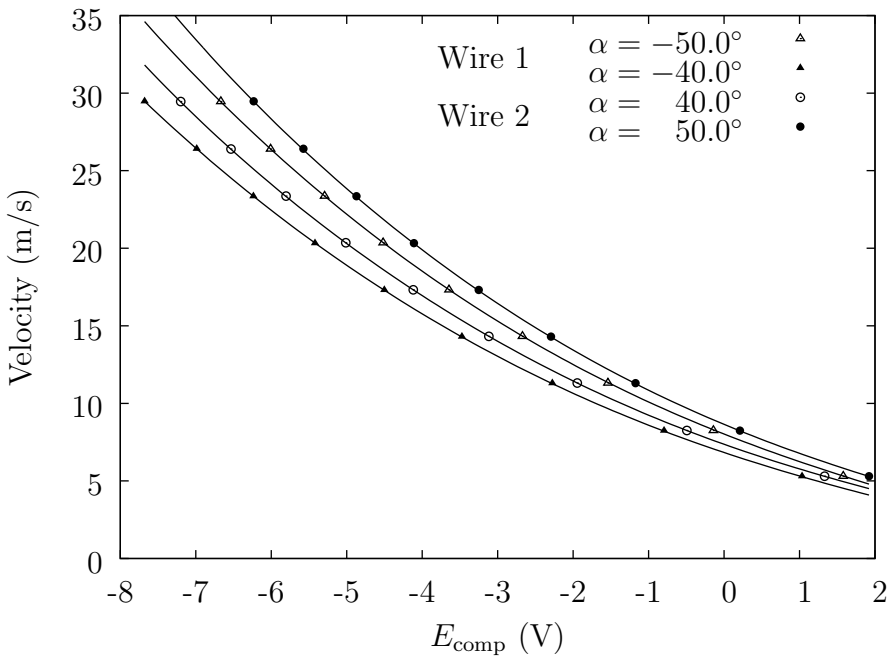

Figure 3.6: Velocity calibration curves for a X-wire probe.

with increasing speed is an artifact inherent to the AN-1003 anemometer used for the measurements. This negative voltage output is only apparent here because the temperature-compensated voltage is not squared (as in the single normal wire calibration scheme).

Signal analysis of the V_e data follows the method given by Bruun (1995) for a pair of single yawed wires. As in Eq. 3.9, the effective cooling velocities measured by the X-wire are related to the normal and tangential components of the freestream velocity, measured relative to the hot-wire sensing element. Transformation of velocities from the global coordinate system to this wire-fixed coordinate system is accomplished using Eq. 3.10.

$$U_n = u\cos\alpha - w\sin\alpha$$

$$U_t = w\cos\alpha + u\sin\alpha \tag{3.10}$$

Following the method of Ergin (2005), by substituting these expressions into Eq. 3.9 and re-grouping the terms, the system in Eq. 3.11 results.

$$\begin{aligned}
\frac{V_{e,1}^2}{\cos^2\alpha_1} &= u^2\left[\left(\frac{w}{u}\right)^2\left(\tan^2\alpha_1+k_1^2\right)+2\frac{w}{u}\tan\alpha_1\left(k_1^2-1\right)+k_1^2\tan^2\alpha_1+1\right] \\
\frac{V_{e,2}^2}{\cos^2\alpha_2} &= u^2\left[\left(\frac{w}{u}\right)^2\left(\tan^2\alpha_2+k_2^2\right)+2\frac{w}{u}\tan\alpha_2\left(k_2^2-1\right)+k_2^2\tan^2\alpha_2+1\right]
\end{aligned} \tag{3.11}$$

This system of equations can be solved for u and w. A flow angle defined by $w/u = \tan\beta$ is introduced and the system in Eq. 3.11 is re-written as a single equation in $\tan\beta$. Following solution of this equation, the calculation of u and w is straightforward. In practice, the voltages measured by the X-wire are compensated for temperature, V_e values are calculated and the u and w (or v) values are computed on a point-by-point basis. Thus, in addition to the transverse velocity component, the X-wire provides an independent measure of the streamwise velocity and its fluctuation level. In the course of the present experiments, the observation that U and u'_{rms} computed from X-wire data and single normal wire data agree within measurement uncertainty gives additional confidence in these measurement techniques.

In the course of these experiments, it was observed that lateral vibration of the probe stand produced spuriously high values of the transverse velocity fluctuation level. This problem was remedied by rotating the probe such that the transverse axis was parallel to the probe stand span line. For example, a wall-mounted X-wire experienced small vibrations in the test section Z direction; only the u' and v' components can be accurately measured using this setup. To measure w', the probe stand is mounted to the test section floor (where it experiences vibration primarily in the Y direction) such that the X-wire remains in approximately the same spatial location and the probe is rotated by 90 degrees about its longitudinal axis.

3. Measurement of Unsteady Velocity

The fluid velocity can be described as a steady velocity with a fluctuating component. The general nomenclature for this relationship is as follows:

$$\begin{aligned} u(x,y,z,t) &= U(x,y,z) + u'(x,y,z,t) \\ v(x,y,z,t) &= V(x,y,z) + v'(x,y,z,t) \\ w(x,y,z,t) &= W(x,y,z) + w'(x,y,z,t) \end{aligned} \tag{3.12}$$

Hot-wire probes are used to measure the total velocity; the steady and unsteady components can be computed in a straightforward manner. The steady velocity can be approximated as the time-mean of the measured velocity. Experimentation with sampling rates and times indicates that the mean values are well-converged after a few seconds sampled at 10 kHz. The unsteady components are then computed by subtracting the mean values from the measured velocities. However, if the fluctuating component is small (as in the present experiments), some additional effort is required to ensure that the fluctuating component is resolved properly.

The difficulty in measuring small values of u' is that small variations in the probe voltage can be obscured during the measurement process. The root of the issue is twofold: the analog voltage signal is subject to electronic noise and the data-acquisition boards have finite resolution. To help address the first issue, shielded cable is used for the hot-wire signals and it is routed separately from power cables and other instrumentation cables. Also, a linear gain is applied to the voltage signal by the anemometer signal conditioner. The primary solution to this problem is the use of a Kemo VBF44 filter and amplifier. The anemometer output voltage is split into two lines: one line is acquired directly. The second voltage output is subject to a 1 Hz to 10 kHz bandpass filter to remove both the steady component and the high-frequency electronic noise. A gain of 30 dB is applied to amplify this AC component

of the voltage, so that the degree to which it is affected by electronic interference is minimized. Additionally, the AC components of the hot-wire signals are acquired on a separate data-acquisition device to minimize crosstalk.

Once the AC voltage signal is acquired and converted to a digital signal, the gain is removed. The mean value of the hot-wire voltage is computed and added to the AC component. In this manner, the total voltage signal (fluctuating plus steady) is re-constructed. The same procedure is used for the boundary-layer measurements. In this case, lower amplifier gains are used to avoid voltage saturation, as the unsteady fluctuations grow much larger in the boundary layer than in the freestream.

4. Separation of Sound and Turbulence

The AC component of the hot-wire probe measurements are affected by both sound and turbulence. Though both sources constitute environmental disturbances and may affect transition, it is freestream turbulence that provides the initial condition for crossflow instability growth in the form of streamwise vorticity. The irrotational fluctuations of the pressure disturbance have little effect on the crossflow instability problem (Bippes, 1999). A method for separating the hot-wire signal into these components is given by Naguib *et al.* (1996). This method is applied to the turbulence measurements; the resulting values are referred to as separated, or uncorrelated components.

The method of separating a hot-wire signal into sound and turbulence components requires simultaneous measurements from two probes separated by a large distance in the same streamwise plane. Subtraction-based techniques are sometimes used to accomplish this task, but the optimal filtering technique of Naguib *et al.* (1996) has the advantage of producing time series for each component. In short, one probe signal is designated as the reference signal and a filter function is constructed

with the goal of transforming the second signal such that the error between the two is minimized. In this context, the sum of the squares of the differences is used as the error. Determining the value of the filter coefficients in this manner is essentially an optimization problem.

The sound may be generated by any of several sources: fan or motor noise, flow separation in the diffusers and structural vibrations, for example. However, these pressure fluctuations are oriented in the streamwise direction and can be considered uniform across a streamwise plane. The turbulent fluctuations are highly three-dimensional and non-uniform. If the probes are separated by a distance greater than the integral length scale of the turbulence (which is on the order of the diameter of the largest eddies present in the flow), then the turbulent components measured by the probes will be uncorrelated. Baseline turbulence measurements are made in an empty test section and the probes are separated by 1.15 m. In the present experiments, these measurements are repeated when a variety of turbulence grids are used to raise the freestream turbulence intensity. In this case, the swept-wing model and wall liners are installed in the test section. As such, the probe mounting locations are somewhat limited: a separation distance of 0.7 m is used.

All measurements of the streamwise component of freestream turbulence represent separated values (unless otherwise noted, as in Table 2.1). For the boundary-layer measurements, the unseparated values of u'_{rms} are used. As such, the u'_{rms} values at the edge of the boundary layer are higher than those quoted for the freestream.

C. Boundary-Layer Measurement

Flow visualization is a useful tool for measuring the transition location and stationary crossflow wavelengths. To understand the process by which the crossflow in-

stability brings about transition, detailed measurements of disturbance growth (both steady and unsteady) are needed. Finely-resolved measurements of the boundary-layer velocity are used to compute these quantities. As discussed in earlier sections, these measurements are made using a pair of single normal hot-wire probes. Point-by-point normalization of the boundary-layer velocity is performed using the velocity measured by the freestream probe. The position of the boundary-layer probe requires rotation in two axes. First, the probe mounting tube is rotated about the Z axis where it is attached to the sting such that the probe is angled toward the model. This rotation is described by the angle β, measured between the X axis and the probe's longitudinal axis (such that $\beta = 0°$ has the probe pointed directly into the flow). The purpose of this rotation is to account for the surface curvature of the swept-wing model by positioning the probe such that the wire is always closest to the surface (rather than the probe prongs). Secondly, the probe is rotated about its longitudinal axis so that the wire is parallel to the model surface. If the entire length of the wire is not at the same boundary-layer height, then the resulting velocity measurements will represent the average velocity over the range of boundary-layer heights spanned by the wire.

The boundary-layer measurements comprise scans in (Y, z) planes, i.e. locations of constant chord. For this model (with no taper), the surface curvature does not change in these spanwise scans and consequently, the probe orientation is only adjusted when it is moved to a new chord location. Angles used for the β rotation are listed at different chord locations in Table 3.1. To ensure repeatability, a printed calibrated dial is affixed to the hot-wire sting. For rotation about the longitudinal axis, the angle is set by inspection at each location. Although this positioning scheme and the use of spanwise scans ensure that the wire retains its orientation relative to model throughout the measurements, it must be noted that wire measures a projection of

the velocity. Since the streamlines curve around the model in the manner of Fig. 2.7 and no commensurate wire rotation is made about the Y axis, the local streamline is typically not perpendicular to the wire. However, since this misalignment can be quantified, a coordinate transformation will allow comparison of experimental and numerical data. In this case, the numerical data can be used to compute the projected velocity that is observed by the hot-wire probe. For the purposes of this experiment, this point is noted and the projected velocity is referred to as u for simplicity.

x/c	β	x/c	β	x/c	β
0.10	20°	0.30	13°	0.50	8°
0.15	16°	0.35	12°	0.55	7°
0.20	14°	0.40	11°	0.60	7°
0.25	13°	0.45	10°	0.65	7°

Table 3.1: Boundary-layer probe rotation angles for Z axis rotation.

The probe-traversing mechanism that controls the boundary-layer measurements is externally mounted on the test section. The hot-wire sting protrudes through a slot in a movable window such that a wide range of motion in X and Z is possible while maintaining the integrity of the test section wall. However, since there is no pressure seal where the sting enters the test section, the entire traverse is encased in a pressure box of clear acrylic panels. This pressure box can maintain the slight negative pressure of the test section so that air does not flow through the slot through which the sting enters the test section. The traverse mechanism is built from commercially available electronics and machine components. Briefly, highly precise stepper motors are used to drive ball screws aligned with the four axes of the traverse (X, Y, Z and

the movable window axis, which is parallel to Z). Loads are carried by linear bearings on stainless steel rails. Optical encoder feedback is used to maintain accurate and precise positioning of the traverse; the resolution of these encoders is taken as the resolution of the traverse motion.

The spatial range and resolution of motion afforded by the traverse are summarized in Table 3.2. Although the resolution of motion along a spanwise line is limited by the X axis resolution, this is acceptable given that the hot-wire length (1.25 mm) acts as a spanwise high-pass filter in the wavelength spectrum. Basic traverse motion is controlled via a Compumotor 4000 motion controller. A resident program on the CM4000 handles the optical encoder feedback and engages automatic position correction moves if a mismatch between the issued command and the recorded travel is observed. Multi-axis moves are also possible; this allows the window to move with the sting in the Z direction, and to move the sting along the spanwise direction. Higher-order functions (e.g. boundary-layer scanning) are controlled by software on the wind tunnel computer. To avoid accumulated discretization error in position, this software moves the traverse based on notional position so that the discrepancy between the intended and actual position is not larger than a single step size. End-of-travel limit switches are installed to prevent a collision and to provide a fixed reference for homing moves. Unfortunately, the need to move the hot-wire probe to within less than a millimeter of the model surface prohibits the use of a limit switch in the negative Y direction.

In this experiment, boundary-layer profiles are measured at regularly-spaced intervals in the spanwise direction. An automated, computer controlled routine is used to make all of the boundary-layer measurements. The boundary-layer scanning routine starts with the probe manually positioned a few millimeters outside of boundary layer. The ratio of the mean velocities measured by the boundary-layer probe (U) and

	X	Y	Z	z ($\Lambda = 45°$)
Range	1400 mm	101 mm	180 mm	255 mm
Resolution	11.9 μm	0.6 μm	1.3 μm	16.8 μm

Table 3.2: Resolution and ranges of travel for the hot-wire probe traversing mechanism.

the freestream probe (U_{fs}) at this point is referred to as the edge velocity, U_e. The probe is moved toward the model and velocity measurements are recorded at each point. Since the location of the model surface relative to the probe traverse coordinate system is generally not known (White & Ergin, 2004), increasingly small steps are taken as the probe descends into the boundary layer. The stepping algorithm is adjusted such that a total of 75 to 100 points are measured (with approximately 10 at the boundary-layer edge) and the minimum step size is set to 10 μm.

Measurement of the boundary-layer profile is controlled using a cut-off velocity. Once a value of $U/U_e < 0.20$ is observed, the stepping algorithm is stopped and the probe is moved back into the freestream and to the next spanwise location. Hot-wire probes are known to be inaccurate at low velocity, where the rate of heat transfer from the wire is increasingly due to natural convection and radiation rather than forced convection. Additionally, the 5-μm-diameter wires used in these experiments are fragile; contact between the wire and the model surface would destroy the probe. For these reasons, measurements are not attempted in regions where $U/U_e < 0.15$.

These boundary-layer profiles are measured under the assumption that the location of the wall is not explicitly known in traverse coordinates *a priori*. Each boundary-layer scan starts with manual adjustment of the probe position, and doing so with micron accuracy is not practical. A small degree of misalignment between the traverse and model or long-wavelength waviness in either of these objects may con-

tribute to this problem. However, the boundary-layer profiles must share a common spatial reference with the model if a meaningful analysis is to be performed. The no-slip condition requires that the velocity is zero at the wall; this fact may be exploited to locate the wall in traverse coordinates. To do so, the boundary-layer velocity is extrapolated to zero and the corresponding Y location is taken as the wall location, Y_{wall}. For a Blasius boundary-layer profile, linear fits to $U(Y)$ for $U/U_e < 0.35$ provide good estimates of the wall location (White & Ergin, 2004). However, for a test condition with a non-zero streamwise pressure gradient, the streamwise momentum equation shows that at the wall, the $\partial^2 U/\partial Y^2$ term is also non-zero. To account for this term, a second-order polynomial is used to fit $U(Y)$ data for $U/U_e < 0.50$ (White, 2000). The correct root of this polynomial is determined by choosing the value closest to the Y location of the point with the lowest measured velocity. In areas with large mean-flow deformation (the more downstream measurement stations), local wall fits across the span are used to correct for wall-location errors, as in Eppink & Wlezien (2011).

Using this procedure, Y_{wall} is determined for each measured boundary-layer profile and the Y coordinates are shifted accordingly. Since the stepping algorithm is based in part on local velocity measurements, the boundary-layer profiles are not necessarily measured on the same Y grid. To facilitate data analysis, all profiles are interpolated onto a common set of Y points. The result is a rectangular grid of points in a (Y, z) plane where $Y = 0$ corresponds to the best estimate of the wall location. The spanwise steps are nominally constant and the precision with which the spanwise steps are taken is such that a similar interpolation is unnecessary.

Some misalignment between the model and the traverse must be accepted. Although it may be possible to fabricate a model and traverse that are parallel with sub-micron accuracy across the span, the straightforward solution to misalignment

ensures that such efforts would meet diminishing returns far short of that goal. Wall location using extrapolation of $U(Y)$ makes local corrections, but a global correction for misalignment simplifies the experiment and can potentially save a significant amount of time (White & Ergin, 2004). Toward that end, the wall location is determined at many points across a spanwise region of interest. When $Y_{\text{wall}}(z)$ is considered, the misalignment is clear. This is shown in Fig. 3.7 for a few chord locations. Linear fits to these data approximate the wall skew well. The misalignment is rather minor: the mean skew is 10.9 μm per millimeter of span, or less than 2 mm across the range of the traverse. The boundary-layer scanning routine uses this measured wall skew to maintain an approximately constant distance from the model when starting each profile. As the traverse is moved in the spanwise direction, wall skew correction steps are taken in Y.

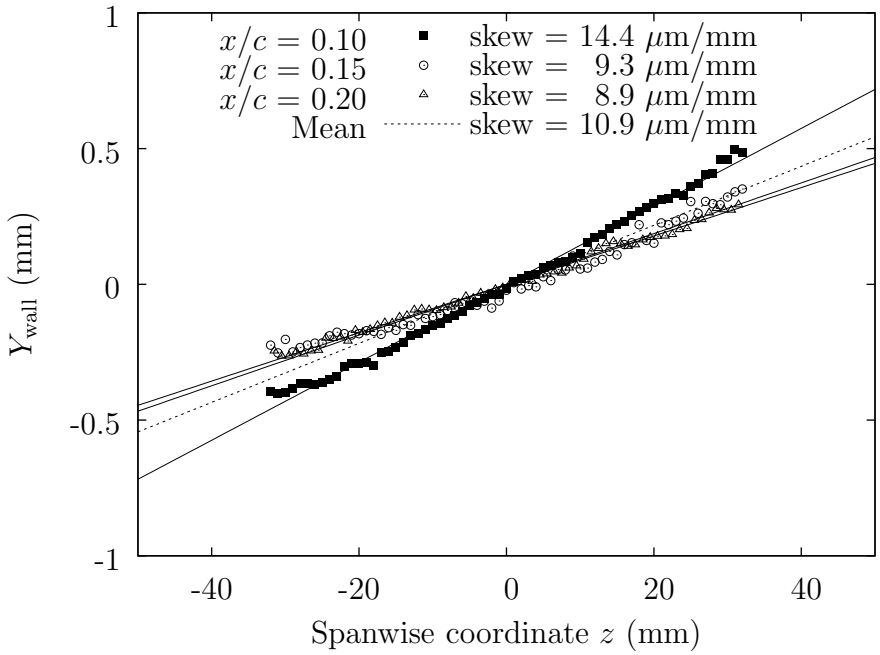

Figure 3.7: Measurements of the model skew in traverse coordinates.

CHAPTER IV

ENHANCED FREESTREAM TURBULENCE

The study of turbulence is a field in itself. Varying the intensity and scale of turbulence to examine its role is a common experimental practice. In the present experiments, the effect of turbulence on crossflow-instability-dominated transition is the primary focus. A brief review of relevant literature concerning manipulation of freestream turbulence is given before describing the experimental techniques used to quantify the character of the resulting turbulence. Finally, the disturbance environments in which the present experiments are performed are characterized. The methods of turbulence generation are described and the resulting fluctuation intensity, temporal spectra and length scales are documented.

A. Manipulation of Freestream Turbulence

Turbulence levels are often raised for the purposes of experimental work. A wide body of research exists encompassing the varied active and passive methods that have been developed. The use of coarse screens or grids of various cross sections are common choices due to their simplicity and low cost. A review of turbulence manipulation via screens is given by Laws & Livesey (1978). A more recent examination of grid-generated turbulence is given by Kurian & Fransson (2009), in which the length scales that characterize the turbulence are varied and measured in detail. However, screens are also commonly used to reduce the intensity of turbulent fluctuations; such turbulence-damping screens are found in most wind tunnels. Groth & Johansson (1988) examined the role of screens in turbulence attenuation and reported on optimal configurations. The dual use of screens for turbulence generation

and reduction highlights the importance of grid geometry and placement.

The stated goal of the present experiments is to examine the effect of moderate turbulence intensity on the crossflow instability. Quantitatively, the range of interest is $0.02\% \leq Tu \leq 0.20\%$. This is a fairly small range; some consideration must be given to ensure that the enhanced turbulence intensity is not too great. In a similar manner, the work of Kendall (1990) sought to examine the role of weak freestream turbulence on the stability of two-dimensional boundary layers. Although the instability mechanisms of these two experiments are different (T–S versus inflectional), much may be learned from Kendall's experiments. Starting with a baseline turbulence intensity of 0.03%, the turbulence was raised to 0.25% using an active jet grid. A series of 1.5-mm-diameter pipes with regularly spaced 0.15-mm-diameter holes were arranged upstream of the test section. The pipes were pressurized up to 5 psi, creating weak, upstream-facing jets of air. By varying the supply pressure, the resulting turbulence level could be adjusted. Though the notion of this so-called Kendall grid is seductive due to the relative ease of varying Tu, passive grids are used in the present experiment for their greater simplicity and low cost. The underlying mechanisms are different (the active grid produces unstable three-dimensional shear layers), but both can effectively increase the freestream turbulence intensity.

The generation of turbulence via passive grids is related to vortex shedding from the grid elements. For a grid element of diameter d, vortex shedding is observed for $Re_d \geq 40$ (White, 1991). The resulting vortices are subject to secondary instabilities leading to breakdown. Though turbulence-damping screens may also function in the supercritical regime, the length scales of the resulting turbulence are smaller than those of the incoming flow (Watmuff, 1998) and thus decay more rapidly. This is accomplished using a sufficiently fine mesh width and settling length. Laws & Livesey (1978) note that 500 mesh widths should be allowed for viscous dissipation of the tur-

bulence contributed to flow. However, Watmuff (1998) reports that spatial variations in the porosity of a turbulence-damping screen may actually excite boundary-layer instabilities. Thus, mesh uniformity is also an important quantity. A turbulence-generating grid, on the other hand, should have a sufficiently large grid diameter and mesh width. As noted by Kurian & Fransson (2009), varying the diameter and mesh width changes the length scales of the resulting turbulence. If the mesh solidity, σ, is held constant then the turbulence intensity is largely unchanged. In this context, σ is the complement of the grid porosity β defined such that $\sigma = 1 - \beta$.

Streamwise placement of turbulence-generating grids is also an important factor. It has long been known (Batchelor & Townsend, 1948) that the turbulence intensity decays in the wake of the instigating grid. This decay follows a power law relationship, but there is some debate in the literature over how the coefficients of this relationship are determined. The location of the grids with respect to the contraction section is also of importance. Westin *et al.* (1994) note that when a grid is installed in the settling chamber upstream of a contraction section, the freestream turbulence in the test section is anisotropic. The effect of the contraction is to decrease the intensity of the streamwise fluctuations at the expense of increased transverse fluctuations. In the present experiments (as in those of Suder *et al.* (1988) and others), the turbulence grids are placed in the settling chamber. This produces more homogeneous turbulence whose rate of decay along the test section length is more gradual than that of turbulence generated by grids at the test section inlet. This approach also facilitates the generation of modest freestream turbulence: a key factor in the present experiments. The anisotropy is the cost of this approach. For this reason, it is important to characterize the freestream turbulence using all three components of the velocity.

In a series of experiments designed to study the combined effect of surface roughness and freestream turbulence on traveling mode initiation, Gladden (2001) raised

the turbulence intensity in the ASU UWT to 0.25% using a grid of stainless steel wires installed in the settling chamber. Unfortunately, few operational details are given concerning this turbulence grid. More recently, Hunt (2011) explored the generation of low levels of freestream turbulence in the same facility as the present experiments. By adhering strips of 0.25-inch-wide Kapton tape to the last screen in the settling chamber, the turbulence intensity was raised to 0.30%. Repeating this procedure on the first (of seven) turbulence-damping screens produced $Tu = 0.03\%$. The results of these experiments are used to guide the selection of turbulence grids for the present work.

B. Disturbance Environments in the Present Experiments

To produce freestream turbulence levels between 0.02% and 0.20% in the test section, several configurations were tested. By varying grid diameter, spacing and streamwise position, four arrangements were found that produced $Tu = 0.03\%$, 0.05%, 0.10% and 0.19%. These values are skewed toward the low end of the range by design and approximately evenly distributed on a logarithmic scale. Data from previous experiments are more sparse at low levels of turbulence intensity, and this research examines that range more closely. The approach taken in grid selection is largely empirical. As a result, the grids chosen are constructed of differing materials from woven stainless steel wire to soldered brass pipes. The criteria for the grids are that they produce the desired turbulence intensity with uniform distribution at the test section inlet, while introducing minimal flow blockage.

The settling chamber for this facility has a cross-section area of over 10 m^2. To reduce flow blockage and turbulence grid size, partial grids are used to produce disturbed flow in the measurement region and neighboring areas. The turbulence

grids are approximately 1 m in vertical extent and centered vertically in the settling chamber. It is important to ensure that the turbulence intensity and mean velocity in the measurement region are uniform. To do so, spanwise hot-wire probe scans are made in the freestream across the traverse range of motion. Experimentation with grid placement is used to calibrate the influence of settling-chamber-mounted elements on test section flow. A series of measurements is presented in Fig. 4.1 demonstrating the uniformity of the freestream turbulence; spatial uniformity of the mean flow is maintained within 0.05 m/s. Due to the difficulties in measuring w' using the sting mount as discussed in the Chapter III, the v' component is used as an analog for turbulence intensity in this plot. The turbulence grids are arranged such that the edge of their influence is beyond the reach of the hot-wire traverse.

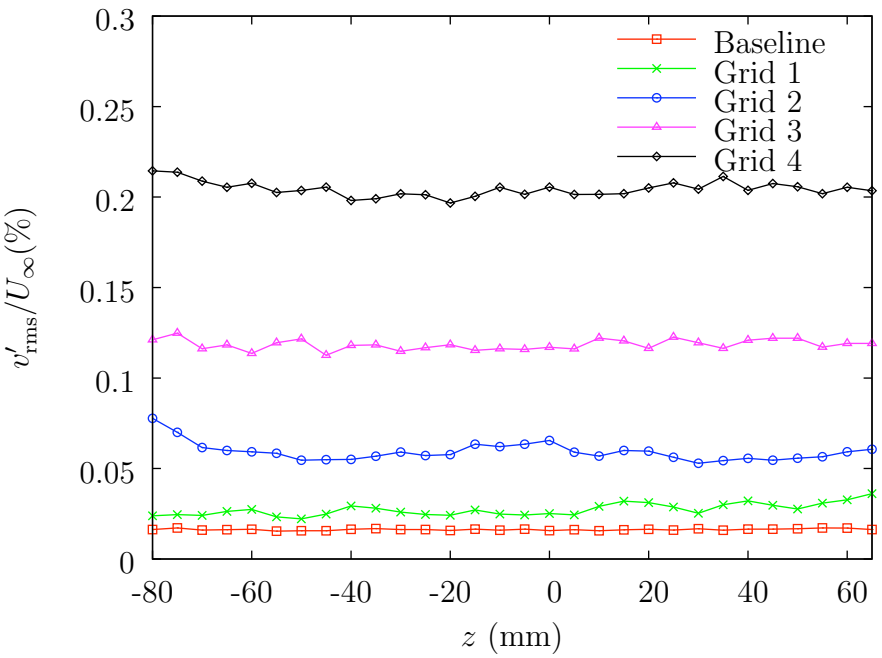

Figure 4.1: Spanwise scan of the freestream turbulence intensity. The test speed is $U_\infty = 24$ m/s.

Although the w' component is not measured using sting-mounted probes, all three components of the fluctuating velocity are measured using a combination of floor-mounted and sting-mounted probes. The transverse components are measured using X-wire probes as described in Chapter III. The streamwise components are measured using two probes separated by a large distance in the same streamwise plane. The quoted values for u' represent the uncorrelated component of these signals. Using these measurements, the freestream turbulence intensity is computed using Eq. 1.2. A summary of turbulence intensity measurements is presented in Table 4.1. These measurements are made at a freestream speed of 24 m/s, which corresponds approximately to the primary test condition ($Re_c = 2.8\times10^6$) at nominal temperature. The grid element diameters are also given for context. As this table shows, the grids placed upstream of the turbulence-damping screens require a larger diameter to produce comparable levels of turbulence. As will be shown, no fundamental differences are observed in the character of the turbulence generated using the grids placed upstream of the screens.

Grid	d	u'_{rms}/U_∞	v'_{rms}/U_∞	w'_{rms}/U_∞	Tu
Baseline	N/A	0.016%	0.016%	0.017%	0.016%
1	5.3 mm	0.017%	0.027%	0.031%	0.027%
2	0.8 mm	0.023%	0.059%	0.069%	0.054%
3	23.6 mm	0.030%	0.118%	0.128%	0.102%
4	4.8 mm	0.069%	0.204%	0.249%	0.190%

Table 4.1: Grid-enhanced turbulence levels measured at $U_\infty = 24$ m/s. Grids 1 and 3 are installed upstream of the screens while grids 2 and 4 are installed in the settling chamber.

These values show a degree of anisotropy, for two reasons. First, placing the grids upstream of the contraction is expected to produce a lower level of fluctuation intensity in the streamwise component. This may be interpreted as a consequence of angular momentum conservation as the turbulent eddies are stretched in the streamwise direction through the contraction. The difference between the transverse components is attributed to the asymmetric contraction ratio. With the wall liners installed, the v component experiences a 2:1 contraction whereas the w component is subject to a 3.4:1 contraction. In the course of these experiments, the primary turbulence values used are 0.02%, 0.05% and 0.19% (the low, middle and high values from the tabulated values). Select tests are run using the interstitial turbulence intensities.

Power spectral densities for each component of the turbulent fluctuations are plotted in Figs. 4.2–4.4. In considering the streamwise spectra, the higher fluctuation levels appear over a broad range of frequencies spanning two orders of magnitude. No particularly prominent spectral peaks are evident for any of the turbulence configurations. The transverse spectra, however, show marked differences in the low-frequency power levels. With the exception of some overlap in the PSDs associated with grids 2 and 3, the spectra all appear fairly distinct. That the turbulent fluctuations vary over such large frequency ranges indicates the suitability of these grids for exciting instabilities across a commensurately large range.

Linear stability theory calculations indicate that the traveling crossflow mode at these test conditions is most unstable for a 120 Hz, 10 mm wave. However, disturbances between 50 Hz and 250 Hz experience amplification ratios within 0.5 of the most unstable disturbance. Likewise, the wavelength range of the most unstable traveling mode is somewhat broad; waves from 8–12 mm have initial growth rates and N factor values at $x/c = 0.20$ and 0.30 that are similar. Although linear stability theory is known to *not* correctly predict the growth of the crossflow instability, it does serve

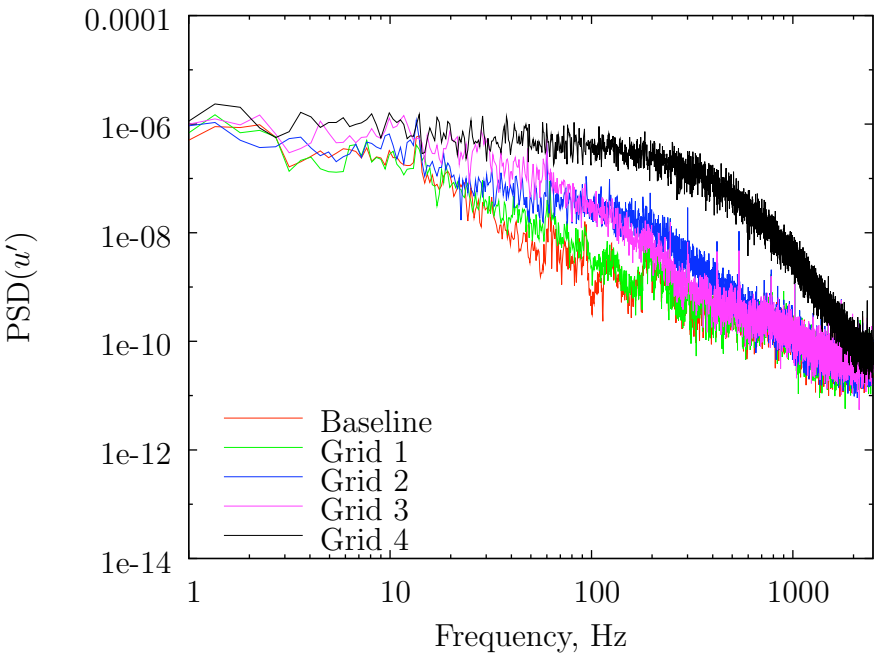

Figure 4.2: Power spectral densities of u' (uncorrelated component) for each turbulence configuration. The test speed is $U_\infty = 24$ m/s.

as a useful guide to mode selection. The PSDs of the velocity fluctuations indicate that the traveling mode should be excited in the higher-turbulence configurations.

C. Turbulence Length Scales

The hot-wire probe is an imperfect instrument. It is, however, the best tool for measuring turbulent flows in the wind tunnel. Due to its finite length and diameter, the smallest scales of turbulence are beyond the reach of direct measurement (though approximations may be made). In order to resolve the length scale of turbulent eddies, the wire length must not be larger than the eddy size. However, wires that are too short suffer from detrimental end effects related to the probe prongs; length-to-diameter ratios of greater than 200 are desired (Bruun, 1995). This places a practical limit on the wire length as sub-micron diameters may be too fragile for regular use.

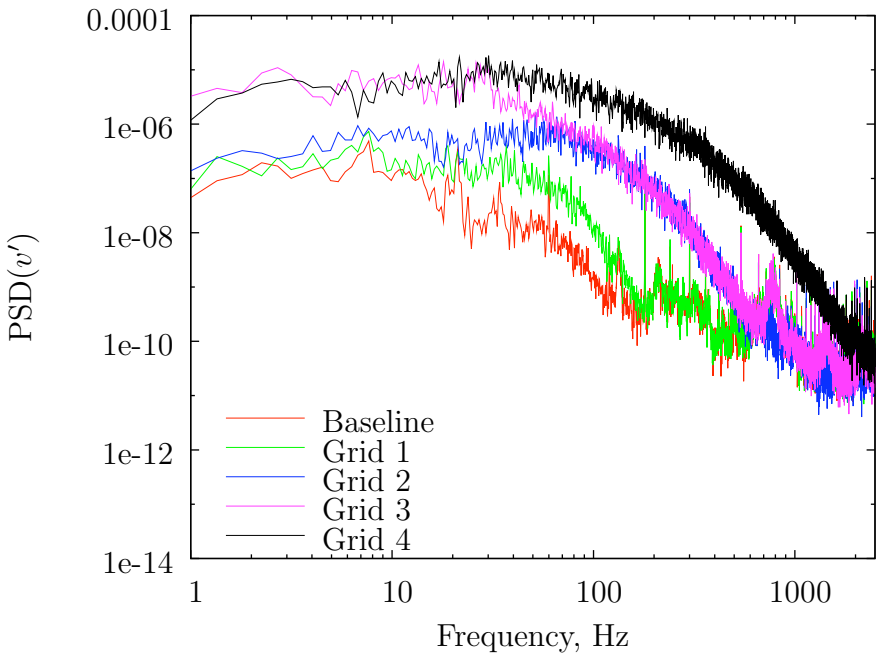

Figure 4.3: Power spectral densities of v' for each turbulence configuration. The test speed is $U_\infty = 24$ m/s.

The miniature wire probes used in the present experiments are of 5 μm diameter with a 1.25 mm length. While the aspect ratio of these wires are suitable, the length places a limit on the smallest scales that can be directly resolved.

Given these caveats, a discussion of the measurement techniques employed is appropriate. Cooper & Tulin (1955) present an early monograph on the subject of turbulence measurement via thermal anemometry. A thorough (though dated) review of the quantities measured is given in an appendix to that work. The standard reference texts for turbulence (Hinze, 1975) and hot-wire anemometry (Bruun, 1995) discuss the key aspects of turbulence measurement. The recent work of Kurian & Fransson (2009) presents several measurement and analysis techniques and compares these with theoretical relations for isotropic turbulence. These are the primary resources that guide the task of measuring turbulence in the present experiments.

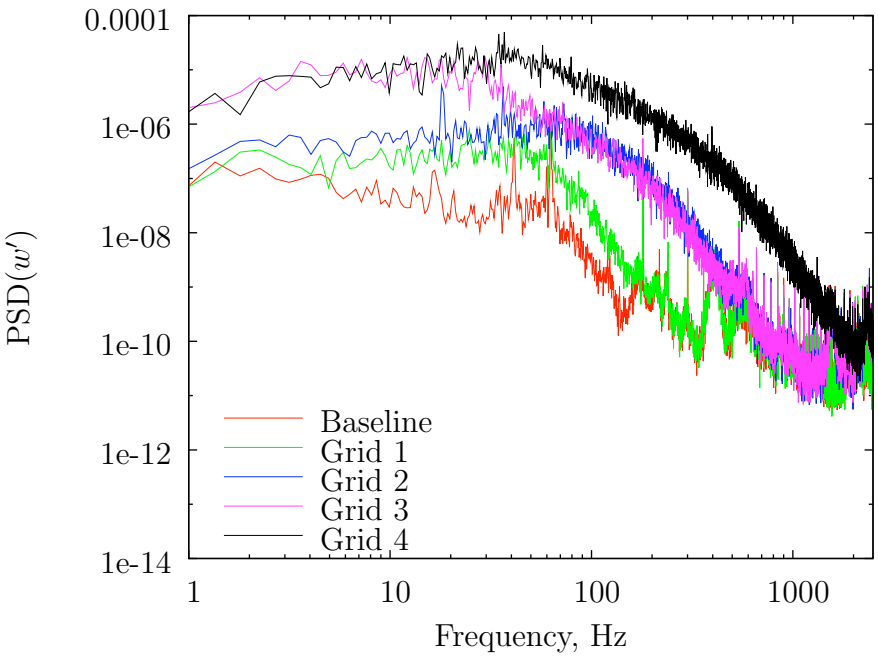

Figure 4.4: Power spectral densities of w' for each turbulence configuration. The test speed is $U_\infty = 24$ m/s.

The largest scale present in a given turbulent flow is known as the integral length scale, Λ. This quantity represents the scale of the largest turbulent eddies in the flow. It is typically defined by the longest distance at which independent velocity measurements show a correlation. Expressed as a function of streamwise separation, r, the correlation function for u' is defined as:

$$f(r) = \frac{\langle u'(X,t)u'(X+r,t)\rangle}{\langle u'^2_{\text{rms}}\rangle}. \tag{4.1}$$

In practice, this quantity is difficult to measure. The chief obstacle is that the wake of the upstream probe (at X) would no doubt influence the measurement of the downstream probe (at $X + r$). The longstanding solution to this problem is to apply Taylor's hypothesis of frozen turbulence. That is, if one considers that the measured fluctuations are the result of a fixed field of turbulence passing by a probe, the streamwise separation r may be converted to a time lag $\tau = r/U_\infty$. In this case,

the autocorrelation f of u' is used. The streamwise integral length scale Λ_x is then defined as

$$\Lambda_x = \int_0^\infty f(r)\mathrm{d}r = U_\infty \int_0^\infty f(\tau)\mathrm{d}\tau \tag{4.2}$$

There is some ambiguity regarding the upper limit of this integral. A measured autocorrelation function may oscillate about zero and any real measurement domain is finite. Several approaches to determining an appropriate integration domain are tested by O'Neill *et al.* (2004) and it is found that integrating up to the point where $f(r) = 0$ is preferred. Using the first zero-crossing point as the upper limit has become a common procedure (Kurian & Fransson, 2009); this is the approach used for the present analysis. For homogeneous isotropic turbulence that may be described as statistically stationary, the theoretical autocorrelation function is $f(r) = \exp(-r/\Lambda_x)$ (Pope, 2000). Though the turbulence in this case has a degree of anisotropy, this relation is used to provide an alternate measure of the integral length scale. Experimental data for $f(r)$ are fitted to this model to determine Λ_x.

Selected autocorrelation functions are plotted in Figs. 4.5–4.7; the experimental data are also plotted in Fig. 4.8 with the streamwise displacement scaled by the computed values of Λ_x. Test points corresponding to the lower turbulence intensities are not shown as the autocorrelation functions exhibit significant deviation from the theoretical curve. It is hypothesized that at these turbulence levels, the turbulent fluctuations are overwhelmed by electronic noise and this precludes accurate computation of the autocorrelation function. To test this assertion, an additional test point is added with $Tu = 0.53\%$. This is accomplished experimentally by placing grid 3 in the settling chamber. The degree to which the measured autocorrelation functions agree with the theoretical curves is deemed acceptable given that the realized turbulence certainly deviates somewhat from the assumed character of the theory.

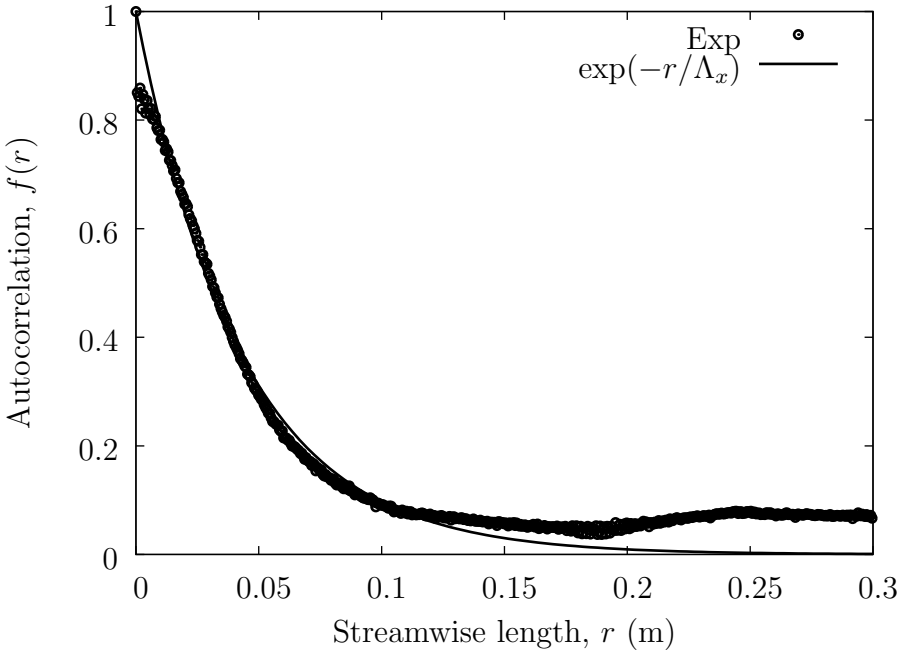

Figure 4.5: Autocorrelation functions of u' for $Tu = 0.05\%$. The test speed is $U_\infty = 24$ m/s.

Tu	Λ_x	
	$\int f(r)$	$\exp(-r/\Lambda_x)$
0.05%	43 mm	43 mm
0.19%	35 mm	34 mm
0.53%	29 mm	24 mm

Table 4.2: Turbulence integral length scales measured at $U_\infty = 24$ m/s. Results from integration of the autocorrelation function and curve fitting to the theoretical function are given.

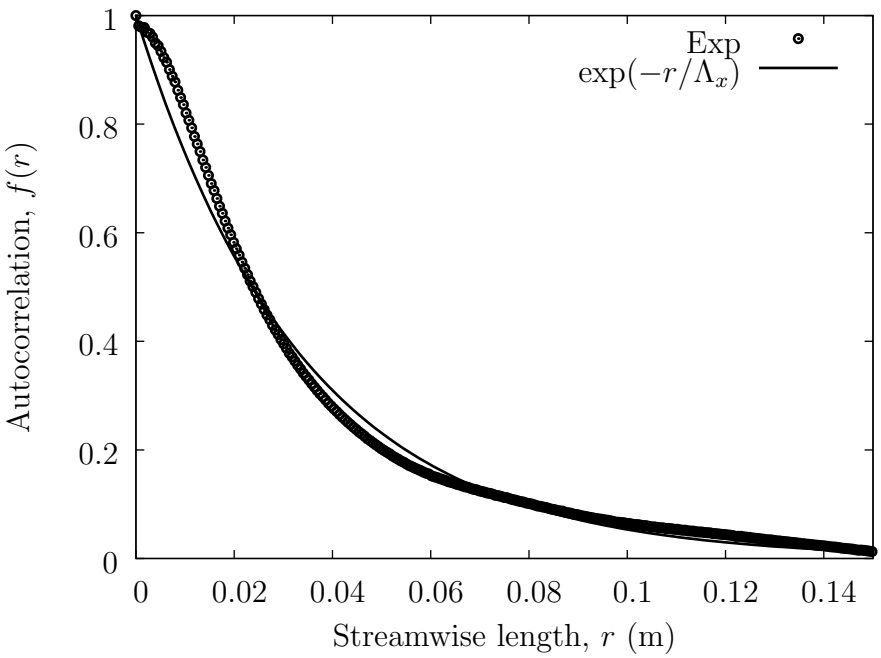

Figure 4.6: Autocorrelation functions of u' for $Tu = 0.19\%$. The test speed is $U_\infty = 24$ m/s.

Computed values of the integral length scale are compiled in Table 4.2. This table is restricted to the turbulence configurations for which the measured autocorrelation functions qualitatively agree with the expected shape. Measurement of the integral length scales for the lower turbulence intensity values appear to be subject to corruption from the comparatively high level of electronic noise. These values are not reported. The reported cases show relatively good agreement between the two methods. For the $Tu = 0.05\%$ case, the length scale originally computed via integration was twice that obtained from the curve fit. However, when the data of Fig. 4.5 are considered, the reason for this is clear. The measured autocorrelation function does not cross zero over a long domain but oscillates around $f = 0.05$. When the integration domain in this case is limited to $r = 0.20$, the corresponding value of Λ_x is computed to be 43 mm, in agreement with the value obtained from the curve fit.

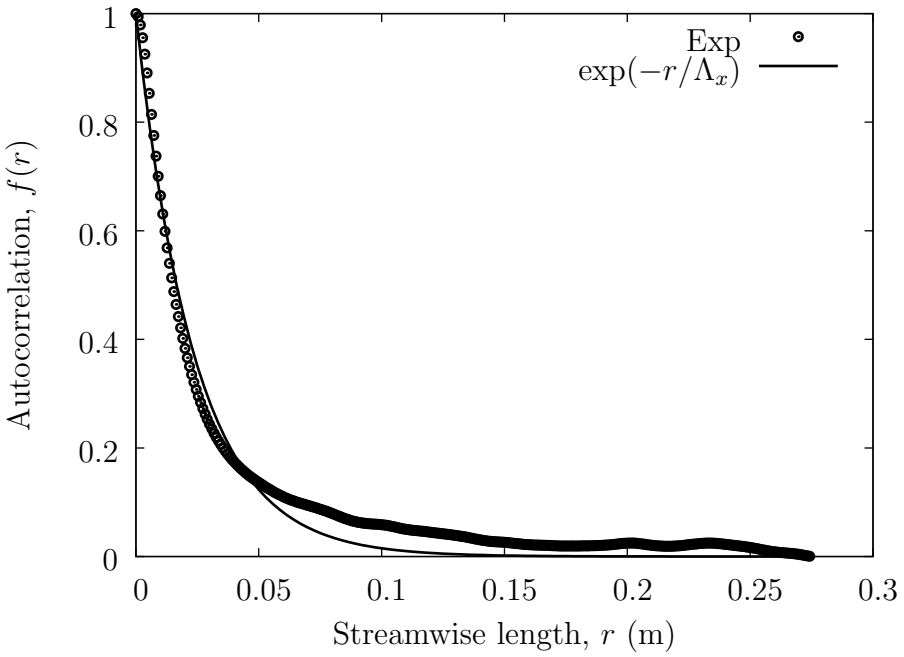

Figure 4.7: Autocorrelation functions of u' for $Tu = 0.53\%$. The test speed is $U_\infty = 24$ m/s.

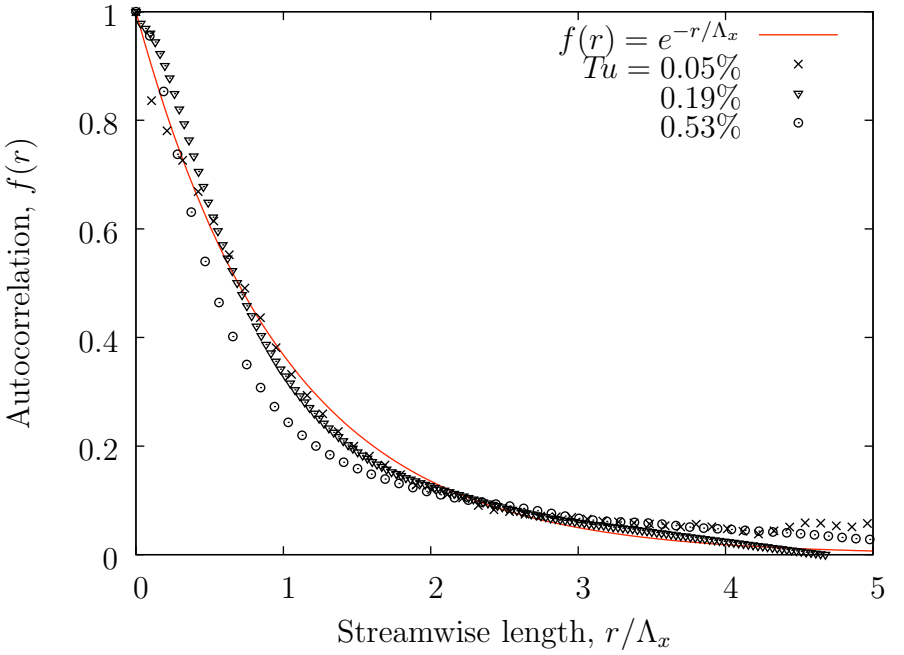

Figure 4.8: Normalized autocorrelation curves of u' at $U_\infty = 24$ m/s.

These values provide an *a posteriori* justification for the probe separation distance used for the optimal filtering technique. That technique requires that the probes are separated by a distance greater than the integral length scale of the turbulence. For those measurements, the separation distance was approximately 690 mm. Although the transverse integral length scale was not directly measured, a test of the isotropy of scales was completed following the methods of Westin *et al.* (1994). Two probes are located in the same streamwise plane and separations in Y and Z are introduced. Cross-correlations between the probes are computed at each point. These data are hampered by the same problem as the autocorrelation data; the quality of the correlation functions increases with turbulence intensity. For this reason, only the higher turbulence case is considered. In Fig. 4.9, the cross-correlations are plotted for Y and Z separations. To protect the hot-wire probes, the minimum separation distances used are $\Delta Y = 2$ mm and $\Delta Z = 1$ mm. As this plot shows, there is some anisotropy of the transverse scales. The larger contraction ratio in the Z direction is the likely cause of this minor difference in scales.

The dissipation microscale (commonly known as the Taylor microscale, after G. I. Taylor) describes the length scale that characterizes the size of the largest turbulent eddies that are responsible for dissipation (Hinze, 1975). Put another way, this length scale marks the divide between the inertial subrange and the dissipation subrange. As with the integral length scale, these are not exact physical relationships but meant to characterize the corresponding average scales. A number of relationships may be exploited to measure this length scale. Numerical differentiation and subsequent extrapolation of the measured autocorrelation function may be used in the definition of the streamwise dissipation scale, λ_x:

$$\frac{2}{\lambda_x} = -\left[\frac{\partial^2 f}{\partial r^2}\right]_{r=0}. \tag{4.3}$$

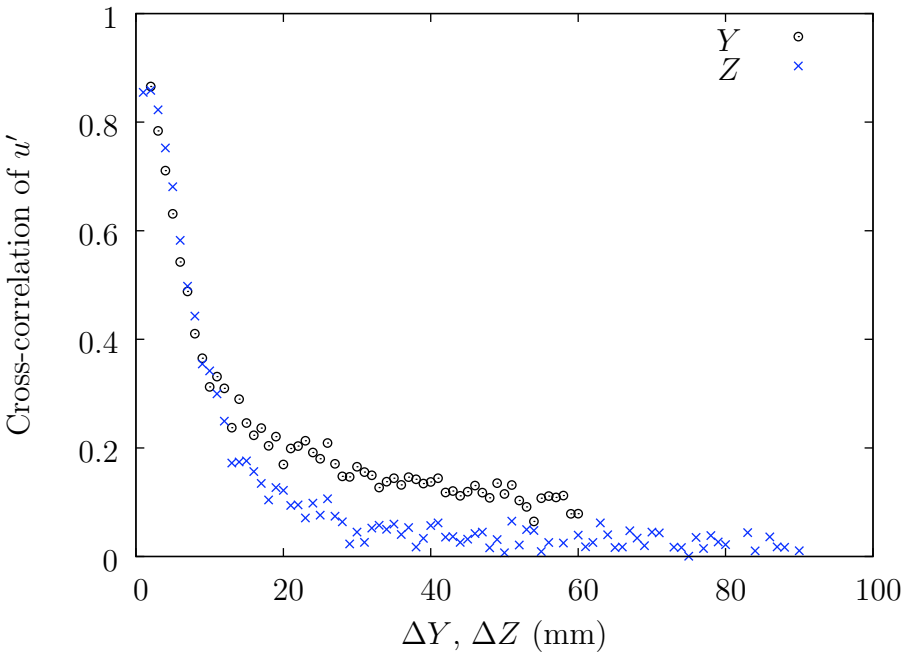

Figure 4.9: Two-probe cross-correlations of u' for $Tu = 0.19\%$. The test speed is $U_\infty = 24$ m/s.

This difficulty in measuring $f(r)$ near $r = 0$ and the numerical manipulation may introduce significant uncertainty into the measured value of λ_x. For this reason, the common procedure is to make use of a Taylor series expansion of Eq. 4.3, as in Kurian & Fransson (2009), for example. Once again applying Taylor's hypothesis to convert a spatial derivative to a temporal derivative, an expression for computing the Taylor microscale is

$$\lambda_x = \sqrt{2}\frac{U_\infty u'_{\text{rms}}}{(\partial u'/\partial t)_{\text{rms}}}. \tag{4.4}$$

In practice, the derivative in the denominator is approximated with a first-order central difference. As noted by Kurian & Fransson (2009) and Westin *et al.* (1994), the sampling rate may strongly influence this measurement. For too high a sampling rate, discretization effects in the data acquisition system and electrical noise will influence the results. The aforementioned references use the following procedure to address

these problems: the sampling rate is gradually increased and $\lambda_{x,m}$ is computed using Eq. 4.4 (the added subscript denotes measured values). These values are plotted as a function of $\Delta X = U_\infty \Delta t$ for decreasing ΔX (increasing sampling rate). The data are then extrapolated to zero using a parabolic curve fit to approximate λ_x. One set of data for the baseline turbulence configuration (0.02%) is shown in Fig. 4.10.

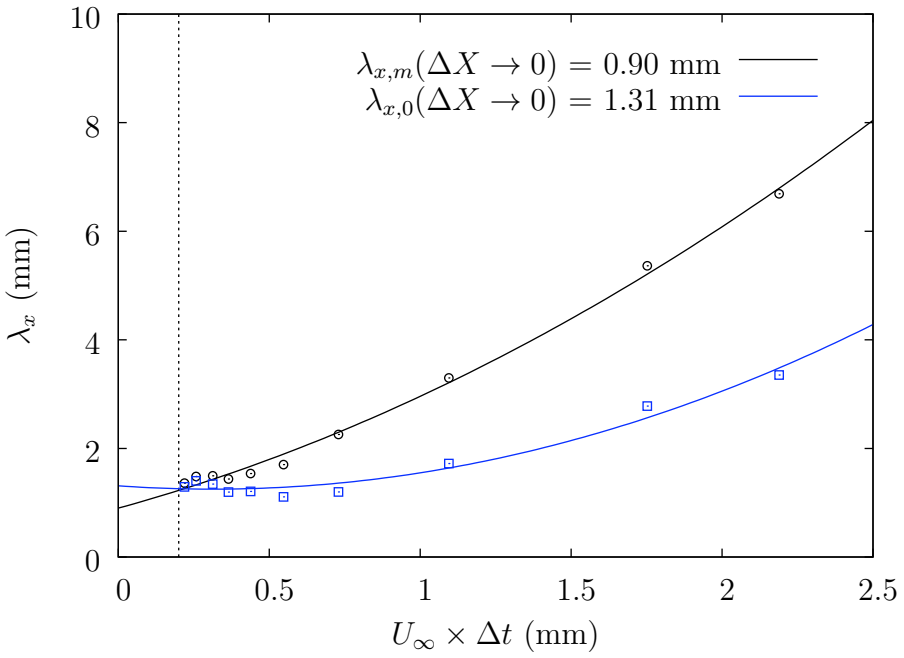

Figure 4.10: Measurements of the dissipation microscale for $Tu = 0.02\%$, $U_\infty = 24$ m/s. The data are extrapolated past the vertical dashed line.

An alternative method for determining the value of the dissipation microscale is given by Hinze (1975). If the turbulence is homogeneous and the fluctuations follow a Gaussian probability distribution, λ_x may be approximated by counting the number of times N_0, that $u'(t)$ crosses zero per unit time. The approximate value for $\lambda_{x,0}$ is given by Eq. 4.5, where the added subscript denotes this zero-crossing method.

$$\lambda_{x,0} = \frac{U_\infty \sqrt{2}}{\pi N_0} \tag{4.5}$$

The indirect nature of this measurement coupled with the availability of modern, high-speed data acquisition hardware seems to have made this method obsolete. Regardless, it is used in the present experiments merely as a check on the primary method derived from the Taylor series expansion. The results from both methods are plotted in Fig. 4.10. These procedures are applied to data from all of the turbulence configurations and the results are tabulated in Table 4.3. The values determined from the two methods are consistent. The apparent trend is that the Taylor microscale is increased in the higher turbulence configurations. Due to the difficulty in measuring the integral length scale at the lower turbulence levels, the relationship (if any) between these two length scales for the present experiments is not clear.

Tu	$\lambda_{x,m}$	$\lambda_{x,0}$
0.02%	0.9 mm	1.3 mm
0.03%	1.0 mm	1.3 mm
0.05%	1.6 mm	2.1 mm
0.10%	2.1 mm	2.7 mm
0.19%	4.5 mm	5.8 mm

Table 4.3: Taylor's dissipation microscale measured at $U_\infty = 24$ m/s. Results are given for numerical differentiation of the streamwise fluctuations ($\lambda_{x,m}$) and for the zero-crossing method ($\lambda_{x,0}$).

In summary, disturbance environments characterized by moderate levels of free-stream turbulence intensity are created using sparse grids upstream of the wind tunnel contraction. All three components of the turbulent fluctuations are measured and the spectra are documented for the test speeds. The two-probe correlations show a modest anisotropy that is expected from experimentally-generated turbulence using grids

in the settling chamber. Integral and dissipation length scales of the turbulence are measured, though the low levels in the present experiment make resolving these values difficult. The difficulties associated with varying turbulence intensity while holding the length scales fixed in an experimental setting are well known (Fransson *et al.*, 2005). The goal of this effort is not necessarily to put forth a correlation between turbulence scale and its effect on crossflow instability, but to document the disturbance environment thoroughly. This additional information will help to facilitate the comparison of experimental results measured across different facilities. A more detailed specification of the disturbance environment will also serve to produce more accurate results from future computational studies. The numerical receptivity studies of Tempelmann (2011), for example, examined the role of optimal disturbances to a swept-wing boundary layer. Select disturbances in the form of surface roughness were used for validation with experimental results. Careful documentation of the freestream turbulence in the experiments will allow for simulations that specify realistic disturbance environments, rather than relying on optimal disturbances.

CHAPTER V

EFFECTS OF FREESTREAM TURBULENCE ON CROSSFLOW INSTABILITY

The first set of experiments examines the polished leading edge without artificial roughness. The distinction should be made that the leading edge is not absent of roughness, as some level of surface roughness is always present. The natural distributed surface roughness level of this polished leading edge is 0.3 μm rms (Hunt, 2011). Although spanwise roughness arrays are commonly used to control the initial disturbance and create a uniform series of crossflow vortices, an initial series of tests with a clean leading edge are completed to better understand the effects of turbulence alone. Chapter VI comprises experiments utilizing regular arrays of surface roughness.

In addition to providing baseline measurements of transition location and disturbance evolution, these preliminary experiments serve to validate the linear stability theory calculations. The LST calculations of Professor Helen Reed and Matt Tufts are used to determine the spanwise wavelength of the most unstable stationary mode. This quantity is used to apply critically-spaced roughness and to guide the selection of subcritical wavelengths. All of the experiments are run at $Re_c = 2.8 \times 10^6$, with the model oriented at $\alpha = -2.9°$. At these conditions, LST calculations show that the wavelength of the most unstable disturbance is 10–12 mm. As will be shown, the critical wavelength determined via experiment matches the predictions of linear stability theory.

A. Transition Location

Prior to detailed boundary-layer measurements using hot-wire probes, flow visualization is used to guide the experiments. The NFV technique described in detail in Chapter III is applied throughout. Perhaps the greatest utility of NFV is the ability to quickly determine the regions where the flow is laminar. In addition to demarcating the usable measurement region, evaluation of the transition location indicates the overall effect of a configuration change (increasing freestream turbulence, in this case). The nature of crossflow-instability-induced transition is such that the determination of transition location requires some consideration.

The characteristic saw-tooth transition pattern induced by the stationary crossflow mode was shown by Dagenhart & Saric (1999) to be model-fixed. That is, changing the flow field (by translating the model, among other approaches) did not change the transition pattern. This result, in conjunction with other experiments confirming that surface roughness sets the initial disturbances for the stationary mode, led to the conclusion that the saw-tooth pattern is related to small variations in natural surface roughness. The transition fronts in this scenario may extend over a streamwise range of several percent chord. In the present experiments, the average location of transition across the span is used to represent the transition location, x/c_{tr}.

The transition pattern measured at the baseline turbulence level (0.02%) is shown in Fig. 5.1(A). The saw-tooth pattern is evident around the 70% chord marker. Streamwise streaks in the surface coating due to the stationary crossflow vortices are also visible; these may be used to measure the wavelength of the crossflow vortices. From this figure, a line profile of the pixel values is measured at $x/c = 0.36$, parallel to the leading edge. A small region in the upper span is used where the streaks are the most evident. The line profile is plotted in Fig. 5.2; spectral analysis

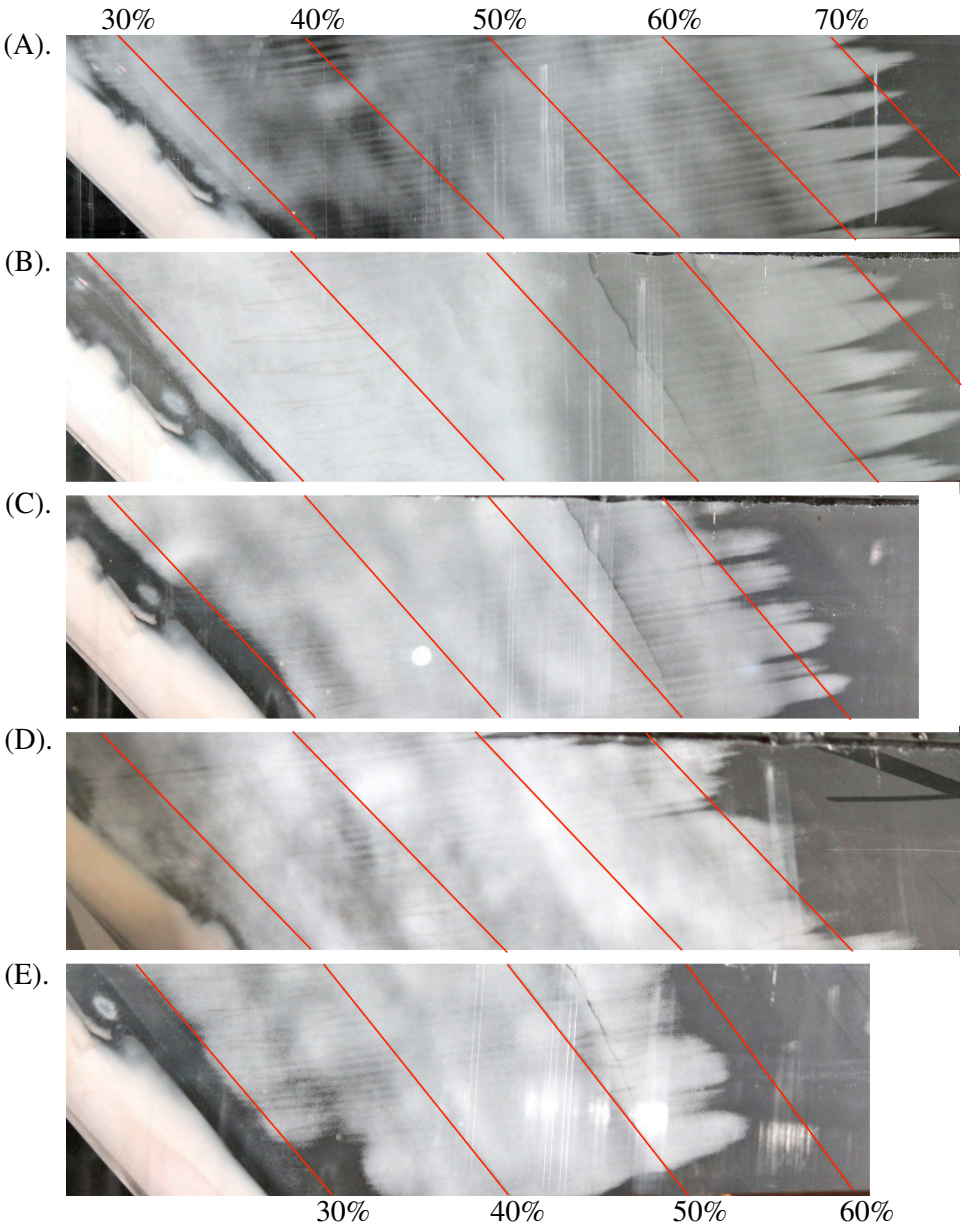

Figure 5.1: Flow visualization results at $Re_c = 2.8\times10^6$, clean leading edge. (A). $Tu =$ 0.02%, (B). 0.03%, (C). 0.05%, (D). 0.10%, (E). 0.19%.

techniques are used to compute the spanwise spatial periodogram plotted in Fig. 5.3. This periodogram shows a clear spectral peak indicating a crossflow wavelength of $\lambda_{cr} = 10.5$ mm. Uncertainty analysis for this type of spectral measurement (Downs & White, 2011) indicates that the uncertainty in this value is on the order of ± 0.3 mm. Thus, for this configuration the NFV results indicate that transition is due to a stationary crossflow mode whose wavelength is within the range expected for the most unstable mode.

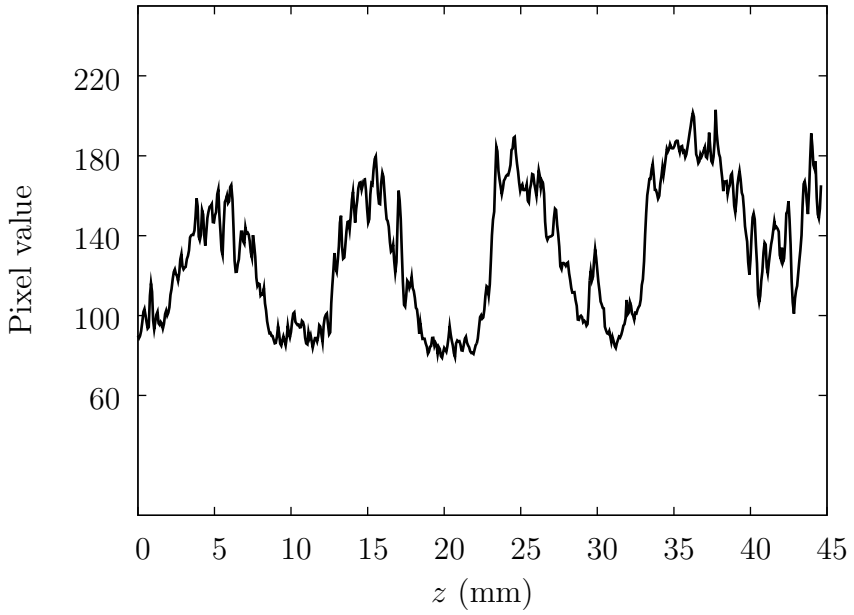

Figure 5.2: Pixel-value line profile of flow visualization streaks. The line profile is taken parallel to the leading edge at $x/c = 0.36$, in the upper span region of Fig. 5.1A.

Similar measurements are made using enhanced freestream turbulence levels as described in Chapter IV and the corresponding NFV results are shown in Fig. 5.1B–E. When Tu is increased from 0.02% to 0.03%, no change is observed in the transition pattern. However, for $Tu = 0.05\%$, the average transition location moves forward by

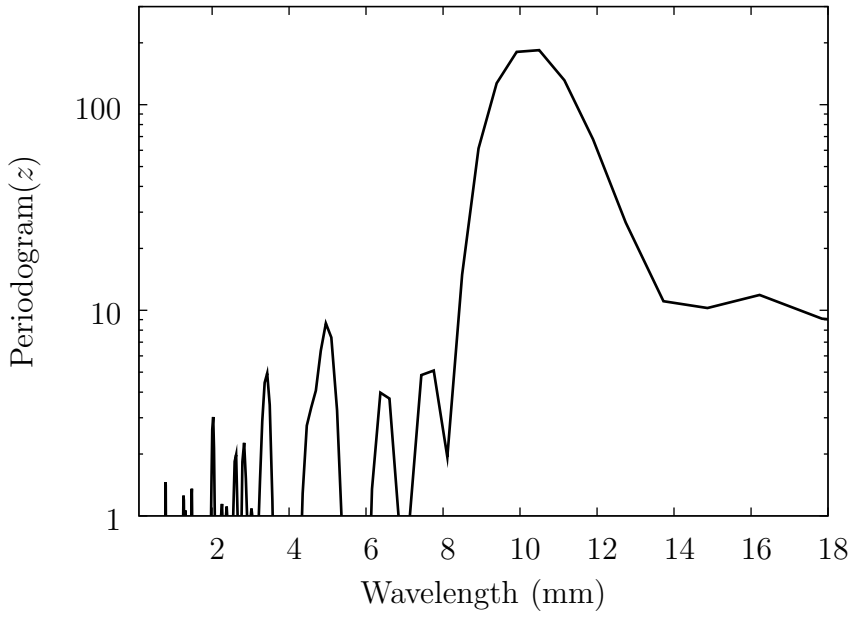

Figure 5.3: Spatial periodogram of the line profile of Fig. 5.2. The spectral peak indicates a crossflow wavelength of 10.5 mm.

a few percent chord and the shape of the transition front changes. The transition pattern has peaks that are less sharp than the distinctive saw-tooth pattern of the previous two results. Based on the findings of Deyhle & Bippes (1996) (among others), it is expected that the traveling crossflow mode will have a larger amplitude in higher-intensity freestream turbulence, and that it will dominate the transition process for $Tu > 0.2\%$. By its nature, it is expected that the traveling crossflow mode will produce a flat transition front. In the range of turbulence intensities where both modes are of significant amplitude, a more diffuse saw-tooth pattern might be expected. As Tu is increased to 0.19% in Fig. 5.1E, this is what is observed. The extent of laminar flow is decreased as the freestream turbulence intensity is increased.

Numerical results of the flow visualization experiments are summarized in Table 5.1. Between the baseline turbulence level and the highest intensity tested, the average transition location moves forward by $0.1c$. In all cases, the images show

streaks that are spaced within the range predicted for the most unstable stationary wavelength. From these results, it can be concluded that increasing the freestream turbulence intensity has a destabilizing effect on the boundary layer.

Tu	x/c_{tr}	λ_{cr}
0.02%	0.67	10.5 mm
0.03%	0.67	11.2 mm
0.05%	0.62	10.8 mm
0.10%	0.62	10.4 mm
0.19%	0.57	10.6 mm

Table 5.1: Transition locations measured at $Re_c = 2.8\times10^6$ using a clean leading edge. Tabulated values represent average transition location across the span. Crossflow wavelengths are measured using spectral analysis of the NFV images.

B. Data Analysis and Baseline Results: $Tu = 0.02\%$

Quantitative assessment of the crossflow disturbance evolution is made using boundary-layer velocity measurements. Constant temperature hot-wire anemometry is used, as described in Chapter III. Analysis of the resulting boundary-layer velocity profiles is discussed in the context of baseline measurements: no artificial roughness and $Tu = 0.02\%$. To properly resolve the boundary layer, it should be on the order of a few millimeters thick. Additionally, the disturbances need to be large enough to distinguish from measurement uncertainty. For these reasons, the first in a series of spanwise boundary-layer scans is started at $x/c = 0.10$. At these test conditions, $x/c_{tr} = 0.67$ with the peaks of the saw-tooth pattern reaching forward a few percent chord. Boundary-layer measurements are therefore not attempted past $x/c = 0.60$.

Results from the first spanwise scan are plotted in Fig. 5.4: 65 boundary-layer profiles are measured at $x/c = 0.10$, spaced at $\Delta z = 1$ mm. These profiles are normalized by the local edge velocity, U_e, measured by extending the boundary-layer probe a few millimeters into the freestream at each chord location. Approximately 70 points are measured per boundary layer, with the measurement density increasing as the probe descends toward the wall. Subsequent data analysis shows that the boundary-layer thickness is $\delta_{99.9} = 1.72$ mm. This definition of the boundary-layer thickness is used for consistency with Deyhle & Bippes (1996). At this streamwise location, the magnitude of the steady disturbance is small, as evident in the minimal distortion of the boundary-layer profiles. The mean profile, $\overline{U}(Y)$ is computed by averaging the velocity across the span at every height in the boundary layer; this plotted as the blue line in Fig. 5.4.

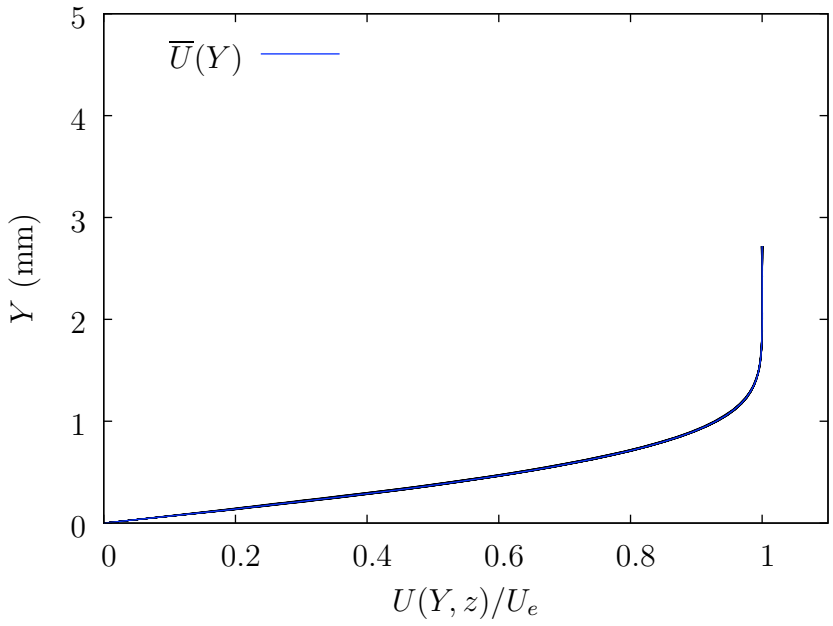

Figure 5.4: A typical set of 65 boundary-layer profiles ($\Delta z = 1$ mm) measured at $x/c = 0.10$. Test conditions are $Re_c = 2.8 \times 10^6$, $Tu = 0.02\%$, clean leading edge.

At $x/c = 0.10$, there is little modulation of the mean flow. However, the profiles measured further downstream ($x/c = 0.50$) show much larger disturbances. A series of profiles at this location is plotted in Fig. 5.5; some inflectional profiles are apparent.

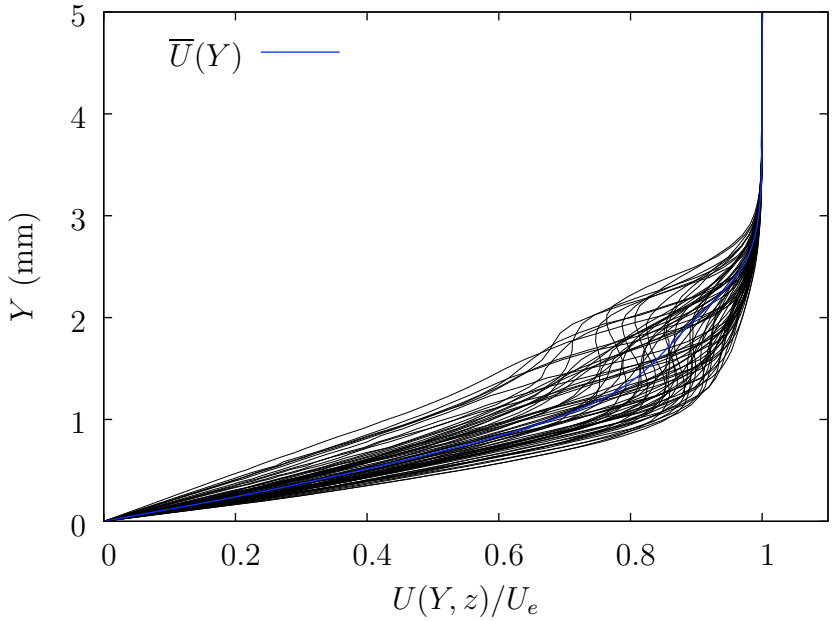

Figure 5.5: A typical set of boundary-layer profiles measured at $x/c = 0.50$. Test conditions are those of Fig. 5.4.

Though it is desirable to have some measure of the basic state (undisturbed) flow, this cannot be directly measured in the present experiment. The mean boundary-layer profile is the sum of the basic state and mean stationary disturbance. The steady disturbances to the flow are obtained by subtracting the mean profile from each individual profile. For illustrative purposes, these steady disturbance profiles, $U'(Y,z) = U(Y,z) - \overline{U}(Y)$ are plotted in Fig. 5.6 for a streamwise location of $x/c = 0.50$. The disturbances, by definition, must go to zero in the freestream. This is observed in the experimental data. As this plot shows, the steady disturbances reach up to 25% of U_e at this location. A more compact measure of the steady boundary-

layer disturbances is the stationary mode shape that is computed from the disturbance profiles. To do so, the spatial rms of the disturbance is computed in the spanwise direction at each measured height in the boundary layer. For n profiles, this operation is expressed as follows.

$$U'_{\mathrm{rms}}(Y) = \sqrt{\frac{1}{n}\sum_{i=0}^{n-1}[U(Y,z_i) - \overline{U}(Y)]^2} \tag{5.1}$$

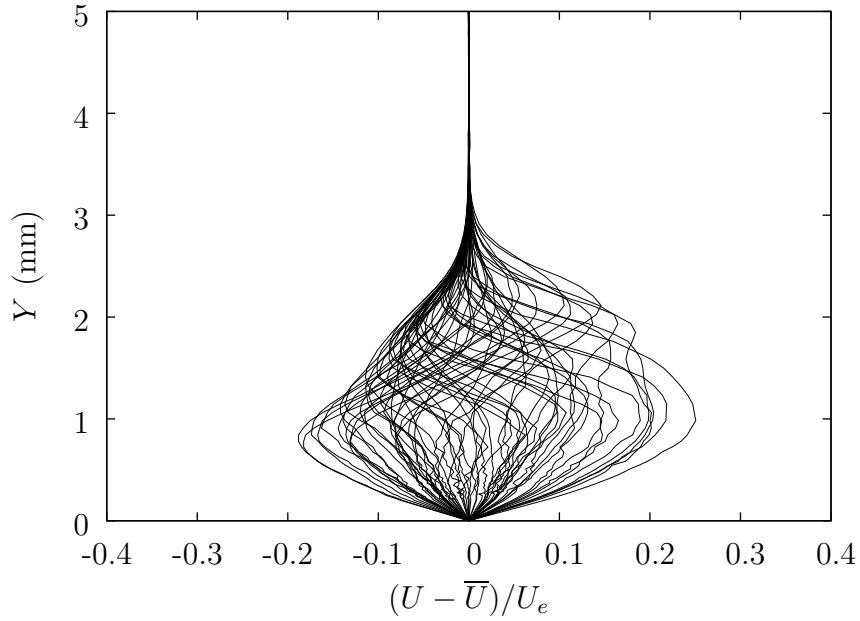

Figure 5.6: Steady disturbance profiles computed from the boundary-layer profiles of Fig. 5.5.

The stationary disturbance mode shapes for the clean leading-edge configuration with baseline turbulence intensity are plotted in Fig. 5.7 for each streamwise measurement station. The data show that the initial stationary disturbance is quite small. At $x/c = 0.10$, the maximum value of U'_{rms} is less than 1% of the edge velocity. Because the stationary crossflow mode acts at fixed locations across the model, the crossflow vortices deform the mean flow by an integrated effect along the streamlines.

As a result, these weak vortices produce stationary mode shapes of relatively large amplitude. In considering these mode shapes, the maximum amplitude grows to over 15% of the edge velocity before transition occurs.

Another important feature of these data is the appearance of nonlinear interactions among stationary crossflow modes. This is manifested as a second lobe in the mode shape profile that appears higher in the boundary layer than the maximum amplitude (Reibert, 1996). For this set of measurements, the onset of this phenomenon is at $x/c = 0.45$, though it is fairly subtle in this case. This is due in part to the absence of artificial roughness: exciting a uniform series of stationary vortices with a spanwise array of discrete roughness elements produces much cleaner disturbance measurements. This technique is now common in crossflow instability experiments (Saric *et al.*, 1998) and is the subject of Chapter VI.

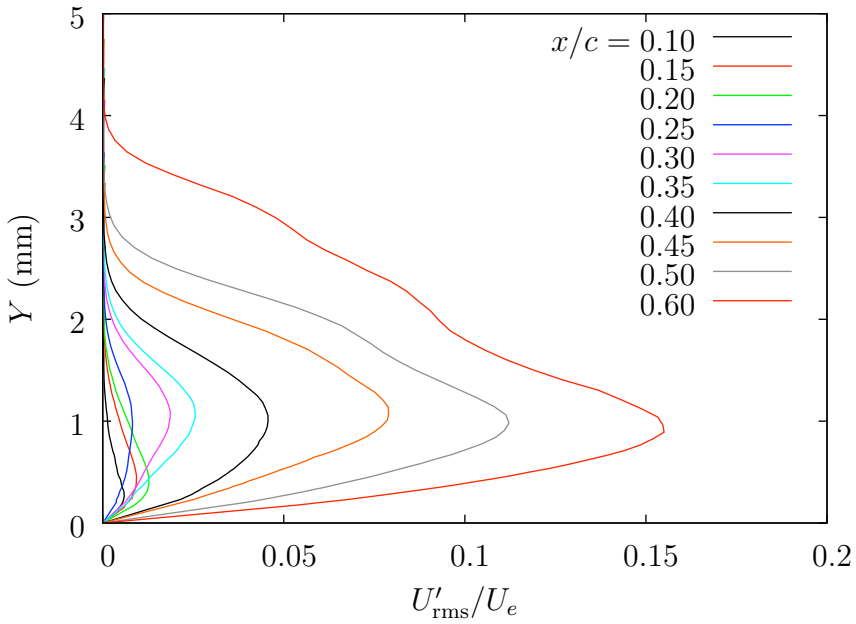

Figure 5.7: Spanwise rms steady disturbance profiles at $Re_c = 2.8 \times 10^6$, $Tu = 0.02\%$, clean leading edge.

The extent of the spatial non-periodicity for natural crossflow is minor; the NFV image showed regularly spaced streaks. The boundary-layer measurements may also be used to visualize the flow field. To do so, iso-velocity contours are plotted for a given measurement plane. In Fig. 5.8, such contours are plotted in increments of 5% of U_e for measurements made at $x/c = 0.60$. The color contours represent the streamwise velocity fluctuation intensity, u'_{rms}. The plot shows the spanwise modulation of the mean flow produced by five crossflow vortices. The middle section clearly shows an area in which the extent of this distortion is greater than its neighbors. The likely cause of this difference is a greater initial disturbance for this particular vortex. A small non-uniformity in the natural surface roughness near the leading edge could produce this result.

The unsteady fluctuation contours are computed using the AC component of the hot-wire measurements as previously described. In addition to the standard 1 Hz–10 kHz passband applied using a hardware filter, a 60 Hz notch filter is also applied in the data post-processing step. The purpose of this notch filter is to remove the component of the signal that is due to the power source. The spatial distribution and periodicity of the unsteady modes is an indication of impending transition via secondary instability (White & Saric, 2005). Though the high-frequency secondary instability is not the focus of the present experiments, tracking the evolution of the traveling modes is an important part of the turbulence receptivity problem. Select figures of the boundary-layer measurements are included in the main text for illustrative purposes. The full series of boundary-layer profiles, steady disturbance profiles and contour plots (of both steady and unsteady velocities) are collected in Appendix A.

To quantify the spanwise periodicity of the mean flow distortion, the PSD of $U'(z)$ is computed at each boundary-layer height. This is completed following the recommendations of Press *et al.* (2007) for spectral analysis. Toward that end, the

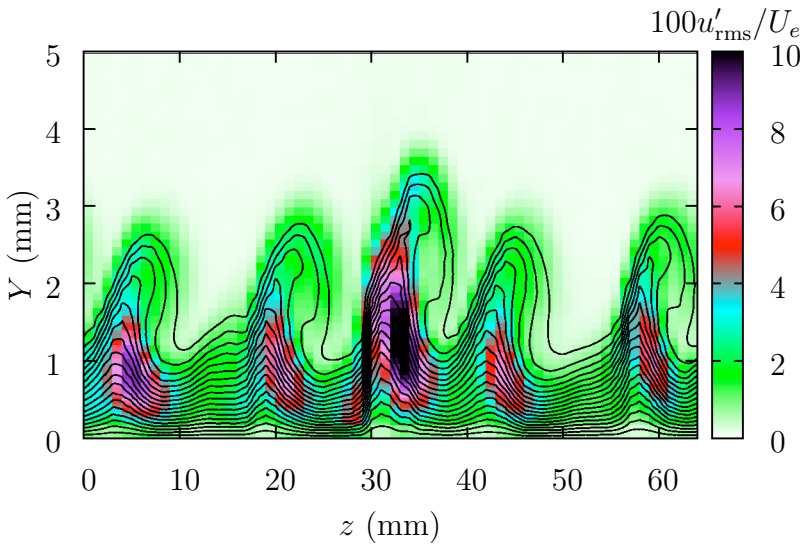

Figure 5.8: Steady and unsteady velocity contours at $x/c = 0.60$. Test conditions are those of Fig. 5.4.

data are windowed using the Welch window. Prior to computation of the PSD coefficients, the data are padded with zeros until the length of the data set is an even multiple of the most unstable wavelength: $\lambda = 12$ mm. For a series of 65 profiles, the data are padded to $N = 72$, such that the fundamental wavelength and its first five harmonics are resolved by the PSD. The raw PSD coefficients are computed by taking a fast Fourier transform of the windowed U' data and squaring the resulting complex values.

The PSD coefficients are normalized by the sum of the squares of the window function, W_{ss}. For N points in z, the corresponding FFT components of $U'(z)$ are denoted as $H_k(U')$, for $k = 0, 1 \ldots N-1$. the PSD components are then computed according to Eq. 5.2.

$$\mathrm{PSD}_k = \frac{1}{W_{ss}} |H_k(U')|^2 \qquad k = 0, 1 \ldots N/2 \tag{5.2}$$

For the boundary-layer height corresponding to the maximum stationary disturbance amplitude, the PSDs for the current configuration are plotted in Fig. 5.9 for each streamwise location. The level of disturbance in the absence of artificial roughness is small; the PSDs for data measured upstream of $x/c = 0.35$ do not produce usable spectral peaks. These spectra are also affected by the sort of non-uniformity observed in the data of Fig. 5.8. As such, the spectral peaks are shifted somewhat (as in the case of the $x/c = 0.45$ data). However, there is still a strong indication that the disturbances are composed primarily of a 12 mm wave. This confirms the expectation that this mode would appear as the dominant steady disturbance in the absence of artificial roughness. As will be shown in Chapter VI, exciting this wavelength with a spanwise array of roughness with $\lambda_k = 12$ mm effectively creates a uniform series of crossflow vortices that quickly grow and move transition forward.

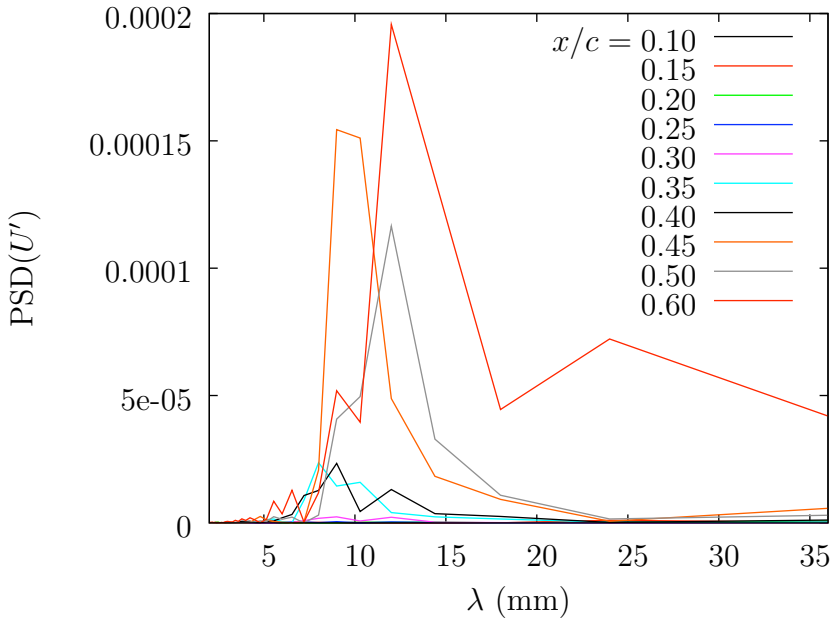

Figure 5.9: Spanwise power spectra at $Re_c = 2.8 \times 10^6$, $Tu = 0.02\%$, clean leading edge.

To track the evolution of the stationary disturbances, a measure of the disturbance amplitude is needed. There are several possibilities that Reibert (1996) shows are largely equivalent. In the present work, the total stationary disturbance amplitude, A, is computed by integrating the stationary mode profiles.

$$A = \frac{1}{\delta_{99.9}} \int_0^{\delta_{99.9}} U'_{\mathrm{rms}}(Y)\mathrm{d}Y \tag{5.3}$$

The N factor is then:

$$N = \ln \frac{A}{A_0} \tag{5.4}$$

In practice, the boundary-layer thickness used corresponds to 99.9% of U_e in the mean profile $\overline{U}$ for consistency with previous research (Deyhle & Bippes, 1996). Likewise, the unsteady disturbance amplitude, a_{rms} is computed by integrating $u'_{\mathrm{rms}}(Y, z)$ in Y and z. This is shown in Eq. 5.5.

$$a_{\mathrm{rms}} = \frac{1}{z_{max}} \frac{1}{\delta_{99.9}} \int_0^{z_{max}} \int_0^{\delta_{99.9}} u'_{\mathrm{rms}}(Y, z)\mathrm{d}Y\mathrm{d}z \tag{5.5}$$

The temporal frequency content of the unsteady fluctuations is of interest. As discussed in Chapter IV, the LST calculations show that the most amplified traveling wave has a frequency of approximately 120 Hz, and that a broad band of disturbances around this value also exhibit strong growth rates. For consistency with previous work using similar test conditions (White & Saric, 2005), a traveling mode passband of 100–300 Hz is used. To compute the traveling mode disturbance amplitude, $u'(t)$ at every spatial point is integrated in the frequency domain over this range.

A series of traveling mode amplitude profiles are shown in Fig. 5.10 for the clean leading edge configuration at $Tu = 0.02\%$. At this lowest turbulence level, the amplitude of the traveling mode is expected to be small compared with the stationary mode. These profiles show that the maximum amplitude grows steadily up to 1% of U_e at $x/c = 0.50$ and then increases sharply at the last measured point. Notwithstanding

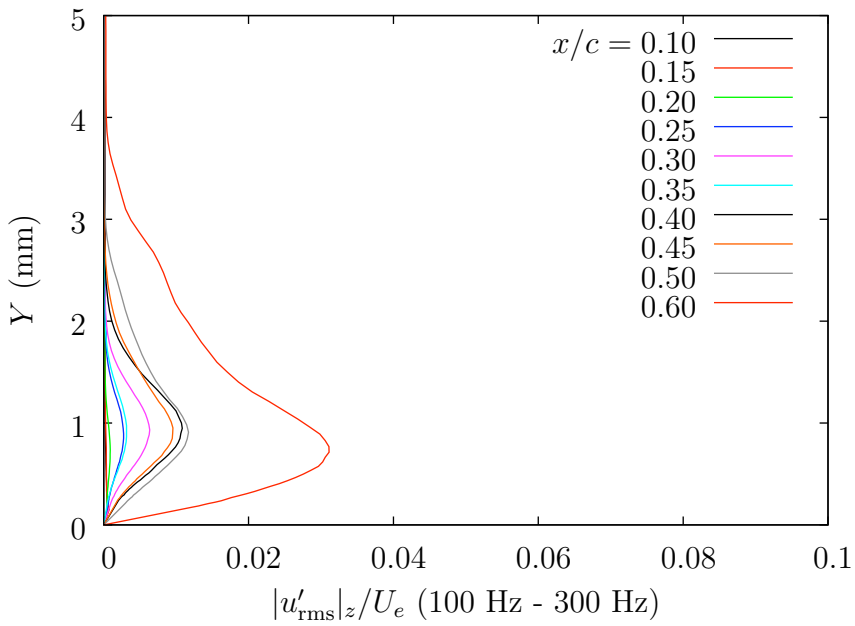

Figure 5.10: Spanwise mean of the unsteady disturbance profiles for the traveling wave passband 100–300 Hz at $Re_c = 2.8 \times 10^6$, $Tu = 0.02\%$, clean leading edge.

this point, the traveling mode amplitude is nearly an order of magnitude less than the stationary mode amplitude. The streamwise evolution of A and a_{rms} are plotted in Figs. 5.11 and 5.12, respectively.

Considering the growth of the stationary disturbance amplitude, it is apparent that saturation is *not* observed. The stationary disturbance amplitude does not show any appreciable growth until $x/c = 0.30$, at which point it rises sharply to its maximum value at the end of the measurement domain. The lack of artificial roughness means that the initial disturbance is very small. At this low turbulence level, the saturation amplitude is expected to be the largest observed in these experiments, as Deyhle & Bippes (1996) demonstrated that increasing the turbulence intensity decreases the saturation amplitude. It appears in this case that the small initial value of stationary disturbance amplitude precludes it from reaching the saturation amplitude upstream of $x/c = 0.60$, which is just a few percent chord forward of transition.

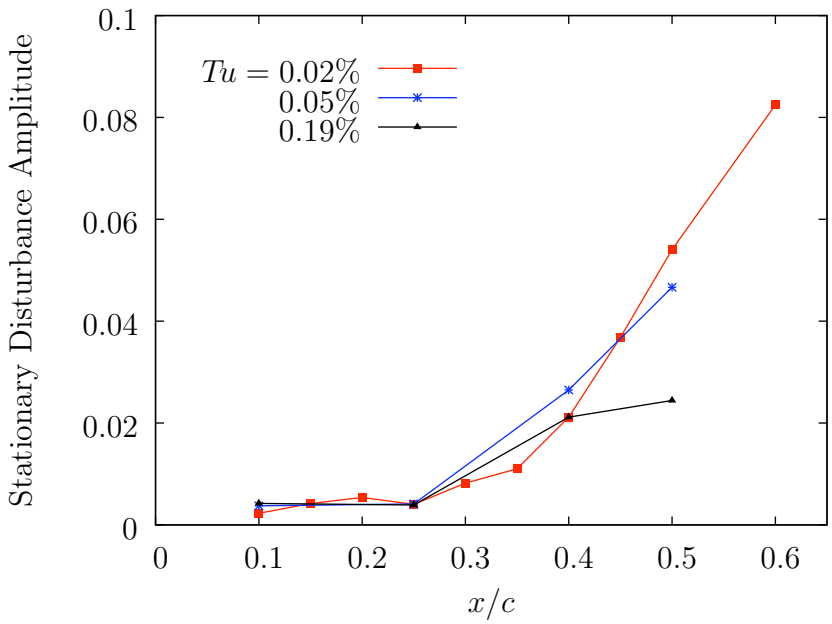

Figure 5.11: Stationary disturbance amplitude evolution at $Re_c = 2.8 \times 10^6$, clean leading edge.

The evolution of the unsteady disturbance amplitude in this baseline turbulence case is largely flat. There appears to be a slight decay from the initial value at $x/c = 0.10$ to the minimum at $x/c = 0.35$ in the total fluctuation level. The a_{rms} level then rises back to its initial value before increasing up to its maximum at $x/c = 0.60$. Put another way, a_{rms} only exceeds its initial value in the last measured point. When the traveling mode component is computed using the aforementioned 100–300 Hz passband, very minor growth is observed. Considering the sharp rise of the stationary disturbance growth and the nearly constant unsteady amplitudes, the stationary disturbance mode is obviously the dominant instability mode at this turbulence level.

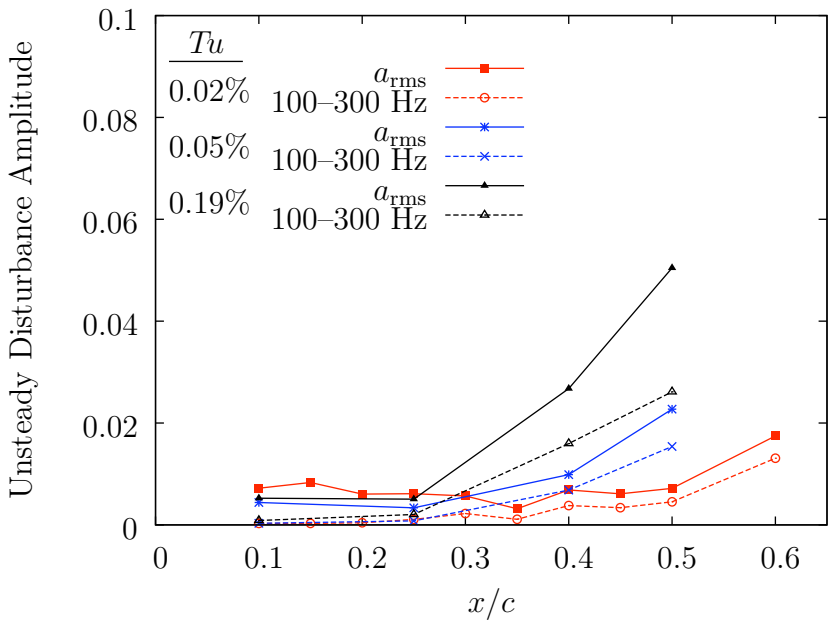

Figure 5.12: Traveling disturbance amplitude evolution at $Re_c = 2.8 \times 10^6$, clean leading edge.

C. Enhanced Turbulence Intensity Results

It was necessary to complete a set of measurements without using artificial roughness to confirm that 12 mm is the wavelength of the most unstable mode. However, these results showed that natural crossflow incited by the inherent model roughness is subject to some measure of non-uniformity in the spatial periodicity. The initial disturbance amplitudes are also rather small and as such, subject to a greater degree of measurement uncertainty. Using artificial roughness of small height to control the initial disturbance and produce a more uniform series of crossflow vortices is a well-known experimental technique that has been used in both wind tunnel and flight experiments (see Hunt & Saric (2011) and Carpenter *et al.* (2010) for recent examples of each). However, before applying this approach to the present experiments, the effects of increasing freestream turbulence intensity on the crossflow instability are

tested using the clean leading-edge configuration and an abbreviated set of measurement locations. Two levels of enhanced turbulence are used: $Tu = 0.05\%$ and 0.19%. These are the intermediate and high levels of the five considered in Chapter IV.

1. Intermediate Turbulence Intensity: $Tu = 0.05\%$

For $Tu = 0.05\%$, the full set of boundary-layer profiles, steady disturbance profiles and velocity contours are given in Appendix A. As with the data from the baseline turbulence case, the initial stationary disturbance is quite low and the mean flow distortion is not readily apparent in the initial measurement locations. This distortion is only evident at $x/c = 0.40$ and 0.50. As the corresponding contour plots show, the dominant wavelength is again approximately 12 mm, with some variability between waves. Considering the spatial PSDs of Fig. 5.13, it is only these two measurement planes that produce spectra of significance. At $x/c = 0.40$, what appears to be two spectral peaks straddling $\lambda = 12$ mm are the result of some non-uniform vortex spacing in the flow. However, the spectrum of the disturbances at $x/c = 0.50$ shows a single peak at 12 mm.

The stationary disturbance mode shapes for this set of conditions are plotted in Fig. 5.14. As before, the initial disturbance is rather small and reaches a maximum value on the order of 1%. Although the maximum disturbance amplitude at $x/c = 0.40$ is slightly larger than in the baseline turbulence case, the next profile at $x/c = 0.50$ is clearly attenuated by the enhanced turbulence intensity. The growth of these disturbances is also plotted in Fig. 5.11. Though the data are somewhat sparse, the behavior is qualitatively similar to that of the baseline turbulence case: a period of relatively constant disturbance amplitude followed by sharp growth in which saturation is not observed. However, the rate of growth toward the end of the measurement domain is lower in the higher-turbulence environment.

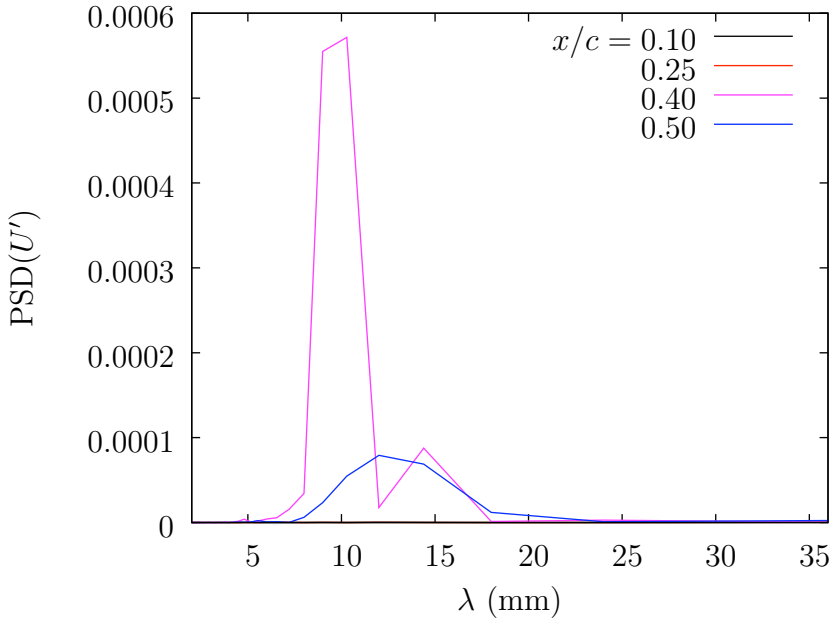

Figure 5.13: Spanwise power spectra at $Re_c = 2.8 \times 10^6$, $Tu = 0.05\%$, clean leading edge.

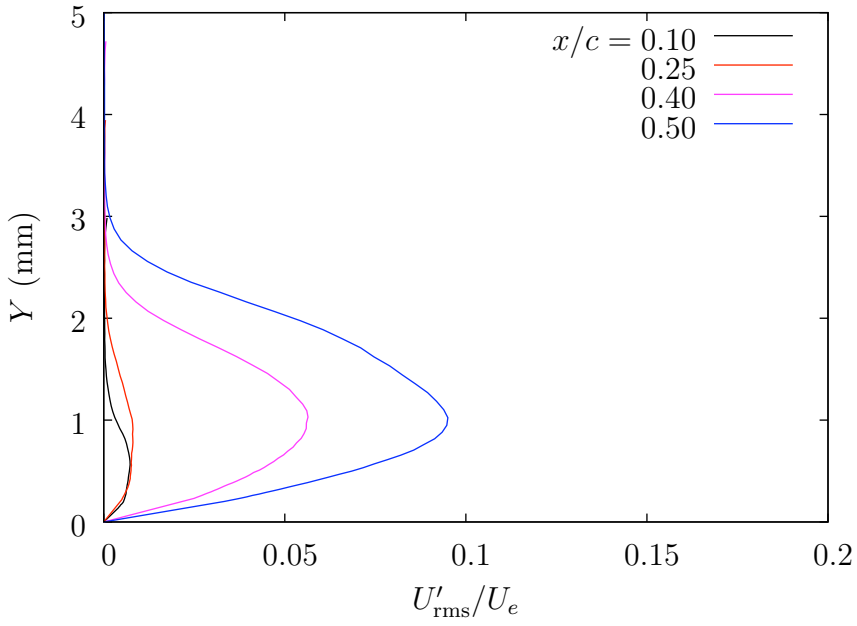

Figure 5.14: Spanwise rms steady disturbance profiles at $Re_c = 2.8 \times 10^6$, $Tu = 0.05\%$, clean leading edge.

Traveling mode disturbance profiles for $Tu = 0.05\%$ are plotted in Fig. 5.15. The initial traveling mode shape is flat on this scale, but grows rapidly aft of $x/c = 0.25$, eventually reaching a maximum value of 4%. Considering the streamwise evolution of these values as plotted in Fig. 5.12, little change from the baseline turbulence case is observed until $x/c = 0.40$. At this point and beyond, the unsteady disturbances grow at a higher rate. Additionally, the amplitude of the traveling mode alone reaches twice that of the total unsteady disturbance amplitude in the low-turbulence environment. This is a preliminary indication that growth of the traveling crossflow mode is highly dependent on freestream turbulence.

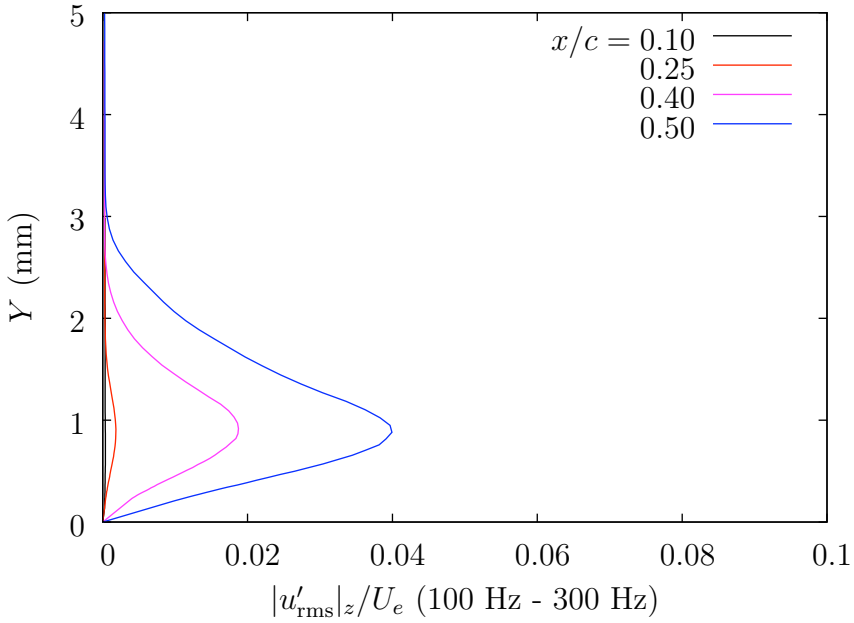

Figure 5.15: Spanwise mean of the unsteady disturbance profiles for the traveling wave passband 100–300 Hz at $Re_c = 2.8 \times 10^6$, $Tu = 0.05\%$, clean leading edge.

2. High Turbulence Intensity: $Tu = 0.19\%$

As with the intermediate turbulence intensity case, an abbreviated set of measurements characterize the higher turbulence intensity case at $Tu = 0.19\%$. The term "high" is used to describe this case relative to the others and it is recognized that this is still of modest intensity on an absolute scale. The full set of boundary-layer profiles, steady disturbance profiles and velocity contours are plotted in Appendix A. In this case, the steady disturbance level appears to be somewhat diffuse compared with the lower-turbulence cases. The mean flow distortion is again not apparent until $x/c = 0.40$ and is marked by the same variability in spanwise periodicity as the other configurations. This is also evident in the PSDs of Fig. 5.16. Here, only the last two points produce spectra indicating significant periodicity. The lower level of mean flow distortion makes it more difficult to identify the dominant spatial mode.

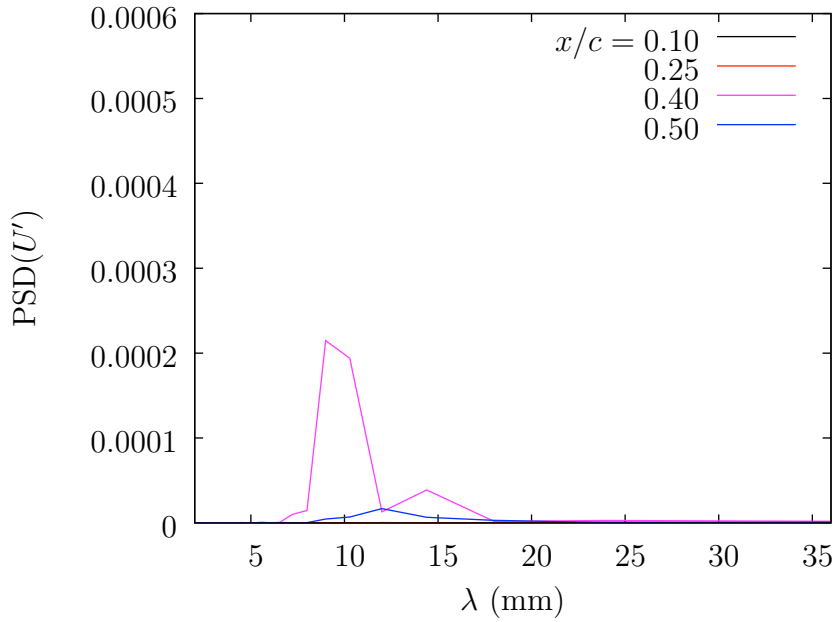

Figure 5.16: Spanwise power spectra at $Re_c = 2.8 \times 10^6$, $Tu = 0.19\%$, clean leading edge.

The stationary mode shapes of Fig. 5.17 show that increasing the turbulence intensity both reduces the maximum stationary disturbance amplitude and produces mode shapes that are more broad in the Y direction. This may be interpreted as a mixing effect of the turbulence; the higher level of velocity fluctuations in the boundary layer does not allow the same level of spatial non-uniformity in the mean flow. This in effect attenuates the growth of the stationary disturbance.

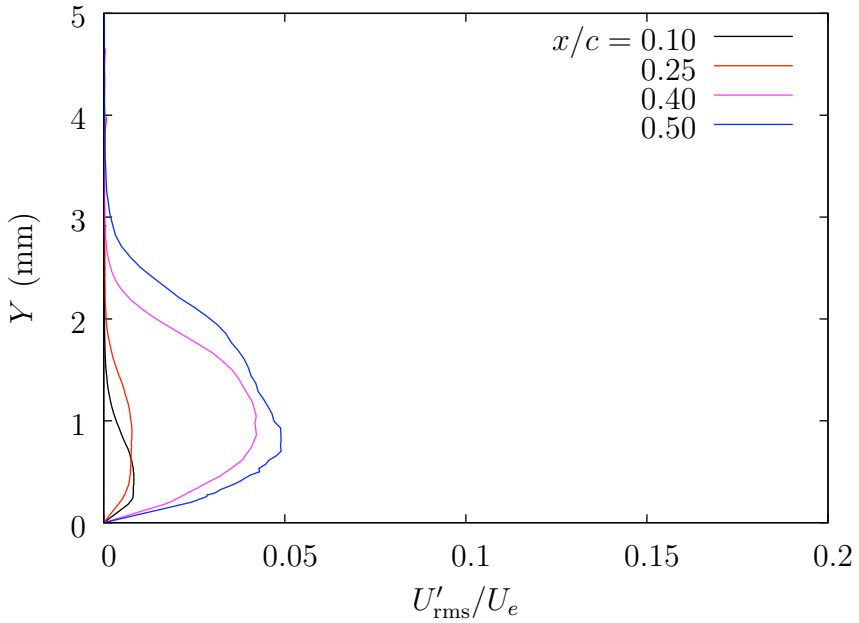

Figure 5.17: Spanwise rms steady disturbance profiles at $Re_c = 2.8\times10^6$, $Tu = 0.19\%$, clean leading edge.

In contrast, the traveling disturbance mode shapes of Fig. 5.18 grow to larger amplitudes. Although the initial mode shape at $x/c = 0.10$ is of very low amplitude, the traveling mode grows rapidly until reaching its maximum amplitude of 5% at $x/c = 0.50$. Comparing the streamwise evolution of these disturbances with those of the lower-turbulence configurations in Fig. 5.11, what appears to be stationary amplitude saturation is observed for the highest turbulence level case. The small number of

data points for the clean leading edge tests precludes a definitive statement regarding amplitude saturation, but the disturbance growth rate has dropped significantly at $x/c = 0.50$ and the value of A here is significantly reduced from the baseline case.

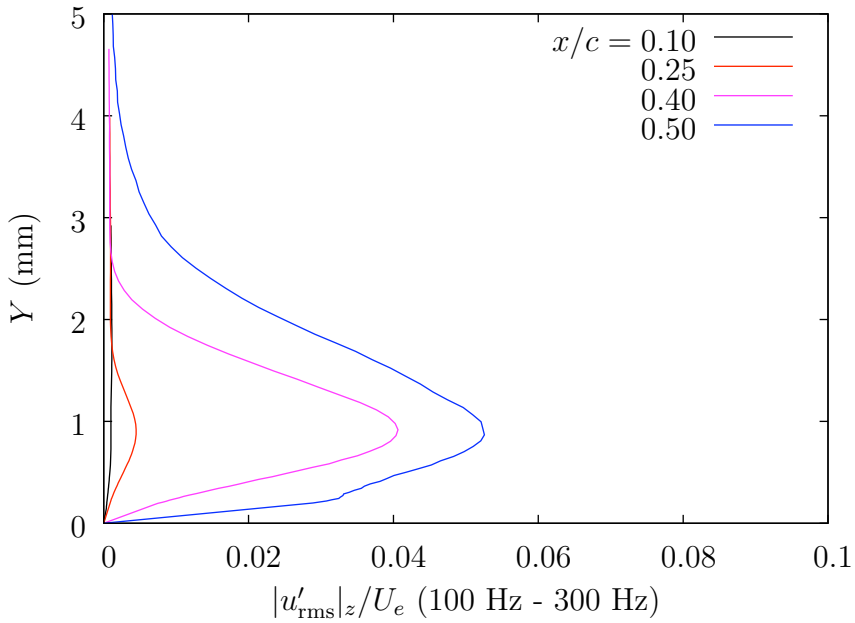

Figure 5.18: Spanwise mean of the unsteady disturbance profiles for the traveling wave passband 100–300 Hz at $Re_c = 2.8 \times 10^6$, $Tu = 0.19\%$, clean leading edge.

As with the intermediate turbulence level case, increasing the intensity of the freestream turbulence has a strong effect on both the value of a_{rms} and the traveling mode disturbance amplitude as evident in Fig. 5.12. Here, the total fluctuation amplitude is rising sharply at the end of measurement domain with an increasing growth rate. The amplitude of the traveling mode at $x/c = 0.50$ is again higher than the total unsteady disturbance amplitude of the lower-turbulence cases. The following section presents a more quantitative comparison of these disturbance amplitudes.

D. Comparison of Disturbance Amplitudes

To better ascertain the effect of freestream turbulence on both the stationary and traveling crossflow modes, the initial disturbance amplitudes are considered first. In this context, initial refers to the first experimentally measured disturbances at $x/c = 0.10$. The true initial disturbances are too small to measure with current technology, but they grow linearly in the initial regime such that the disturbances at $x/c = 0.10$ are proportional. In the absence of artificial roughness, the initial disturbances are nearly too small to measure. These values are given in Table 5.2, and are nearly the same for each value of the turbulence intensity. Although it is difficult to draw a strong conclusion from these data, it is observed that increasing Tu does not markedly increase the initial stationary disturbance amplitude. The results of Hunt & Saric (2011) show that the initial disturbance amplitude increases linearly with roughness height. Thus, quantifying the effect of turbulence intensity on initial disturbance amplitude is deferred to Chapter VI, where the artificial roughness produces suitably high initial disturbance amplitudes.

Tu	A_0
0.02%	0.002
0.05%	0.004
0.19%	0.004

Table 5.2: Initial stationary disturbance amplitudes measured using a clean leading edge. The test condition is $Re_c = 2.8 \times 10^6$ and values are measured at $x/c = 0.10$.

The effect of turbulence intensity on disturbance growth has already been observed in the stationary and unsteady amplitude evolution curves. The modes shapes measured at $x/c = 0.50$ are plotted together for the three turbulence configurations

in Fig. 5.19. As this plot shows, the maximum amplitude is reduced significantly. By increasing the turbulence intensity to 0.19%, the maximum value of the stationary mode shape is reduced to 45% of the corresponding value in the baseline turbulence case. A similar comparison is made for the traveling mode amplitude curves in Fig. 5.20. The effect of increasing Tu is to raise the maximum of the traveling mode amplitude by a factor of 4.5 over the baseline case. However, it is noted that merely increasing the turbulence intensity from 0.02% to 0.05% raises the maximum traveling mode amplitude by a factor of 3.4.

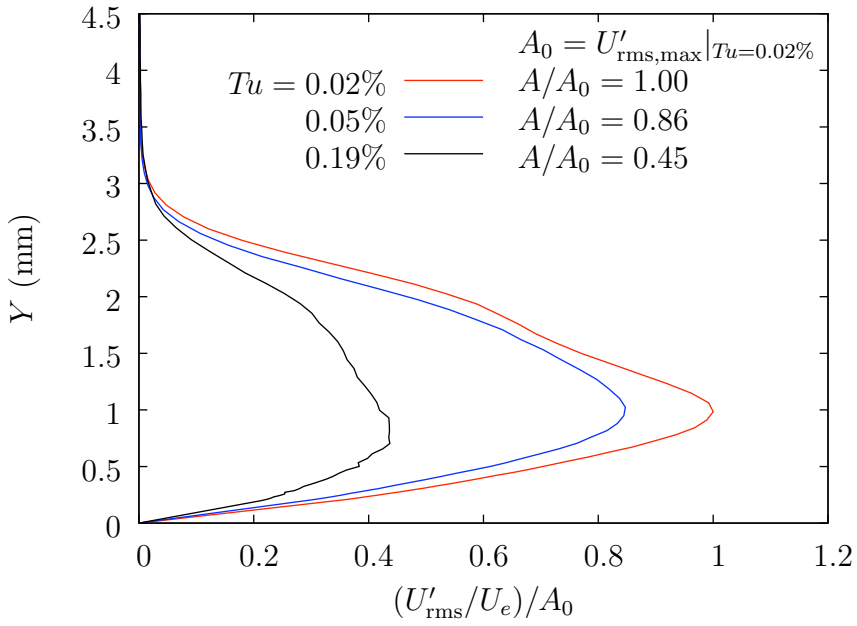

Figure 5.19: Stationary disturbance amplitude comparison at $x/c = 0.50$, $Re_c = 2.8 \times 10^6$, clean leading edge.

In addition to comparing the maxima of the mode amplitude curves, the integrated values (A and a) are another suitable measure of disturbance growth as discussed previously. These values are given in Table 5.3 for the stationary and traveling modes at $x/c = 0.50$. At this location, the cumulative effects of freestream

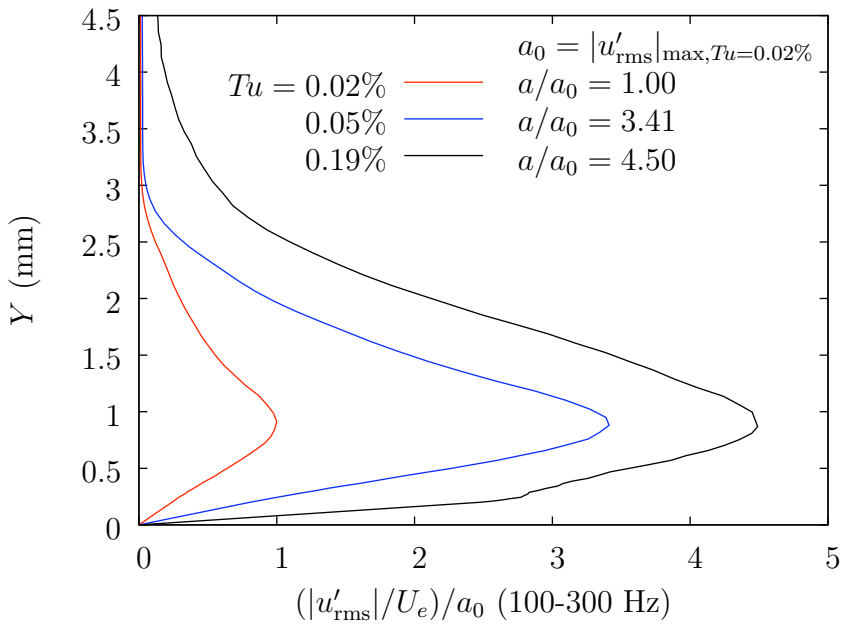

Figure 5.20: Traveling disturbance amplitude comparison at $x/c = 0.50$, $Re_c = 2.8 \times 10^6$, clean leading edge.

turbulence on disturbance growth can be compared. The tabulated values show that the stationary mode amplitude is reduced by half at the higher turbulence level, and that the traveling mode amplitude is raised by a factor of five. Perhaps the most striking result in this table is the sharp rise in the traveling mode amplitude from the baseline level.

Tu	$A(0.50)$	$a(0.50)$
0.02%	0.054	0.005
0.05%	0.047	0.015
0.19%	0.024	0.026

Table 5.3: Stationary and traveling disturbance amplitudes measured at $x/c = 0.50$, $Re_c = 2.8 \times 10^6$ using a clean leading edge.

The preliminary result from these tests is that while freestream turbulence does not appear to have a large effect on the initial disturbance generation for stationary disturbances, it does affect disturbance growth significantly. Moreover, the traveling mode growth is strongly affected by freestream turbulence. The criterion for a low-disturbance wind tunnel is generally given as $Tu \leq 0.05\%$ (Reshotko *et al.*, 1997). However, the result of these experiments suggests that the study of crossflow instability may be affected by minute differences in Tu that otherwise meet this criterion. These results are tested in Chapter VI using artificial roughness arrays to set the initial disturbances.

CHAPTER VI

EFFECTS OF FREESTREAM TURBULENCE AND SURFACE ROUGHNESS ON CROSSFLOW INSTABILITY

Freestream turbulence and surface roughness are two environmental disturbances that start the path to transition. Previous research (Deyhle & Bippes, 1996) has shown that surface roughness is the dominant provider of initial disturbances for stationary crossflow modes while freestream turbulence provides the initial disturbances leading to traveling mode growth. It has been observed that the subsequent disturbance evolution is dependent on both the initial conditions and the freestream turbulence. To further understand this process, the effect of freestream turbulence on stationary mode growth excited by surface roughness is examined. Two roughness configurations are tested: a spanwise array of cylindrical elements spaced at the most-unstable wavelength ($\lambda_k = 12$ mm) and roughness spaced at half of that wavelength (the so-called subcritical roughness). In both cases, the elements are 3 mm in diameter. Recent measurements (Hunt & Saric, 2011) have shown some batch-to-batch variability in roughness height. As such, the critical roughness is approximately 12 μm tall and the subcritical roughness is 14 μm tall. The standard notation (Saric *et al.*, 1998) for spanwise roughness arrays is $[k|\lambda|d]$, where k is the height in μm, λ is the spanwise spacing in mm and d is the diameter in mm. The two roughness configurations are then [14|6|3] (subcritical) and [12|12|3] (critical). As with the experiments completed using a nominally smooth leading edge, all tests are run at $Re_c = 2.8 \times 10^6$.

A. Subcritically-Spaced Roughness

The subcritical roughness spacing is chosen to be 6 mm (among the other possibilities) for consistency with previous work. The LST calculations show that a stationary disturbance with this spacing undergoes a brief period of growth followed by decay aft of $x/c = 0.30$.

1. Transition Location

In the absence of artificial roughness, the average transition location at these test conditions with the baseline turbulence level is $x/c_{tr} = 0.67$. Increasing the turbulence intensity to 0.19% moves the average transition location forward to $x/c_{tr} = 0.57$ (from Table 5.1). Flow visualization results from the corresponding experiments utilizing subcritical roughness are shown in Fig. 6.1 for the five turbulence levels tested. Considering the lowest turbulence level first, it is observed that the transition front extends over a larger streamwise range and that the average transition location is moved slightly forward from that of the nominally smooth leading edge. The transition pattern follows a saw-tooth shape that is indicative of the stationary crossflow mode.

As the turbulence intensity is increased, little change in the pattern of transition is observed. As with the previous results, the demarcation between laminar and turbulent as indicated by the edge of the naphthalene coating becomes slightly diffuse and the saw-tooth pattern is less distinct at higher turbulence levels. These trends indicate that the traveling mode becomes the dominant instability at the higher turbulence level. The average transition locations are listed in Table 6.1 for the five test points. These results show that the average transition location is largely unaffected by increasing the turbulence intensity. A series of tests were completed

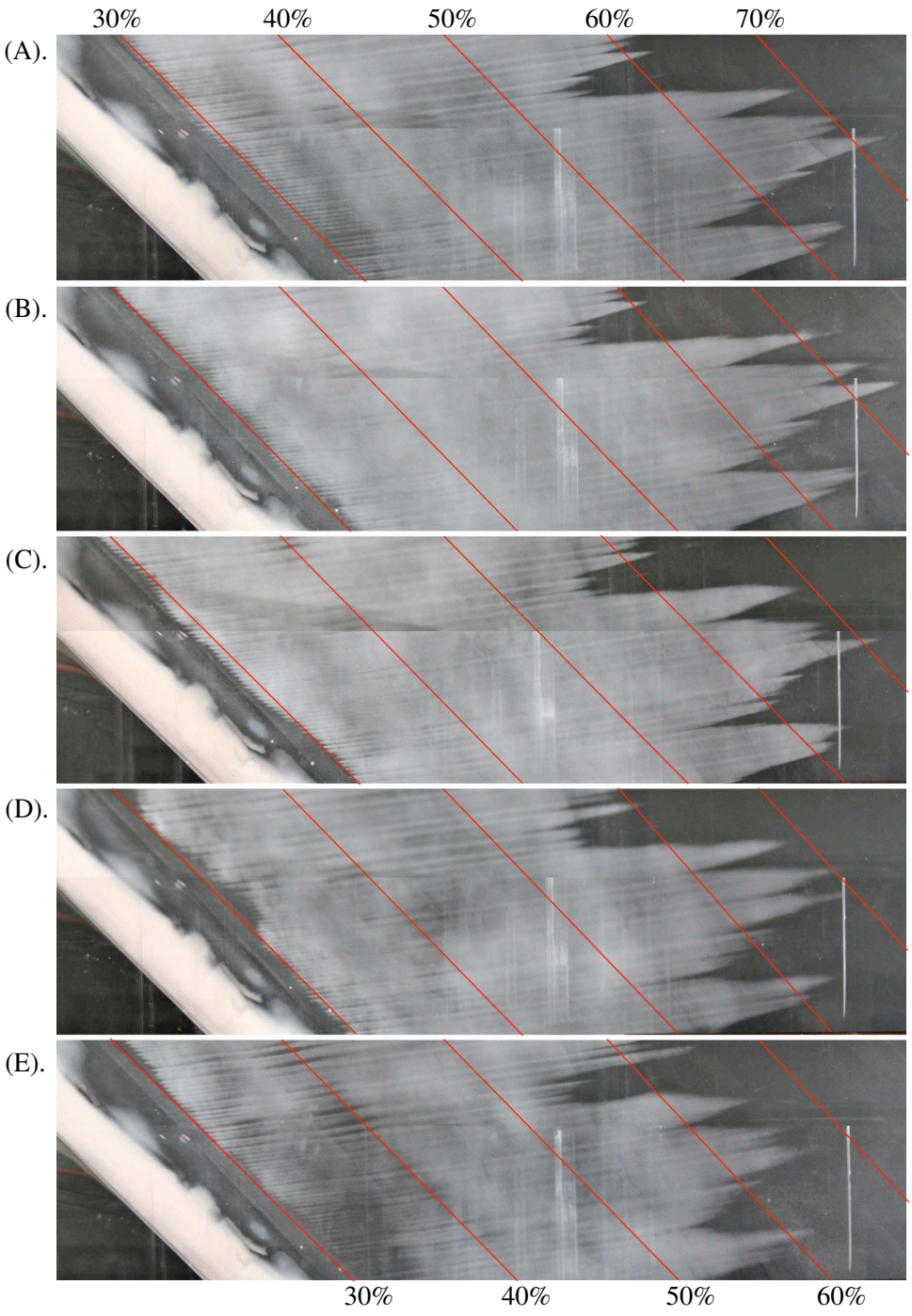

Figure 6.1: Flow visualization results at $Re_c = 2.8 \times 10^6$, [14|6|3] roughness. (A). $Tu =$ 0.02%, (B). 0.03%, (C). 0.05%, (D). 0.10%, (E). 0.19%.

with increased roughness heights (accomplished by stacking layers of the appliqué roughness elements) of $k = 28$, 42 and 54 μm. As with the single-layer results, little change in the transition location is noted with increasing turbulence intensity. As the roughness height is increased, the most upstream turbulent wedges in the transition pattern gradually move forward to $x/c = 0.50$; this is attributed to imperfections in the roughness array.

Tu	x/c_{tr}
0.02%	0.63
0.03%	0.64
0.05%	0.63
0.10%	0.62
0.19%	0.61

Table 6.1: Transition locations measured at $Re_c = 2.8 \times 10^6$ using subcritical [14|6|3] roughness. Tabulated values represent average transition location across the span.

Another important piece of information that may be gleaned from the flow visualization is the appearance of 6-mm-spaced streaks. These streaks are particularly evident in the baseline turbulence case, immediately aft of $x/c = 0.30$. As discussed in Chapter III, the naphthalene coating is not applied on the leading edge of the model. The 6 mm streaks are only visible for a short streamwise extent before they are replaced by more widely-spaced streaks whose spacing is not as regular. This seems to indicate that although the roughness array is effectively exciting a stationary crossflow mode with the forced wavelength, the growth of a disturbance of greater wavelength eventually outpaces it. Detailed boundary-layer velocity measurements are used to quantitatively assess this phenomenon.

2. Baseline Turbulence Level: $Tu = 0.02\%$

The boundary-layer measurements are made following the same procedure as in the previous tests. However, the presence of a forced roughness wavelength allows a change to be made regarding the manner in which the spatial power spectra are normalized. The modal components of the PSD are those at λ_k/m, where $m = 1, 2, 3, \ldots$. For configurations with artificial roughness, λ_k is the spanwise wavelength of the array. The modal amplitudes of the steady disturbances are computed in a fashion similar to the total stationary disturbance amplitude.

$$A_{\lambda,m} = \frac{1}{\delta_{99.9}} \int_0^{\delta_{99.9}} \mathrm{PSD}_{\lambda,m} \mathrm{d}Y \tag{6.1}$$

The modal amplitudes are then normalized such that they sum to the stationary disturbance amplitude.

$$A = \sum_m A_{\lambda,m} \tag{6.2}$$

For the baseline turbulence level, measurements are made at a limited number of streamwise stations. The complete test matrix is given in Appendix B, along with the corresponding collection of boundary-layer velocity plots. The purpose of these measurements is to confirm that the roughness is exciting the desired crossflow wavelength and to measure the initial and final disturbance amplitudes. The boundary-layer measurements confirm the spatial periodicity of disturbances observed in the flow visualization experiments. Spectra for $U'(z)$ at the boundary-layer height corresponding to the maximum disturbance level are plotted in Fig. 6.2. The minimal disturbance level at $x/c = 0.10$ does not produce a large spectral peak, but the measurements at $x/c = 0.25$ show a strong spanwise modulation at the roughness wavelength. Contours of the steady velocity in Appendix B show a regular pattern in the mean flow distortion. By $x/c = 0.40$, the λ_k disturbance has decayed to a negligible level and is replaced by a disturbance of longer wavelength. Though the

velocity contours show a disturbance field that is less periodic, the spatial spectrum has a broad peak centered at approximately 12 mm. Thus, it appears that once the subcritical disturbance decays, the most unstable wavelength re-appears. It is this disturbance that leads to transition.

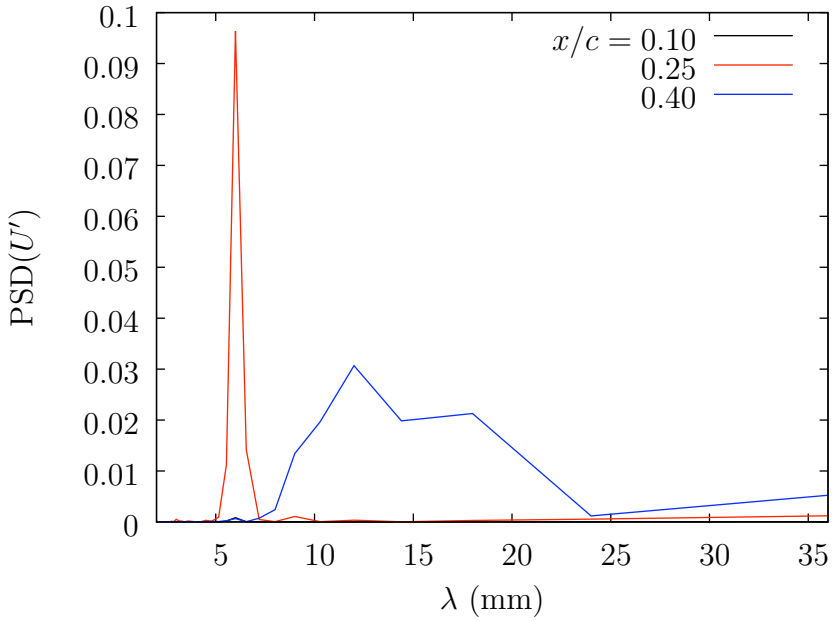

Figure 6.2: Spanwise power spectra at $Re_c = 2.8 \times 10^6$, $Tu = 0.02\%$, [14|6|3] roughness.

The stationary mode shapes for these disturbances are plotted in Fig. 6.3. Compared with the stationary mode shapes for natural crossflow disturbances (Fig. 5.7), it is clear that the initial disturbances created by the artificial roughness are larger than those that arise from the base level of surface roughness. Consequently, the onset of nonlinear disturbance growth (indicated here by the appearance of a secondary lobe in the mode shape profile) is advanced in this case. However, it is the traveling mode amplitude that is of primary interest presently. The traveling mode profiles (100–300 Hz passband) are plotted in Fig. 6.4. For the three measured locations,

the traveling mode is weak: the maximum amplitude is less than 1% of U_e. This is approximately half of the traveling mode amplitude that is measured using a clean leading edge at this streamwise location. Due to the limited number of measurement points, however, broad conclusions can not be drawn from these data.

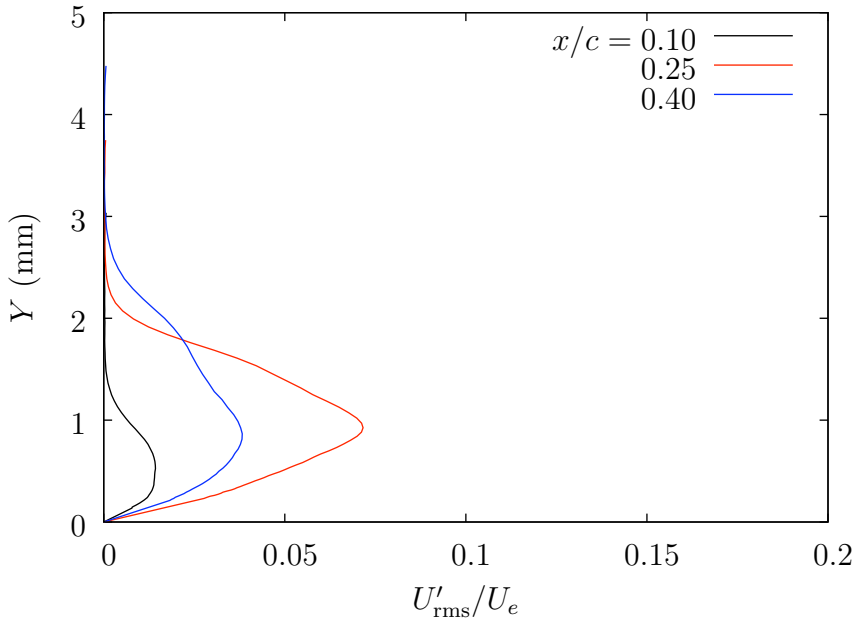

Figure 6.3: Spanwise rms steady disturbance profiles at $Re_c = 2.8 \times 10^6$, $Tu = 0.02\%$, [14|6|3] roughness.

The stationary disturbance amplitudes of Fig. 6.5 show that for $Tu = 0.02\%$, a local maximum occurs somewhere in the mid-range. Based on the flow visualization results as well as the spatial hot-wire spectra, this is the point at which the 6 mm disturbance begins to decay. The LST calculations for this condition show that the 6 mm wave reaches its maximum amplitude at approximately 30% chord. At the baseline turbulence level, the unsteady amplitudes show little growth. The extent to which the traveling mode grows is small on the absolute scale of Fig. 6.6.

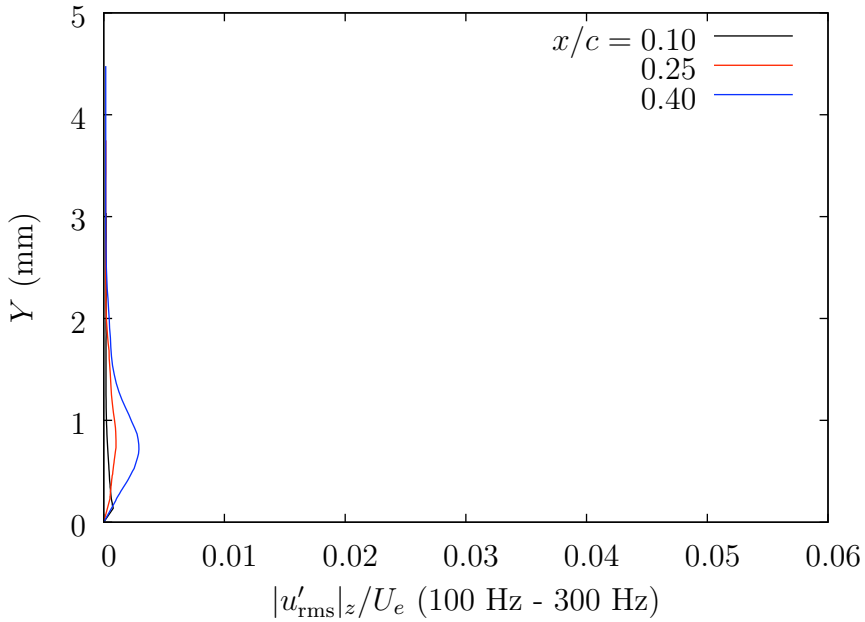

Figure 6.4: Spanwise mean of the unsteady disturbance profiles for the traveling wave passband 100–300 Hz at $Re_c = 2.8 \times 10^6$, $Tu = 0.02\%$, [14|6|3] roughness.

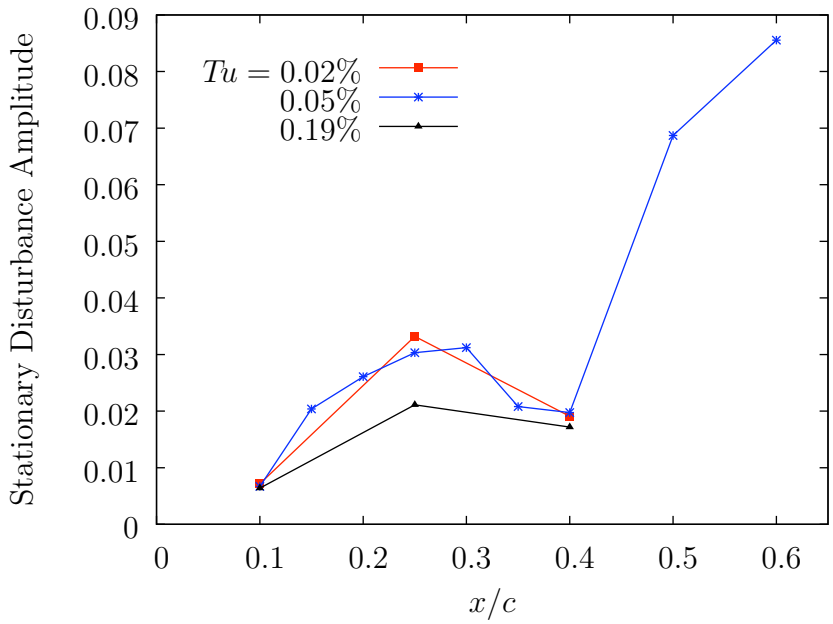

Figure 6.5: Stationary disturbance amplitude evolution at $Re_c = 2.8 \times 10^6$, [14|6|3] roughness.

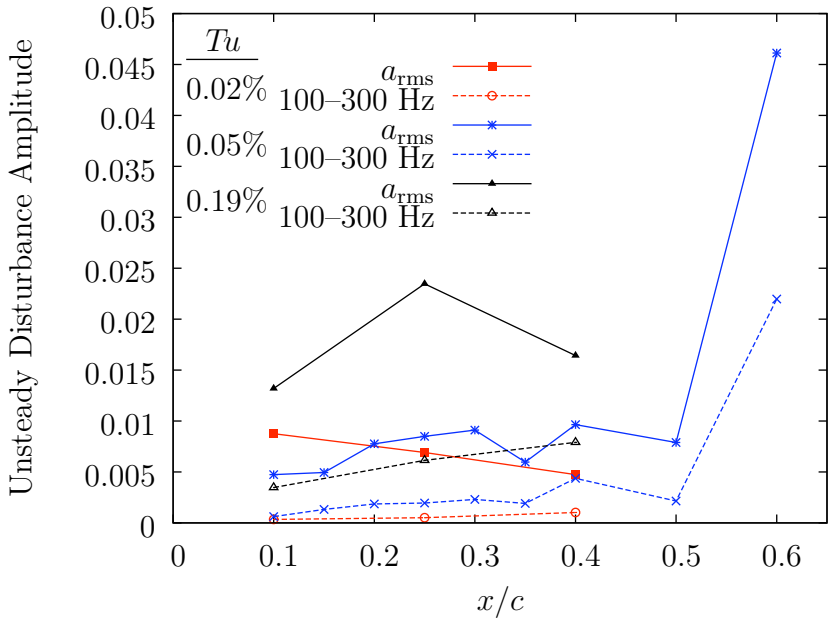

Figure 6.6: Traveling disturbance amplitude evolution at $Re_c = 2.8 \times 10^6$, [14|6|3] roughness.

3. Intermediate Turbulence Level: $Tu = 0.05\%$

One goal of these experiments is to examine the effect of subcritical roughness on the crossflow instability in a modestly-enhanced freestream turbulence environment. The purpose of this test, in particular, is to determine the degree to which the results from similar experiments in the ASU UWT might differ from results produced in the KSWT. The transition location measurements showed almost no difference when the turbulence intensity was raised to 0.03%. The majority of the test points in the subcritical roughness experiments are completed using $Tu = 0.05\%$ rather than the lower-intensity 0.03% turbulence configuration.

The velocity contours plots in Appendix B show a regularly-spaced distortion of the mean flow corresponding to $\lambda_k = 6$ that appears by $x/c = 0.20$. This disturbance persists until around $x/c = 0.35$, and further downstream measurements show that a

more irregularly-spaced disturbance with a greater wavelength grows before transition occurs. The spatial spectra of Fig. 6.7 confirm the growth and decay of the 6 mm disturbance. However, the spanwise extent of the sampling region (65 mm) is not long enough to properly resolve the wavelength of the disturbance that appears between $x/c = 0.40$ and the end of the measurement domain. For N spatial locations, the wavelengths resolved in Fourier space are given by:

$$\lambda_n = \frac{N\Delta z}{n} \qquad n = 1, 2, \ldots, N/2 \tag{6.3}$$

From this expression, the wavelength resolution diminishes as λ_n increases. This may be addressed by sampling more points in z. However, transition for this roughness configuration appears to be affected to some degree by long-wavelength or aperiodic disturbance growth. Time constraints precluded making the additional measurements required to spectrally resolve these disturbances.

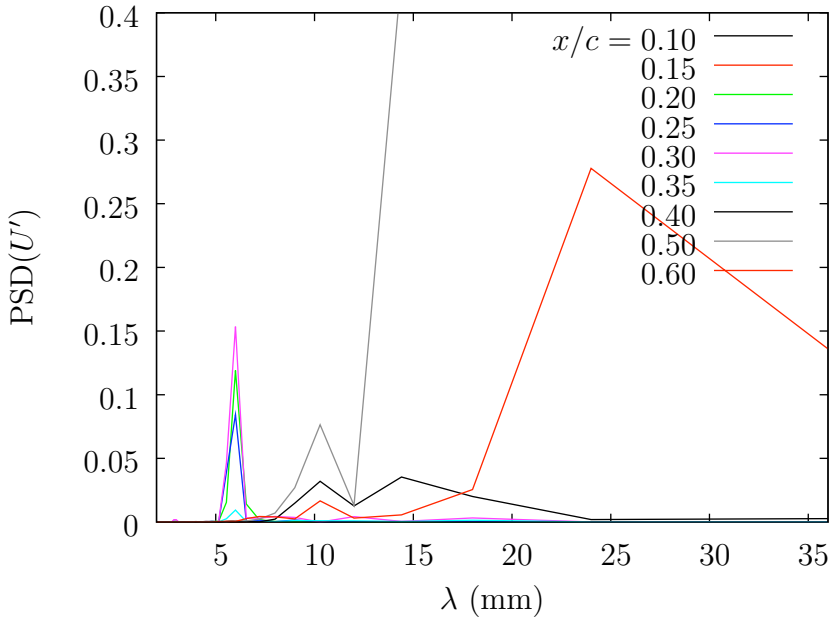

Figure 6.7: Spanwise power spectra at $Re_c = 2.8 \times 10^6$, $Tu = 0.05\%$, [14|6|3] roughness.

The stationary mode shapes in Fig. 6.8 show linear disturbance growth until the 6 mm wave begins to decay near $x/c = 0.30$. The irregularity in the U'_{rms} profile at $x/c = 0.15$ is due to some local anomalous behavior near $z = 20$ mm at this streamwise location. As the disturbance characterized by the 6 mm wave decays, the amplitude of the corresponding mode shapes also decay, before increasing sharply at $x/c = 0.50$. Here, both the amplitude and wall-normal extent of the disturbance is increased greatly over the previous points. While some of the latter is expected due to the larger boundary-layer thickness at this point, the velocity contours at these locations indicate that the stationary disturbances have grown rapidly in the spanwise direction as well. From these data, it appears that although a 6 mm disturbance is excited by the roughness array, its subsequent decay allows a more unstable, longer-wavelength disturbance to grow in its absence. The high intensity of the unsteady fluctuations associated with this disturbance are the harbinger of transition.

In addition to a large stationary disturbance, the amplitude of the velocity fluctuations in the traveling mode passband also increases sharply in advance of transition. These profiles are plotted in Fig. 6.9. The amplitude of the traveling mode appears to grow to a maximum of 0.5% before increasing sharply to nearly 5% at the end of the measurement domain. The streamwise evolution of this quantity is shown explicitly in Fig. 6.6.

The increased disturbance environment of this subset of tests did not appear to have an effect on the stationary disturbance growth, though data from the baseline turbulence level are somewhat sparse. Amplitude saturation was not observed. Although the level of the unsteady fluctuations as well as the traveling mode amplitude are increased in the higher freestream turbulence, the location of transition is effectively unchanged.

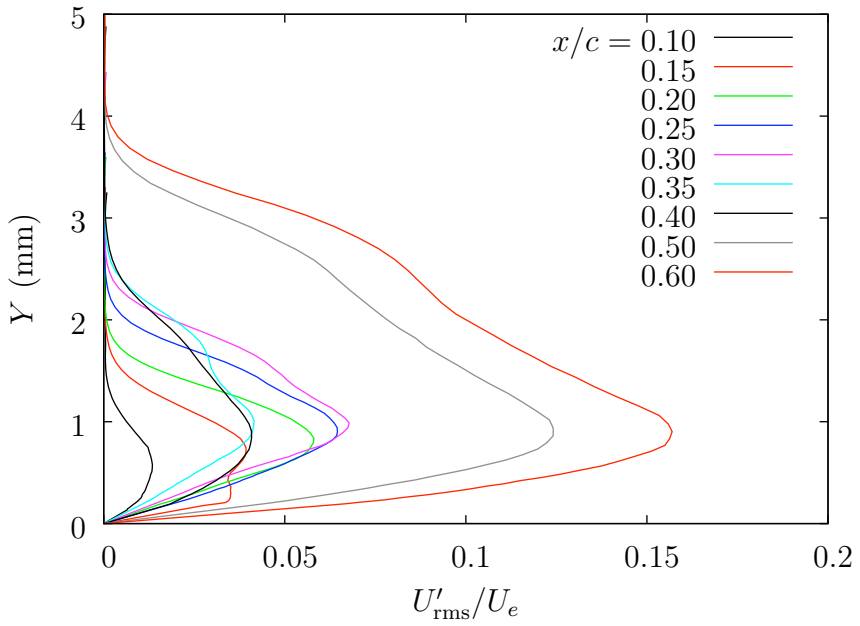

Figure 6.8: Spanwise rms steady disturbance profiles at $Re_c = 2.8 \times 10^6$, $Tu = 0.05\%$, [14|6|3] roughness.

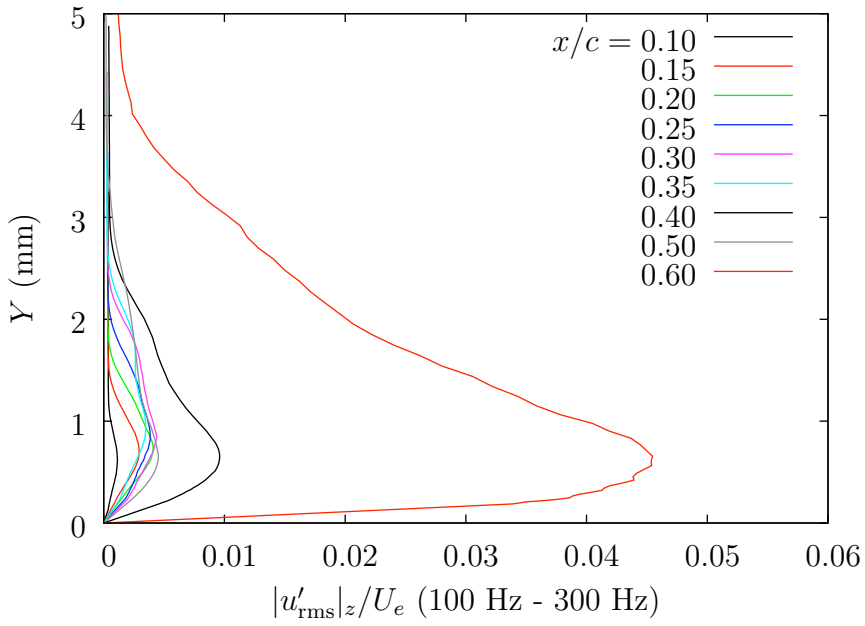

Figure 6.9: Spanwise mean of the unsteady disturbance profiles for the traveling wave passband 100–300 Hz at $Re_c = 2.8 \times 10^6$, $Tu = 0.05\%$, [14|6|3] roughness.

4. High Turbulence Level: $Tu = 0.19\%$

As with the baseline turbulence level, a few points are measured using the high-turbulence configuration to give some insight into the effectiveness of subcritical roughness at varying turbulence levels. The number of points is limited to allow for a full series of measurements using critical roughness. The spectral content of the steady disturbance velocities (plotted in Fig. 6.10) is like that of the previous measurements: a 6 mm disturbance is evident in the upstream measurement locations but is replaced by longer-wavelength disturbances after it decays. The results of the flow visualization experiment at this turbulence level confirm this result.

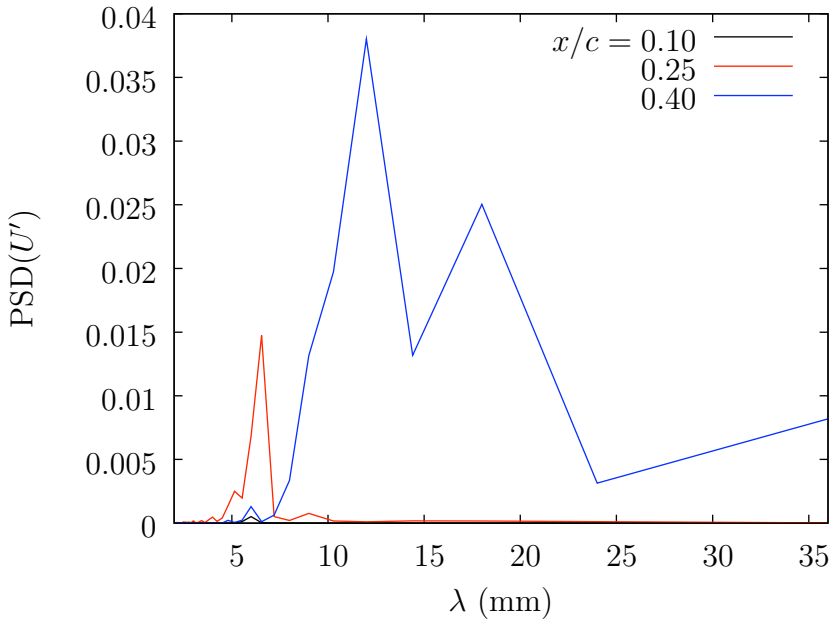

Figure 6.10: Spanwise power spectra at $Re_c = 2.8 \times 10^6$, $Tu = 0.19\%$, [14|6|3] roughness.

As the stationary mode shapes demonstrate in Fig. 6.11, the disturbance amplitudes are reduced by the higher level of freestream turbulence. The effect on the unsteady fluctuations is more pronounced, however. The unsteady velocity fluctua-

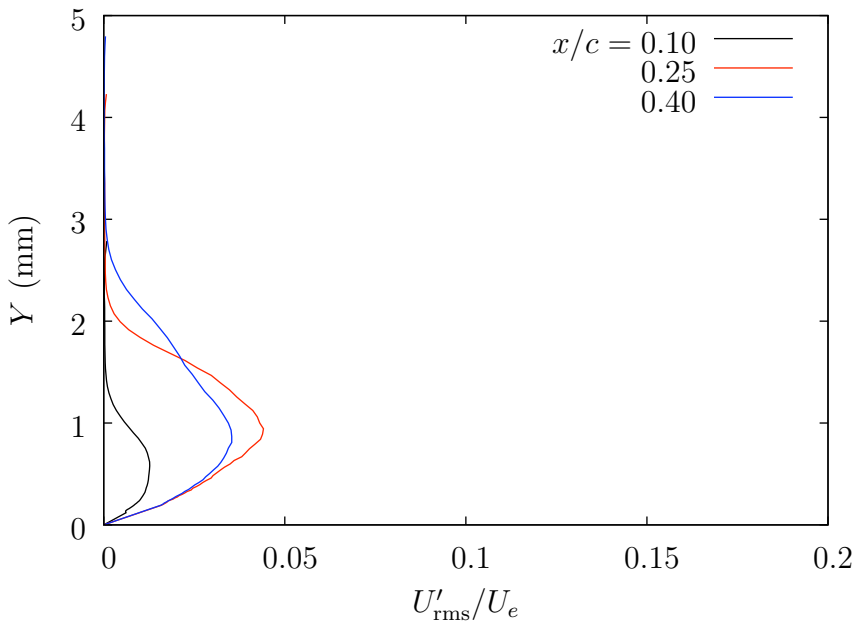

Figure 6.11: Spanwise rms steady disturbance profiles at $Re_c = 2.8\times10^6$, $Tu = 0.19\%$, [14|6|3] roughness.

tion contours show that not only is the intensity of these fluctuations increased, they are also modulated in the spanwise direction with the 6 mm wavelength. An example of this is shown in Fig. 6.12.

As with the measurements made without artificial roughness, the traveling mode amplitude is affected by increasing the turbulence level. The profiles of Fig. 6.13 show that the traveling mode amplitude grows substantially between each streamwise measurement location. When the unsteady amplitude evolution plot of Fig. 6.6 is considered, this trend is observed in the traveling mode points. The total level of unsteady fluctuation, however, has a local maximum near the maximum level of stationary disturbance amplitude. The balance is likely due to the increased fluctuations due to shear instability in the distorted mean flow.

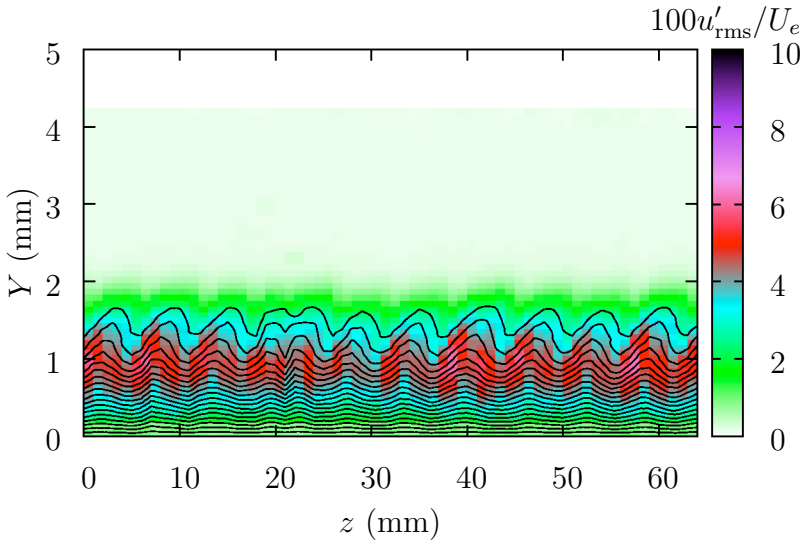

Figure 6.12: Spanwise modulation of U and u'_{rms} at $x/c = 0.25$. The test conditions are $Re_c = 2.8 \times 10^6$, $Tu = 0.19\%$, [14|6|3] roughness.

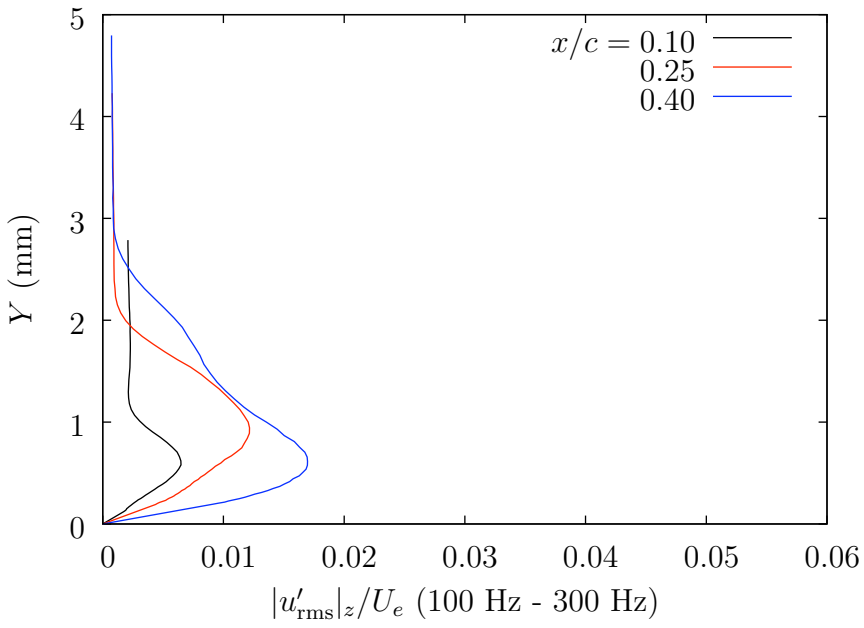

Figure 6.13: Spanwise mean of the unsteady disturbance profiles for the traveling wave passband 100–300 Hz at $Re_c = 2.8 \times 10^6$, $Tu = 0.19\%$, [14|6|3] roughness.

5. Combined Effect of Freestream Turbulence and Subcritically-Spaced Roughness

The initial amplitude of the stationary mode is primarily set by the height of the surface roughness. The surface roughness, however, is applied at $x/c = 0.029$ and the most upstream disturbance measurements are made at $x/c = 0.10$. As discussed previously, this concession still allows for an accurate comparison of initial disturbance amplitudes if all measurements are made at this point. It has been observed thus far that the freestream turbulence affects the growth of the stationary mode throughout its evolution. The measured initial disturbance amplitudes of Table 6.2 show that the extent to which increasing the turbulence level affects these values via growth rate attenuation in the region $0.029 < x/c < 0.10$ is minimal.

Tu	A_0
0.02%	0.007
0.05%	0.007
0.19%	0.006

Table 6.2: Initial stationary disturbance amplitudes measured at $Re_c = 2.8 \times 10^6$ using [14|6|3] roughness. Values are measured at $x/c = 0.10$.

Likewise, the amplified stationary mode shapes (measured at $x/c = 0.40$) are largely unaffected by the increased freestream turbulence level. Comparing the normalized maxima of the curves in the legend of Fig. 6.14, the modest increase to the steady disturbance amplitude at $Tu = 0.05\%$ is unexpected. Similarly, the results of Chapter V showed a marked reduction in the stationary disturbance amplitude at the high turbulence level (0.19%). In this case, the measurements are not made a few percent chord upstream of transition (as with the previous results), but in the region

where the 6 mm wave has decayed significantly and before the longer-wavelength disturbances are greatly amplified. Thus, increasing the turbulence level appears to have little effect on stationary disturbance amplitude measured in the wake of the decay of the 6 mm disturbance.

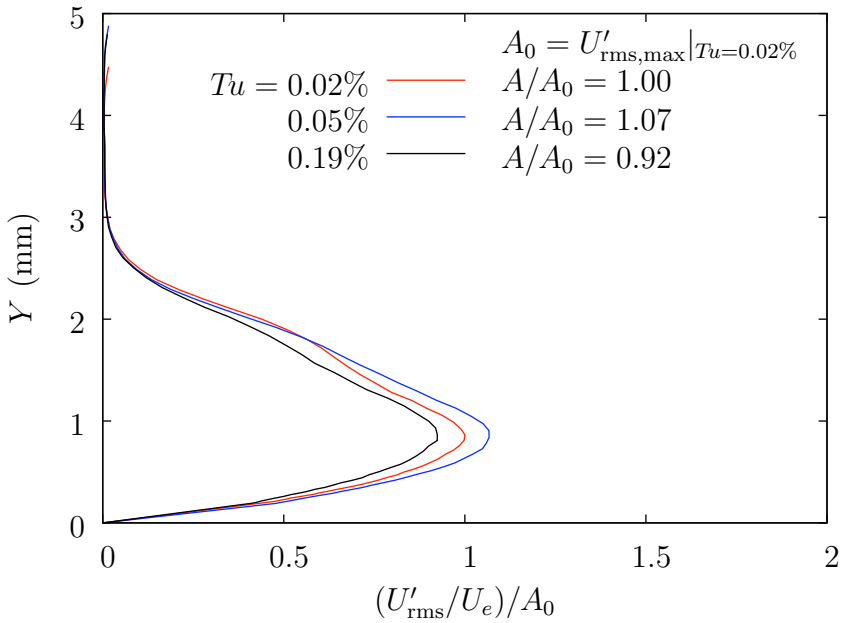

Figure 6.14: Stationary disturbance amplitude comparison at $x/c = 0.40$, $Re_c = 2.8 \times 10^6$, [14|6|3] roughness.

The traveling mode amplitudes measured at this location, however, are greatly enhanced by increasing the freestream turbulence level. As the normalized mode profiles of Fig. 6.15 show, the traveling mode is amplified significantly by modest increases to Tu. As with the traveling mode amplitudes measured using a smooth leading edge, increasing Tu to 0.05% shows that the traveling mode amplification is highly affected by freestream turbulence. The stationary and traveling mode amplitudes computed via integration of the mode profiles are given in Table 6.3. These values confirm the trends observed in their corresponding mode shapes.

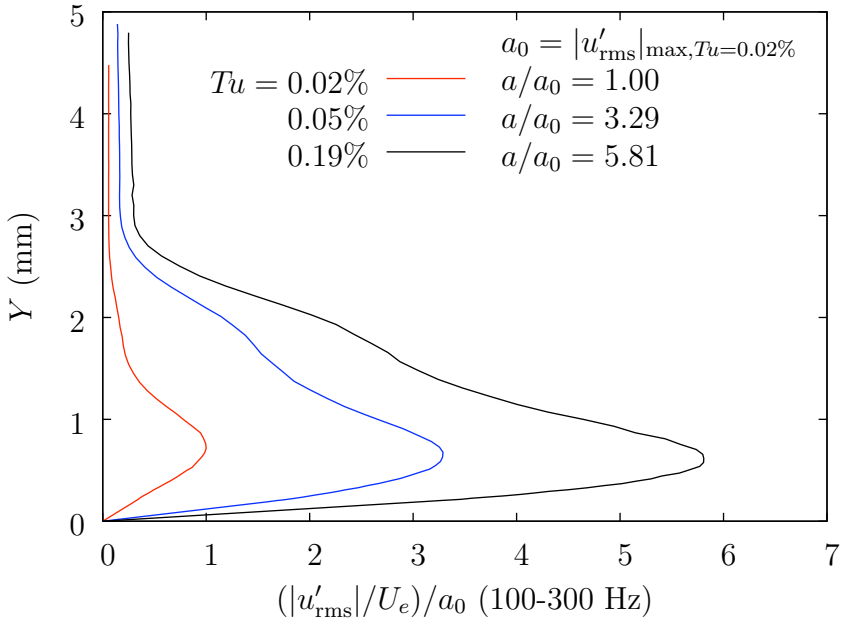

Figure 6.15: Traveling disturbance amplitude comparison at $x/c = 0.40$, $Re_c = 2.8 \times 10^6$, [14|6|3] roughness.

Tu	$A(0.40)$	$a(0.40)$
0.02%	0.019	0.001
0.05%	0.020	0.004
0.19%	0.017	0.008

Table 6.3: Stationary and traveling disturbance amplitudes measured at $x/c = 0.40$, $Re_c = 2.8 \times 10^6$ using [14|6|3] roughness.

B. Critically-Spaced Roughness

The critically-spaced roughness configuration consists of an array with λ_k = 12 mm applied at $x/c = 0.029$. This is the same configuration as in the experiments of Hunt & Saric (2011). For the present experiments, a thorough text matrix is completed to measure transition and disturbance evolution at the same three turbulence levels as in the previous roughness configurations. Additionally, a few points are tested using $Tu = 0.03\%$.

1. Transition Location

Flow visualization is used as before to measure the transition location. For the critically-spaced roughness configuration, measurements are only made at the low, medium and high intensity turbulence levels. The previous tests have shown that the transition locations at the interstitial levels follow the pattern established by these tests. Results of the flow visualization tests are collected in Fig. 6.16. A strong pattern of streamwise streaks is observed and subsequent image analysis shows that the spacing is the same as the roughness wavelength: 12 mm. These streaks persist until the transition front, indicating that the 12 mm disturbance leads to transition. Of course, given that this is the most unstable wavelength, this phenomenon is not unexpected. The average transition location at the low turbulence level is x/c_{tr} = 0.48. These images show that the transition location moves forward with each increase to the turbulence level. Tabulated values (Table 6.4) of the average transition location reflect this as well.

Although the expected saw-tooth transition pattern is more uniform at the baseline turbulence level than in the previous tests, this is due to the strong growth of the most unstable crossflow mode. The effect of the small variations in initial disturbance

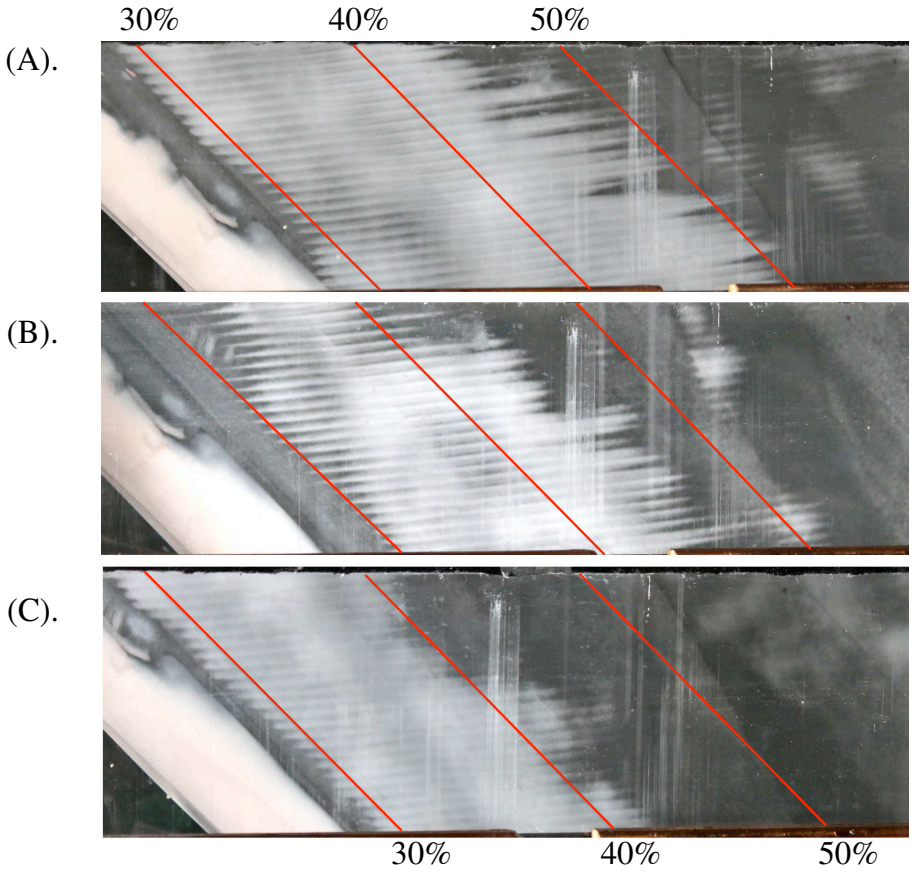

Figure 6.16: Flow visualization results at $Re_c = 2.8 \times 10^6$, [12|12|3] roughness. (A). $Tu = 0.02\%$, (B). 0.05%, (C). 0.19%.

amplitude that produce this pattern are overshadowed by the effect of the critically-spaced roughness. However, some regions of the transition front retain a semblance of the saw-tooth pattern. As the turbulence level is increased, the transition front becomes more uniform. At the highest turbulence level, the transition is nearly flat and aligned with the 40% chord marker. This indicates that the traveling crossflow mode is responsible for transition in this case.

Tu	x/c_{tr}
0.02%	0.48
0.05%	0.45
0.19%	0.41

Table 6.4: Transition locations measured at $Re_c = 2.8 \times 10^6$ using [12|12|3] roughness. Tabulated values represent average transition location across the span.

2. Baseline Turbulence Level: $Tu = 0.02\%$

As with the other roughness configurations, boundary-layer profiles, steady disturbance profiles and velocity contours are plotted in full in Appendix C. Examining these plots, and the velocity contours of Fig. C.22 in particular, a strong periodicity is observed. The stationary crossflow vortices excited by the array of roughness with $\lambda_k = 12$ mm distort the mean flow into the recognizable contours of Fig. C.22 with its characteristic "roll-over". The spatially-uniform initial disturbances provided by the roughness array are useful because streamlines curve around the swept-wing model. Without a uniform series of crossflow vortices, an observed change in A may be attributed to either streamwise evolution or spatially non-uniform initial conditions due to minor variations in surface roughness near the leading edge.

The spanwise modulation of the distorted mean flow with wavelength λ_k is evident in the velocity contours. The spatial spectra shown in Fig. 6.17 reveal harmonics at $\lambda_k/2$ and $\lambda_k/3$ whose amplitudes are significantly large aft of $x/c = 0.20$. The appearance of these harmonics is expected (Saric *et al.*, 1998). It is also noted that no subharmonic disturbances (those with wavelengths that are integer multiples λ_k) of are observed, in agreement with previous results. These spectra confirm that the forced wavelength characterizes the dominant spatial feature from the initial disturbance through a few percent chord upstream of transition.

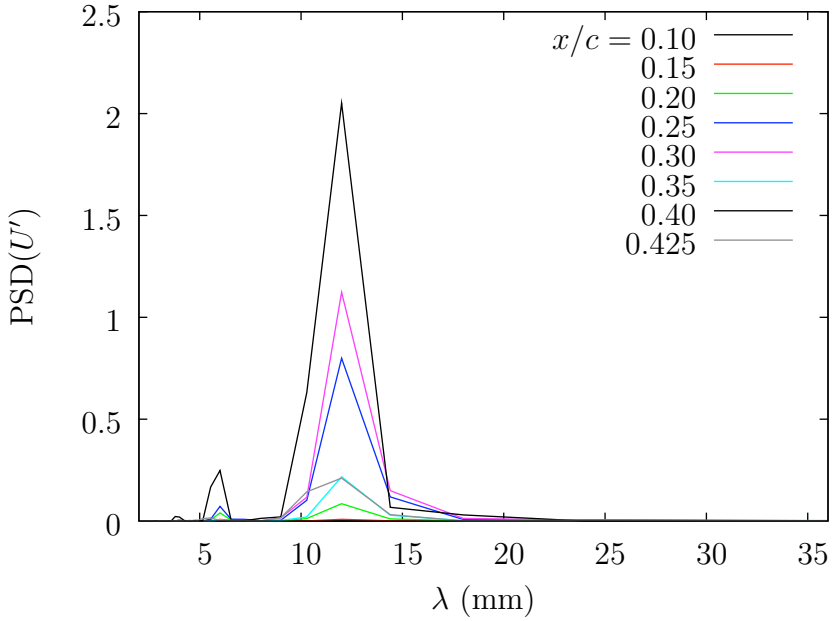

Figure 6.17: Spanwise power spectra at $Re_c = 2.8 \times 10^6$, $Tu = 0.02\%$, [12|12|3] roughness.

The stationary mode shapes of Fig. 6.18 show that linear disturbance growth persists through $x/c = 0.30$, before the clear appearance of a secondary lobe in the mode shape profile of $x/c = 0.35$. As the stationary disturbances become large, their nonlinear interactions become significant. In this case, the maximum amplitude is

over 20% of U_e. The critical roughness is a suitable environmental disturbance for producing strong stationary mode growth, which is needed to examine the effect of freestream turbulence on disturbance amplitude saturation.

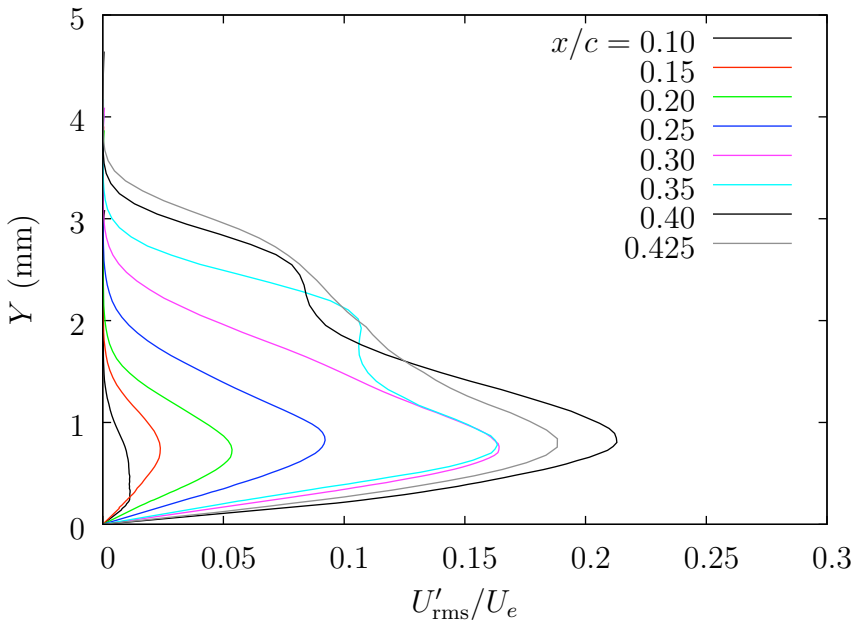

Figure 6.18: Spanwise rms steady disturbance profiles at $Re_c = 2.8\times10^6$, $Tu = 0.02\%$, [12|12|3] roughness.

Integrated values of the stationary disturbance profiles are plotted in Fig. 6.19. The strong disturbance growth through $x/c = 0.30$ is expected given the shapes of the stationary modes. A second period of disturbance growth follows, which may be attributed to nonlinear growth. In a mathematical sense, the secondary lobes that appear in the U'_{rms} profiles can produce a larger integrated value despite the lower maximum values of these profiles. This is one reason that it is important to use both of these quantities as a metric of disturbance growth. Following a peak value at $x/c = 0.40$, the disturbance amplitude is observed to decay in the last measured point.

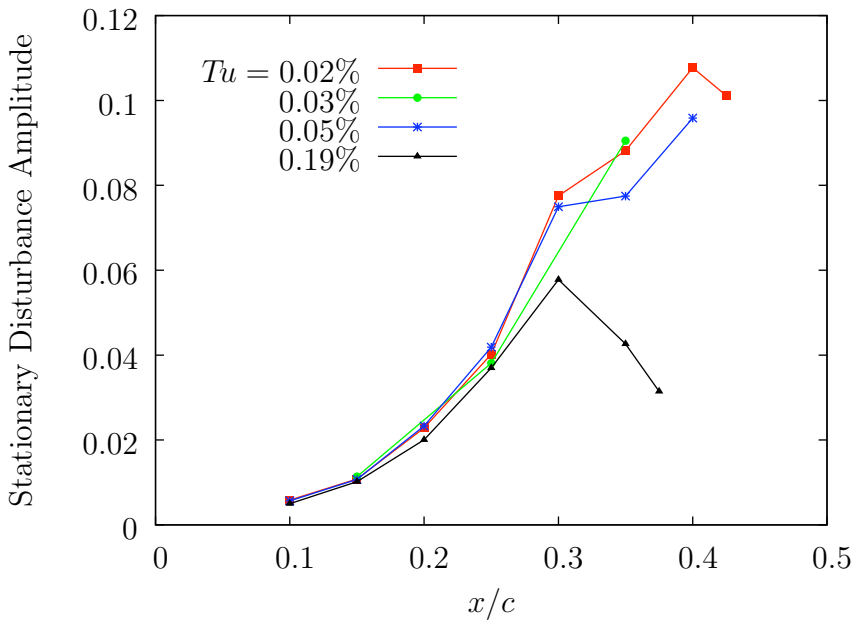

Figure 6.19: Stationary disturbance amplitude evolution at $Re_c = 2.8 \times 10^6$, [12|12|3] roughness.

The growth of the traveling mode amplitudes of Fig. 6.20 is relatively sedate. The maximum amplitude never climbs above 1% and is far less for most of the measurement domain. Comparing this with the traveling mode profiles of the other roughness configurations, it appears that roughness plays little role in initiating the traveling crossflow mode at this turbulence level. Examining the streamwise evolution of the unsteady modes in Fig. 6.21, a slight decay is observed in the unsteady mode before it begins to grow at $x/c = 0.30$. A similar trend is observed in the traveling mode, albeit at a much lower value. At the baseline turbulence level, the stationary mode is clearly the dominant instability.

A small number of measurements are made with $Tu = 0.03\%$. The corresponding boundary-layer profiles and velocity contours are given in Appendix C and the computed amplitudes are plotted along with the three main turbulence levels. The stationary amplitudes of Fig. 6.19 are nearly the same as the baseline turbulence

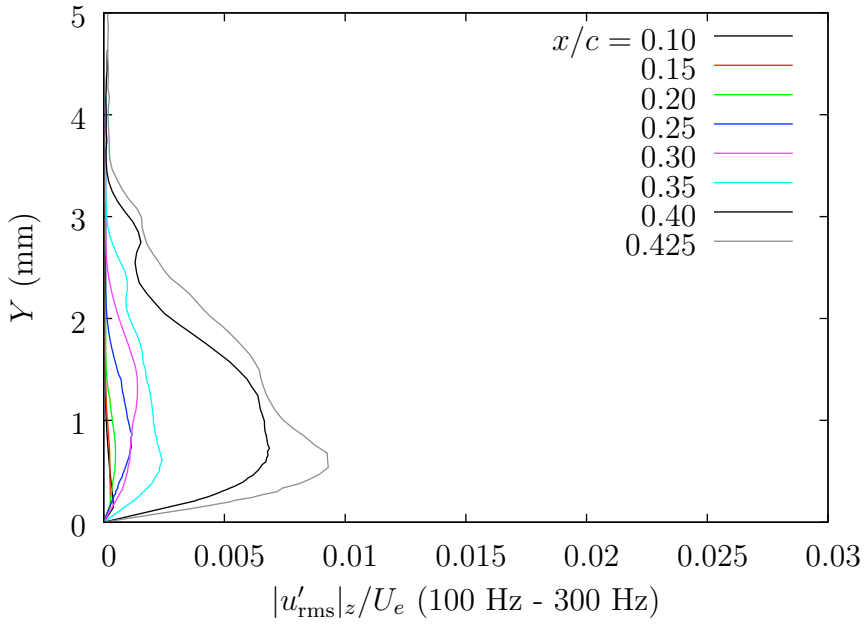

Figure 6.20: Spanwise mean of the unsteady disturbance profiles for the traveling wave passband 100–300 Hz at $Re_c = 2.8 \times 10^6$, $Tu = 0.02\%$, [12|12|3] roughness.

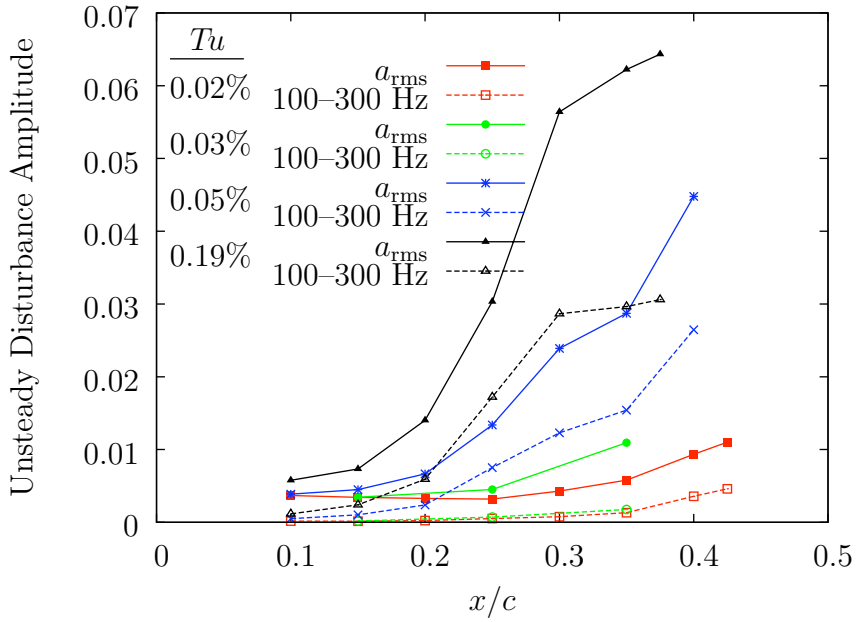

Figure 6.21: Traveling disturbance amplitude evolution at $Re_c = 2.8 \times 10^6$, [12|12|3] roughness.

level. At $x/c = 0.35$, the stationary amplitude is marginally larger than in the baseline case, but this may be within the measurement uncertainty. However, the unsteady amplitude growth is markedly increased. The traveling mode amplitude is approximately the same as in the baseline case. However, the total fluctuation level in Fig. 6.21 shows the surprising result that increasing the turbulence intensity to 0.03% produces a measurable increase in the growth rate of this quantity.

3. Intermediate Turbulence Level: $Tu = 0.05\%$

When the turbulence level is increased to 0.05%, qualitatively similar results are observed in the boundary-layer measurements. The roughness array produces strong spanwise modulation of the mean flow and 12 mm periodicity is evident. As before, the spatial spectra of $U'(z)$ at the boundary-layer height corresponding to the maxima of U'_{rms} are computed; these are plotted in Fig. 6.22. These spectra show that in addition to λ_k, the first two harmonics are also observed in locations $x/c \geq 0.20$. No other components are observed, indicating that the roughness array (rather than natural surface roughness) is the dominant source of stationary disturbance initiation.

The stationary mode shapes of Fig. 6.23 show steady, linear disturbance growth until $x/c = 0.35$, at which point secondary lobes are measured above the mode shape maxima. The boundary-layer measurements are stopped at $x/c = 0.40$ to avoid attempts at wall-finding in turbulent profiles. At this location, the maximum value of the stationary disturbance amplitude is slightly less than 0.2. This is less than in the baseline turbulence case, indicating that the increased turbulence level has attenuated the stationary disturbance amplitude as in the other tests. This is shown directly in the stationary amplitudes of Fig. 6.19. At $Tu = 0.05\%$, the stationary mode amplitude follows that of the baseline turbulence level through $x/c = 0.30$, at which point the amplitude is measurably reduced from the baseline level.

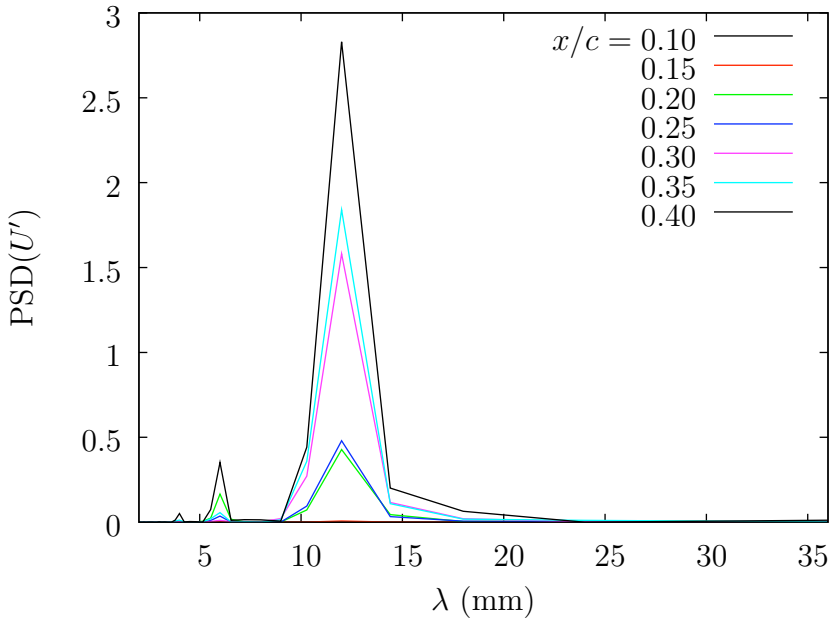

Figure 6.22: Spanwise power spectra at $Re_c = 2.8 \times 10^6$, $Tu = 0.05\%$, [12|12|3] roughness.

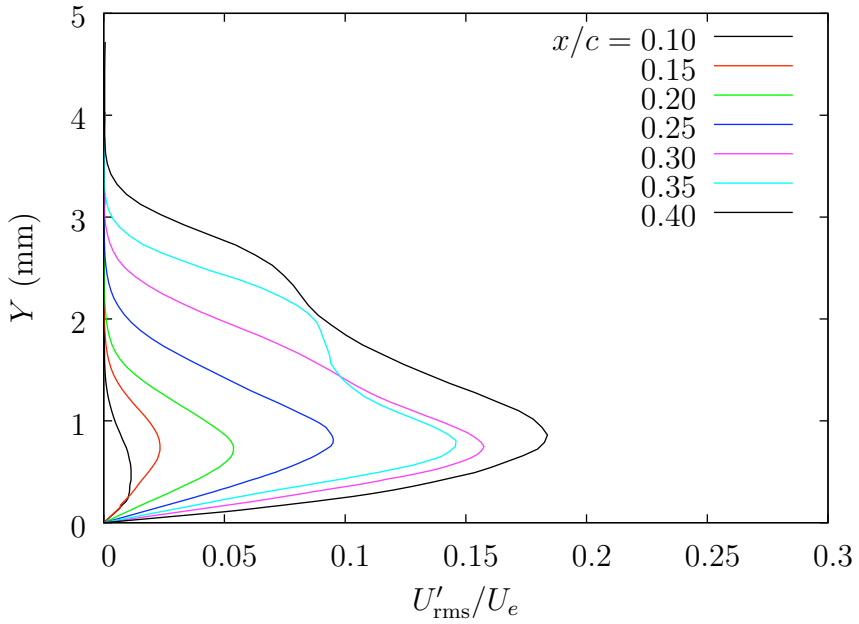

Figure 6.23: Spanwise rms steady disturbance profiles at $Re_c = 2.8 \times 10^6$, $Tu = 0.05\%$, [12|12|3] roughness.

The traveling mode amplitudes are increased in the presence of elevated freestream turbulence. The mode shapes of Fig. 6.24 show that the traveling mode grows in amplitude and wall-normal extent as it moves downstream: no saturation or decay of this mode is evident. The amplitudes of the fluctuation velocity and the traveling mode are observed to grow with increasing growth rate in Fig. 6.21 at this level of turbulence. For each set of amplitudes, the rate of growth is at its highest at the end of the measurement domain. This is in contrast with the baseline turbulence case, in which the unsteady fluctuations initially decayed in amplitude and never attained a significant amplitude. This is another demonstration of the high sensitivity of the traveling mode to freestream turbulence.

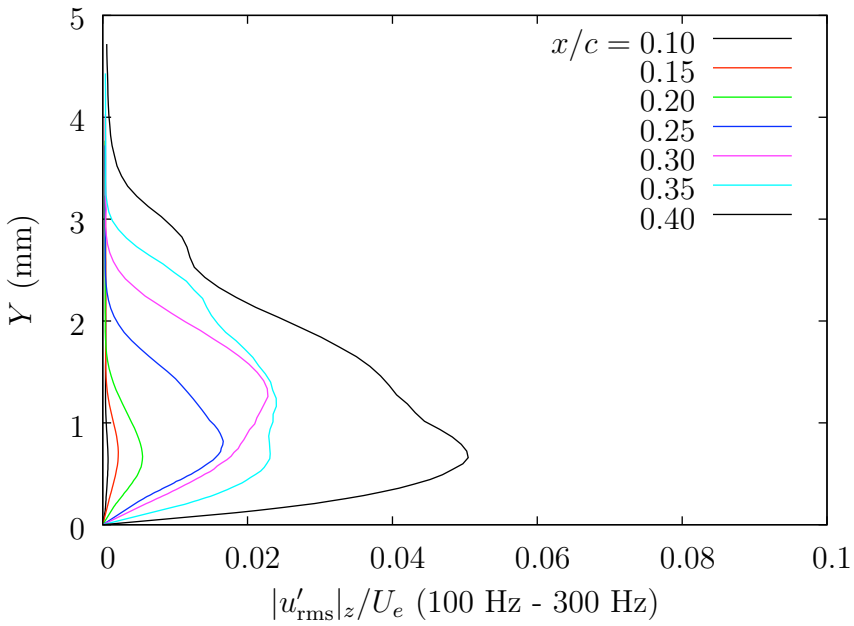

Figure 6.24: Spanwise mean of the unsteady disturbance profiles for the traveling wave passband 100–300 Hz at $Re_c = 2.8 \times 10^6$, $Tu = 0.05\%$, [12|12|3] roughness.

4. High Turbulence Level: $Tu = 0.19\%$

To complete this set of experiments, the turbulence level is raised to 0.19% and boundary-layer measurements are made through $x/c = 0.375$. The average transition location for this turbulence level is $x/c_{tr} = 0.41$; the hot-wire measurements are stopped before reaching areas where the flow is turbulent. This is to avoid attempts at wall-finding where high $\partial U/\partial y$ values might allow the probe to be moved too close to the wall. The contours of the steady and unsteady velocities are plotted in Appendix C. As with the other turbulence levels, the mean flow is distorted by the stationary crossflow vortices into a periodic structure. The unsteady fluctuation levels are also strongly periodic. However, close examination of these plots reveals that the expected "roll-over" shape in the steady velocity contours is not as well-defined as in the lower turbulence cases. This is the physical manifestation of the reduced stationary disturbance amplitude. Similarly, the spatial periodicity of U' as plotted in Fig. 6.25 shows a reduction in the power of the harmonics. The λ_k component is still the dominant feature, but $\lambda_k/2$ is only observed at significant levels at $x/c = 0.25$. The $\lambda_k/3$ harmonic is not observed. The shorter-wavelength components of the mean flow distortion appear to be more susceptible to amplitude reduction by the increased turbulence level.

Contours of the steady and unsteady velocity fields measured at $x/c = 0.35$ are shown in Figs. 6.26 and 6.27, for $Tu = 0.05\%$ and 0.19% respectively. Comparing these figures demonstrates the attenuation of the steady disturbances at the higher turbulence level. In addition, the distribution of the unsteady fluctuations is affected by the turbulence level. At $Tu = 0.05\%$, the highest levels of u'_{rms} are concentrated along the left sides of the mean-flow structures (near $Y = 2$ mm, $z = 38$ mm, for example). However, when Tu is increased to 0.19%, the maximum fluctuation levels

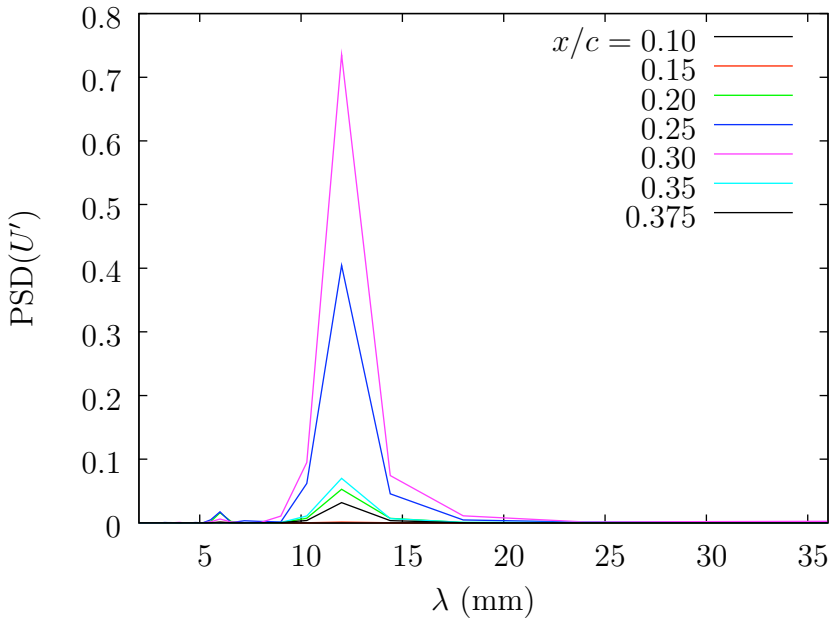

Figure 6.25: Spanwise power spectra at $Re_c = 2.8 \times 10^6$, $Tu = 0.19\%$, [12|12|3] roughness.

are observed lower in the boundary-layer: $Y = 0.5$ mm, $z = 40$ mm for that same flow structure. This indicates that the character of the instability may have changed at the higher turbulence level.

The stationary mode shapes of Fig. 6.28 have two notable features. The maximum amplitude of these modes are reduced significantly by increasing the turbulence level. Additionally, the appearance of nonlinear growth is advanced somewhat. The profile measured at $x/c = 0.30$ has the appearance of a secondary lobe above the profile maximum. In the previous measurements, this was not observed until the next measurement at $x/c = 0.35$. The appearance of this feature is taken to signify that the disturbance levels are high enough that disturbance interactions are of significant strength. As the stationary disturbances are clearly reduced by the freestream turbulence, the appearance of this second lobe may also indicate that the increased fluctuation levels are distorting the mean flow such that the mode shapes are affected.

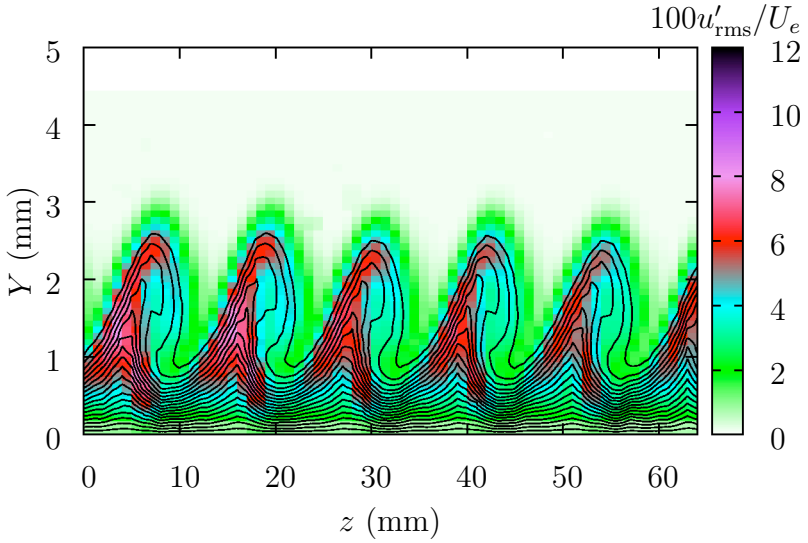

Figure 6.26: Spanwise modulation of U and u'_{rms} at $x/c = 0.35$. Test conditions are $Re_c = 2.8 \times 10^6$, $Tu = 0.05\%$, [12|12|3] roughness.

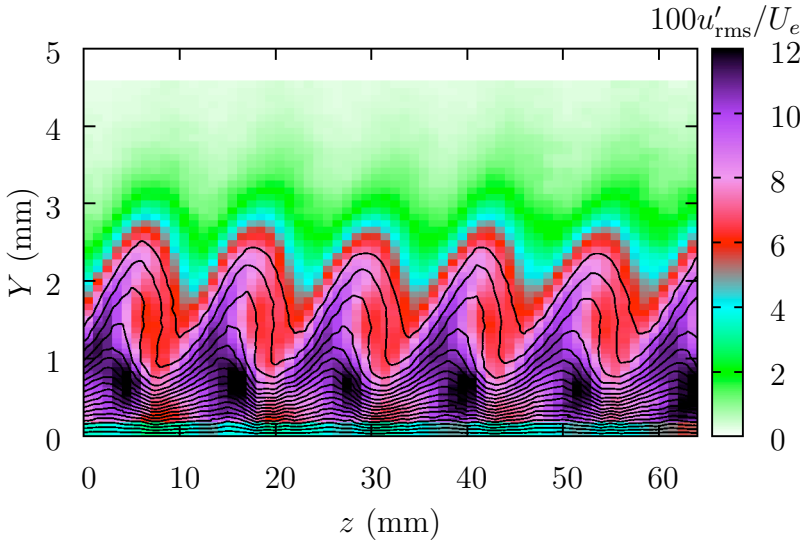

Figure 6.27: U' distortion is reduced and u'_{rms} distribution is affected by increased Tu. Test conditions are $x/c = 0.35$, $Re_c = 2.8 \times 10^6$, $Tu = 0.19\%$, [12|12|3] roughness.

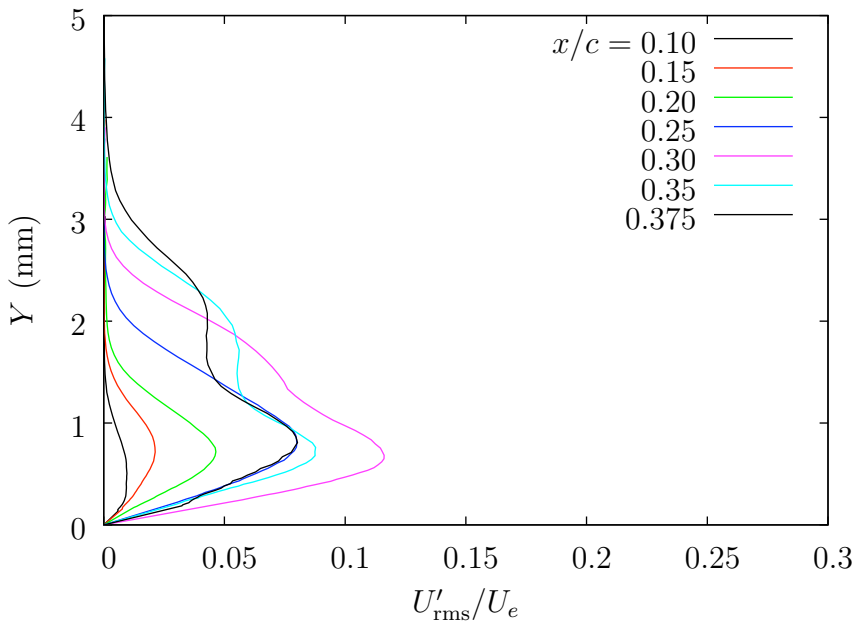

Figure 6.28: Spanwise rms steady disturbance profiles at $Re_c = 2.8\times10^6$, $Tu = 0.19\%$, [12|12|3] roughness.

The steady disturbance amplitudes of Fig. 6.19 show a significant change in the behavior of the stationary crossflow mode in this case. The initial value is approximately the same as in the other turbulence levels, but the growth rate is somewhat reduced. This is evident in the increasing disparity between the stationary disturbance at $Tu = 0.19\%$ and those of the lower turbulence levels. At $x/c = 0.30$, however, the stationary disturbance reaches its peak and decays significantly thereafter. The evolution of the unsteady disturbances provide insight into the path taken to transition.

The traveling mode profiles grow sharply in amplitude and wall-normal extent throughout the measurement domain, as shown in Fig. 6.29. The integrated amplitude values in Fig. 6.21 reflect this strong growth. The total fluctuation amplitude experiences a high rate of growth through $x/c = 0.30$, at which point the growth rate is decreased (though still positive). The traveling mode amplitude also rises

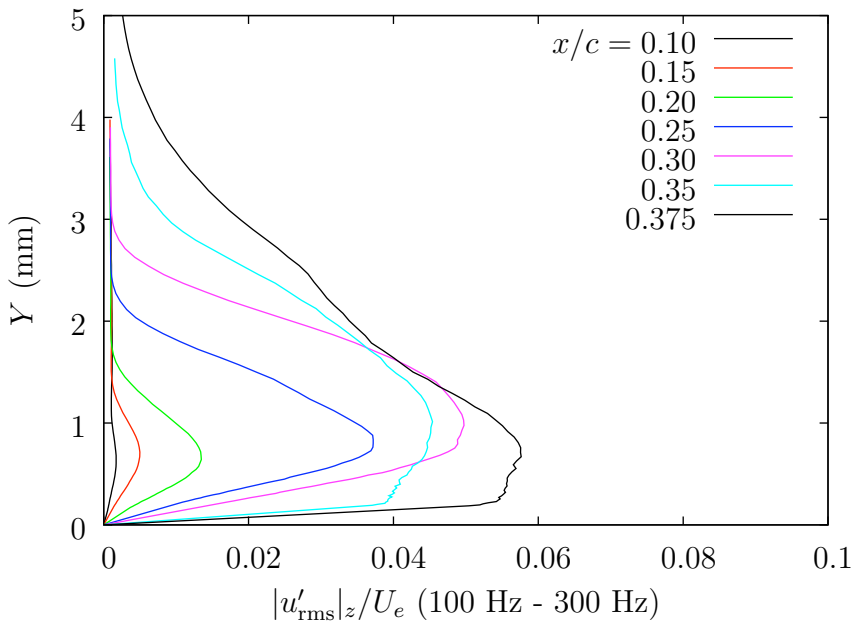

Figure 6.29: Spanwise mean of the unsteady disturbance profiles for the traveling wave passband 100–300 Hz at $Re_c = 2.8 \times 10^6$, $Tu = 0.19\%$, [12|12|3] roughness.

sharply but appears to stabilize at this point. The terminal value of the traveling mode amplitude is not that much greater than the value observed at $Tu = 0.05\%$. From these plots, transition at the high turbulence level appears to be a result of the traveling mode. The growth of this mode coupled with the decay of stationary mode in the downstream region indicates that the traveling mode has outpaced the stationary mode.

5. Combined Effect of Freestream Turbulence and Critically-Spaced Roughness

From the preceding sections, it has been shown that increasing freestream turbulence effectively decreases the amplitude of the stationary disturbances. As with the subcritically-spaced roughness, it does not appear that the initial measured am-

plitudes are affected to a large degree. The initial amplitudes measured in these tests are tabulated in Table 6.5 and confirm this observation.

Tu	A_0
0.02%	0.006
0.05%	0.006
0.19%	0.005

Table 6.5: Initial stationary disturbance amplitudes measured at $Re_c = 2.8 \times 10^6$ using [12|12|3] roughness. Values are measured at $x/c = 0.10$.

Examination of the spatial spectra of $U'(z)$ indicates that the shorter wavelengths may be more affected by the freestream turbulence. The stationary mode amplitudes for disturbances of wavelength λ_k and its harmonics are computed and plotted in Fig. 6.30. As this plot shows, the λ_k component represents the majority of the total disturbance amplitude. The evolution of this spectral mode follows closely that of the total stationary disturbance amplitudes. Though the $\lambda_k/2$ mode is of relatively small amplitude, it does appear that it contributes more to the stationary disturbance at the lowest turbulence level. Additionally, the disparity among the levels of this mode becomes more pronounced aft of $x/c = 0.30$.

The stationary mode shapes measured for each turbulence level at $x/c = 0.35$ are plotted together in Fig. 6.31 and normalized by the maximum value of U'_{rms} in the baseline turbulence case. As this plot shows, a measurable reduction in the stationary mode amplitude is evident at $Tu = 0.05\%$ and the reduction at the highest turbulence level is nearly half. The mode shapes are similar, however. Together with the initial disturbance values, this suggests that freestream turbulence acts to reduce the growth rate of the stationary disturbance, but does not affect the initiation of this mode.

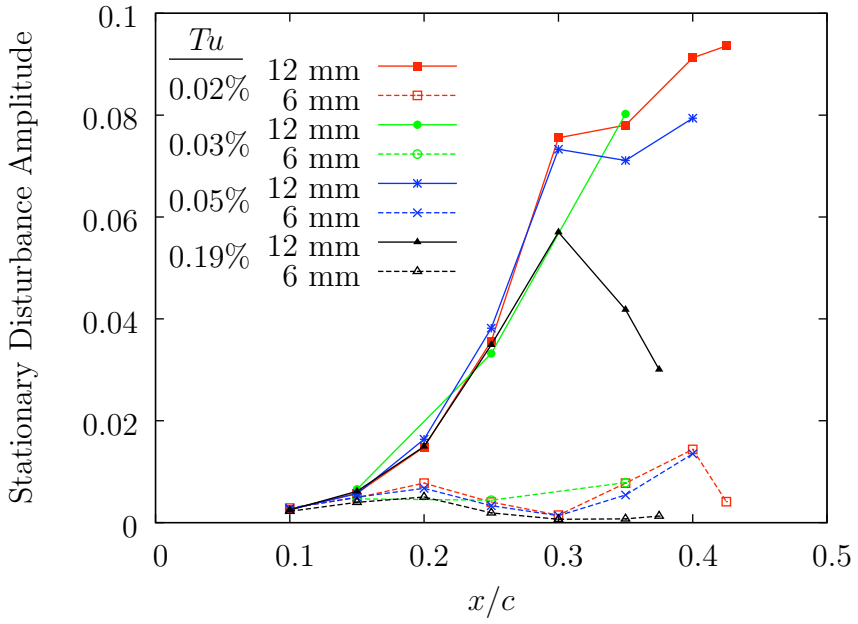

Figure 6.30: Stationary disturbance amplitude evolution for forced and harmonic wavelengths at $Re_c = 2.8 \times 10^6$, [12|12|3] roughness.

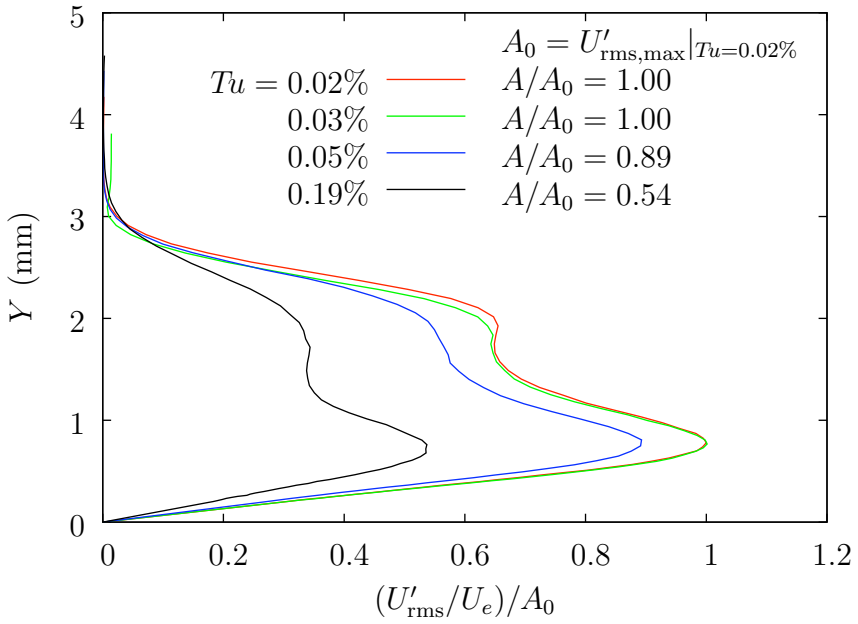

Figure 6.31: Stationary disturbance amplitude comparison at $x/c = 0.35$, $Re_c = 2.8 \times 10^6$, [12|12|3] roughness.

Growth of the traveling mode is affected by both the freestream turbulence and the surface roughness array. As was observed in tests using the other roughness configurations, the amplitude of the traveling mode is greatly increased with small increases to the freestream turbulence. However, the effect is even more pronounced in the presence of critically-spaced roughness. Traveling mode amplitude profiles measured at $x/c = 0.35$ are plotted together in Fig. 6.32. These profiles are normalized by the maximum value of the traveling mode profile in the baseline turbulence case. As this plot and the figure key show, the maximum amplitudes observed at the higher turbulence levels are much higher than in the other roughness configurations. In particular, the amplitude of the traveling mode is nearly 20 times greater when Tu is increased to 0.19% in the presence of critically-spaced roughness. Initiation and growth of the traveling mode are affected by both surface roughness and freestream turbulence in this configuration.

Considering the integrated values of these disturbance amplitudes, this trend is confirmed. As before, the stationary and traveling mode profiles are integrated in the wall-normal direction to give a measure of the disturbance amplitude that accounts for mode shape as well as maxima. The values of these quantities at $x/c = 0.35$ are tabulated in Table 6.6. Even though the amplitude of the stationary mode is greater than the traveling mode in all cases, transition at $Tu = 0.19\%$ is clearly due to the traveling mode. Perhaps the most important result in this table is the relative strengths of the traveling mode at the baseline turbulence level and at 0.05%. Though both levels qualify as low-disturbance environments (Reshotko *et al.*, 1997), the prevalence of the traveling mode in the latter is significant.

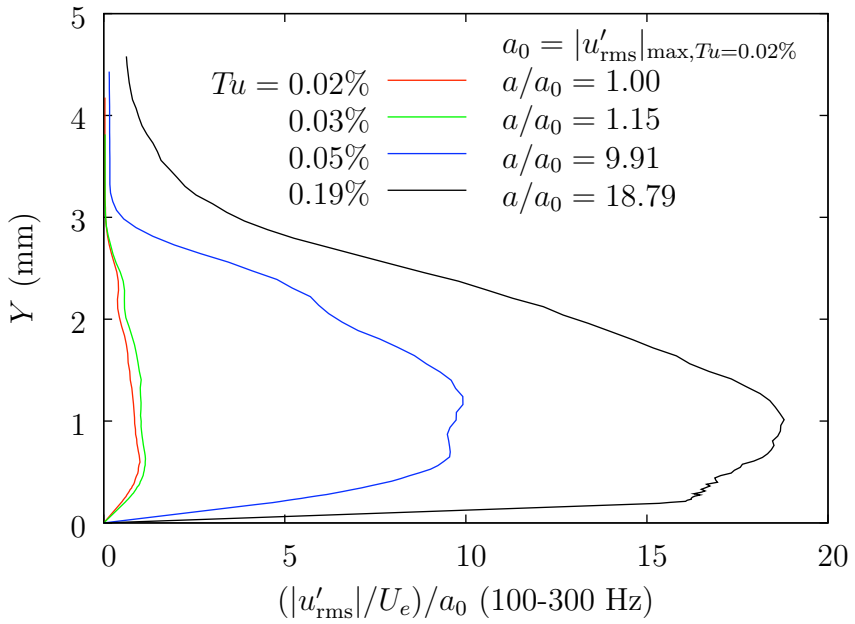

Figure 6.32: Traveling disturbance amplitude comparison at $x/c = 0.35$, $Re_c = 2.8 \times 10^6$, [12|12|3] roughness.

Tu	$A(0.35)$	$a(0.35)$
0.02%	0.088	0.001
0.03%	0.091	0.002
0.05%	0.077	0.015
0.19%	0.043	0.030

Table 6.6: Stationary and traveling disturbance amplitudes measured at $x/c = 0.35$, $Re_c = 2.8 \times 10^6$ using [12|12|3] roughness.

CHAPTER VII

SUMMARY

In the course of these experiments, amplitudes of the traveling and stationary crossflow modes are measured in flows whose freestream turbulence intensity is varied from 0.02% to 0.19%. The freestream turbulence intensity is increased using high open-area-ratio grids of various shape and element diameter. The grids are mounted upstream of the contraction, which has the side effect of producing anisotropic turbulence by reducing the streamwise component of the fluctuations. It is noted by Tan-atichat *et al.* (1980) that for low turbulence flows, this reduction is due to the increase in the streamwise velocity rather than a change in the streamwise turbulent kinetic energy. The transverse components of Tu are higher than the streamwise component as noted in Chapter IV. As streamwise vorticity is the important initiating disturbance for crossflow instability growth, this enhanced freestream turbulence will effectively excite the traveling crossflow mode.

The test model is a 45-degree swept wing with a 1.83 m chord. The airfoil shape is designed to suppress the growth of streamwise and centrifugal instabilities to ensure that the crossflow instability sets the path to transition. All experiments are run at a chord-based Reynolds number of $Re_c = 2.8 \times 10^6$. Three different roughness configurations are tested: baseline (characterized by 0.3-μm-rms random distributed roughness) and arrays of $[k|\lambda|d] = [12|12|3]$ and $[14|6|3]$ roughness. This research seeks answers to the effects of this modest level of freestream turbulence intensity on roughness receptivity, stationary disturbance amplitude saturation levels and transition location. The key results from these experiments are summarized and these open research questions are addressed.

The question of roughness receptivity—how the surface roughness creates disturbances to the boundary-layer velocity—may be addressed by examining the measured initial disturbance amplitudes. The stationary disturbance amplitudes are computed by integrating $U'_{\mathrm{rms}}(Y)$ profiles in the wall-normal direction, as in Eq. 5.3. Normalizing this quantity by the boundary-layer thickness is a suitable means of rendering it dimensionless. Though the artificial roughness is placed at $x/c = 0.029$, the initial measurements are made at $x/c = 0.10$ because a sufficiently large disturbance and boundary-layer thickness are needed to properly resolve the initial disturbance. The initial disturbances are summarized in Table 7.1. In the case of artificial roughness, the initial disturbances are approximately equal in the three turbulence environments. There is some indication that the initial amplitudes are lower in the higher turbulence environments. However, it has been demonstrated that the effect of turbulence is to reduce the growth of stationary disturbances. The lower initial amplitudes are attributed to disturbance attenuation between the roughness location and the measurement location. It is concluded that across the measured range of Tu, freestream turbulence plays little role in the receptivity to surface roughness.

Tu	Baseline	[14|6|3]	[12|12|3]
0.02%	0.002	0.007	0.006
0.05%	0.004	0.007	0.006
0.19%	0.004	0.006	0.005

Table 7.1: Summary of initial stationary disturbance amplitudes measured at $x/c = 0.10$, $Re_c = 2.8\times10^6$. Baseline roughness is 0.3-μm-rms random distributed roughness

Because the initial amplitudes are mostly unaffected by increasing the freestream turbulence, amplification ratios of the stationary disturbance amplitudes computed

using Eq. 5.4 will be directly comparable due to their approximately equal A_0 values. The traveling disturbance mode amplitudes, computed using Eq. 5.5 with a 100–300 Hz passband, are observed to have increasing initial values as the turbulence level is increased. However, N factors of the traveling modes will not reflect this by definition; these values represent disturbance change from the measured initial value. N factors for the baseline roughness experiments are plotted in Fig. 7.1. Measurements for the high turbulence case do not extend as far downstream due to the advanced transition front in this case. Saturation of the stationary disturbance amplitude is not observed in the low turbulence case. Though the measurements at the enhanced turbulence levels are comparatively sparse (the purpose of these tests is primarily to determine the most unstable natural disturbance), growth of these stationary disturbances are reduced. Amplification ratios are also plotted for the subcritical roughness measurements in Fig. 7.2. The majority of these measurements are made at $Tu = 0.05\%$ to examine how this roughness wavelength affects the growth of stationary crossflow vortices.

The N factor plot reflects the growth of the $\lambda_k = 6$ mm disturbance, followed by its decay. Disturbance growth aft of $x/c = 0.40$ is attributed to a longer-wavelength disturbance that is more unstable than the 6 mm disturbance. Regarding prospects for transition delay with subcritical roughness, it is recommended that a longer-wavelength roughness array is tested. The LST computations show that a disturbance with $\lambda = 8$ mm is more unstable than $\lambda = 6$ mm, but less critical than $\lambda = 12$ mm. An array of roughness with $\lambda_k = 8$ mm may produce a mean flow distortion that persists over a longer streamwise distance before decaying, while suppressing growth of the more unstable 12 mm disturbance.

A complete series of disturbance evolution measurements are made in the three turbulence environments using critically-spaced roughness. N factors for the crit-

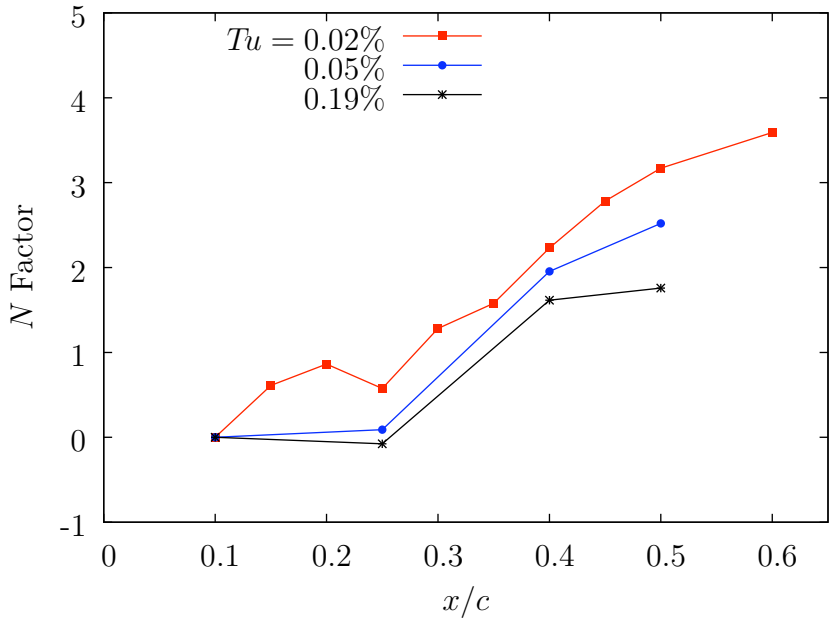

Figure 7.1: Stationary disturbance amplification ratios at $Re_c = 2.8 \times 10^6$, clean leading edge.

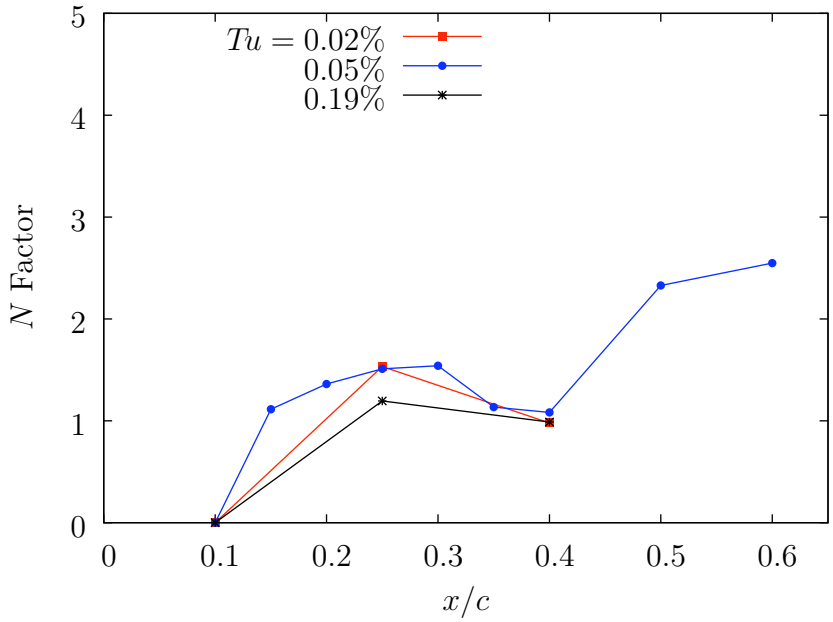

Figure 7.2: Stationary disturbance amplification ratios at $Re_c = 2.8 \times 10^6$, with subcritically-spaced [14|6|3] roughness.

ical roughness experiments are plotted in Fig. 7.3. Data from the experiments of Gladden (2001) are also included: these experiments used [6|12|3] roughness on the same swept-wing model in a freestream turbulence environment of 0.25%. With the exception of the highest turbulence case, the growth rates are approximately equal through $x/c = 0.25$. The data at $Tu = 0.25\%$ have slightly smaller amplification ratios. However, the effect of freestream turbulence on stationary disturbance amplitude saturation is evident in the way the N factor curves begin to separate upstream of transition. As before, because the transition location moves forward with increasing freestream turbulence, the boundary-layer measurements are not carried as far downstream in these cases. From these data, it can be concluded that increasing freestream turbulence intensity acts to reduce the stationary disturbance amplitude, and that this reduction is measurable at values as low as $Tu = 0.05\%$.

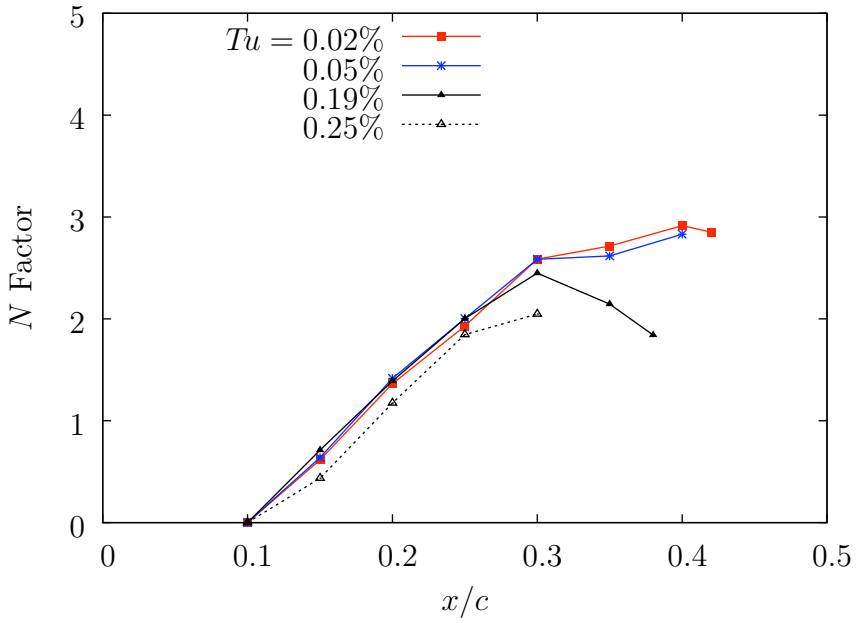

Figure 7.3: Stationary disturbance amplification ratios at $Re_c = 2.8 \times 10^6$, with critically-spaced [12|12|3] roughness. Data at $Tu = 0.25\%$ are from Gladden (2001) for [6|12|3] roughness.

The traveling mode amplification factors are plotted in Fig. 7.4, where as before, the data at $Tu = 0.25\%$ are from Gladden (2001). Note that the initial values in this case are different. Disturbance growth in the traveling mode passband is referenced to the initial value at $x/c = 0.15$ in this case. The growth rate of the traveling mode in the baseline turbulence case is lower than that of the elevated turbulence configurations. The data at $Tu = 0.25\%$ and the two intermediate values experience nearly the same growth rates. However, due to the larger initial values in the high turbulence cases, the terminal traveling mode amplitudes in these cases are much higher.

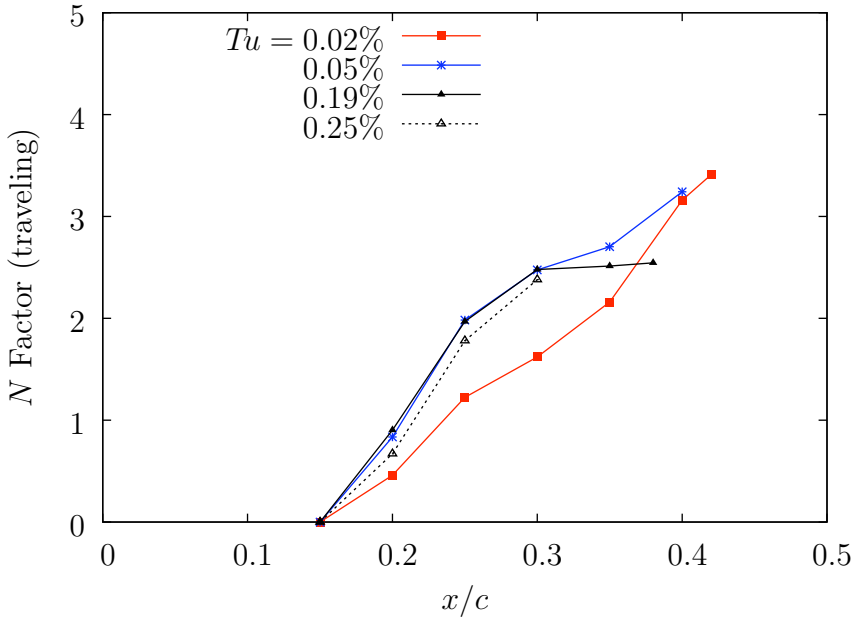

Figure 7.4: Traveling mode amplification ratios at $Re_c = 2.8\times10^6$, [12|12|3] roughness. Data at $Tu = 0.25\%$ are from Gladden (2001) for [6|12|3] roughness.

Amplified values of the stationary and traveling mode amplitudes are tabulated in Table 7.2. For each roughness configuration, the values are given for the most downstream position for which data are available across all turbulence levels. Thus,

for the subcritical roughness, the limited number of measurements precludes comparison of saturated amplitudes. In the baseline roughness configuration, it is observed that the stationary mode amplitude is reduced by over 50% when the freestream turbulence is increased to 0.19%. Conversely, the traveling mode amplitude is increased substantially. Comparing the amplitudes of these modes, the stationary mode is dominant at $Tu = 0.02\%$, although they are of approximately the same amplitude at $Tu = 0.19\%$. Similar trends are observed when critically-spaced roughness is used. A significant reduction in the stationary mode amplitude is observed with increasing turbulence in concert with greatly increased traveling mode amplitudes. Although the stationary mode is still of higher amplitude in the high turbulence case, the flow visualization results indicate that transition is dominated by the traveling mode.

The amplitude values measured at $Tu = 0.05\%$ serve an important purpose. This is the highest turbulence level that might still be considered a low-turbulence environment (this is not necessarily a hard cutoff point). Compared with the data at the lowest turbulence levels, this modest increase in Tu produces a small but measurable attenuation of the stationary mode as well as a significant increase in the traveling mode amplitude. Thus, for the study of the stationary crossflow mode, the lowest possible turbulence level is recommended. For comparison to simulations and other experiments, documentation of the turbulence is critical.

It is known that the turbulence intensity encountered in the flight environment is typically on the order of 0.05% (as in Carpenter (2009), for example). In-flight measurements by Riedel & Sitzmann (1998) produced values as low as $Tu = 0.034\%$ and there is some indication that these values are artificially raised by the presence of electronic noise. Thus, the stationary crossflow mode is the relevant instability mode to be considered for swept-wing boundary-layer stability in the flight environment. As such, efforts should be made to ensure that the freestream turbulence environ-

Tu	Baseline ($x/c = 0.50$)		[14|6|3] ($x/c = 0.40$)		[12|12|3] ($x/c = 0.35$)	
	Stationary	Traveling	Stationary	Traveling	Stationary	Traveling
0.02%	0.054	0.005	0.019	0.001	0.088	0.001
0.03%	—	—	—	—	0.091	0.002
0.05%	0.047	0.015	0.020	0.004	0.077	0.015
0.19%	0.024	0.026	0.017	0.008	0.043	0.030

Table 7.2: Summary of amplified disturbance amplitudes measured at $Re_c = 2.8 \times 10^6$.

ment is at least as low as 0.05% in experimental study of the crossflow instability. Moreover, decreasing the freestream turbulence intensity further will allow stronger growth of the stationary mode. Though perhaps an artificial inflation over the stationary mode amplitudes likely to exist in flight, this would be beneficial for the purpose of experimental measurement.

It has been observed that freestream turbulence affects the growth of the stationary crossflow mode by reducing its saturation amplitude. Initial disturbance amplitudes and growth rates in the linear stability regime appear largely unaffected by modest increases to the freestream turbulence. However, as the disturbances grow toward nonlinearity and amplitude saturation, increased turbulence intensity will attenuate the stationary mode amplitudes. The traveling mode is found to be highly receptive to freestream turbulence. That is, the traveling mode amplitudes increase sharply when the freestream turbulence intensity is increased. Comparing the relative values of these amplitudes, the $Tu = 0.2\%$ criterion of Deyhle & Bippes (1996) and White *et al.* (2001) has been confirmed. This is not an exact value, but the traveling mode is found to be the dominant instability and the cause of transition at $Tu = 0.19\%$ in the present experiments.

When Tu is increased from its baseline level of 0.02%, the average transition location is observed to march forward as much as 10% of the chord length. However, when subcritically-spaced roughness is applied, little change to the average transition location is observed. Thus, the criteria for traveling mode dominance (0.2%) and low-turbulence flow (0.05%) do not form a complete description of the turbulence environment in the context of crossflow-instability-dominated transition. The intensity, spectra and degree of anisotropy of the freestream turbulence should be documented as small variations may produce measurably different results in disturbance amplitude and transition location.

Toward that end, the role of turbulence intensity anisotropy should be investigated further. The contraction ratios used in various wind tunnel facilities might be expected to produce differences among the components of the turbulence intensity and grid placement is also known to introduce differences. All three components of the turbulence must be measured as high contraction ratios produce low streamwise fluctuations at the cost of increased transverse components. Careful measurement of freestream turbulence can provide realistic disturbance environments for computational work. In conclusion, the crossflow instability is strongly affected by both surface roughness and freestream turbulence. It is only with careful characterization of both of these quantities that the understanding and potential for control of this instability will advance.

REFERENCES

Agarwal, N. K., Maddalon, D. V., Mangalam, S. M. & Collier, F. S. 1992 Crossflow vortex and transition measurements by use of multielement hot films. *AIAA J.* **30** (9), 2212–2218.

Anderson, J. D. 1998 *A History of Aerodynamics*. Cambridge University Press.

Anderson, J. D. 2001 *Fundamentals of Aerodynamics*, 3rd edn. New York: McGraw-Hill.

Batchelor, G. K. & Townsend, A. A. 1948 Decay of isotropic turbulence in the initial period. *Proc. R. Soc. Lon. A* **193**, 539–558.

Bippes, H. 1990 Instability features appearing on swept wing configurations. In *IUTAM Symposium on Laminar-Turbulent Transition, Toulouse, France* (ed. D. Arnal & R. Michel), pp. 1–12. Springer.

Bippes, H. 1999 Basic experiments on transition in three-dimensional boundary layers dominated by crossflow instability. *Prog. Aerosp. Sci.* **35**, 363–412.

Bippes, H. & Lerche, T. 1997 Transition prediction in three-dimensional boundary-layer flows unstable to crossflow instability. *AIAA Paper* 97-1906.

Bruun, H. H. 1995 *Hot-Wire Anemometry*. New York: Oxford University Press.

Carpenter, A. L. 2009 In-Flight Receptivity Experiments on a 30-degree Swept-Wing Using Micron-sized Discrete Roughness Elements. PhD thesis, Texas A&M University.

Carpenter, A. L., Saric, W. S. & Reed, H. L. 2010 Roughness receptivity in swept-wing boundary layers—Experiments. *Int. J. Eng. Syst. Model. Simul.* **2** (1/2), 128–138.

Cooper, R. D. & Tulin, M. P. 1955 Turbulence Measurements with the Hot-wire Anemometer. NATO AGARD.

Crouch, J. D. 1994 Theoretical studies on receptivity of boundary layers. *AIAA Paper* 94-2224.

Dagenhart, J. R. & Saric, W. S. 1999 Crossflow stability and transition experiments in swept-wing flow. *NASA TP*-1999-209344.

Dagenhart, J. R., Saric, W. S., Mousseux, M. C. & Stack, J. P. 1989 Crossflow-vortex instability and transition on a 45-degree swept wing. *AIAA Paper* 89-1892.

Deyhle, H. & Bippes, H. 1996 Disturbance growth in an unstable three-dimensional boundary layer and its dependence on environmental conditions. *J. Fluid Mech.* **316**, 73–113.

Deyhle, H., Höhler, G. & Bippes, H. 1993 Experimental investigation of instability wave propagation in a three-dimensional boundary-layer flow. *J. Fluid Mech.* **31** (4), 637–645.

Downs, R. S. & White, E. B. 2011 Spectral analysis of phase-shifting measurements of crossflow waves. *Exp. Fluids* **51** (6), 1673–1684.

Drazin, P. G. 2002 *Introduction to Hydrodynamic Stability*. Cambridge University Press.

Eppink, J. & Wlezien, R. 2011 Data analysis for the NASA/Boeing hybrid laminar flow control crossflow experiment. *AIAA Paper* 2011-3879.

Ergin, F. G. 2005 Roughness Induced Transition. PhD thesis, Case Western Reserve University.

Ergin, F. G. & White, E. B. 2005 Multicomponent and unsteady velocity measurements of transient disturbances. *AIAA Paper* 2005-527.

Fransson, J. H. M., Matsubara, M. & Alfredsson, P. H. 2005 Transition induced by free-stream turbulence. *J. Fluid Mech.* **527**, 1–25.

Gladden, R. D. 2001 Crossflow Transition in Elevated Freestream Turbulence. Master's thesis, Arizona State University.

Gray, W. E. 1952 The effect of wing sweep on laminar flow. *Tech. Memo. Aero.* 255, British RAE.

Green, J. E. 2008 Laminar flow control—Back to the future? *AIAA Paper* 2008-3738.

Gregory, N., Stuart, J. T. & Walker, W. S. 1955 On the stability of three-dimensional boundary layers with application to the flow due to a rotating disk. *Philos. T. R. Soc. A* **248**, 155–199.

Groth, J. & Johansson, A. V. 1988 Turbulence reduction by screens. *J. Fluid Mech.* **197**, 139–55.

Haynes, T. S. & Reed, H. L. 2000 Simulation of swept-wing vortices using nonlinear parabolized stability equations. *J. Fluid Mech.* **405**, 325–349.

Hinze, J. O. 1975 *Turbulence*, 2nd edn. McGraw-Hill.

Hunt, L. E. 2011 Boundary-Layer Receptivity of Three-Dimensional Roughness Arrays on a Swept-Wing. PhD thesis, Texas A&M University.

Hunt, L. E., Downs, R. S., Kuester, M. S., White, E. B. & Saric, W. S. 2010 Flow quality measurements in the Klebanoff–Saric Wind Tunnel. *AIAA Paper* 2010-4538.

Hunt, L. E. & Saric, W. S. 2011 Boundary-layer receptivity of three-dimensional roughness arrays on a swept-wing. *AIAA Paper* 2011-3881.

van Ingen, J. L. 2008 The e^N method for transition prediction. Historical review of work at TU Delft. *AIAA Paper* 2008-3830.

Jones, R. T. 1945 Wing Plan Forms for High-Speed Flight. *NACA-TR*-863.

Joslin, R. D. 1998 Aircraft laminar flow control. *Annu. Rev. Fluid Mech.* **30**, 1–29.

Kendall, J. M. 1990 Boundary layer receptivity to freestream turbulence. *AIAA Paper* 90-1504.

Kohama, Y., Saric, W. S. & Hoos, J. A. 1991 A high-frequency, secondary instability of crossflow vortices that leads to transition. In *Proc. of the Royal Aero. Soc. Conf. on Boundary-Layer Trans. and Control*, pp. 1–12.

Kurian, T. & Fransson, J. H. M. 2009 Grid-generated turbulence revisited. *Fluid Dyn. Res.* **41** (021403), 1–32.

Kurian, T., Fransson, J. H. M. & Alfredsson, P. H. 2011 Boundary layer receptivity to free-stream turbulence and surface roughness over a swept flat plate. *Phys. Fluids* **23** (034107), 1–13.

Laws, E. M. & Livesey, J. L. 1978 Flow through screens. *Annu. Rev. Fluid Mech.* **10**, 247–66.

Mavris, D. M., Saric, W. S., Ran, H., Belisle, M. J., Woodruff, M. J. & Reed, H. L. 2010 Investigation of a health monitoring methodology for future natural laminar flow transport aircraft. In *27th Congress of International Council of the Aeronautical Sciences, Nice, France*, pp. 1–16.

Morkovin, M. V., Reshotko, E. & Herbert, Th. 1994 Transition in open flow systems—A reassessment. *Bull. APS* **39** (9), 1882.

Morkovin, M. V. 1969 On the many faces of transition. In *Viscous Drag Reduction* (ed. C. S. Wells), pp. 1–31. New York: Plenum.

Müller, B. & Bippes, H. 1989 Experimental study of instability modes in a three-dimensional boundary layer. In *Fluid Dynamics of Three-Dimensional Turbulent Shear Flows and Transition*, *AGARD CP* 438, pp. 1–15. NATO AGARD.

Naguib, A. M., Gravante, S. P. & Wark, C. E. 1996 Extraction of turbulent wall-pressure time-series using an optimal filtering scheme. *Exp. Fluids* **22**, 14–22.

O'Neill, P. L., Nicolaides, D., Honnery, D. & Soria, J. 2004 Autocorrelation functions and the determination of integral length with reference to experimental and numerical data. In *15th Austr. Fluid Mech. Conf.*, pp. 1–4. The University of Sydney.

Pope, S. B. 2000 *Turbulent Flows*. New York: Cambridge University Press.

Press, W. H., Teukolsky, S. A., Vetterling, W. T. & Flannery, B. P. 2007 *Numerical Recipes: The Art of Scientific Computing*, 3rd edn. New York: Cambridge University Press.

Radeztsky, R.H., Reibert, M. S. & Takagi, S. 1993 A software solution to temperature-induced hot-wire voltage drift. In *Proceedings of Third International Symposium on Thermal Anemometry*, pp. 49–55.

Radeztsky, R. H., Reibert, M. S. & Saric, W. S. 1994 Development of stationary crossflow vortices on a swept wing. *AIAA Paper* 94-2373.

Radeztsky, R. H., Reibert, M. S. & Saric, W. S. 1999 Effect of isolated micron-sized roughness on transition in swept-wing flows. *AIAA J.* **37** (11), 1370–1377.

Reed, H. L. & Saric, W. S. 1989 Stability of three-dimensional boundary layers. *Annu. Rev. Fluid Mech.* **21**, 235–284.

Reibert, M. S. 1996 Nonlinear Stability, Saturation, and Transition in Crossflow-Dominated Boundary Layers. PhD thesis, Arizona State University.

Reibert, M. S. & Saric, W. S. 1997 Review of swept-wing transition. *AIAA Paper* 97-1816.

Reibert, M. S., Saric, W. S., Carrillo, R. B. & Chapman, K. L. 1996 Experiments in nonlinear saturation of stationary crossflow vortices in a swept-wing boundary layer. *AIAA Paper* 96-0184.

Reshotko, E. 1975 A program for transition research. *AIAA J.* **13** (3), 261–265.

Reshotko, E., Saric, W. S. & Nagib, H. M. 1997 Flow quality issues for large wind tunnels. *AIAA Paper* 97-0225.

Riedel, H. & Sitzmann, M. 1998 In-flight investigations of atmospheric turbulence. *Aerosp. Sci. Technol.* **5**, 301–319.

Rizzetta, D. P., Visbal, M. R., Reed, H. L. & Saric, W. S. 2010 Direct numerical simulation of discrete roughness on a swept-wing leading edge. *AIAA J.* **48** (11), 2660–2673.

Saric, W. S. 1992 The ASU transition research facility. *AIAA Paper* 92-3910.

Saric, W. S. 1994 Görtler vortices. *Annu. Rev. Fluid Mech.* **26**, 379–409.

Saric, W. S. 2007 Boundary-Layer Stability and Transition. In *Springer Handbook of Experimental Fluid Mechanics* (ed. C. Tropea, A. L. Yarin & J. F. Foss), pp. 886–896. Springer.

Saric, W. S., Carpenter, A. L. & Reed, H. L. 2011 Passive control of transition in three-dimensional boundary layers, with emphasis on discrete roughness elements. *Philos. T. R. Soc. A* **369**, 1352–1364.

Saric, W. S., Carrillo, R. B. & Reibert, M. S. 1998 Nonlinear stability and transition in 3-D boundary layers. *Meccanica* **33**, 469–487.

Saric, W. S., Reed, H. L. & Kerschen, E. J. 2002 Boundary-layer receptivity to freestream disturbances. *Annu. Rev. Fluid Mech.* **34**, 291–319.

Saric, W. S., Reed, H. L. & White, E. B. 2003 Stability and transition of three-dimensional boundary layers. *Annu. Rev. Fluid Mech.* **35**, 413–440.

Saric, W. S. & Reshotko, E. 1998 Review of flow quality issues in wind tunnel testing. *AIAA Paper* 98-2613.

Saric, W. S. & Yeates, L. G. 1985 Experiments on the stability of crossflow vortices in swept-wing flows. *AIAA Paper* 85-0493.

Schrader, L. U., Brandt, L. & Henningson, D. S. 2009 Receptivity mechanisms in three-dimensional boundary-layer flows. *J. Fluid Mech.* **618**, 209–241.

Schubauer, G. B. & Skramstad, H. K. 1947 Laminar boundary-layer oscillations and stability of laminar flow. *J. Aeronaut. Sci.* **14** (2), 69–78.

Suder, K. L., O'Brien, J. E. & Reshotko, E. 1988 Experimental Study of Bypass Transition in a Boundary Layer. *NASA-TM*-100913.

Takagi, S. & Itoh, N. 1994 Observation of traveling waves in the three-dimensional boundary layer along a yawed cylinder. *Fluid Dyn. Res.* **14**, 167–189.

Tan-atichat, J., Nagib, H. M. & Drubka, R. E. 1980 Effects of axisymmetric contractions on turbulence of various scales. *NASA CR*-165136.

Tempelmann, D. 2011 Receptivity of Crossflow-Dominated Boundary Layers. PhD thesis, Royal Institute of Technology.

Wassermann, P. & Kloker, M. 2002 Mechanisms and passive control of crossflow-vortex-induced transition in a three-dimensional boundary layer. *J. Fluid Mech.* **456**, 49–84.

Watmuff, J. H. 1998 Detrimental effects of almost immeasurably small freestream nonuniformities generated by wind-tunnel screens. *AIAA J.* **36** (3), 379–386.

Westin, K. J. A., Boiko, A. V., Klingmann, B. G. B., Kozlov, V. V. & Alfredsson, P. H. 1994 Experiments in a boundary layer subjected to free stream turbulence. Part 1. Boundary layer structure and receptivity. *J. Fluid Mech.* **281**, 193–218.

White, E. B. 2000 Breakdown of Crossflow Vortices. PhD thesis, Arizona State University.

White, E. B. & Ergin, F. G. 2004 Using laminar-flow velocity profiles to locate the wall behind roughness elements. *Exp. Fluids* **36**, 805–812.

White, E. B., Kutz, D., Freels, J., Hidore, J. P., Grife, R., Sun, Y. & Chao, D. 2011 Leading-edge roughness effects on 63_3-418 airfoil performance. *AIAA Paper* 2011-0352.

White, E. B. & Saric, W. S. 2005 Secondary instability of crossflow vortices. *J. Fluid Mech.* **525**, 275–308.

White, E. B., Saric, W. S., Gladden, R. D. & Gabet, P. M. 2001 Stages of swept-wing transition. *AIAA Paper* 2001-0271.

White, F. M. 1991 *Viscous Fluid Flow*, 2nd edn. McGraw-Hill.

Wlezien, R. W., Spencer, S. A. & Grubb, J. P. 1994 Comparison of flow quality in subsonic pressure tunnels. *AIAA Paper* 94-2503.

Woodruff, M. J., Saric, W. S. & Reed, H. L. 2011 Receptivity measurements on a swept-wing model. *AIAA Paper* 2011-3882.

APPENDIX A

BOUNDARY-LAYER PLOTS: BASELINE ROUGHNESS

	Tu		
x/c	0.02%	0.05%	0.19%
0.10	•	•	•
0.15	•		
0.20	•		
0.25	•	•	•
0.30	•		
0.35	•		
0.40	•	•	•
0.45	•		
0.50	•	•	•
0.60	•		

Table A.1: Test matrix for nominally smooth leading edge: boundary-layer scans at $Re_c = 2.8 \times 10^6$.

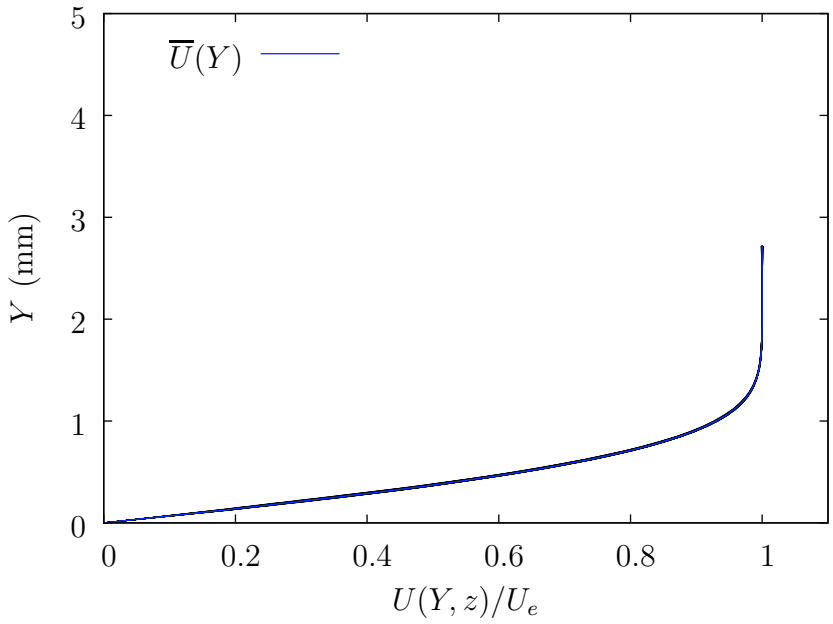

Figure A.1: Boundary-layer profiles at $x/c = 0.10$, $Re_c = 2.8 \times 10^6$, $Tu = 0.02\%$, clean leading edge.

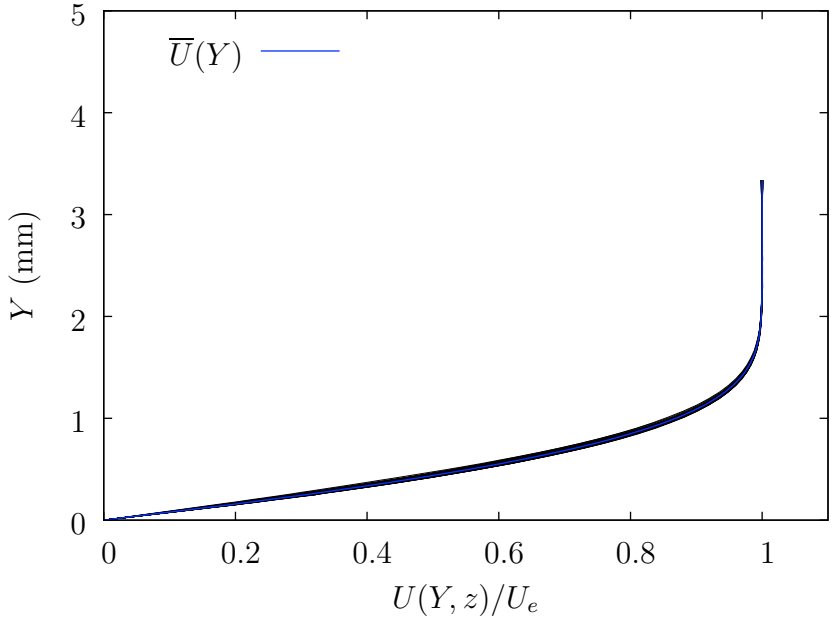

Figure A.2: Boundary-layer profiles at $x/c = 0.15$, $Re_c = 2.8 \times 10^6$, $Tu = 0.02\%$, clean leading edge.

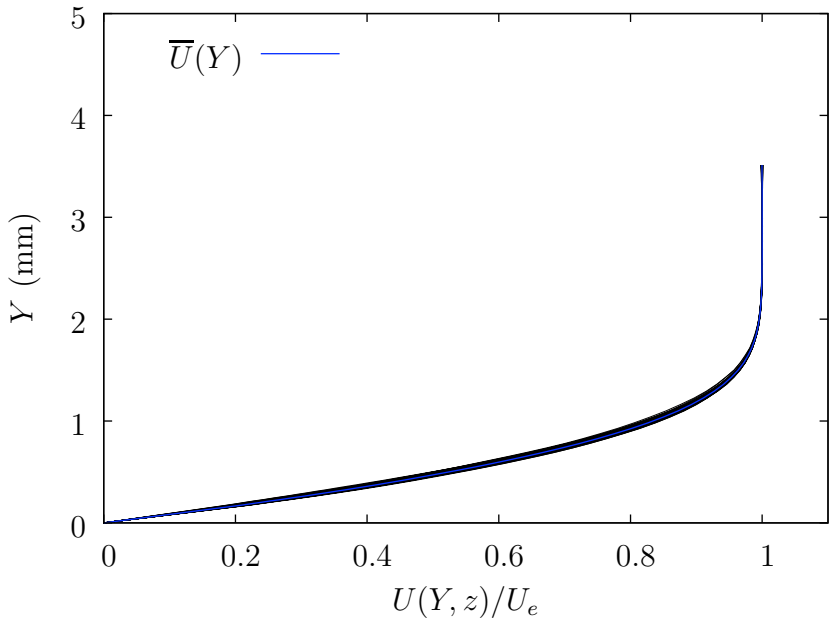

Figure A.3: Boundary-layer profiles at $x/c = 0.20$, $Re_c = 2.8 \times 10^6$, $Tu = 0.02\%$, clean leading edge.

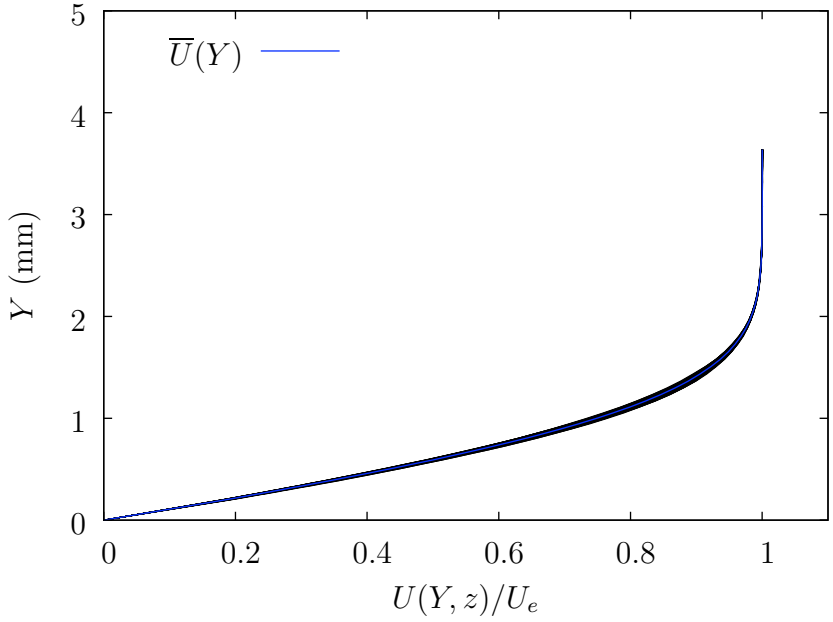

Figure A.4: Boundary-layer profiles at $x/c = 0.25$, $Re_c = 2.8 \times 10^6$, $Tu = 0.02\%$, clean leading edge.

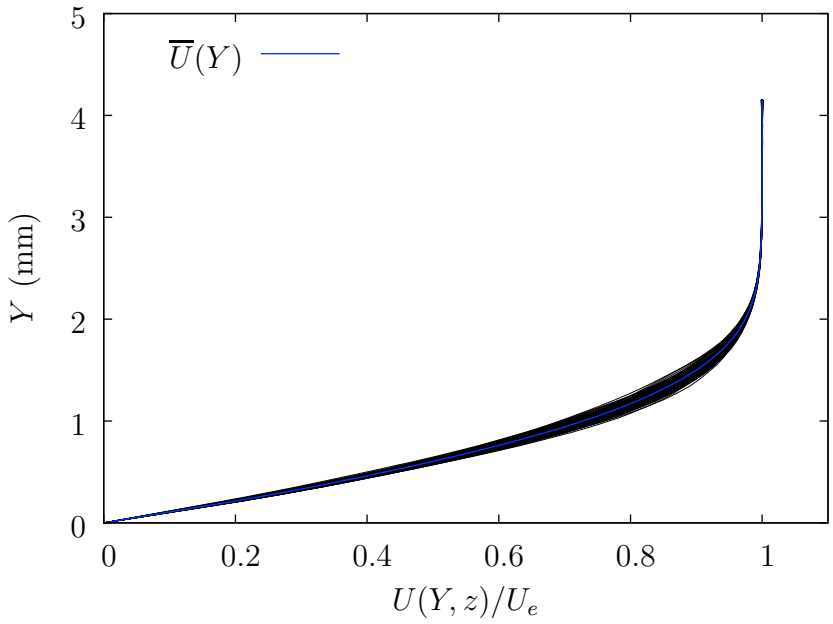

Figure A.5: Boundary-layer profiles at $x/c = 0.30$, $Re_c = 2.8 \times 10^6$, $Tu = 0.02\%$, clean leading edge.

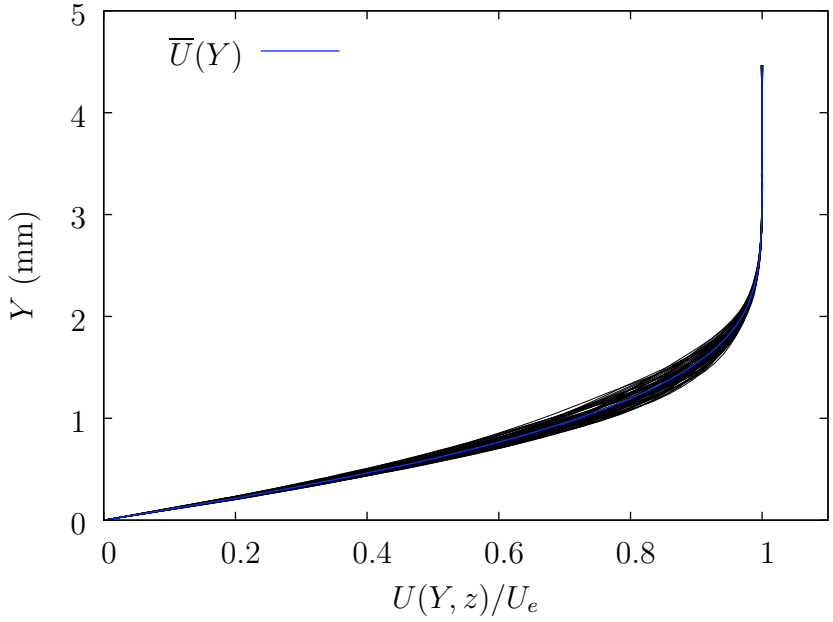

Figure A.6: Boundary-layer profiles at $x/c = 0.35$, $Re_c = 2.8 \times 10^6$, $Tu = 0.02\%$, clean leading edge.

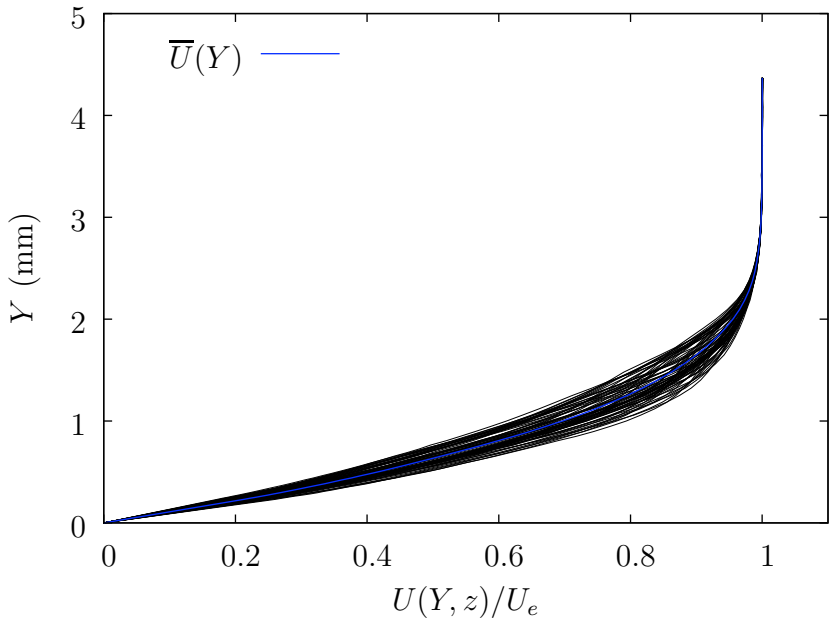

Figure A.7: Boundary-layer profiles at $x/c = 0.40$, $Re_c = 2.8 \times 10^6$, $Tu = 0.02\%$, clean leading edge.

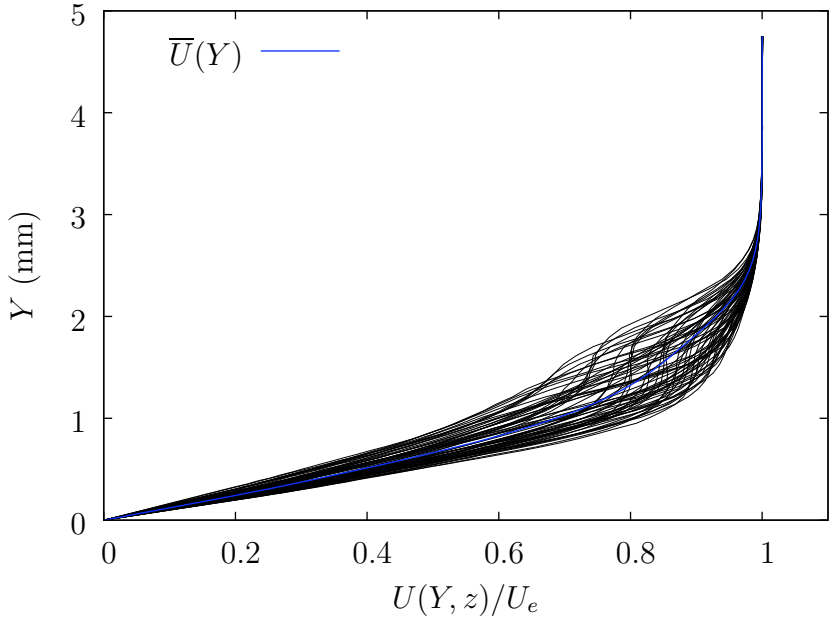

Figure A.8: Boundary-layer profiles at $x/c = 0.45$, $Re_c = 2.8 \times 10^6$, $Tu = 0.02\%$, clean leading edge.

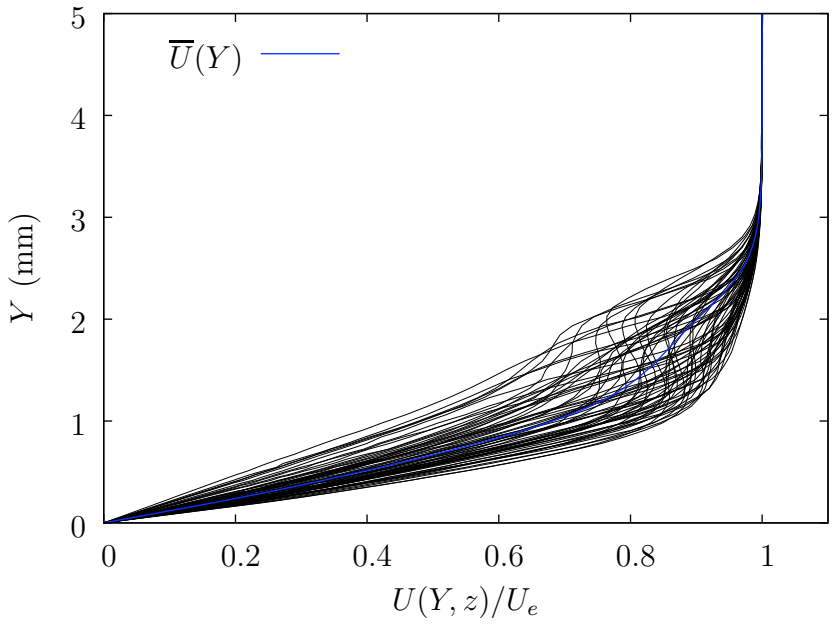

Figure A.9: Boundary-layer profiles at $x/c = 0.50$, $Re_c = 2.8 \times 10^6$, $Tu = 0.02\%$, clean leading edge.

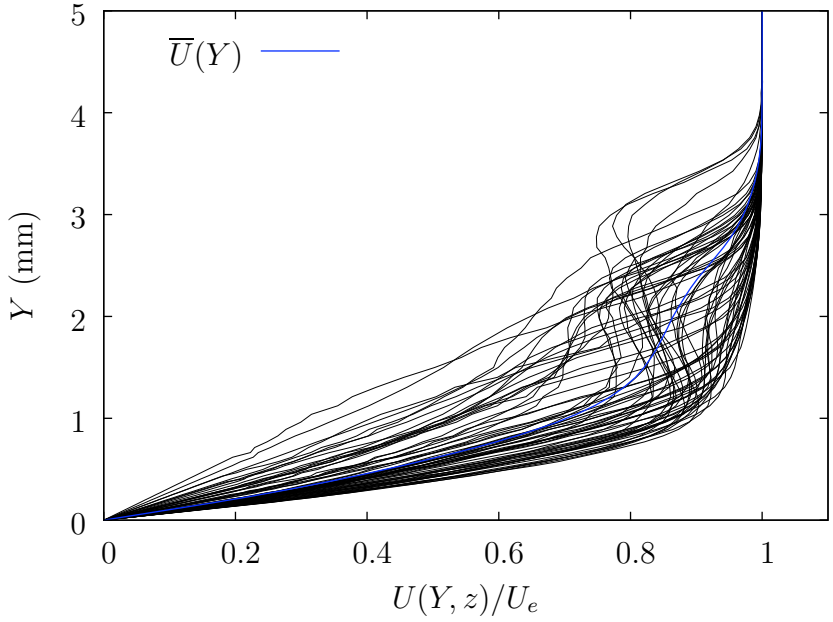

Figure A.10: Boundary-layer profiles at $x/c = 0.60$, $Re_c = 2.8 \times 10^6$, $Tu = 0.02\%$, clean leading edge.

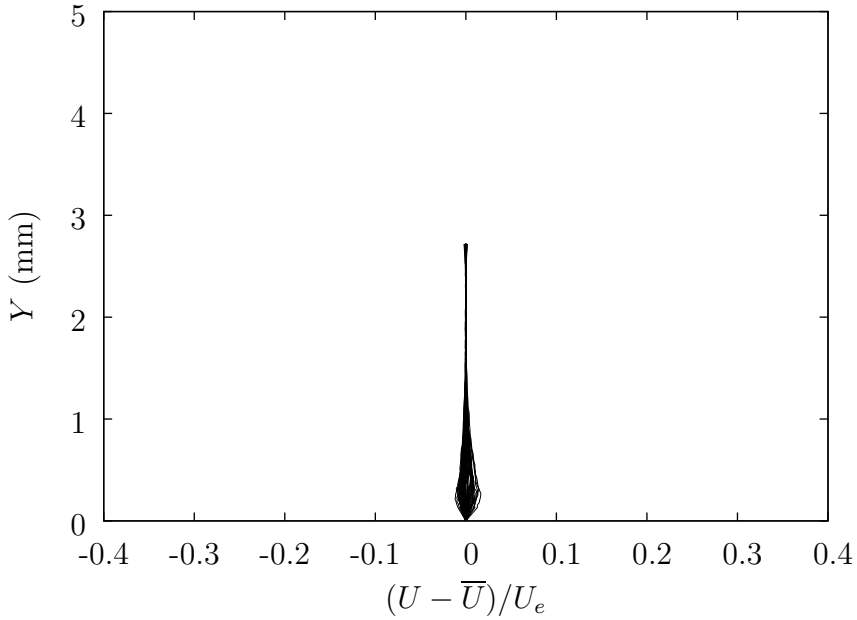

Figure A.11: Steady disturbance profiles at $x/c = 0.10$, $Re_c = 2.8 \times 10^6$, $Tu = 0.02\%$, clean leading edge.

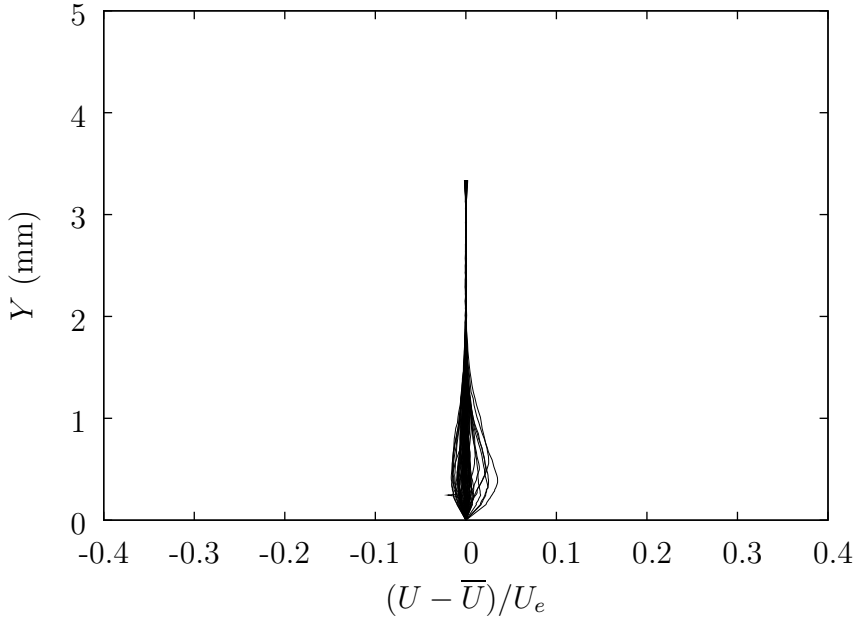

Figure A.12: Steady disturbance profiles at $x/c = 0.15$, $Re_c = 2.8 \times 10^6$, $Tu = 0.02\%$, clean leading edge.

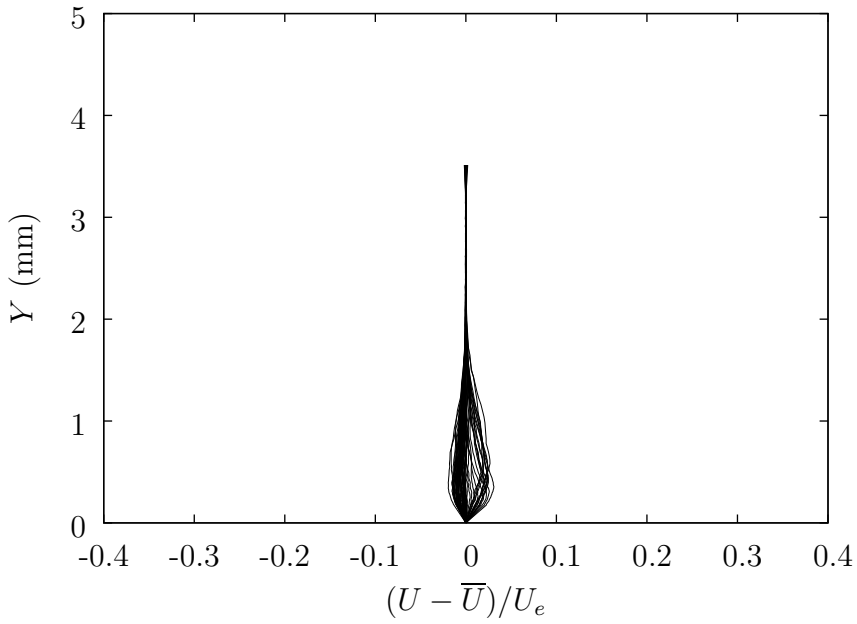

Figure A.13: Steady disturbance profiles at $x/c = 0.20$, $Re_c = 2.8 \times 10^6$, $Tu = 0.02\%$, clean leading edge.

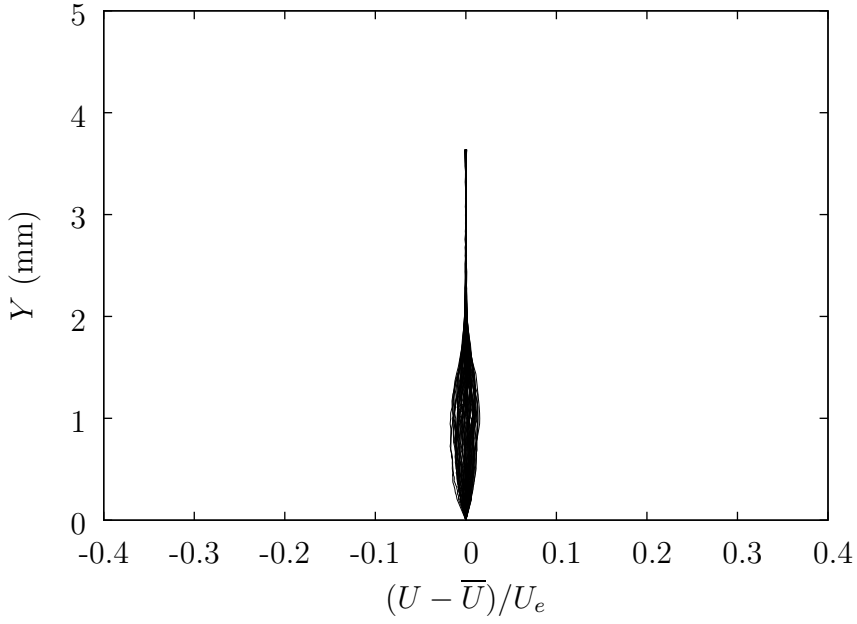

Figure A.14: Steady disturbance profiles at $x/c = 0.25$, $Re_c = 2.8 \times 10^6$, $Tu = 0.02\%$, clean leading edge.

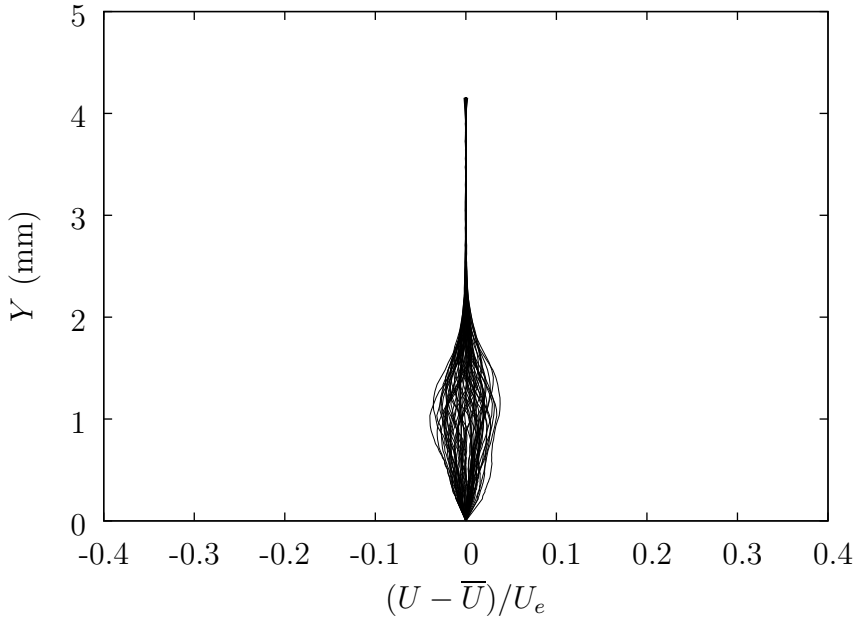

Figure A.15: Steady disturbance profiles at $x/c = 0.30$, $Re_c = 2.8 \times 10^6$, $Tu = 0.02\%$, clean leading edge.

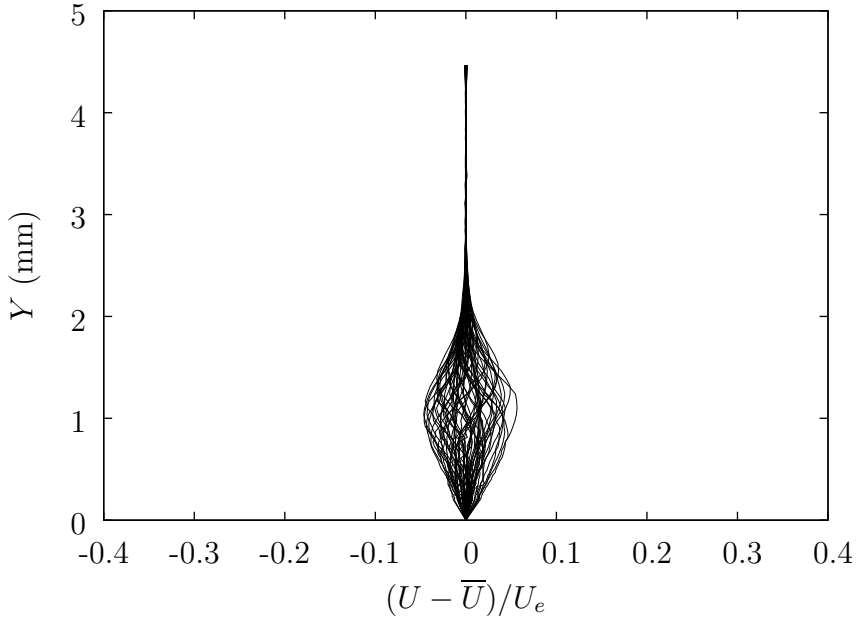

Figure A.16: Steady disturbance profiles at $x/c = 0.35$, $Re_c = 2.8 \times 10^6$, $Tu = 0.02\%$, clean leading edge.

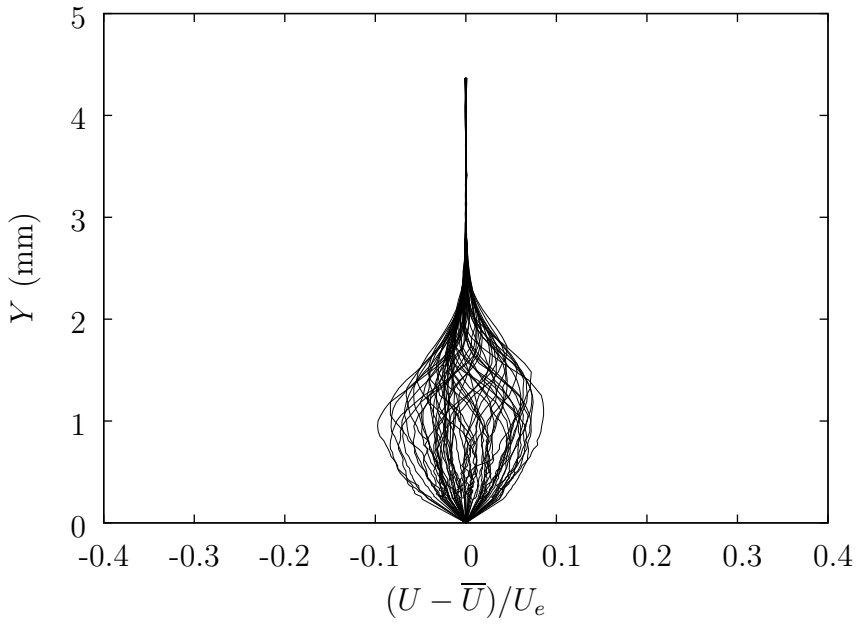

Figure A.17: Steady disturbance profiles at $x/c = 0.40$, $Re_c = 2.8 \times 10^6$, $Tu = 0.02\%$, clean leading edge.

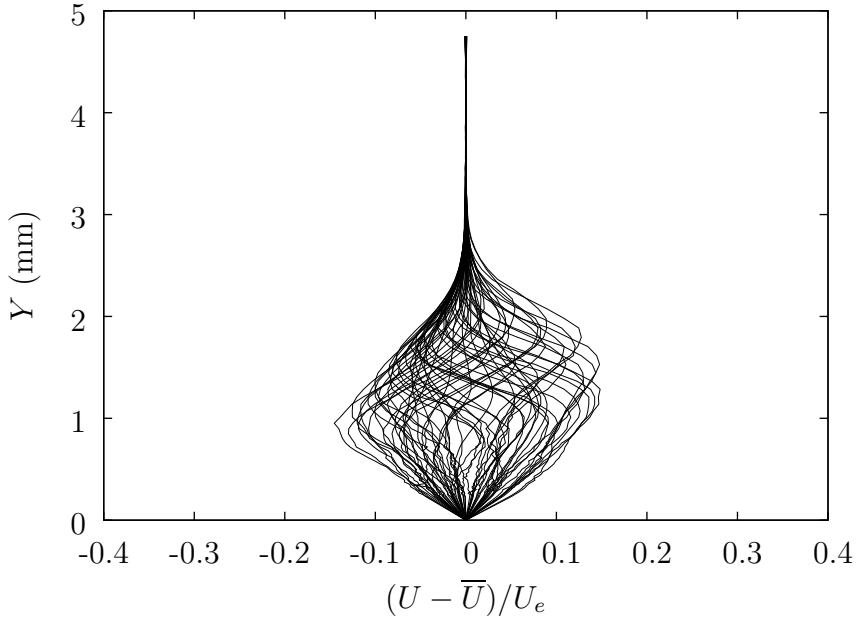

Figure A.18: Steady disturbance profiles at $x/c = 0.45$, $Re_c = 2.8 \times 10^6$, $Tu = 0.02\%$, clean leading edge.

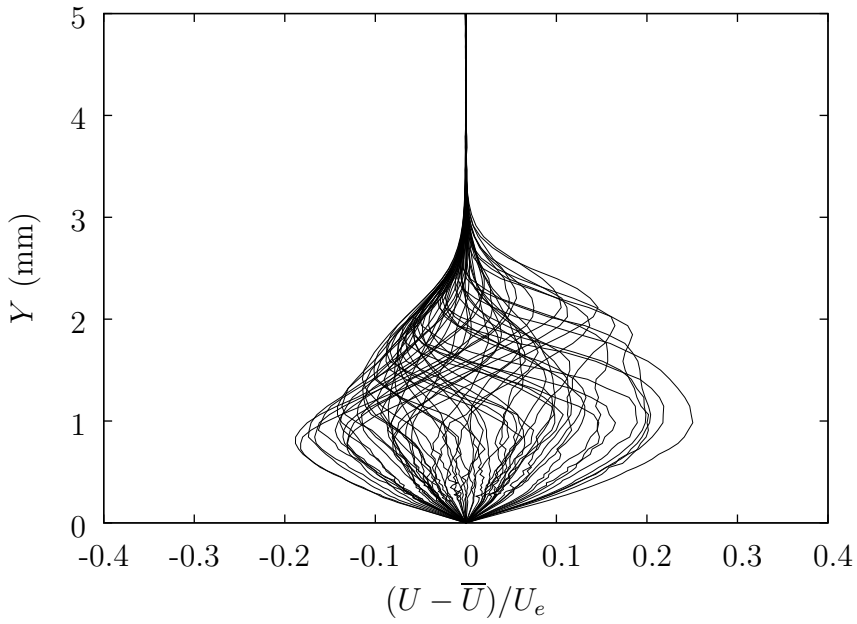

Figure A.19: Steady disturbance profiles at $x/c = 0.50$, $Re_c = 2.8 \times 10^6$, $Tu = 0.02\%$, clean leading edge.

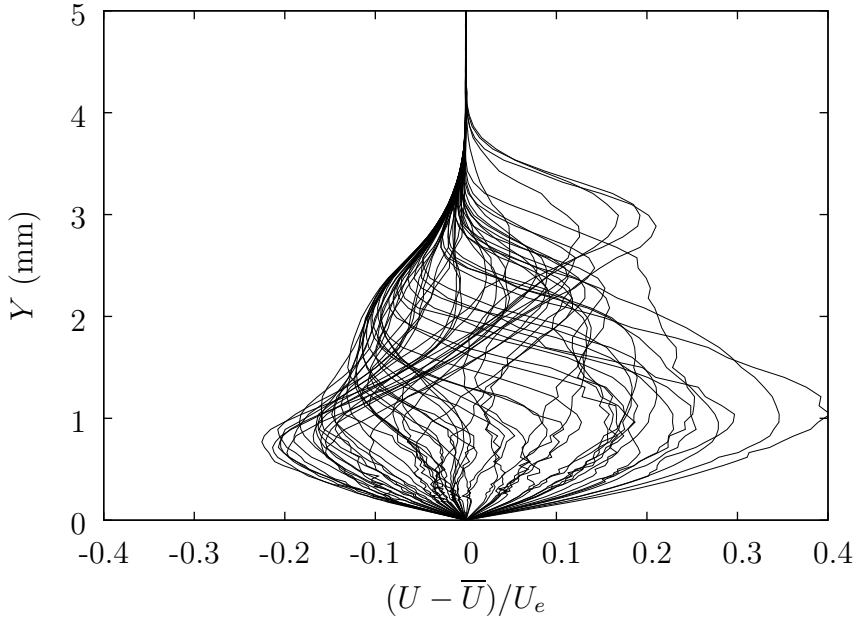

Figure A.20: Steady disturbance profiles at $x/c = 0.60$, $Re_c = 2.8 \times 10^6$, $Tu = 0.02\%$, clean leading edge.

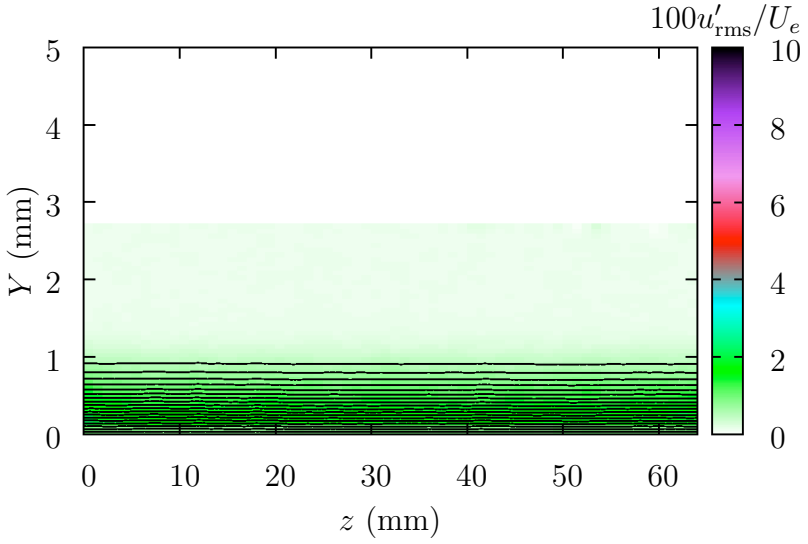

Figure A.21: U and u'_{rms} contours at $x/c = 0.10$, $Re_c = 2.8 \times 10^6$, $Tu = 0.02\%$, clean leading edge.

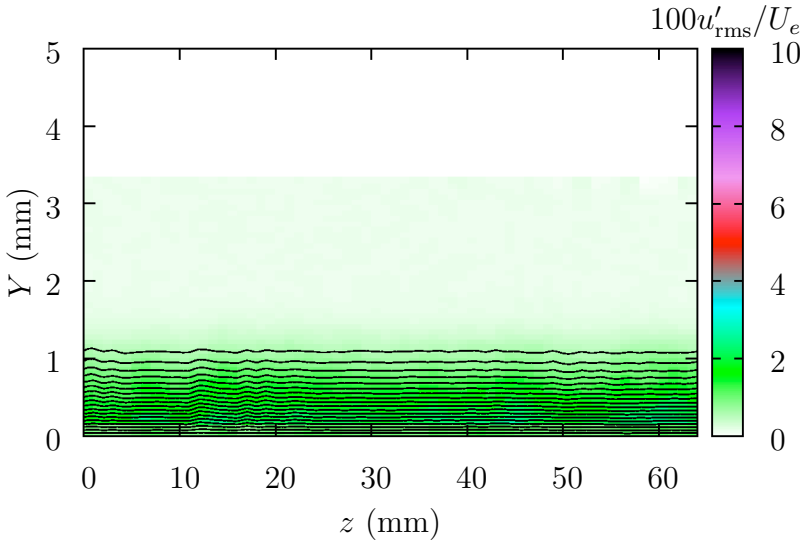

Figure A.22: U and u'_{rms} contours at $x/c = 0.15$, $Re_c = 2.8 \times 10^6$, $Tu = 0.02\%$, clean leading edge.

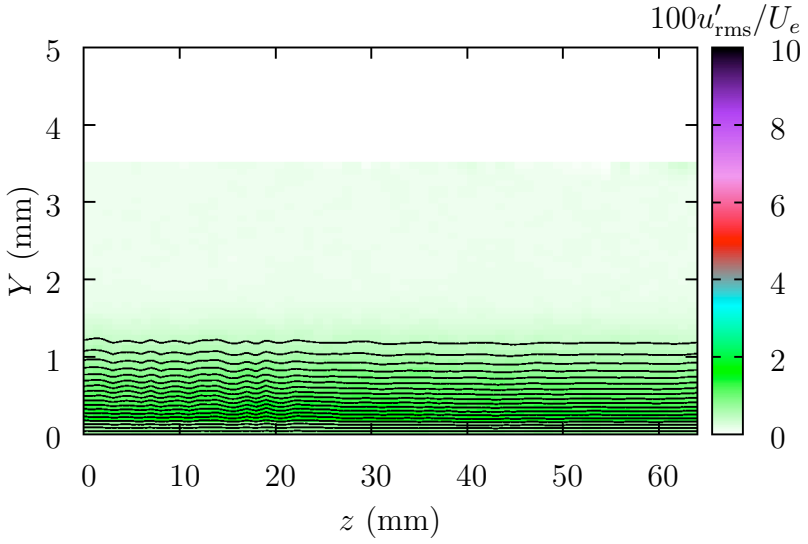

Figure A.23: U and u'_{rms} contours at $x/c = 0.20$, $Re_c = 2.8 \times 10^6$, $Tu = 0.02\%$, clean leading edge.

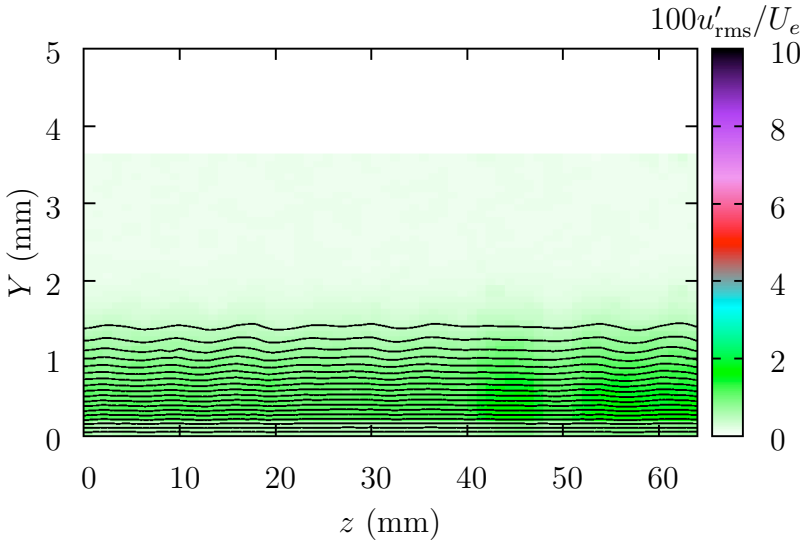

Figure A.24: U and u'_{rms} contours at $x/c = 0.25$, $Re_c = 2.8 \times 10^6$, $Tu = 0.02\%$, clean leading edge.

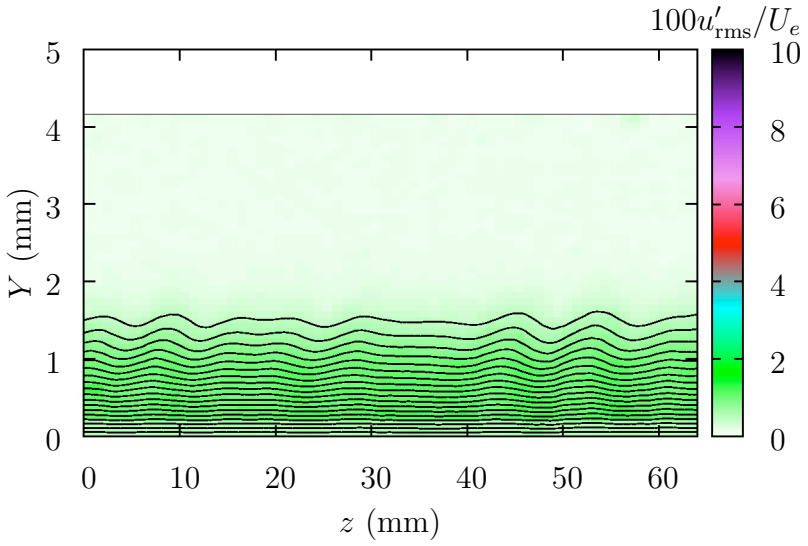

Figure A.25: U and u'_{rms} contours at $x/c = 0.30$, $Re_c = 2.8 \times 10^6$, $Tu = 0.02\%$, clean leading edge.

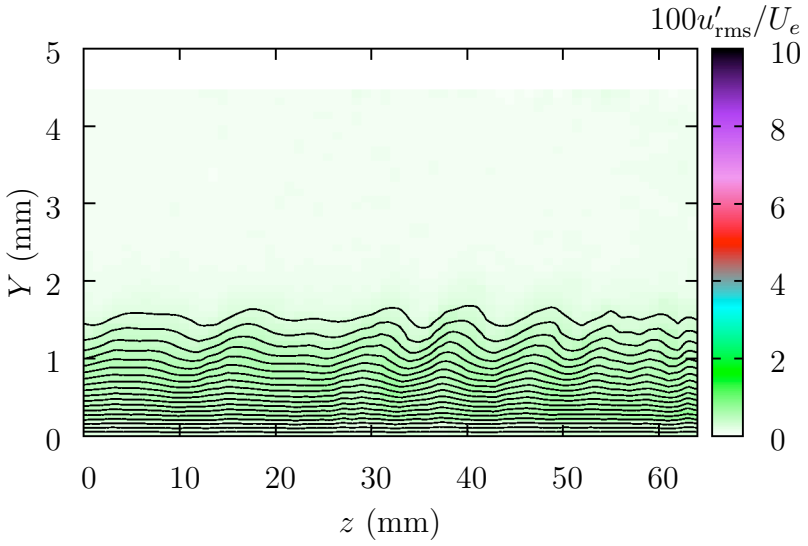

Figure A.26: U and u'_{rms} contours at $x/c = 0.35$, $Re_c = 2.8 \times 10^6$, $Tu = 0.02\%$, clean leading edge.

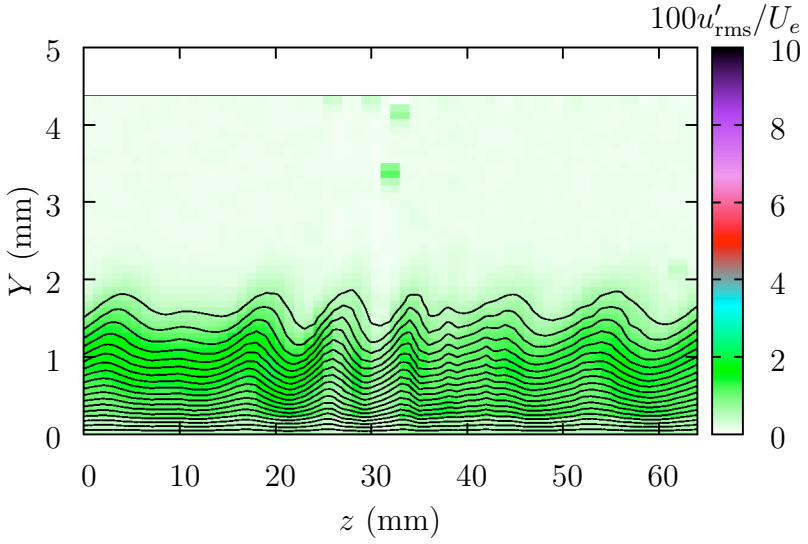

Figure A.27: U and u'_{rms} contours at $x/c = 0.40$, $Re_c = 2.8 \times 10^6$, $Tu = 0.02\%$, clean leading edge.

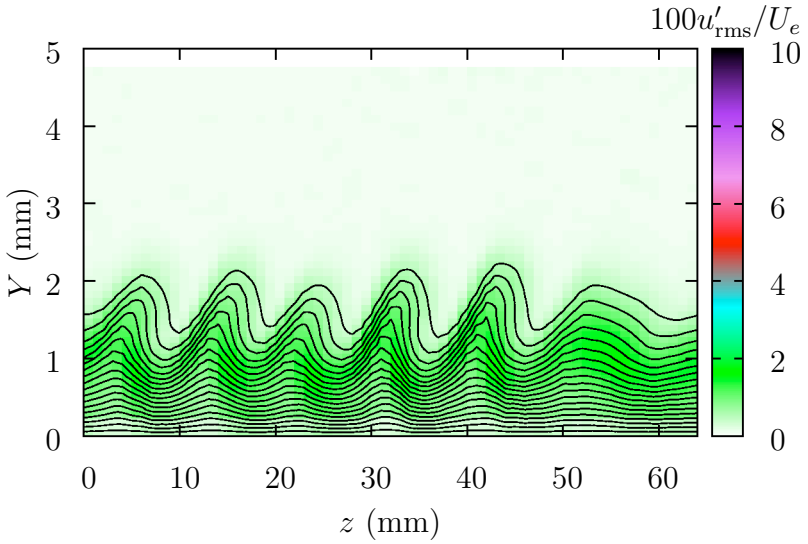

Figure A.28: U and u'_{rms} contours at $x/c = 0.45$, $Re_c = 2.8 \times 10^6$, $Tu = 0.02\%$, clean leading edge.

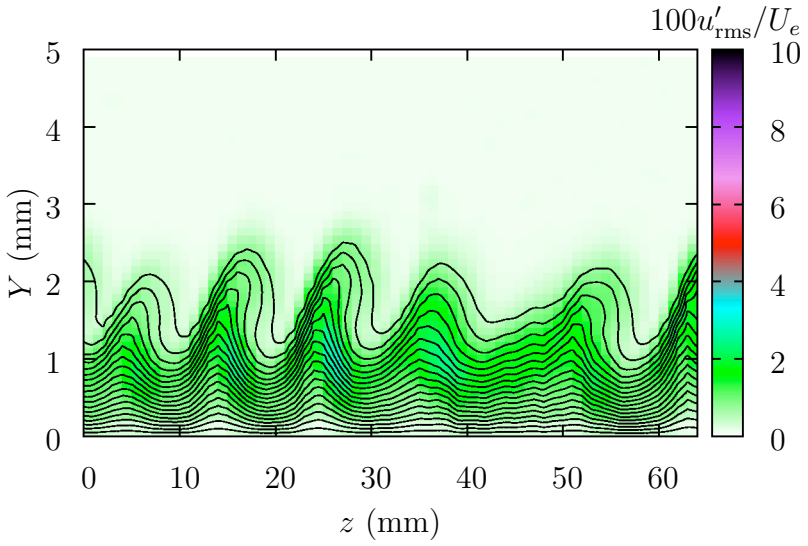

Figure A.29: U and u'_{rms} contours at $x/c = 0.50$, $Re_c = 2.8 \times 10^6$, $Tu = 0.02\%$, clean leading edge.

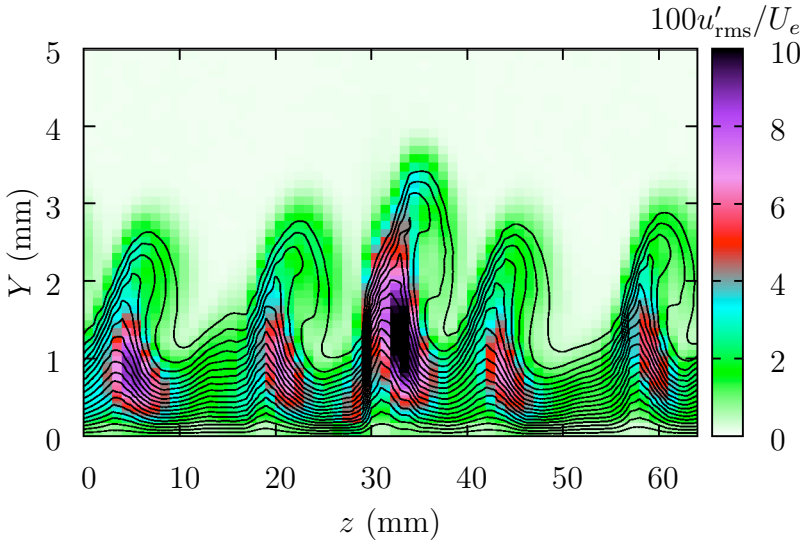

Figure A.30: U and u'_{rms} contours at $x/c = 0.60$, $Re_c = 2.8 \times 10^6$, $Tu = 0.02\%$, clean leading edge.

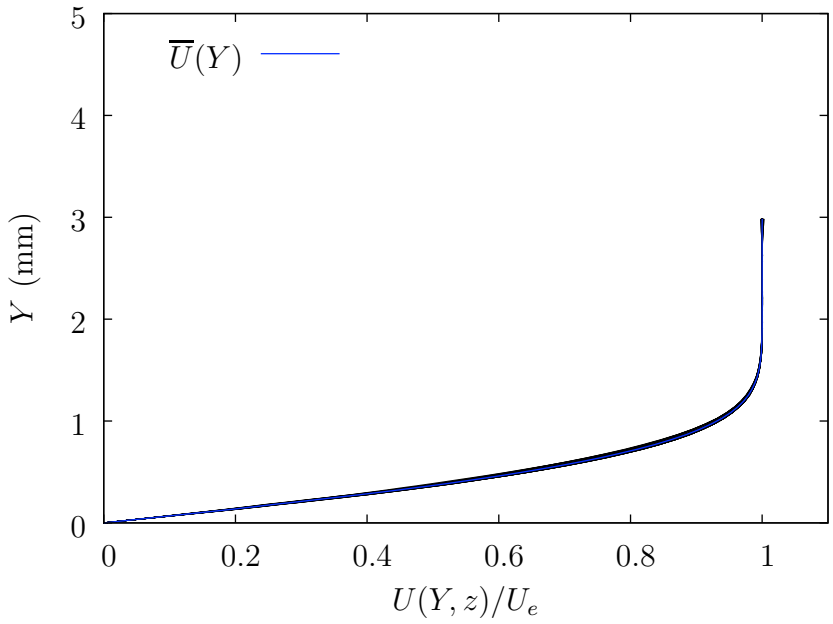

Figure A.31: Boundary-layer profiles at $x/c = 0.10$, $Re_c = 2.8 \times 10^6$, $Tu = 0.05\%$, clean leading edge.

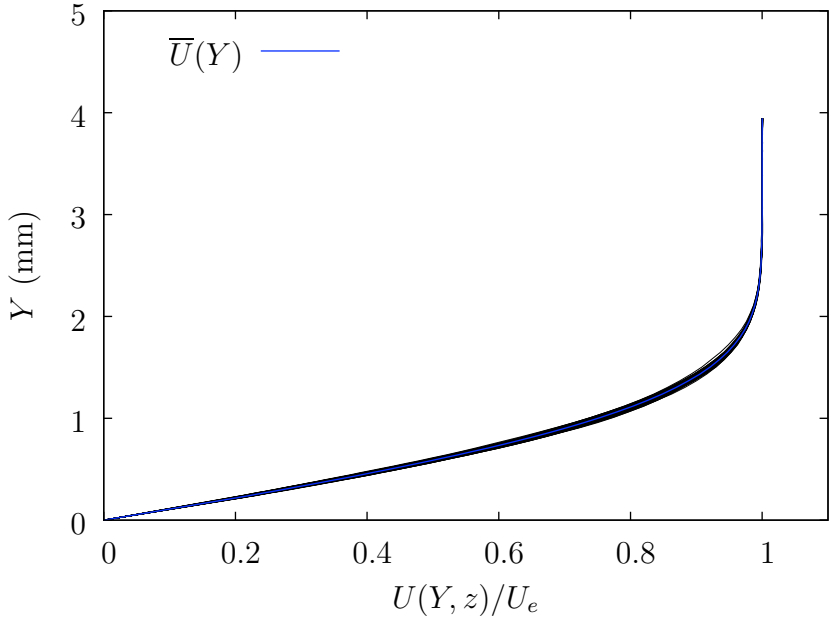

Figure A.32: Boundary-layer profiles at $x/c = 0.25$, $Re_c = 2.8 \times 10^6$, $Tu = 0.05\%$, clean leading edge.

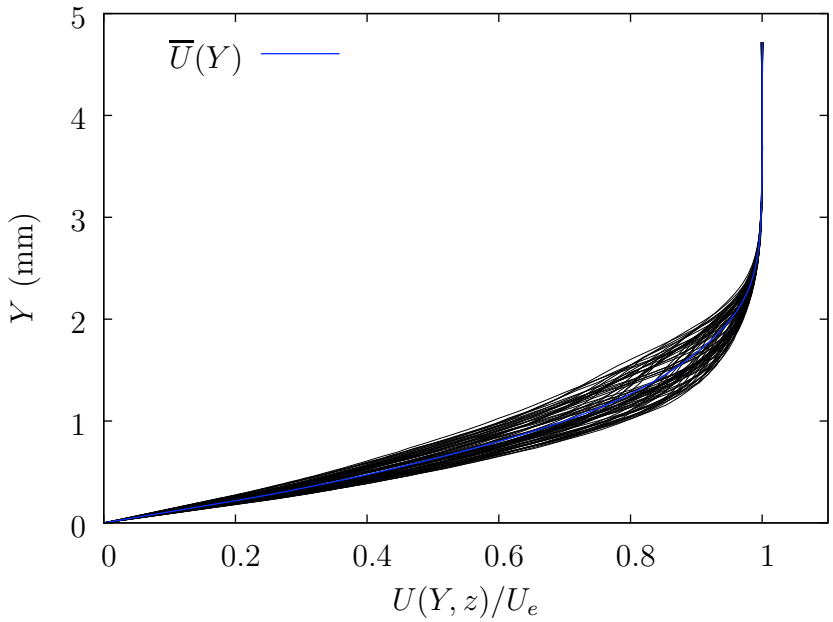

Figure A.33: Boundary-layer profiles at $x/c = 0.40$, $Re_c = 2.8 \times 10^6$, $Tu = 0.05\%$, clean leading edge.

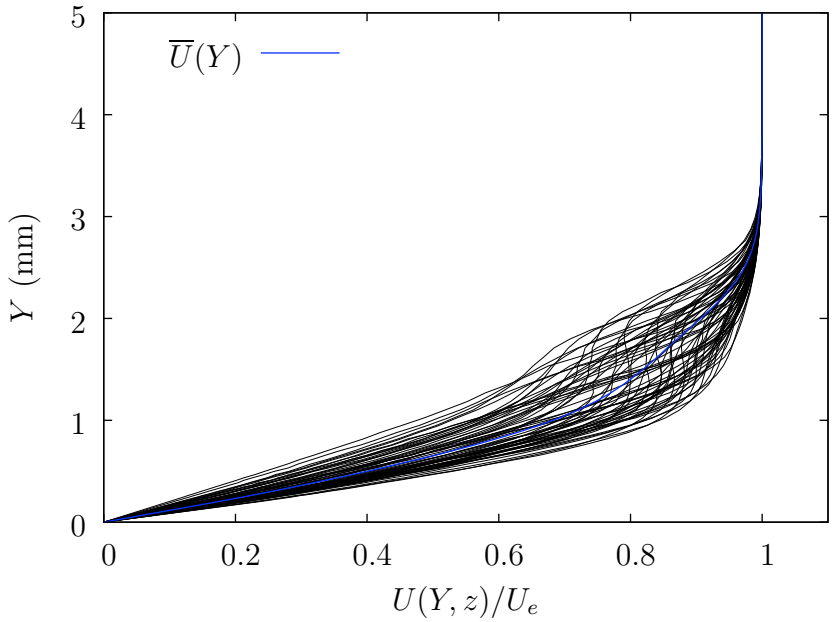

Figure A.34: Boundary-layer profiles at $x/c = 0.50$, $Re_c = 2.8 \times 10^6$, $Tu = 0.05\%$, clean leading edge.

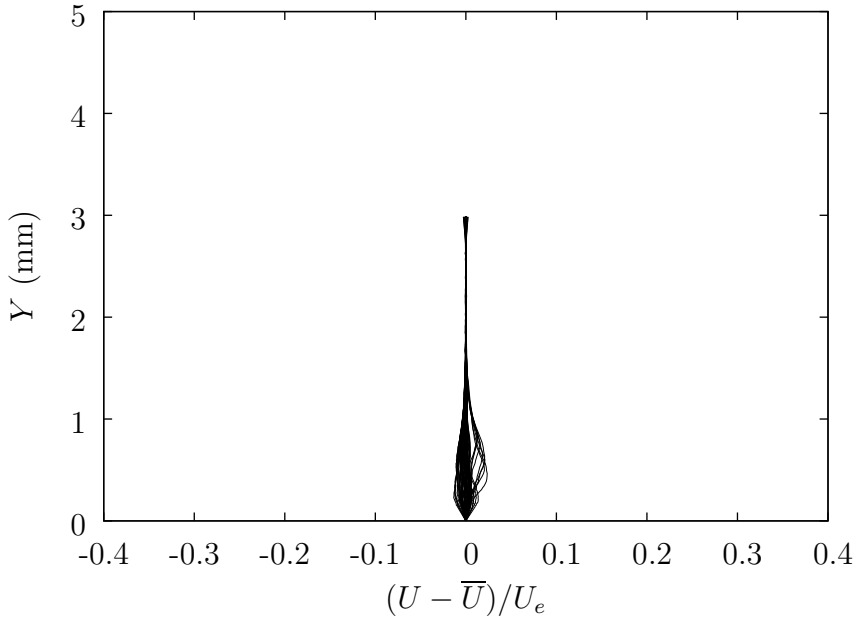

Figure A.35: Steady disturbance profiles at $x/c = 0.10$, $Re_c = 2.8 \times 10^6$, $Tu = 0.05\%$, clean leading edge.

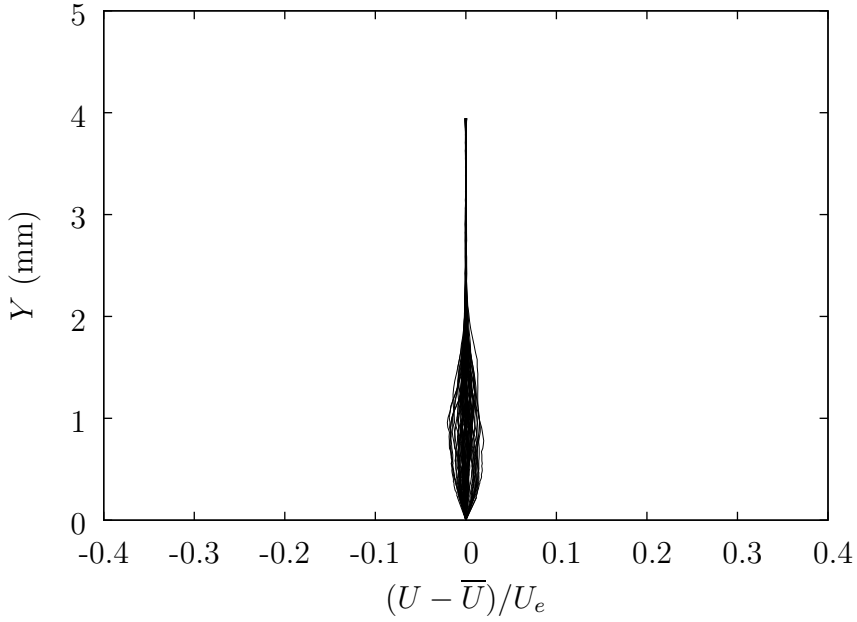

Figure A.36: Steady disturbance profiles at $x/c = 0.25$, $Re_c = 2.8 \times 10^6$, $Tu = 0.05\%$, clean leading edge.

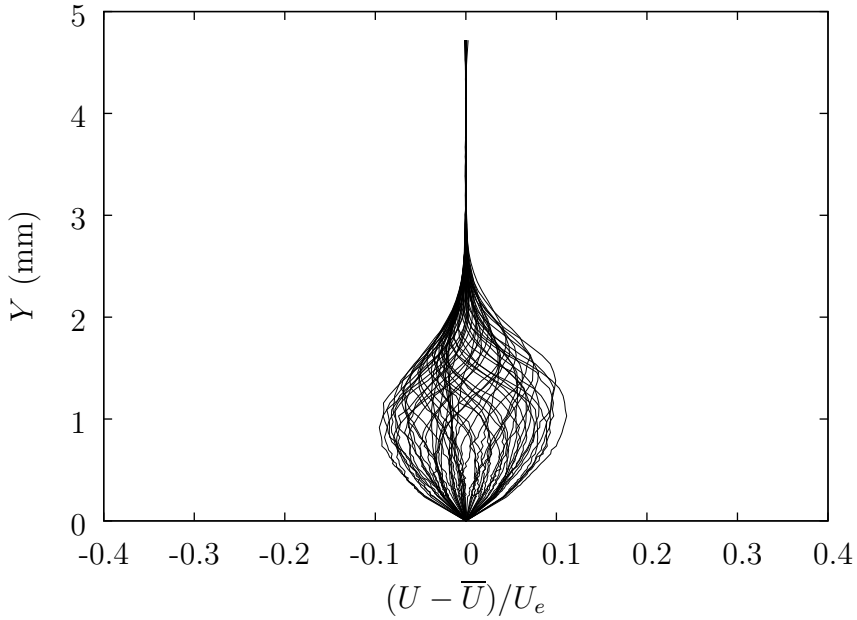

Figure A.37: Steady disturbance profiles at $x/c = 0.40$, $Re_c = 2.8 \times 10^6$, $Tu = 0.05\%$, clean leading edge.

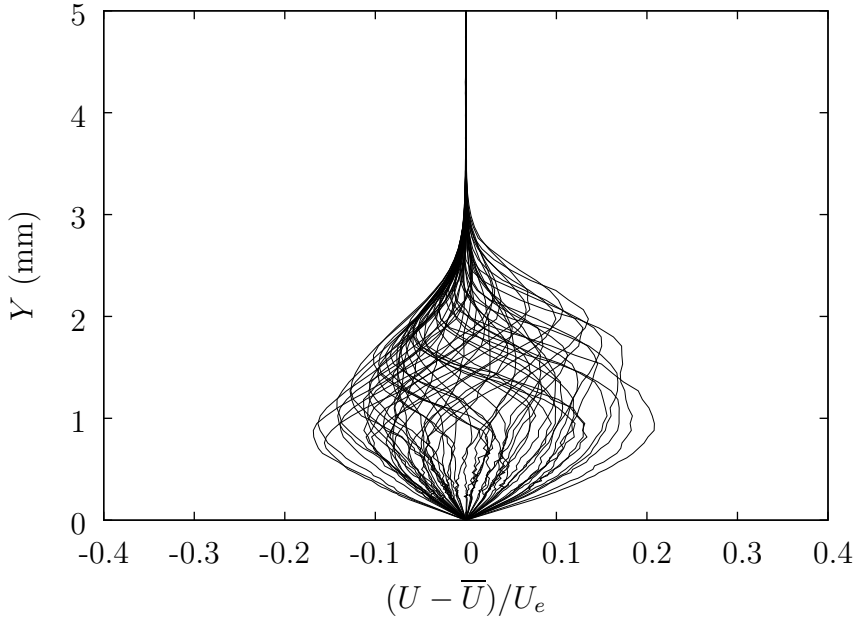

Figure A.38: Steady disturbance profiles at $x/c = 0.50$, $Re_c = 2.8 \times 10^6$, $Tu = 0.05\%$, clean leading edge.

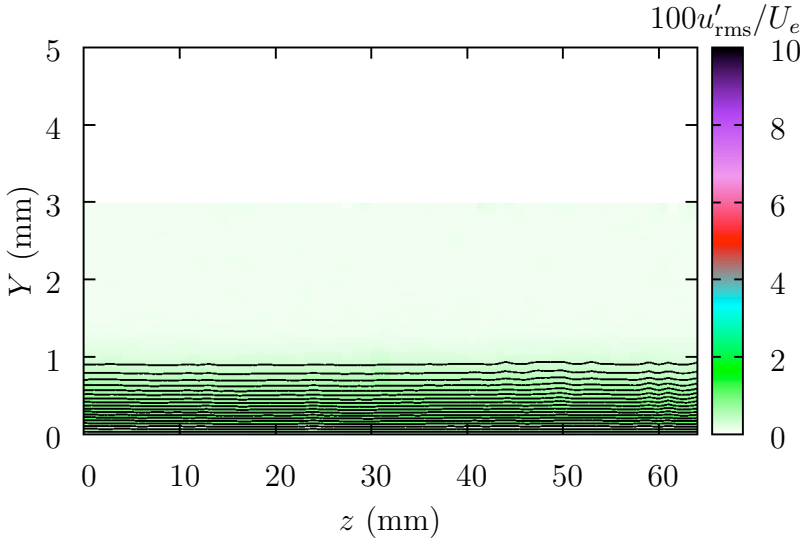

Figure A.39: U and u'_{rms} contours at $x/c = 0.10$, $Re_c = 2.8 \times 10^6$, $Tu = 0.05\%$, clean leading edge.

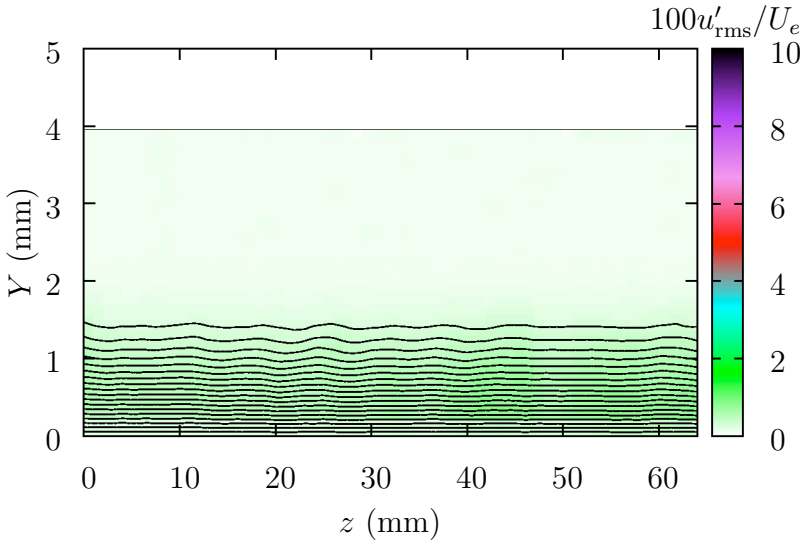

Figure A.40: U and u'_{rms} contours at $x/c = 0.25$, $Re_c = 2.8 \times 10^6$, $Tu = 0.05\%$, clean leading edge.

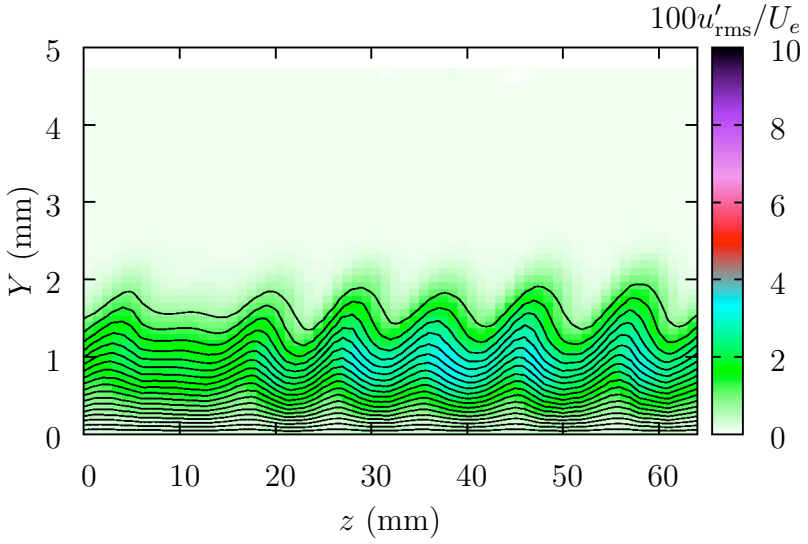

Figure A.41: U and u'_{rms} contours at $x/c = 0.40$, $Re_c = 2.8 \times 10^6$, $Tu = 0.05\%$, clean leading edge.

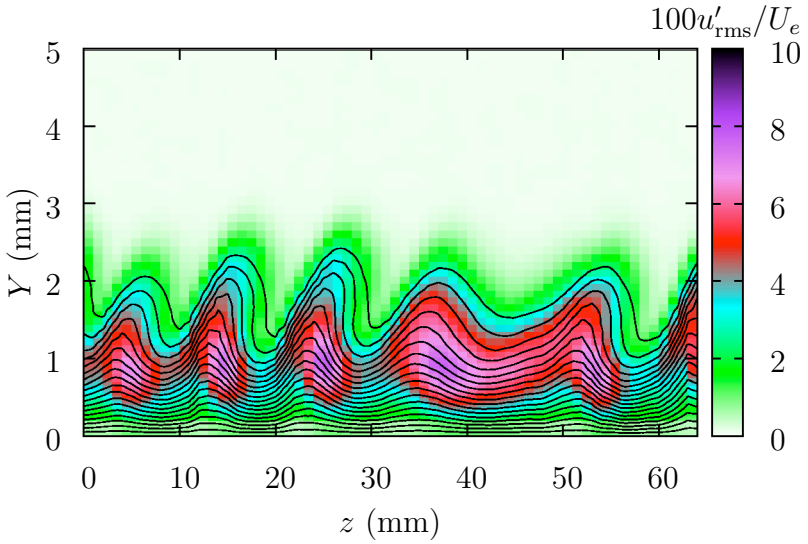

Figure A.42: U and u'_{rms} contours at $x/c = 0.50$, $Re_c = 2.8 \times 10^6$, $Tu = 0.05\%$, clean leading edge.

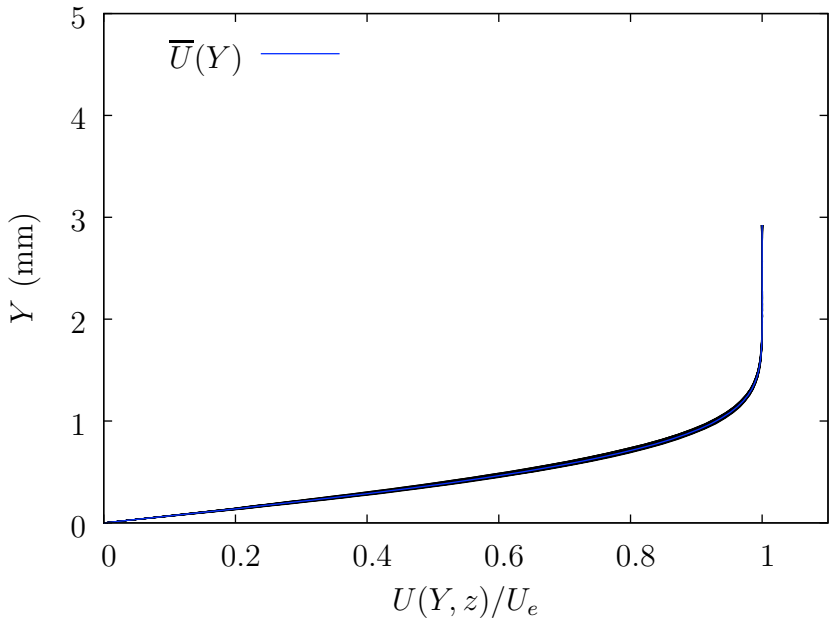

Figure A.43: Boundary-layer profiles at $x/c = 0.10$, $Re_c = 2.8 \times 10^6$, $Tu = 0.19\%$, clean leading edge.

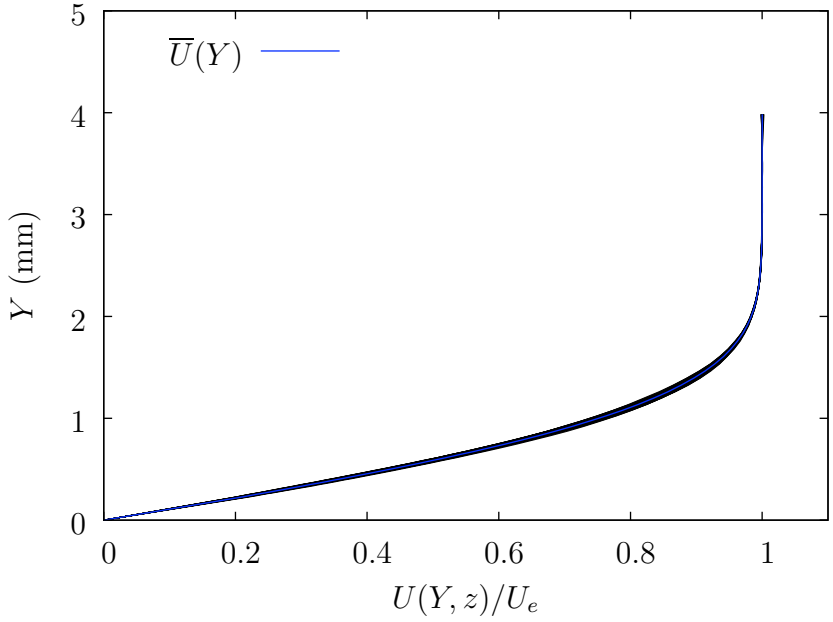

Figure A.44: Boundary-layer profiles at $x/c = 0.25$, $Re_c = 2.8 \times 10^6$, $Tu = 0.19\%$, clean leading edge.

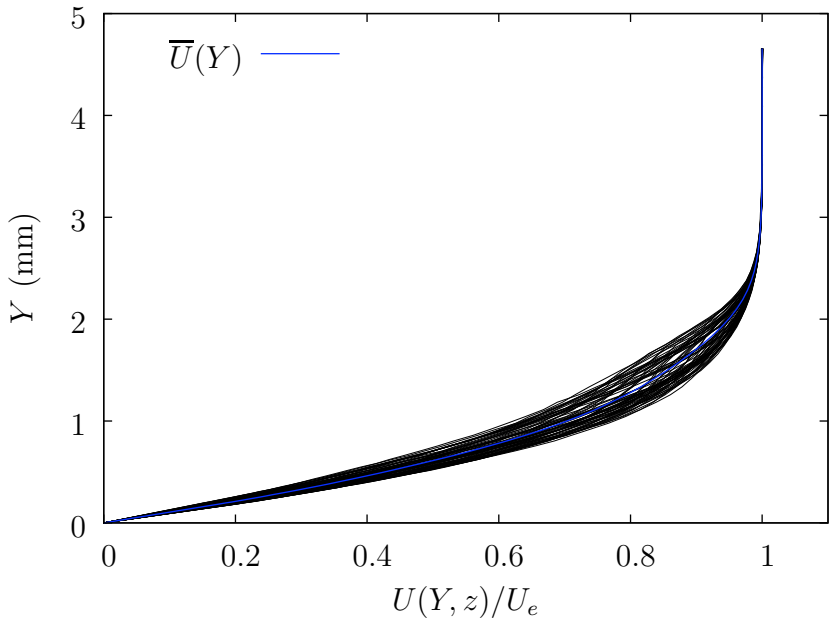

Figure A.45: Boundary-layer profiles at $x/c = 0.40$, $Re_c = 2.8 \times 10^6$, $Tu = 0.19\%$, clean leading edge.

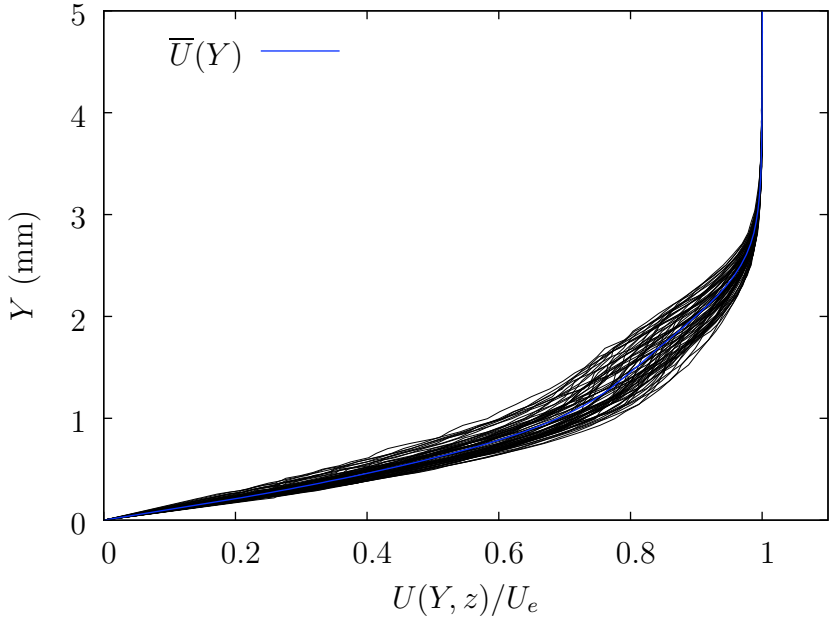

Figure A.46: Boundary-layer profiles at $x/c = 0.50$, $Re_c = 2.8 \times 10^6$, $Tu = 0.19\%$, clean leading edge.

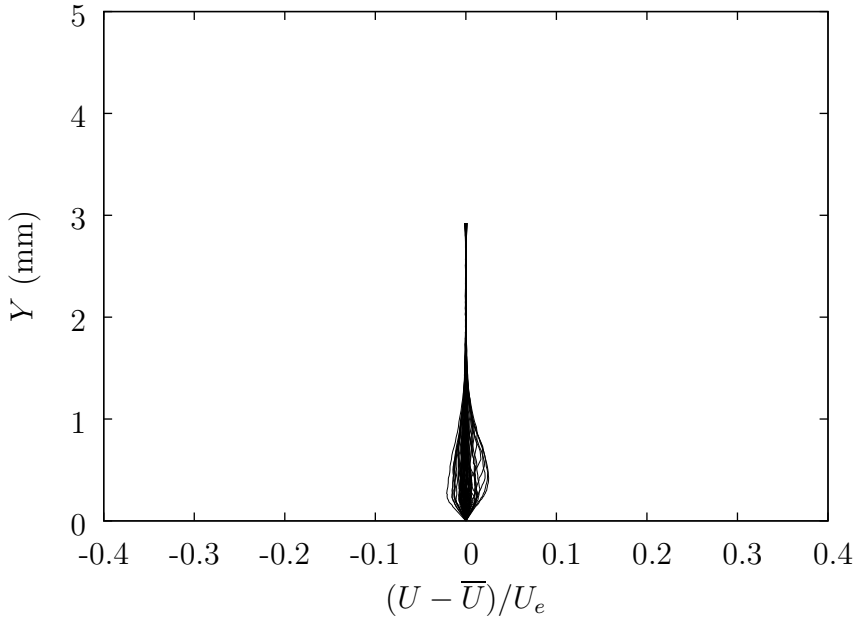

Figure A.47: Steady disturbance profiles at $x/c = 0.10$, $Re_c = 2.8 \times 10^6$, $Tu = 0.19\%$, clean leading edge.

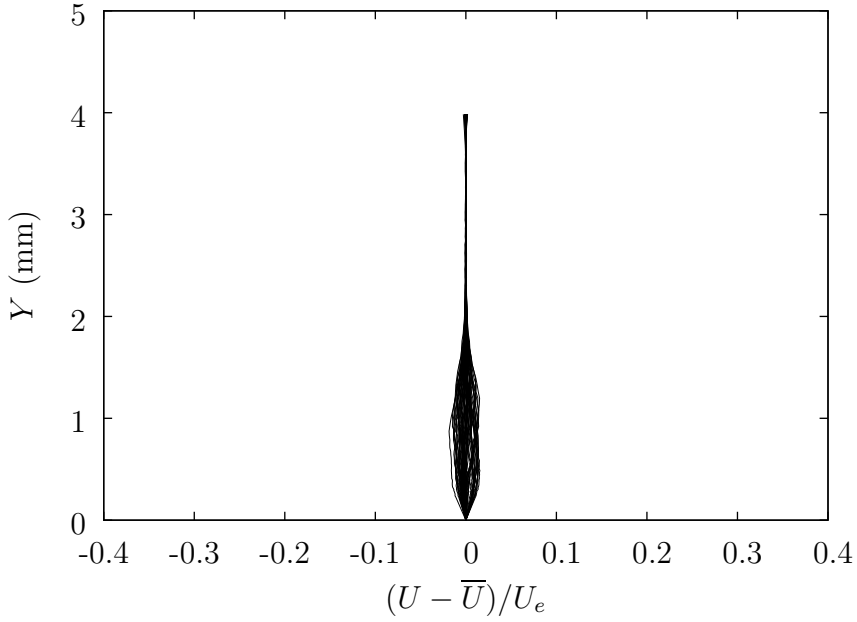

Figure A.48: Steady disturbance profiles at $x/c = 0.25$, $Re_c = 2.8 \times 10^6$, $Tu = 0.19\%$, clean leading edge.

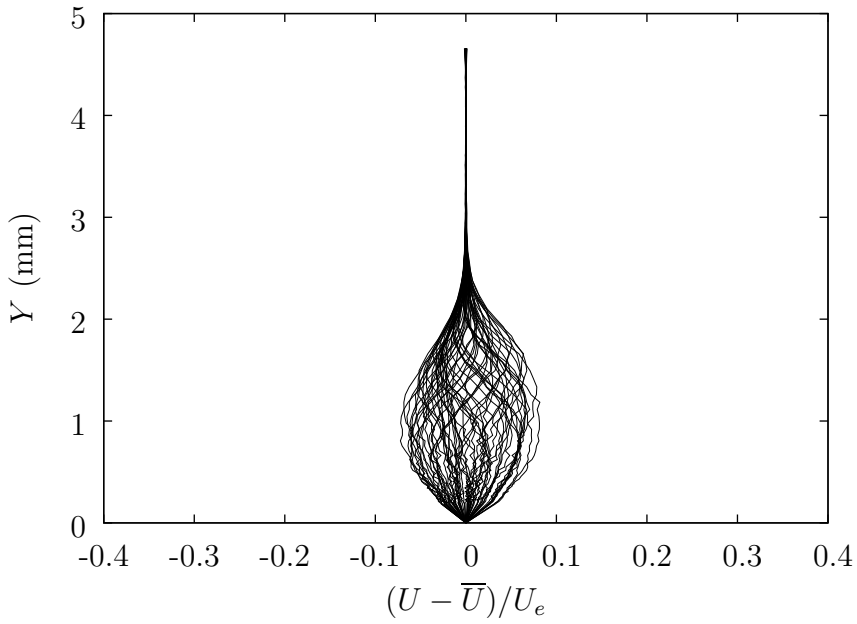

Figure A.49: Steady disturbance profiles at $x/c = 0.40$, $Re_c = 2.8 \times 10^6$, $Tu = 0.19\%$, clean leading edge.

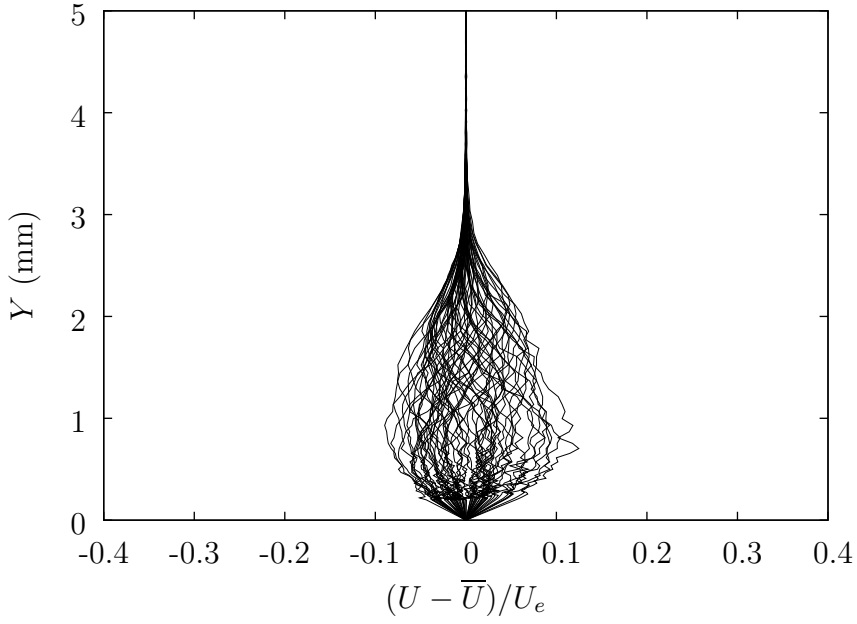

Figure A.50: Steady disturbance profiles at $x/c = 0.50$, $Re_c = 2.8 \times 10^6$, $Tu = 0.19\%$, clean leading edge.

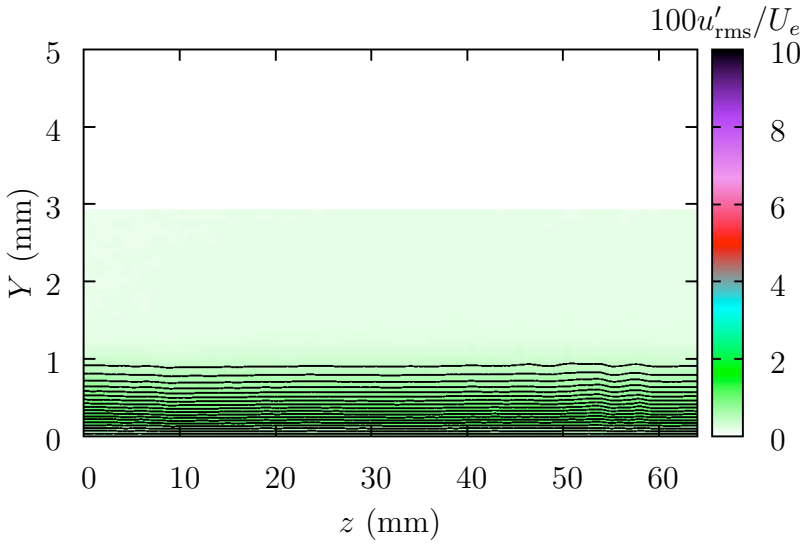

Figure A.51: U and u'_{rms} contours at $x/c = 0.10$, $Re_c = 2.8 \times 10^6$, $Tu = 0.19\%$, clean leading edge.

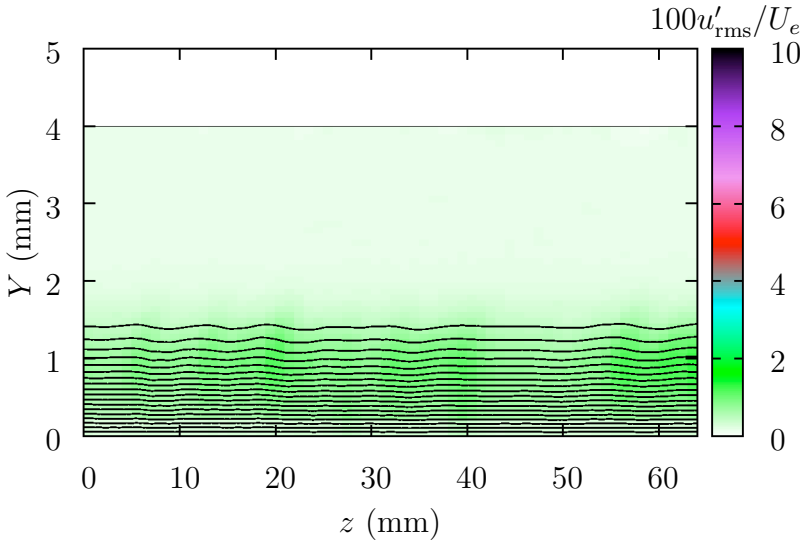

Figure A.52: U and u'_{rms} contours at $x/c = 0.25$, $Re_c = 2.8 \times 10^6$, $Tu = 0.19\%$, clean leading edge.

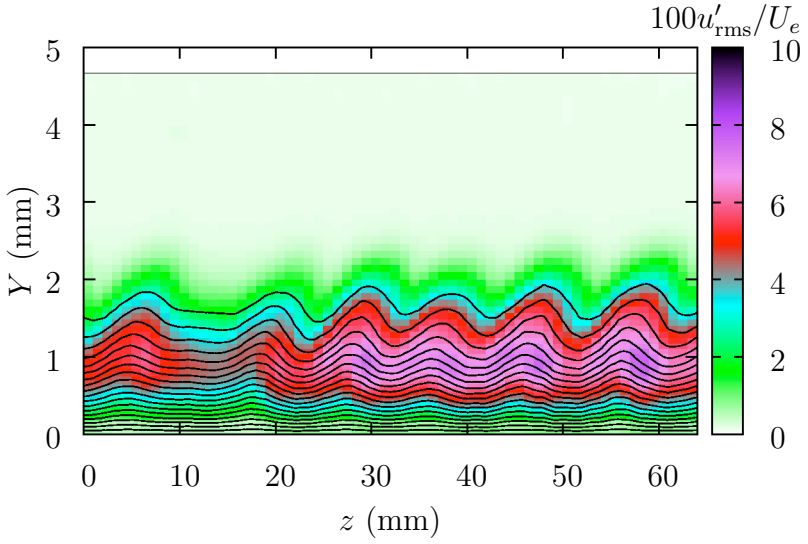

Figure A.53: U and u'_{rms} contours at $x/c = 0.40$, $Re_c = 2.8 \times 10^6$, $Tu = 0.19\%$, clean leading edge.

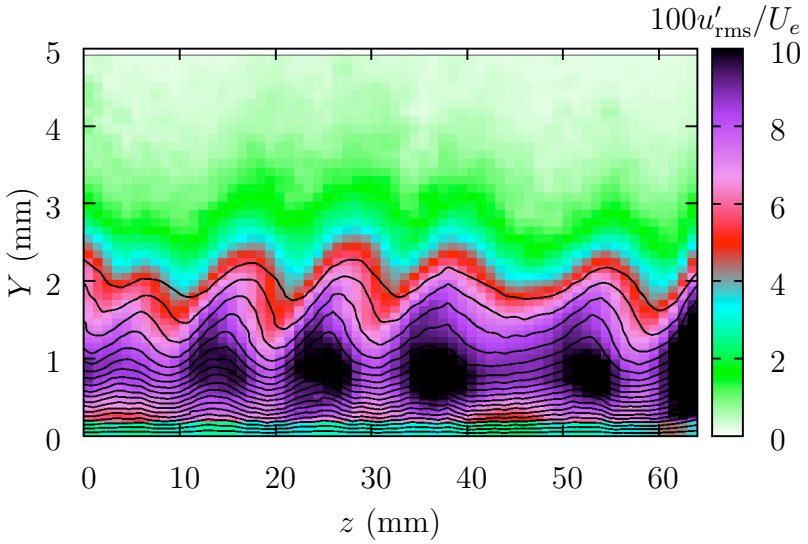

Figure A.54: U and u'_{rms} contours at $x/c = 0.50$, $Re_c = 2.8 \times 10^6$, $Tu = 0.19\%$, clean leading edge.

APPENDIX B

BOUNDARY-LAYER PLOTS: [14|6|3] ROUGHNESS

	Tu		
x/c	0.02%	0.05%	0.19%
0.10	•	•	•
0.15		•	
0.20		•	
0.25	•	•	•
0.30		•	
0.35		•	
0.40	•	•	•
0.50		•	
0.60		•	

Table B.1: Test matrix for [14|6|3] subcritically-spaced roughness: boundary-layer scans at $Re_c = 2.8 \times 10^6$.

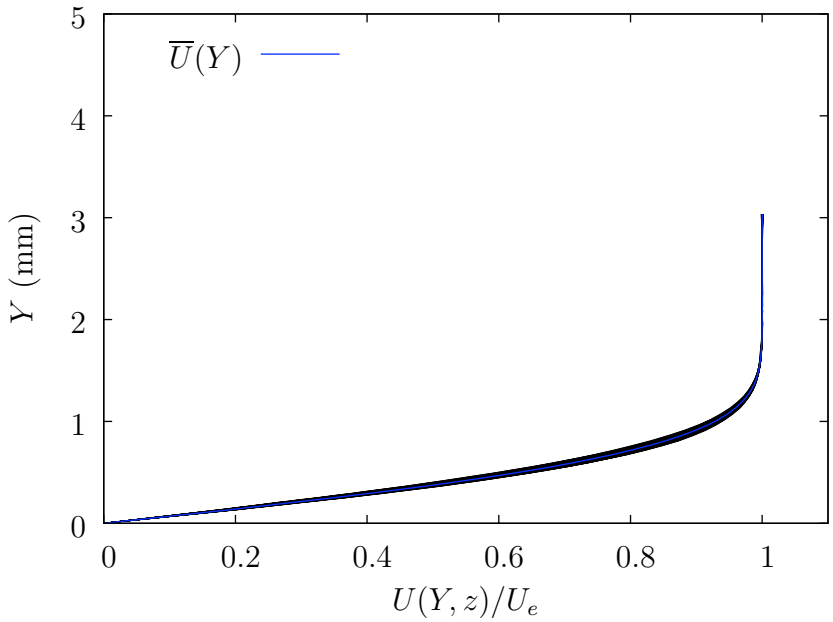

Figure B.1: Boundary-layer profiles at $x/c = 0.10$, $Re_c = 2.8 \times 10^6$, $Tu = 0.02\%$, [14|6|3] roughness.

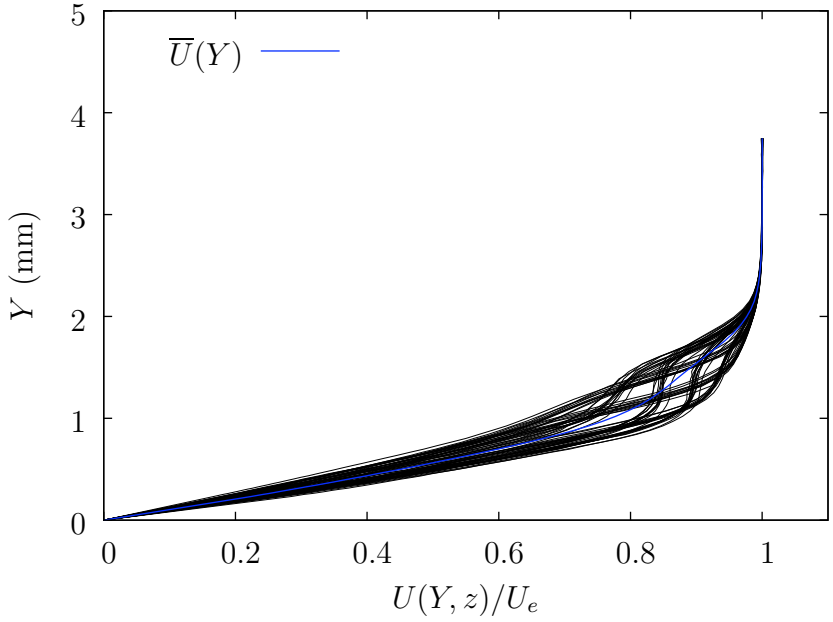

Figure B.2: Boundary-layer profiles at $x/c = 0.25$, $Re_c = 2.8 \times 10^6$, $Tu = 0.02\%$, [14|6|3] roughness.

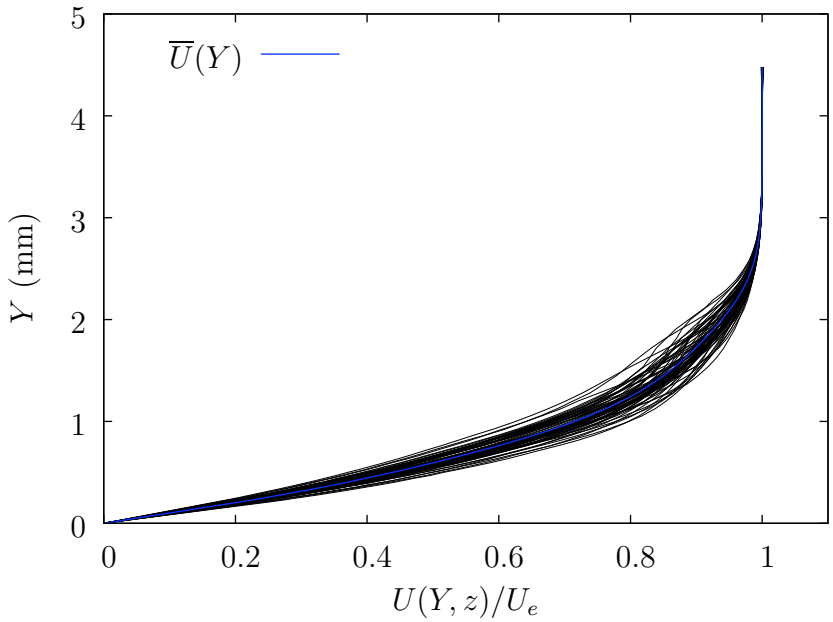

Figure B.3: Boundary-layer profiles at $x/c = 0.40$, $Re_c = 2.8 \times 10^6$, $Tu = 0.02\%$, [14|6|3] roughness.

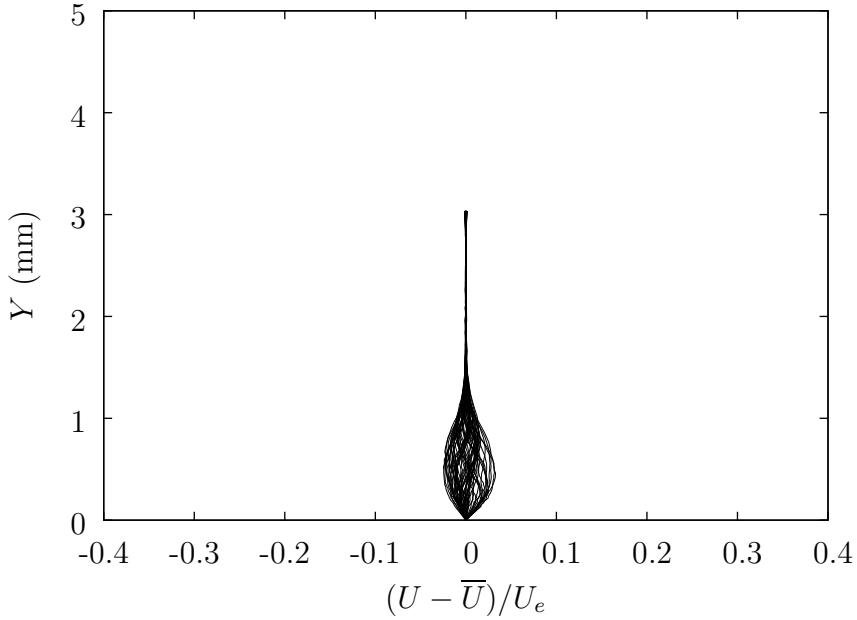

Figure B.4: Steady disturbance profiles at $x/c = 0.10$, $Re_c = 2.8 \times 10^6$, $Tu = 0.02\%$, [14|6|3] roughness.

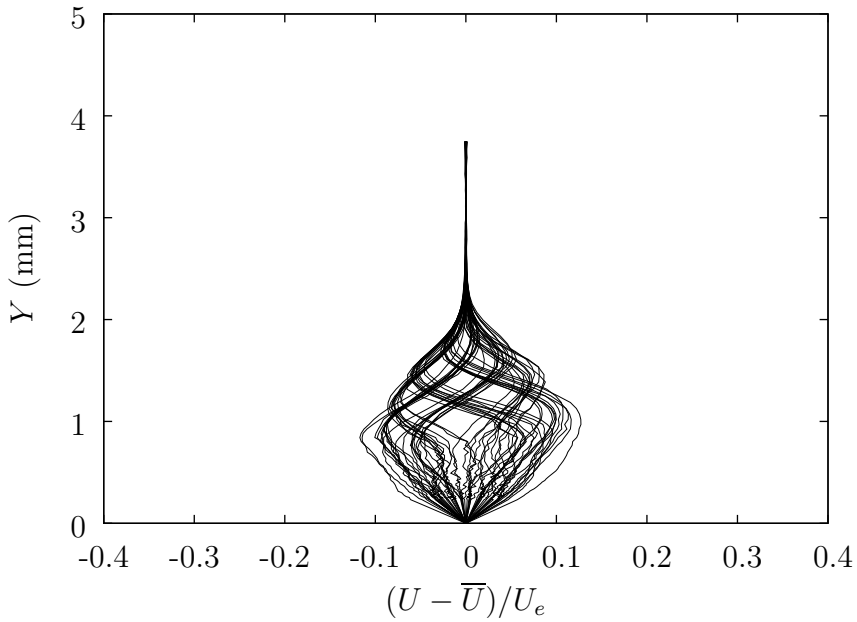

Figure B.5: Steady disturbance profiles at $x/c = 0.25$, $Re_c = 2.8 \times 10^6$, $Tu = 0.02\%$, [14|6|3] roughness.

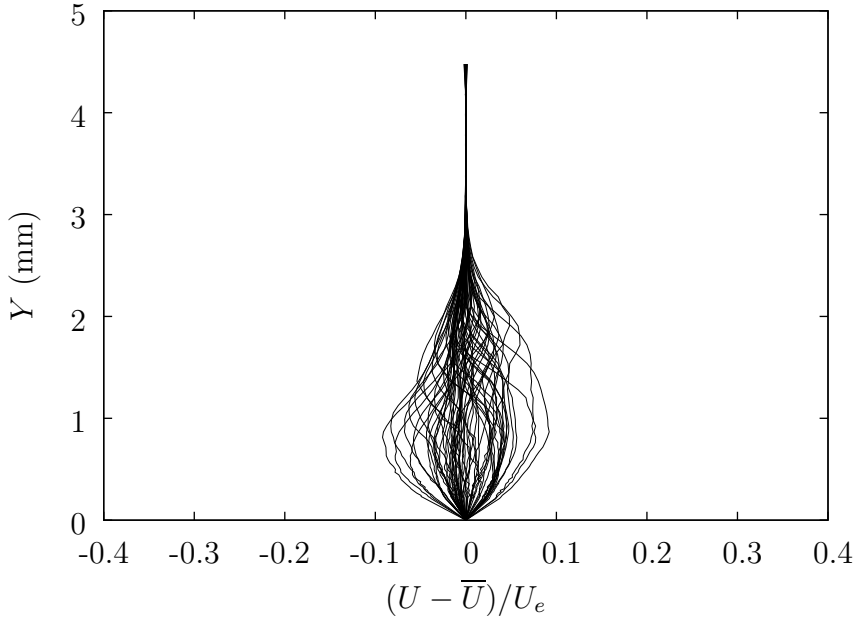

Figure B.6: Steady disturbance profiles at $x/c = 0.40$, $Re_c = 2.8 \times 10^6$, $Tu = 0.02\%$, [14|6|3] roughness.

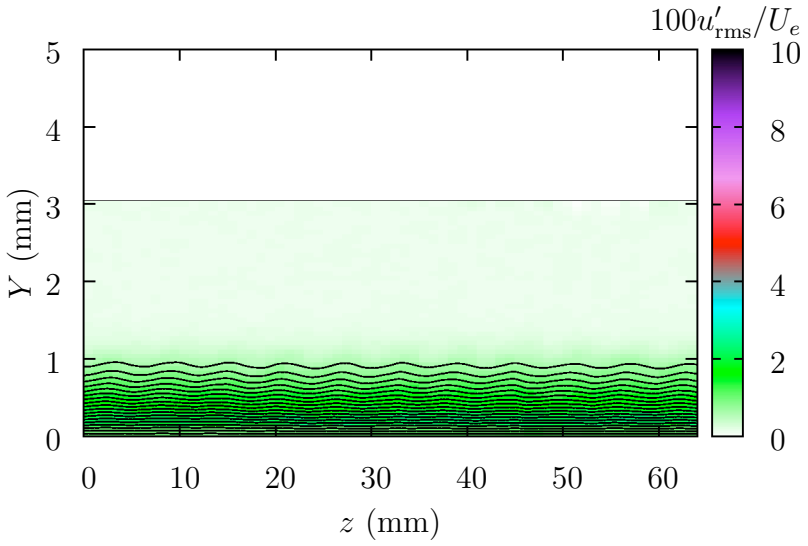

Figure B.7: U and u'_{rms} contours at $x/c = 0.10$, $Re_c = 2.8 \times 10^6$, $Tu = 0.02\%$, [14|6|3] roughness.

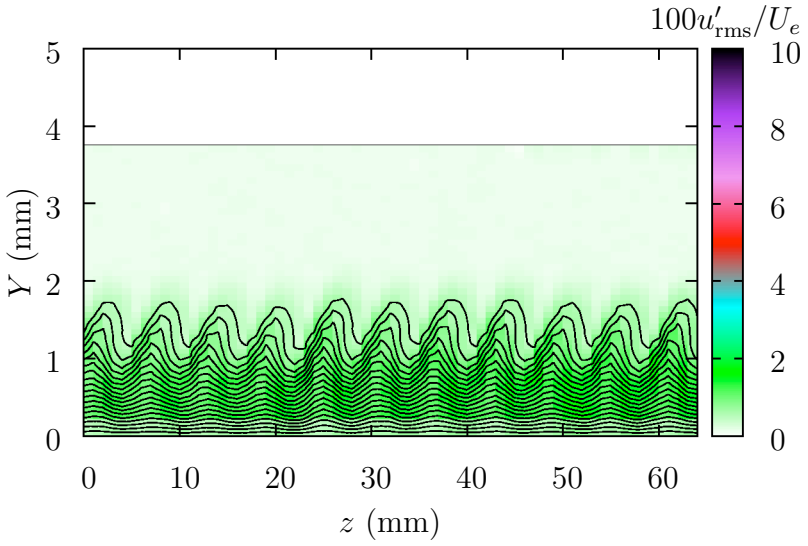

Figure B.8: U and u'_{rms} contours at $x/c = 0.25$, $Re_c = 2.8 \times 10^6$, $Tu = 0.02\%$, [14|6|3] roughness.

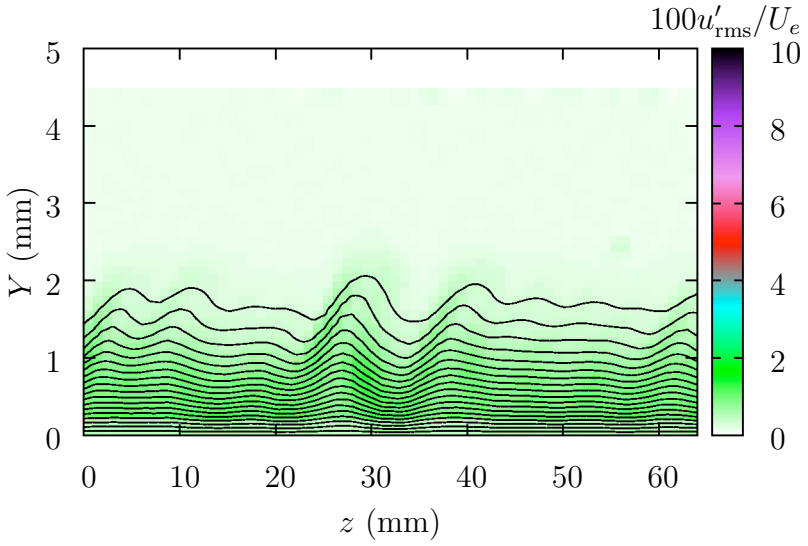

Figure B.9: U and u'_{rms} contours at $x/c = 0.40$, $Re_c = 2.8 \times 10^6$, $Tu = 0.02\%$, [14|6|3] roughness.

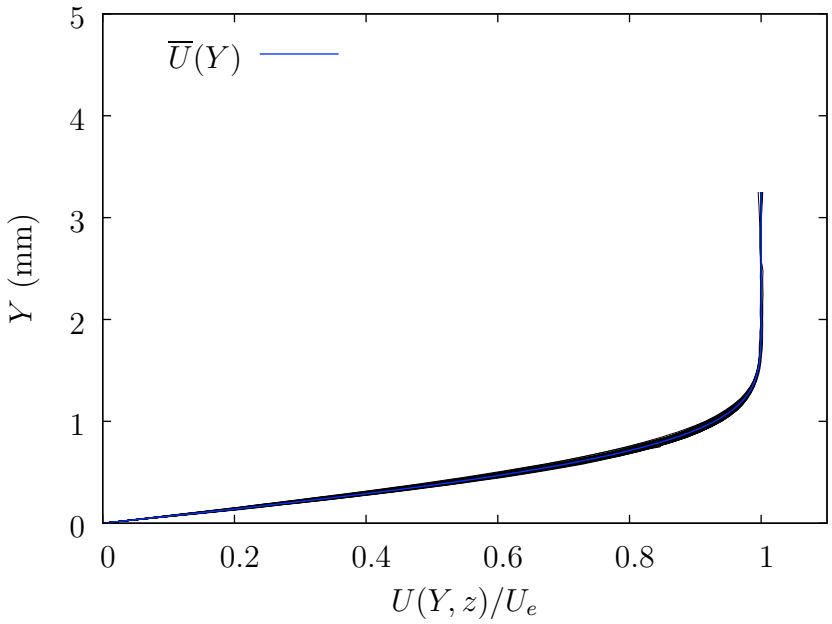

Figure B.10: Boundary-layer profiles at $x/c = 0.10$, $Re_c = 2.8 \times 10^6$, $Tu = 0.05\%$, [14|6|3] roughness.

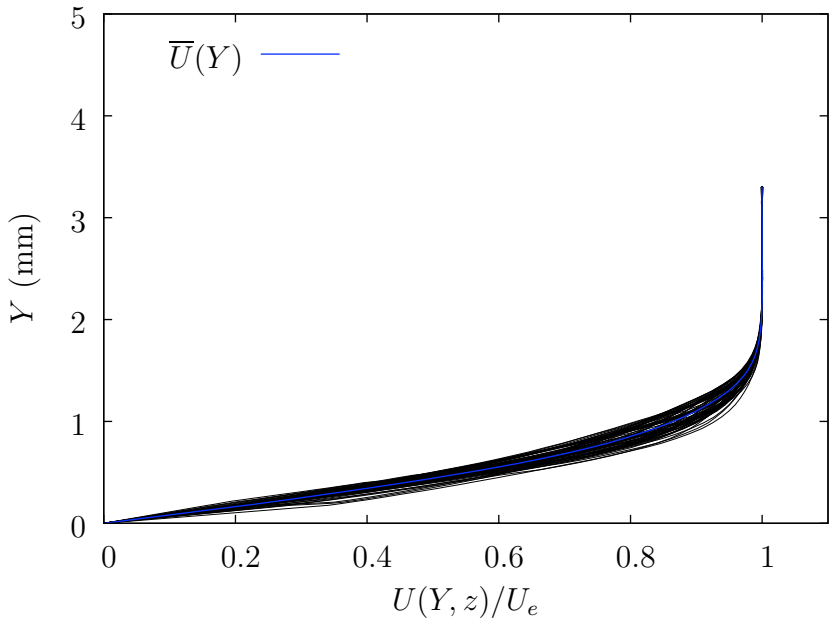

Figure B.11: Boundary-layer profiles at $x/c = 0.15$, $Re_c = 2.8 \times 10^6$, $Tu = 0.05\%$, [14|6|3] roughness.

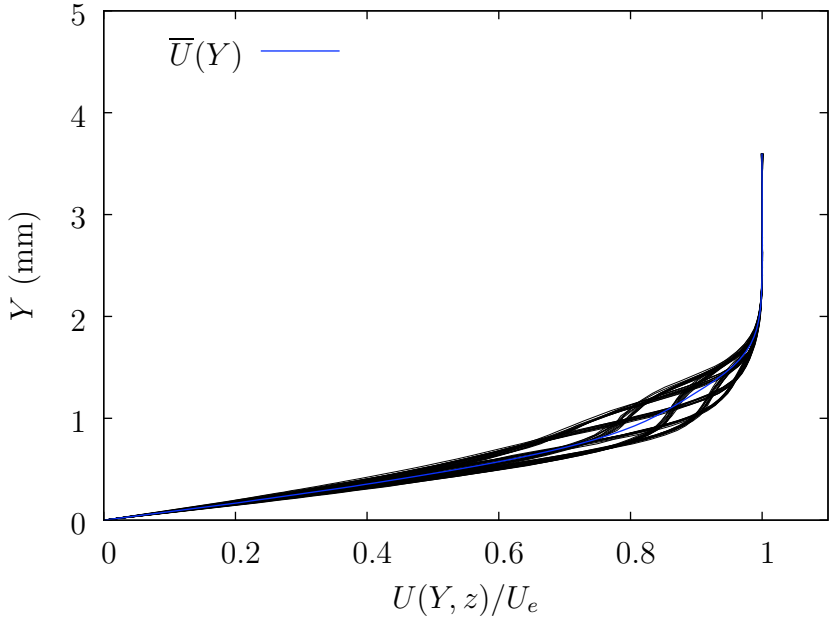

Figure B.12: Boundary-layer profiles at $x/c = 0.20$, $Re_c = 2.8 \times 10^6$, $Tu = 0.05\%$, [14|6|3] roughness.

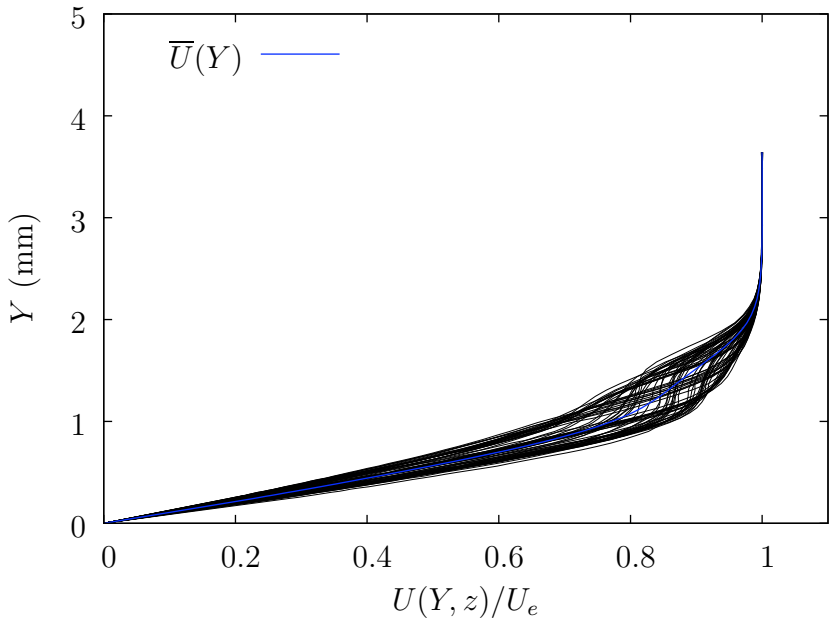

Figure B.13: Boundary-layer profiles at $x/c = 0.25$, $Re_c = 2.8 \times 10^6$, $Tu = 0.05\%$, [14|6|3] roughness.

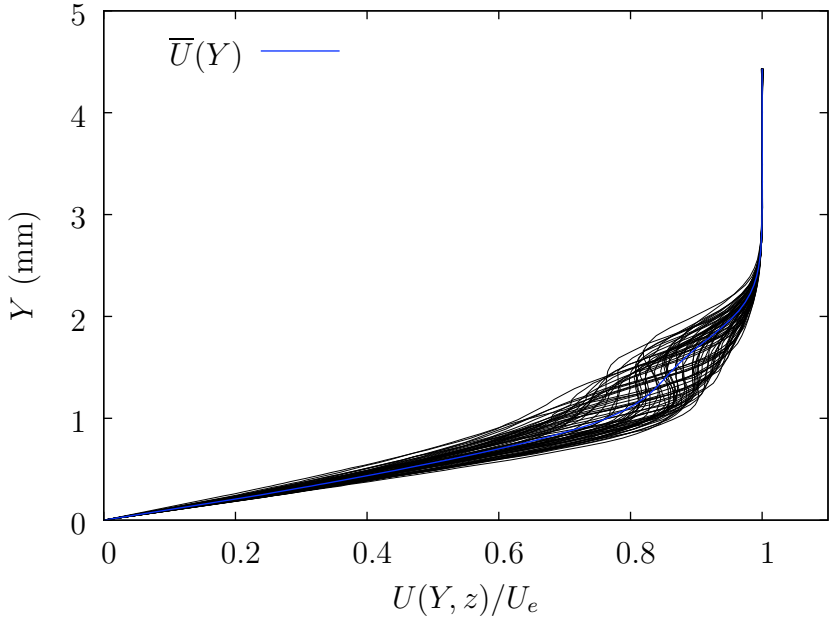

Figure B.14: Boundary-layer profiles at $x/c = 0.30$, $Re_c = 2.8 \times 10^6$, $Tu = 0.05\%$, [14|6|3] roughness.

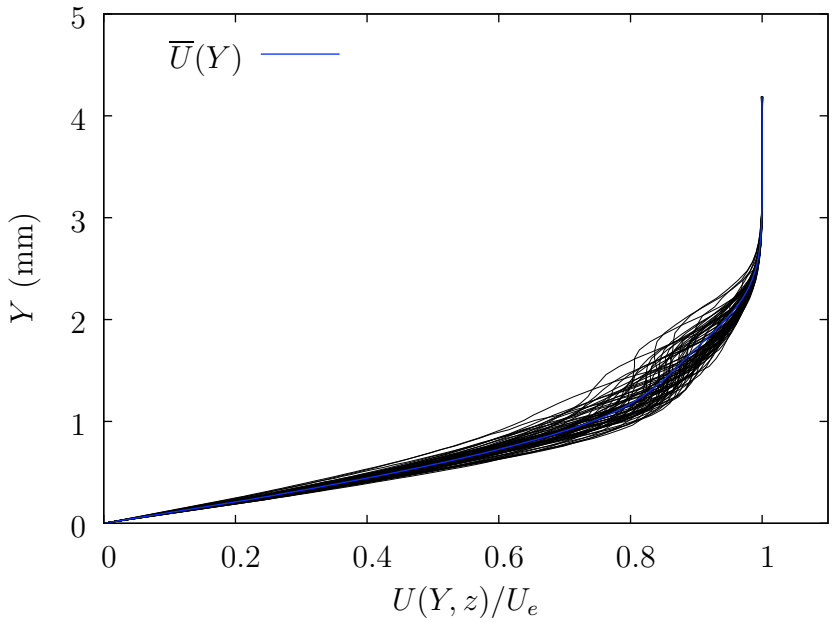

Figure B.15: Boundary-layer profiles at $x/c = 0.35$, $Re_c = 2.8 \times 10^6$, $Tu = 0.05\%$, [14|6|3] roughness.

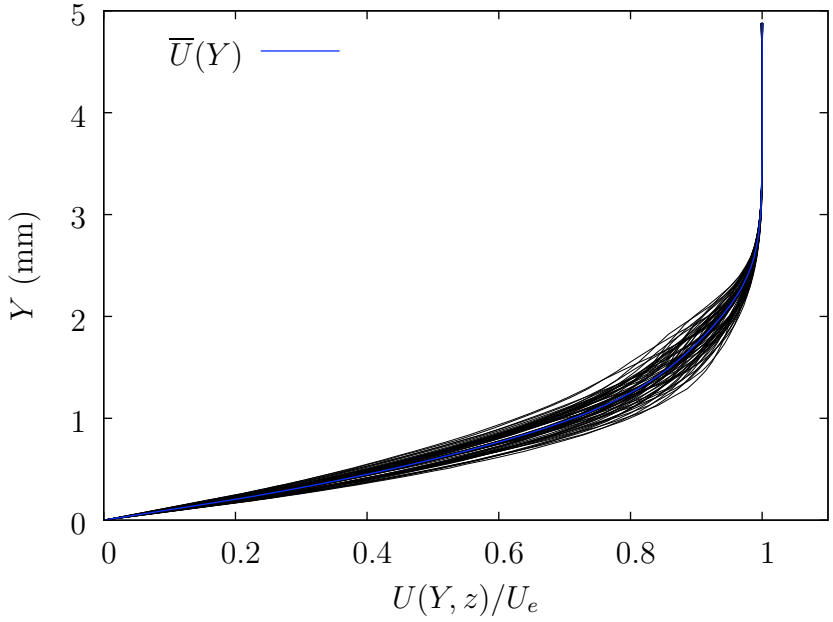

Figure B.16: Boundary-layer profiles at $x/c = 0.40$, $Re_c = 2.8 \times 10^6$, $Tu = 0.05\%$, [14|6|3] roughness.

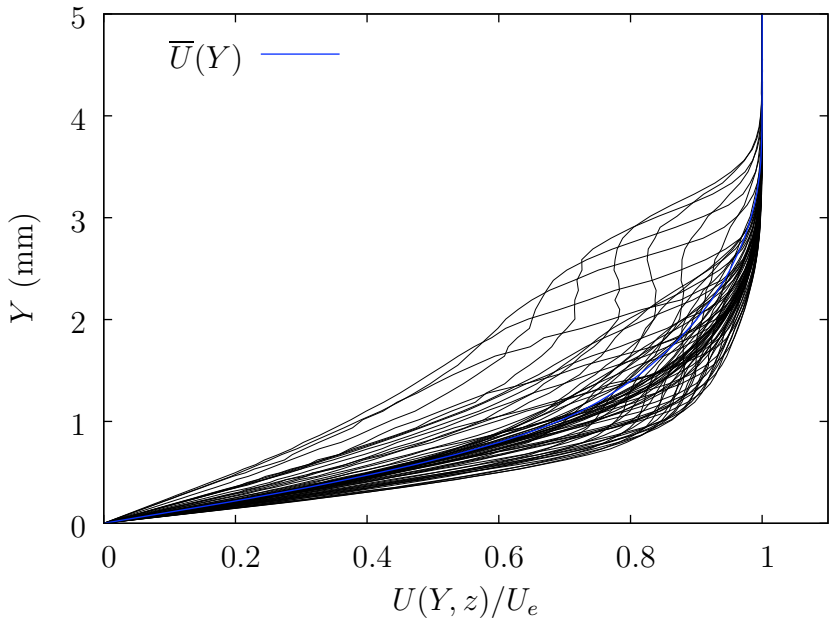

Figure B.17: Boundary-layer profiles at $x/c = 0.50$, $Re_c = 2.8 \times 10^6$, $Tu = 0.05\%$, [14|6|3] roughness.

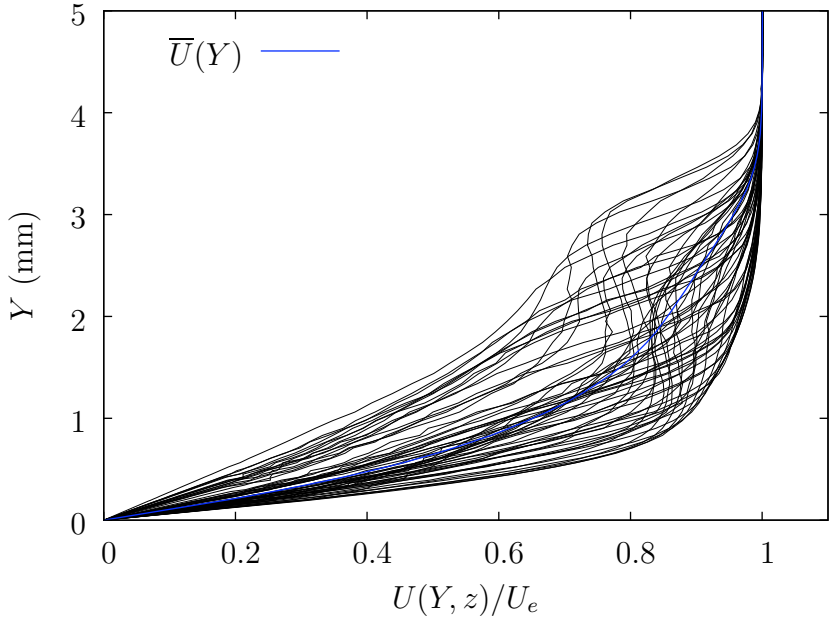

Figure B.18: Boundary-layer profiles at $x/c = 0.60$, $Re_c = 2.8 \times 10^6$, $Tu = 0.05\%$, [14|6|3] roughness.

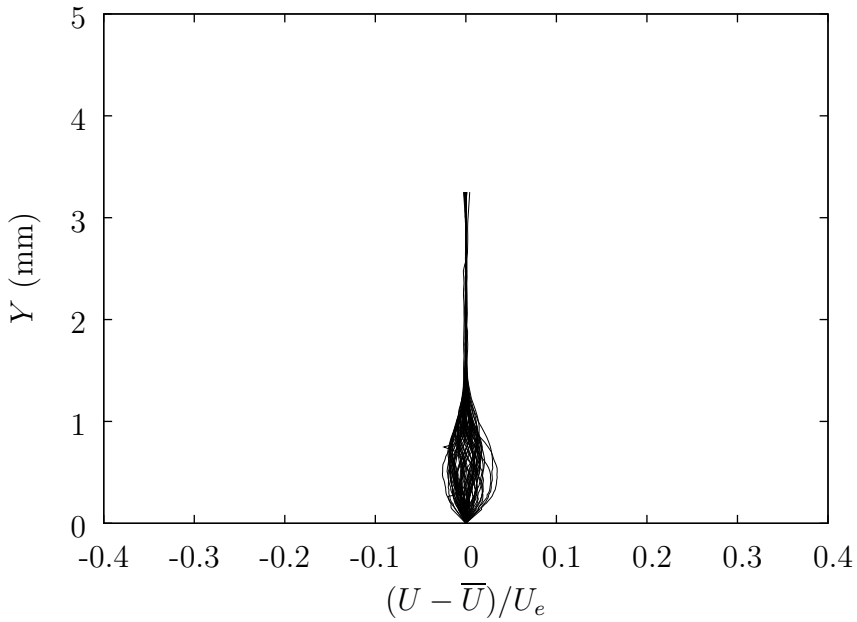

Figure B.19: Steady disturbance profiles at $x/c = 0.10$, $Re_c = 2.8 \times 10^6$, $Tu = 0.05\%$, [14|6|3] roughness.

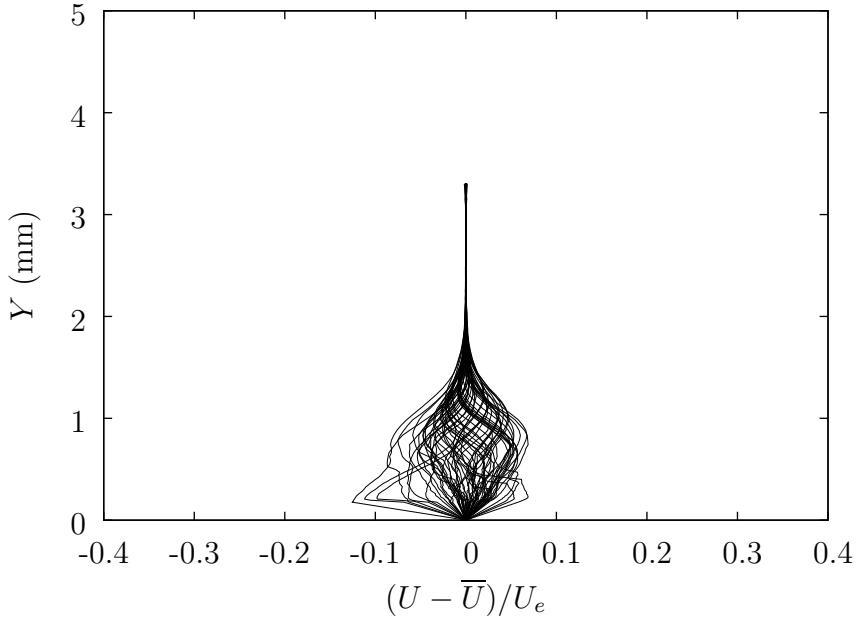

Figure B.20: Steady disturbance profiles at $x/c = 0.15$, $Re_c = 2.8 \times 10^6$, $Tu = 0.05\%$, [14|6|3] roughness.

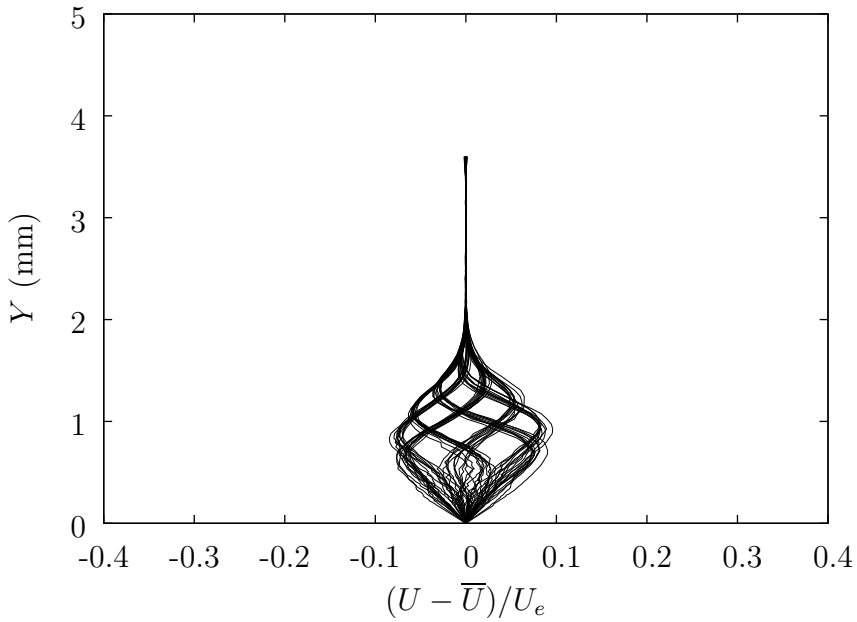

Figure B.21: Steady disturbance profiles at $x/c = 0.20$, $Re_c = 2.8 \times 10^6$, $Tu = 0.05\%$, [14|6|3] roughness.

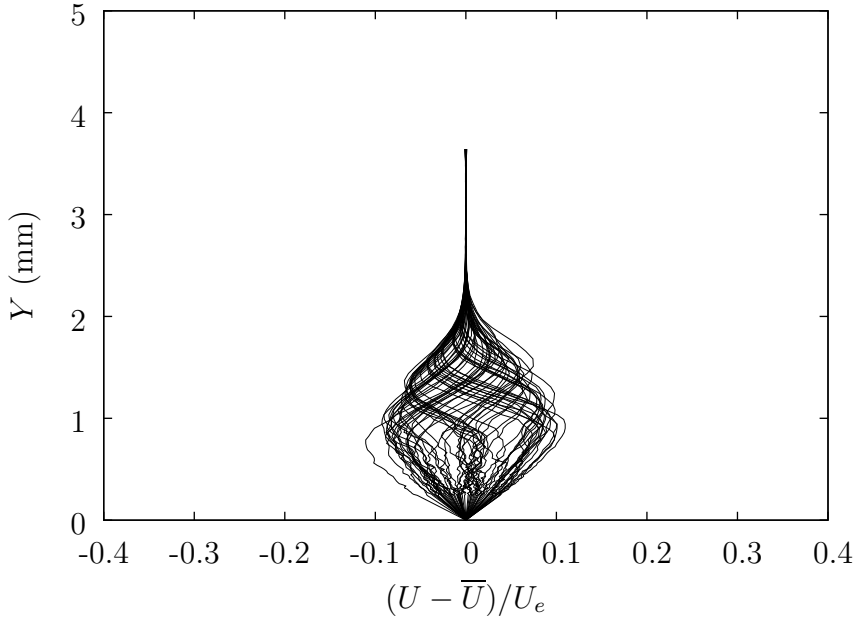

Figure B.22: Steady disturbance profiles at $x/c = 0.25$, $Re_c = 2.8 \times 10^6$, $Tu = 0.05\%$, [14|6|3] roughness.

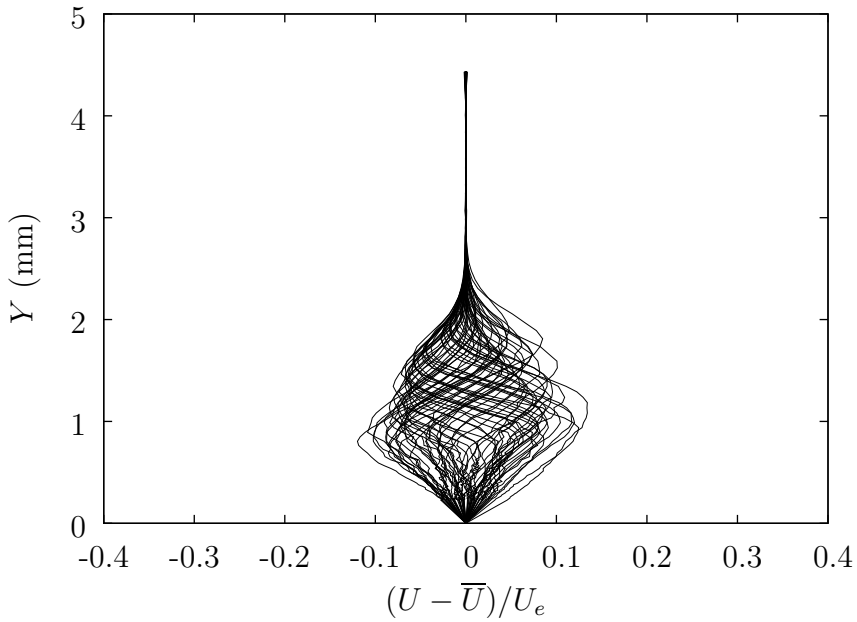

Figure B.23: Steady disturbance profiles at $x/c = 0.30$, $Re_c = 2.8 \times 10^6$, $Tu = 0.05\%$, [14|6|3] roughness.

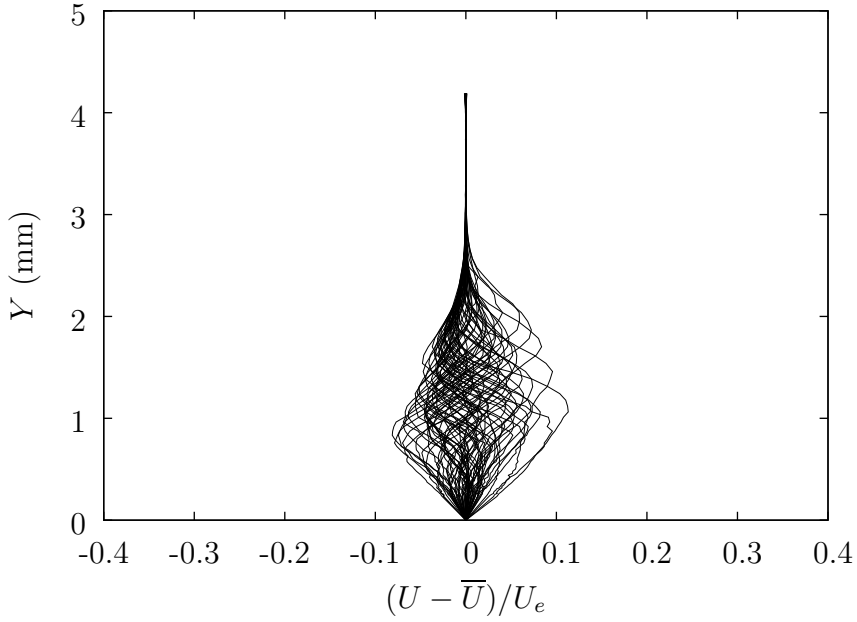

Figure B.24: Steady disturbance profiles at $x/c = 0.35$, $Re_c = 2.8 \times 10^6$, $Tu = 0.05\%$, [14|6|3] roughness.

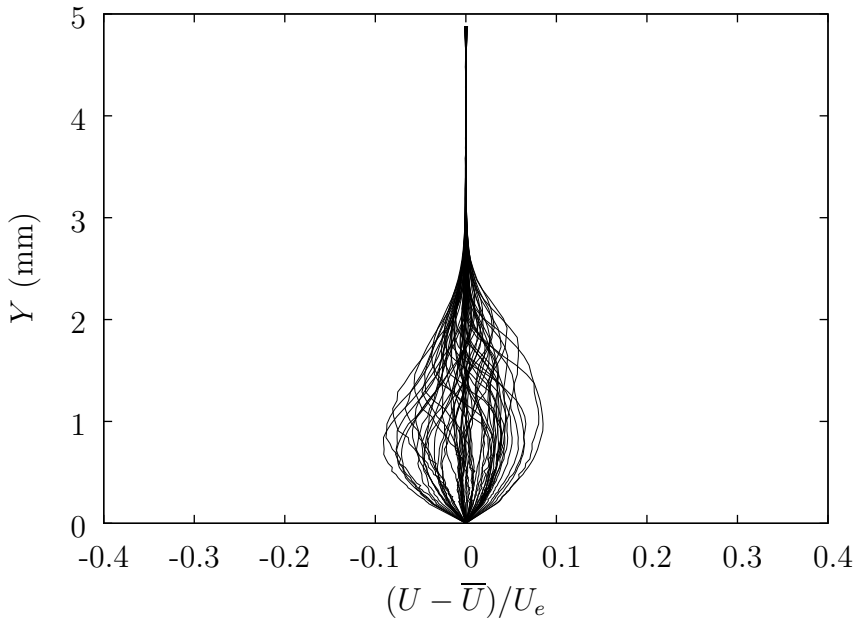

Figure B.25: Steady disturbance profiles at $x/c = 0.40$, $Re_c = 2.8 \times 10^6$, $Tu = 0.05\%$, [14|6|3] roughness.

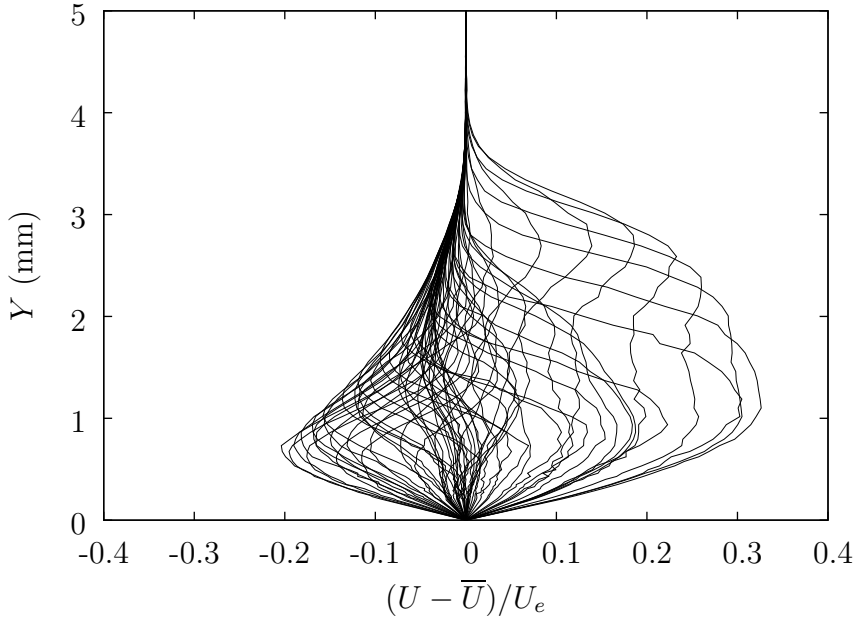

Figure B.26: Steady disturbance profiles at $x/c = 0.50$, $Re_c = 2.8 \times 10^6$, $Tu = 0.05\%$, [14|6|3] roughness.

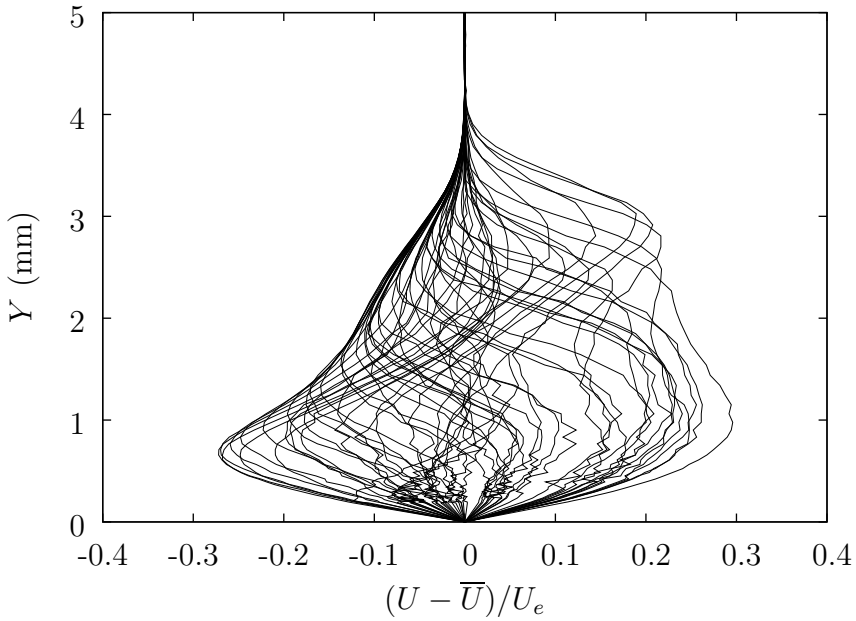

Figure B.27: Steady disturbance profiles at $x/c = 0.60$, $Re_c = 2.8 \times 10^6$, $Tu = 0.05\%$, [14|6|3] roughness.

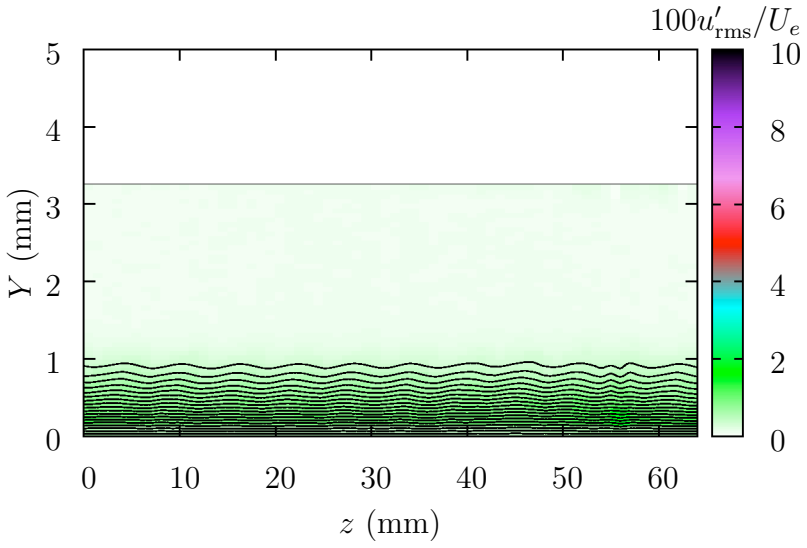

Figure B.28: U and u'_{rms} contours at $x/c = 0.10$, $Re_c = 2.8 \times 10^6$, $Tu = 0.05\%$, [14|6|3] roughness.

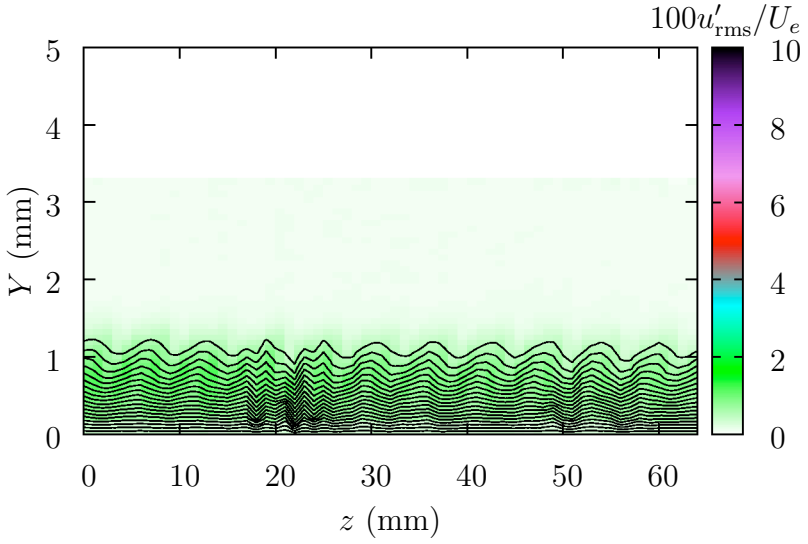

Figure B.29: U and u'_{rms} contours at $x/c = 0.15$, $Re_c = 2.8 \times 10^6$, $Tu = 0.05\%$, [14|6|3] roughness.

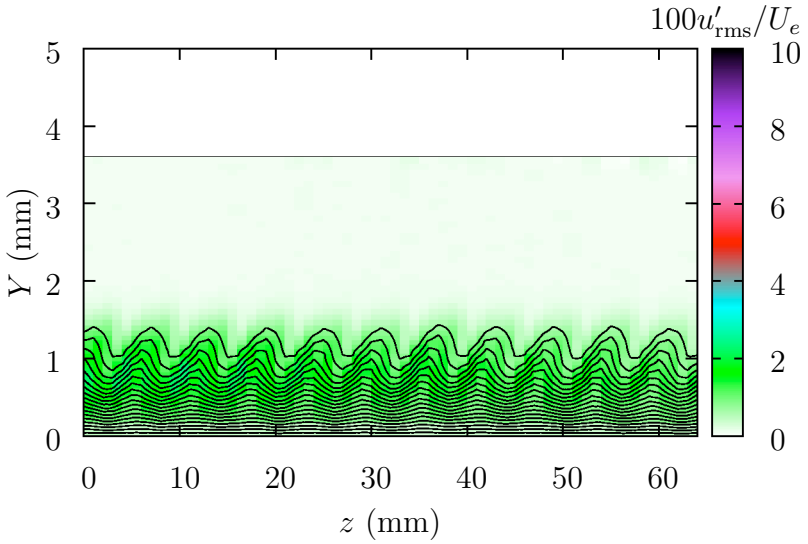

Figure B.30: U and u'_{rms} contours at $x/c = 0.20$, $Re_c = 2.8 \times 10^6$, $Tu = 0.05\%$, [14|6|3] roughness.

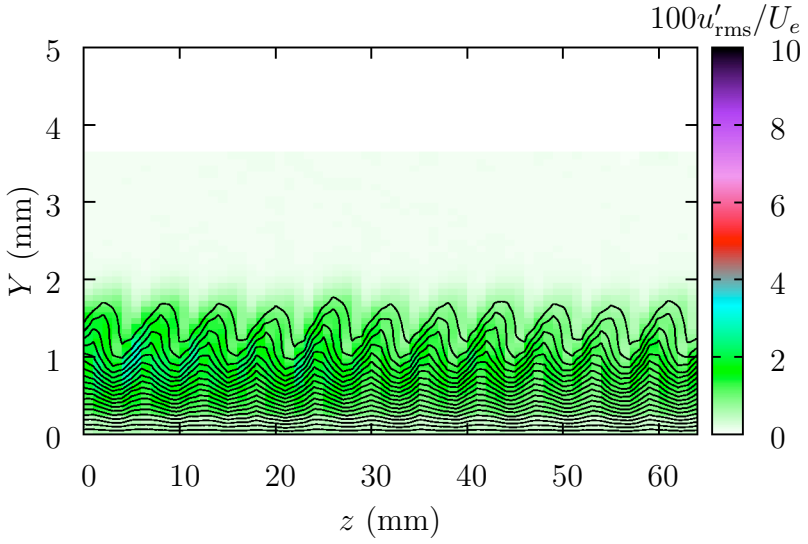

Figure B.31: U and u'_{rms} contours at $x/c = 0.25$, $Re_c = 2.8 \times 10^6$, $Tu = 0.05\%$, [14|6|3] roughness.

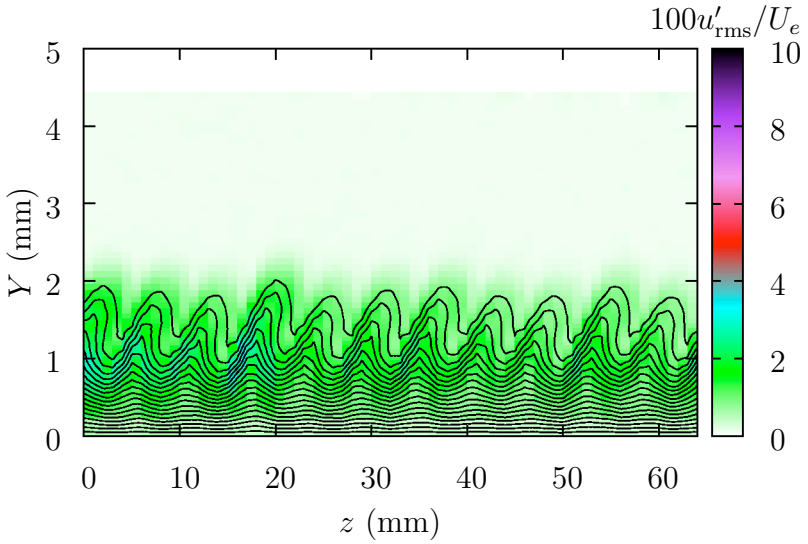

Figure B.32: U and u'_{rms} contours at $x/c = 0.30$, $Re_c = 2.8 \times 10^6$, $Tu = 0.05\%$, [14|6|3] roughness.

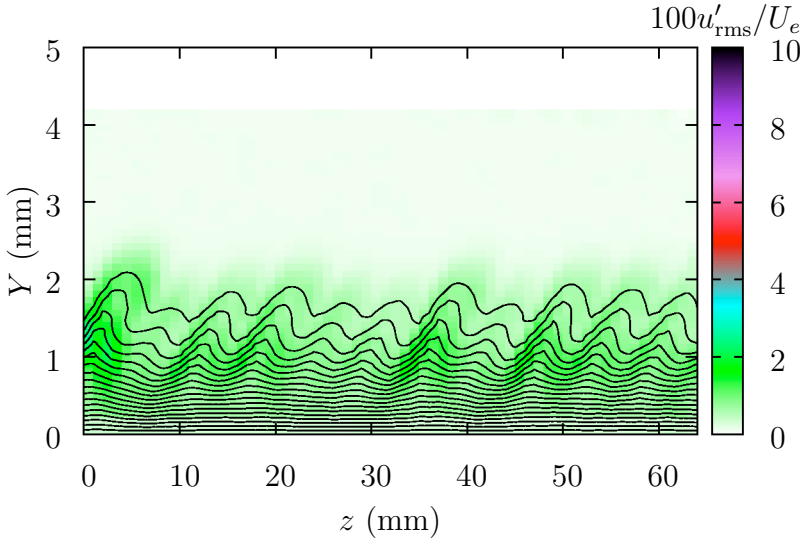

Figure B.33: U and u'_{rms} contours at $x/c = 0.35$, $Re_c = 2.8 \times 10^6$, $Tu = 0.05\%$, [14|6|3] roughness.

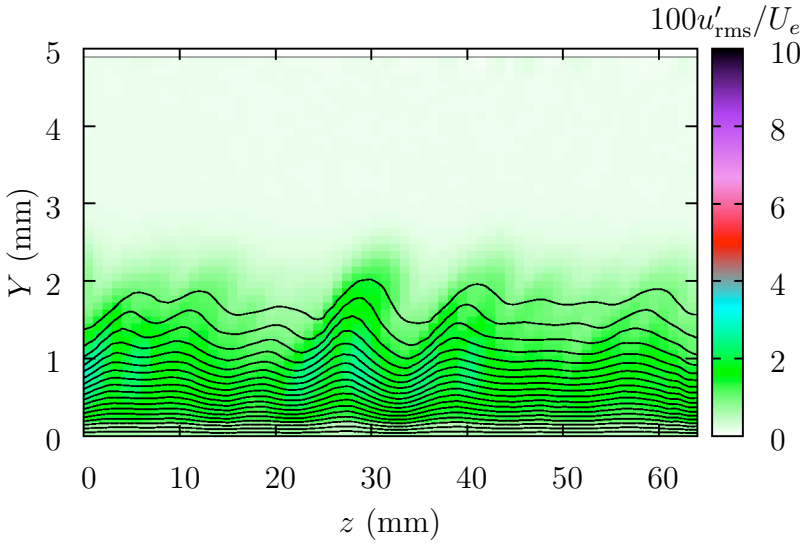

Figure B.34: U and u'_{rms} contours at $x/c = 0.40$, $Re_c = 2.8 \times 10^6$, $Tu = 0.05\%$, [14|6|3] roughness.

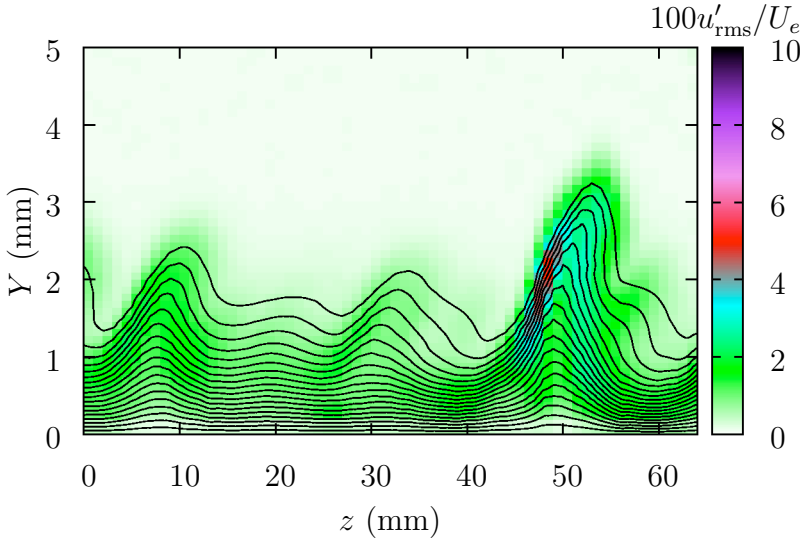

Figure B.35: U and u'_{rms} contours at $x/c = 0.50$, $Re_c = 2.8 \times 10^6$, $Tu = 0.05\%$, [14|6|3] roughness.

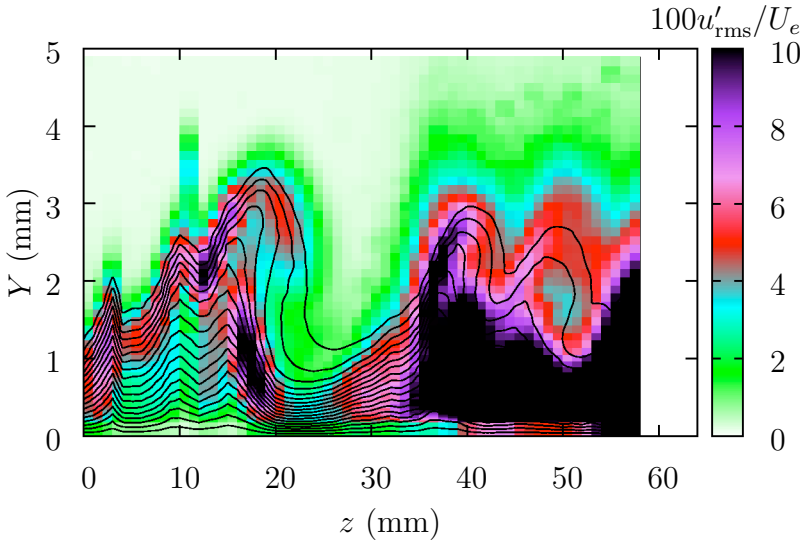

Figure B.36: U and u'_{rms} contours at $x/c = 0.60$, $Re_c = 2.8 \times 10^6$, $Tu = 0.05\%$, [14|6|3] roughness.

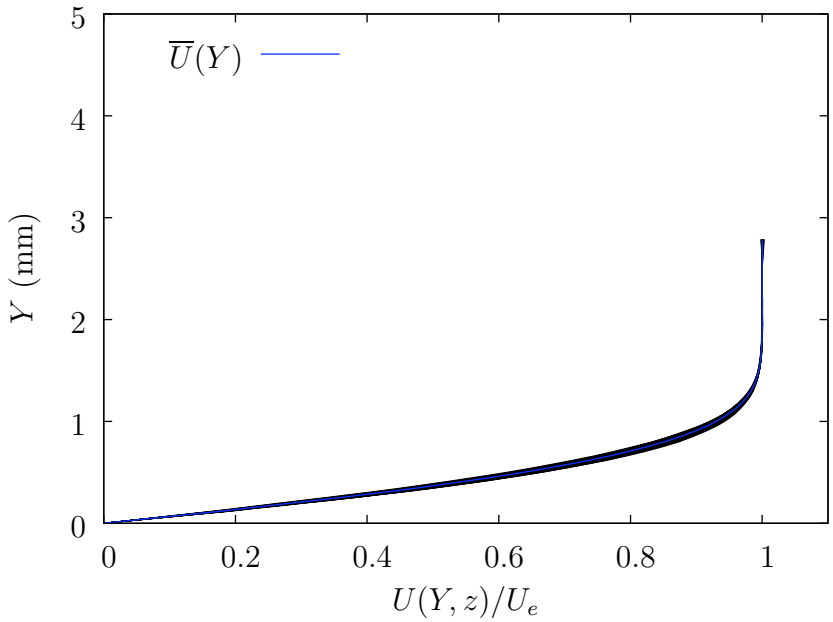

Figure B.37: Boundary-layer profiles at $x/c = 0.10$, $Re_c = 2.8 \times 10^6$, $Tu = 0.19\%$, [14|6|3] roughness.

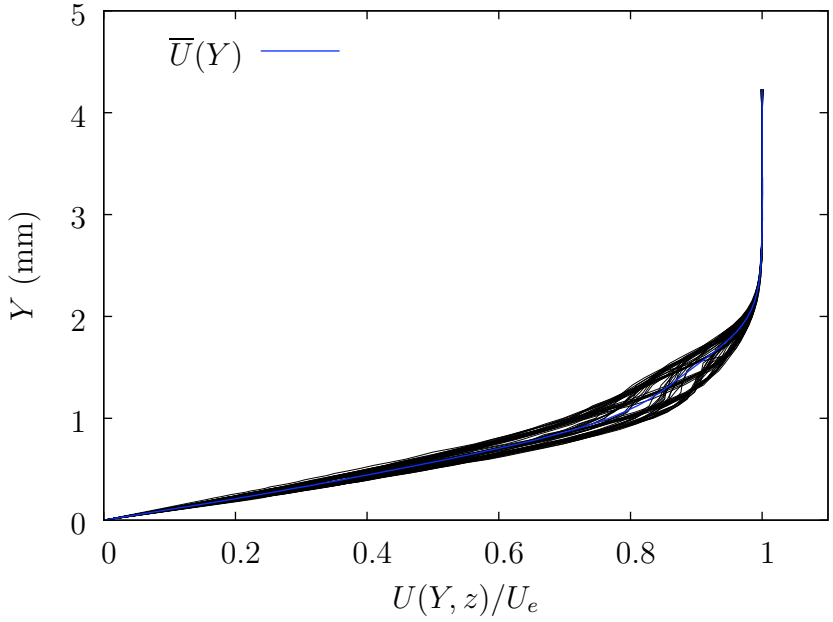

Figure B.38: Boundary-layer profiles at $x/c = 0.25$, $Re_c = 2.8 \times 10^6$, $Tu = 0.19\%$, [14|6|3] roughness.

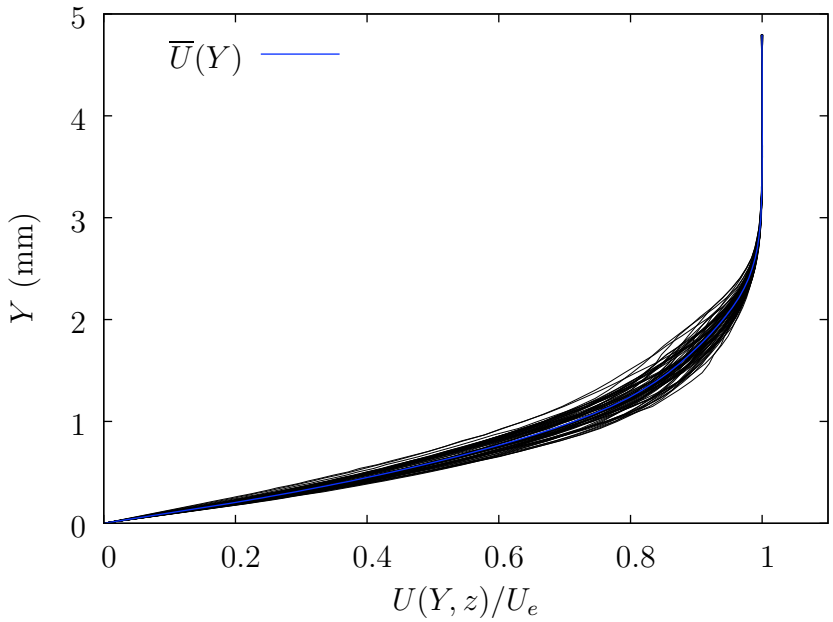

Figure B.39: Boundary-layer profiles at $x/c = 0.40$, $Re_c = 2.8 \times 10^6$, $Tu = 0.19\%$, [14|6|3] roughness.

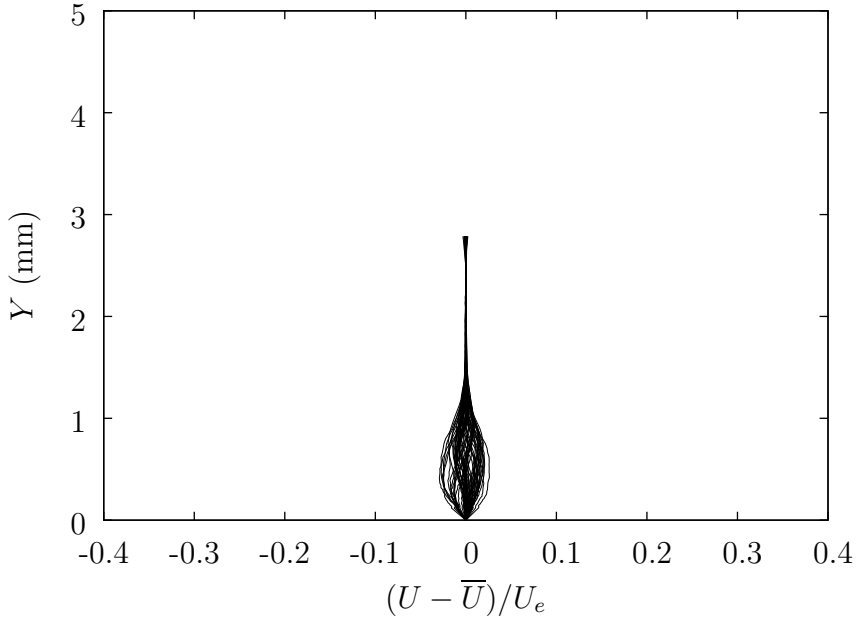

Figure B.40: Steady disturbance profiles at $x/c = 0.10$, $Re_c = 2.8 \times 10^6$, $Tu = 0.19\%$, [14|6|3] roughness.

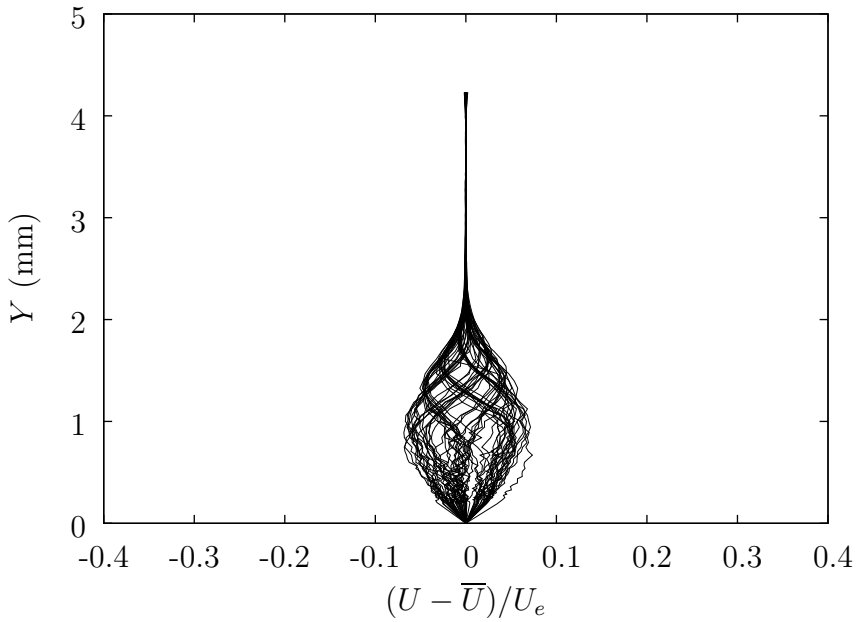

Figure B.41: Steady disturbance profiles at $x/c = 0.25$, $Re_c = 2.8 \times 10^6$, $Tu = 0.19\%$, [14|6|3] roughness.

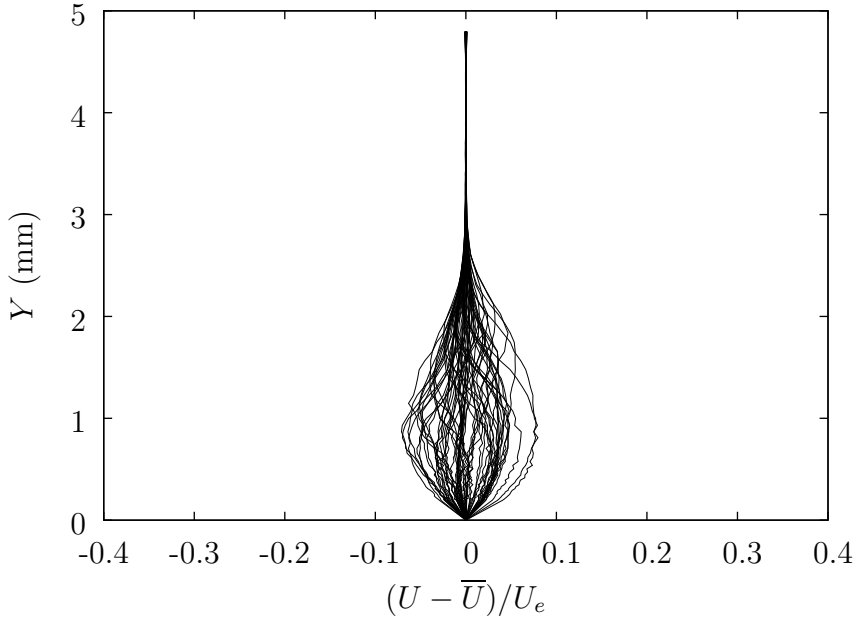

Figure B.42: Steady disturbance profiles at $x/c = 0.40$, $Re_c = 2.8 \times 10^6$, $Tu = 0.19\%$, [14|6|3] roughness.

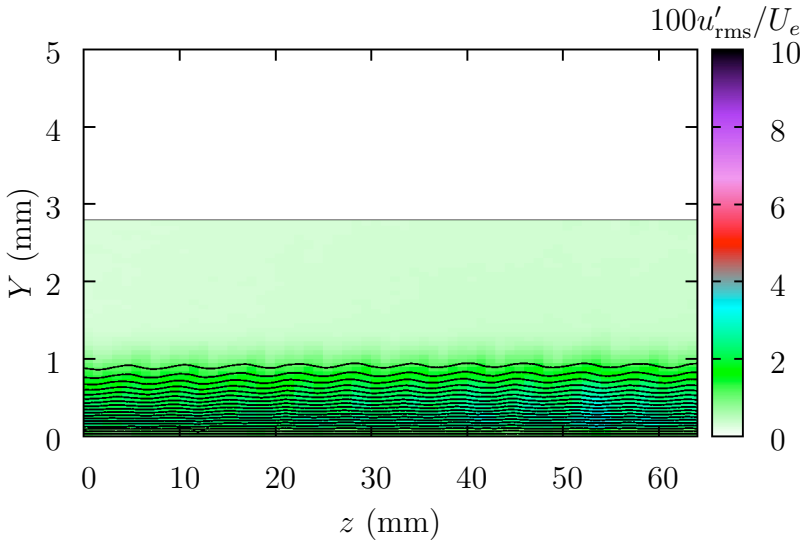

Figure B.43: U and u'_{rms} contours at $x/c = 0.10$, $Re_c = 2.8 \times 10^6$, $Tu = 0.19\%$, [14|6|3] roughness.

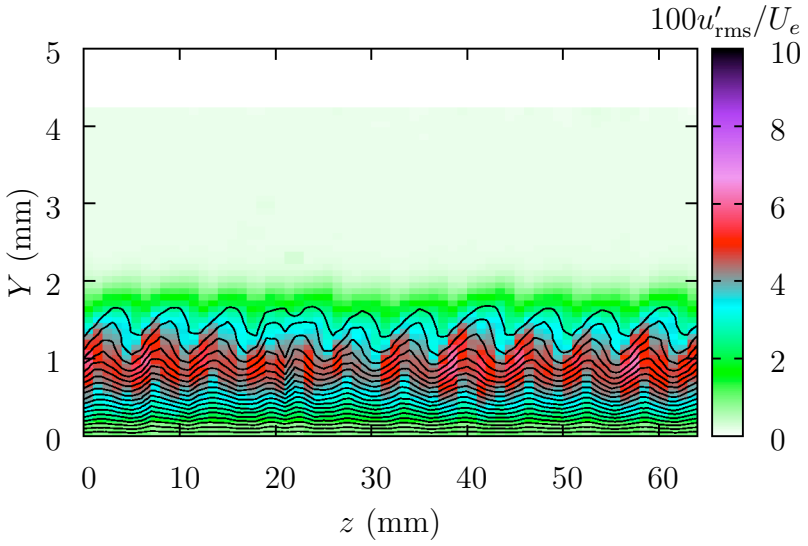

Figure B.44: U and u'_{rms} contours at $x/c = 0.25$, $Re_c = 2.8 \times 10^6$, $Tu = 0.19\%$, [14|6|3] roughness.

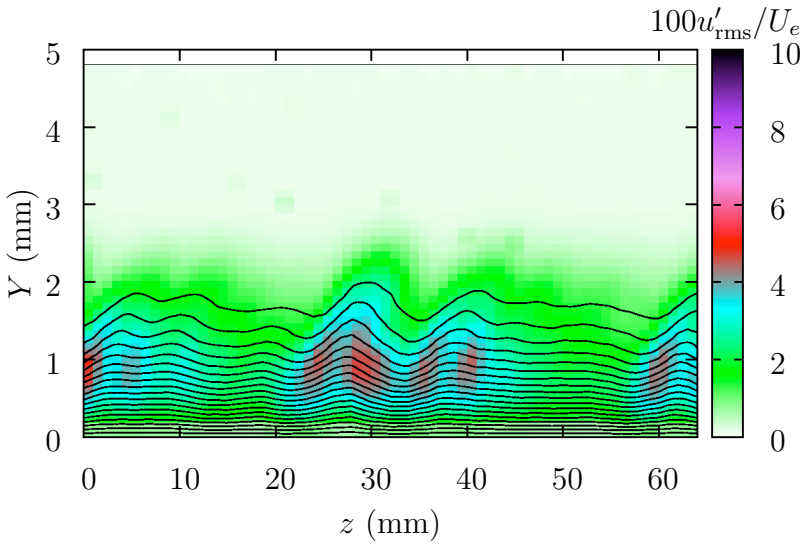

Figure B.45: U and u'_{rms} contours at $x/c = 0.40$, $Re_c = 2.8 \times 10^6$, $Tu = 0.19\%$, [14|6|3] roughness.

APPENDIX C

BOUNDARY-LAYER PLOTS: [12|12|3] ROUGHNESS

	Tu			
x/c	0.02%	0.03%	0.05%	0.19%
0.10	•		•	•
0.15	•	•	•	•
0.20	•		•	•
0.25	•	•	•	•
0.30	•		•	•
0.35	•	•	•	•
0.375				•
0.40	•		•	
0.425	•			

Table C.1: Test matrix for [12|12|3] critically-spaced roughness: boundary-layer scans at $Re_c = 2.8 \times 10^6$.

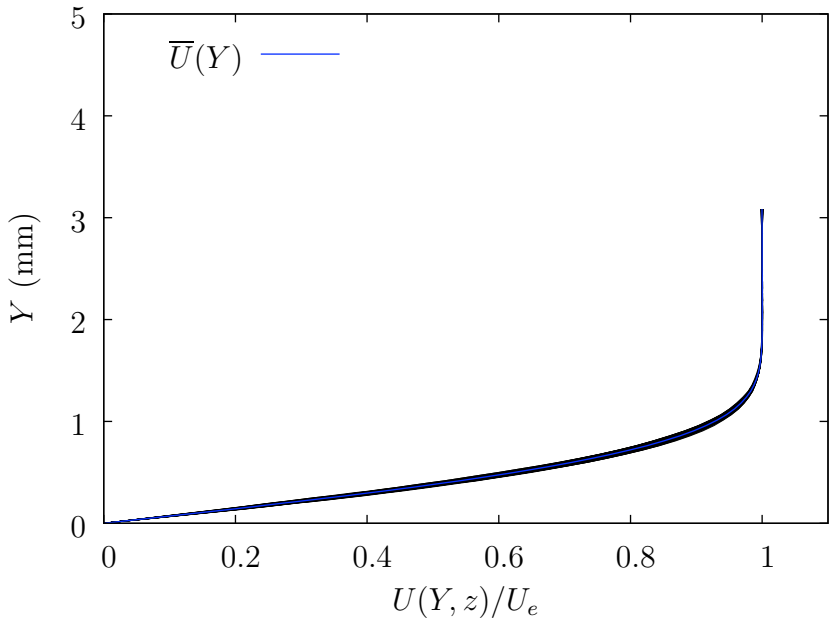

Figure C.1: Boundary-layer profiles at $x/c = 0.10$, $Re_c = 2.8 \times 10^6$, $Tu = 0.02\%$, [12|12|3] roughness.

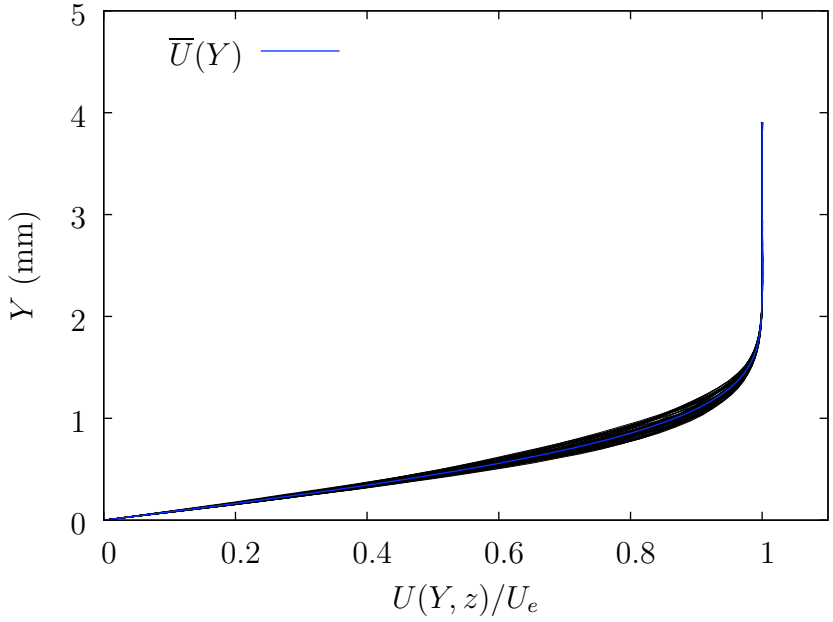

Figure C.2: Boundary-layer profiles at $x/c = 0.15$, $Re_c = 2.8 \times 10^6$, $Tu = 0.02\%$, [12|12|3] roughness.

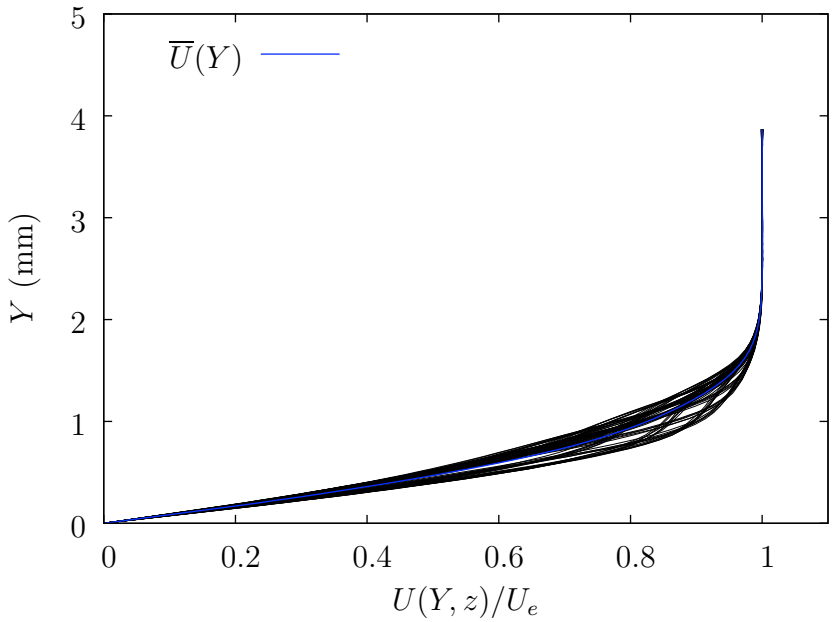

Figure C.3: Boundary-layer profiles at $x/c = 0.20$, $Re_c = 2.8 \times 10^6$, $Tu = 0.02\%$, [12|12|3] roughness.

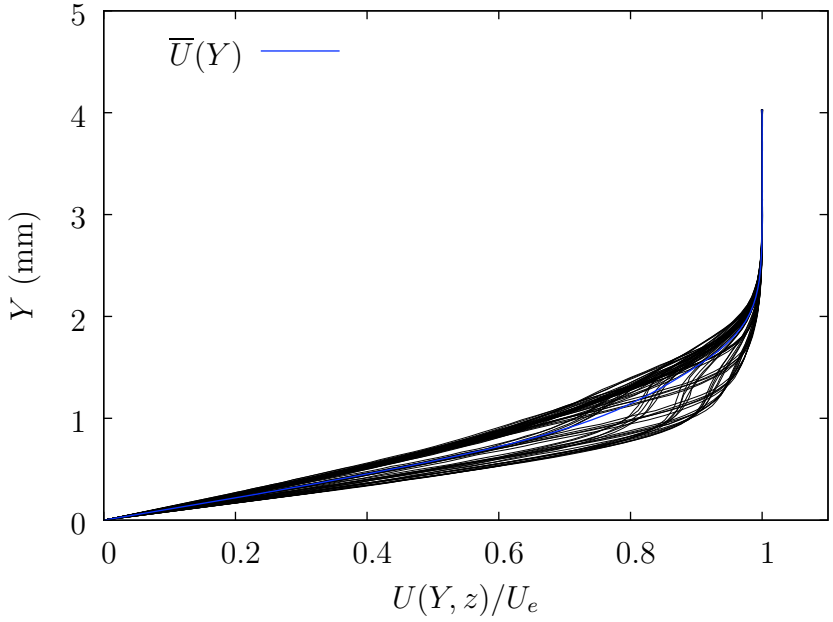

Figure C.4: Boundary-layer profiles at $x/c = 0.25$, $Re_c = 2.8 \times 10^6$, $Tu = 0.02\%$, [12|12|3] roughness.

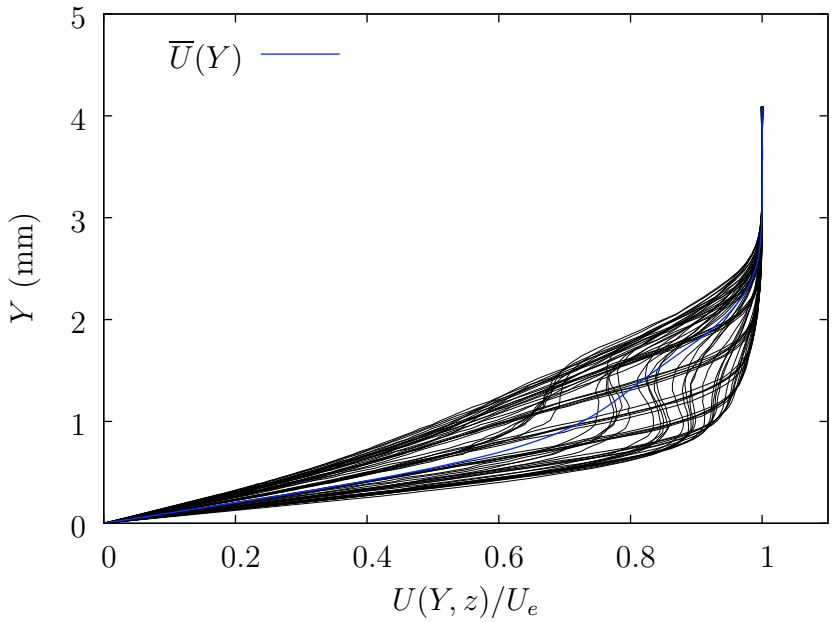

Figure C.5: Boundary-layer profiles at $x/c = 0.30$, $Re_c = 2.8 \times 10^6$, $Tu = 0.02\%$, [12|12|3] roughness.

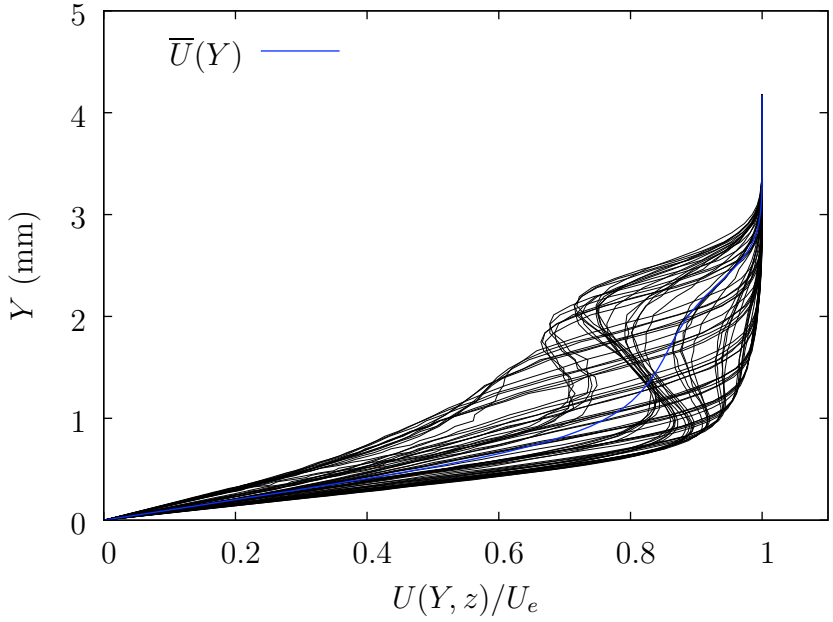

Figure C.6: Boundary-layer profiles at $x/c = 0.35$, $Re_c = 2.8 \times 10^6$, $Tu = 0.02\%$, [12|12|3] roughness.

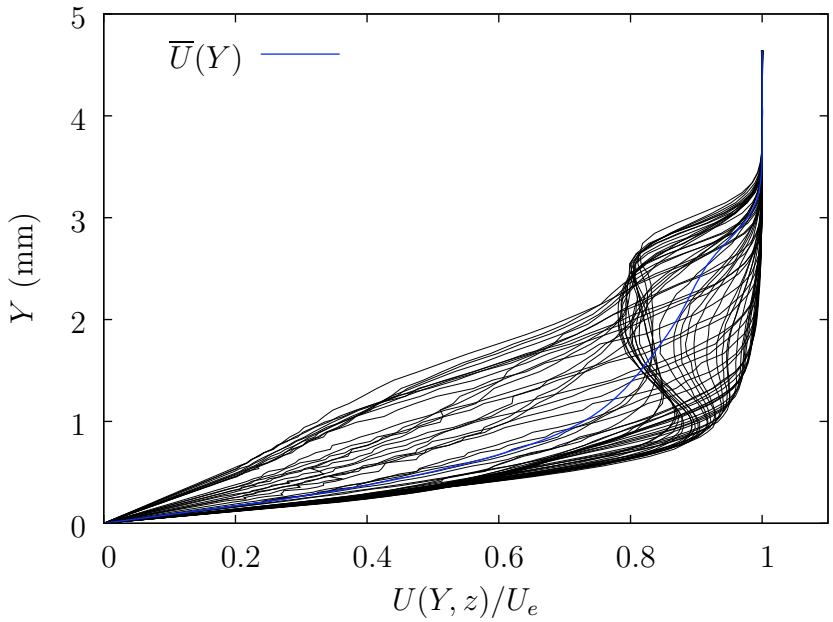

Figure C.7: Boundary-layer profiles at $x/c = 0.40$, $Re_c = 2.8 \times 10^6$, $Tu = 0.02\%$, [12|12|3] roughness.

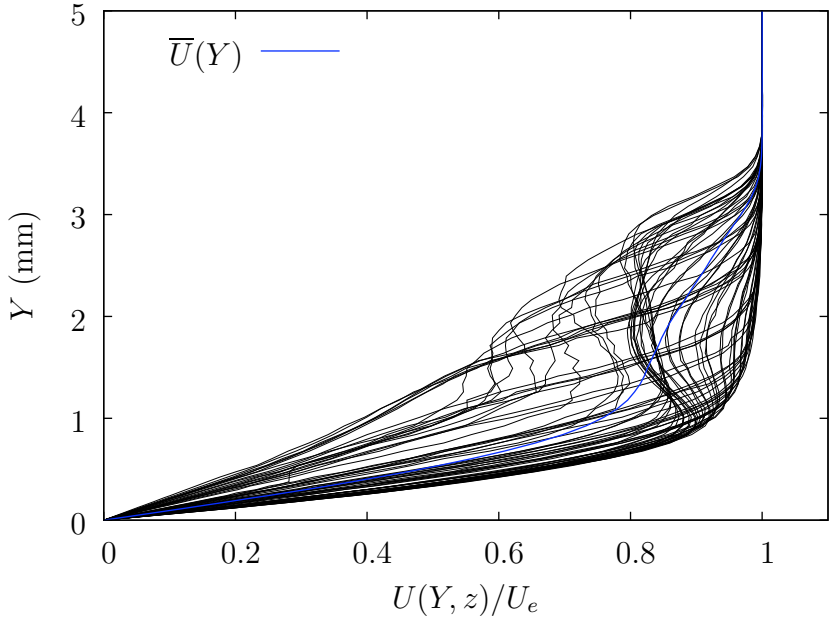

Figure C.8: Boundary-layer profiles at $x/c = 0.425$, $Re_c = 2.8 \times 10^6$, $Tu = 0.02\%$, [12|12|3] roughness.

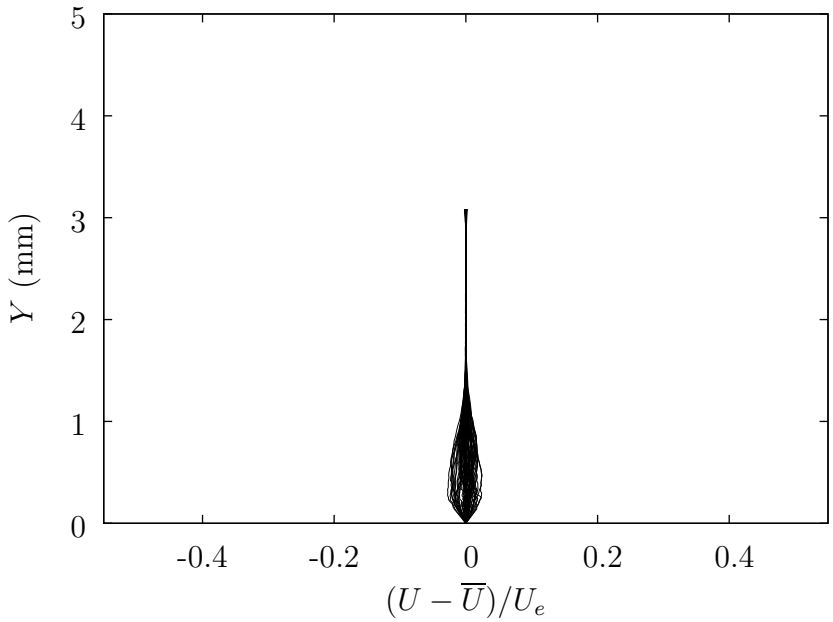

Figure C.9: Steady disturbance profiles at $x/c = 0.10$, $Re_c = 2.8 \times 10^6$, $Tu = 0.02\%$, [12|12|3] roughness.

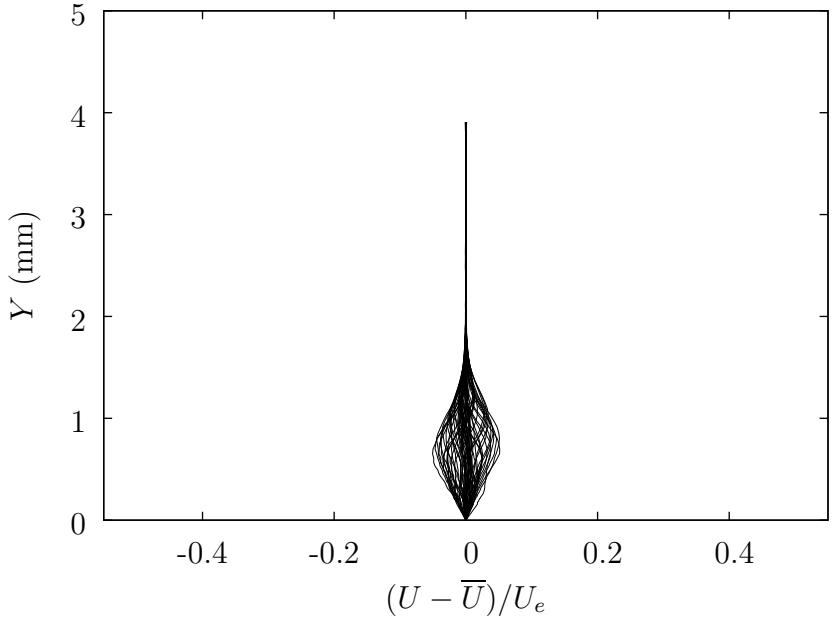

Figure C.10: Steady disturbance profiles at $x/c = 0.15$, $Re_c = 2.8 \times 10^6$, $Tu = 0.02\%$, [12|12|3] roughness.

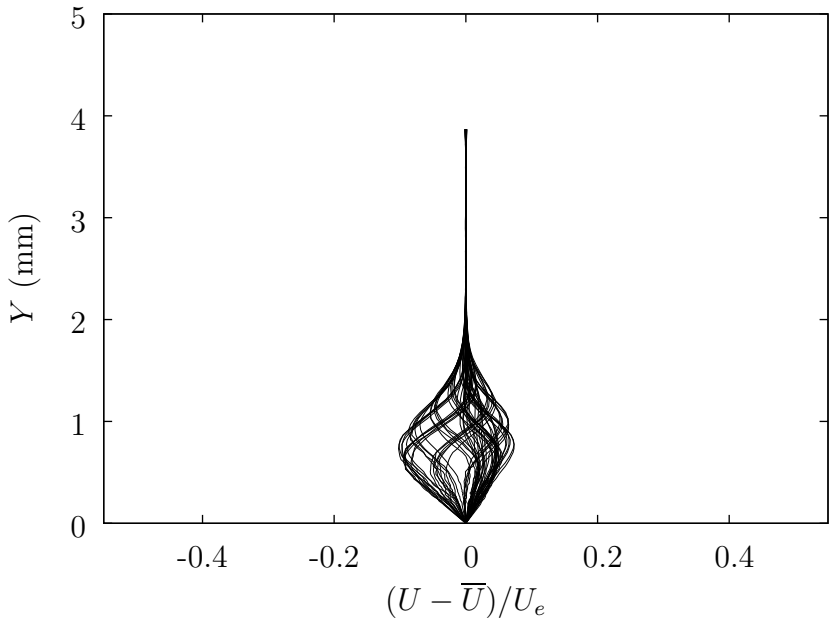

Figure C.11: Steady disturbance profiles at $x/c = 0.20$, $Re_c = 2.8 \times 10^6$, $Tu = 0.02\%$, [12|12|3] roughness.

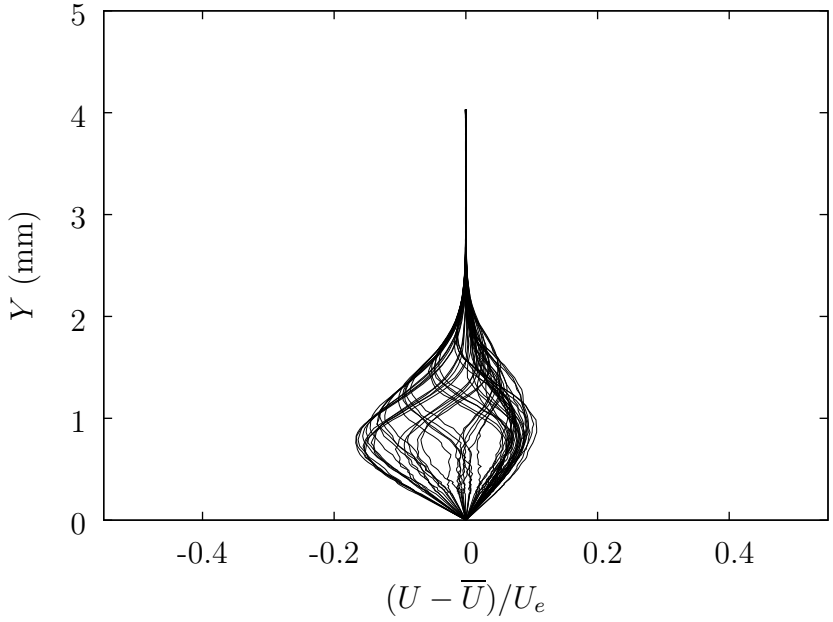

Figure C.12: Steady disturbance profiles at $x/c = 0.25$, $Re_c = 2.8 \times 10^6$, $Tu = 0.02\%$, [12|12|3] roughness.

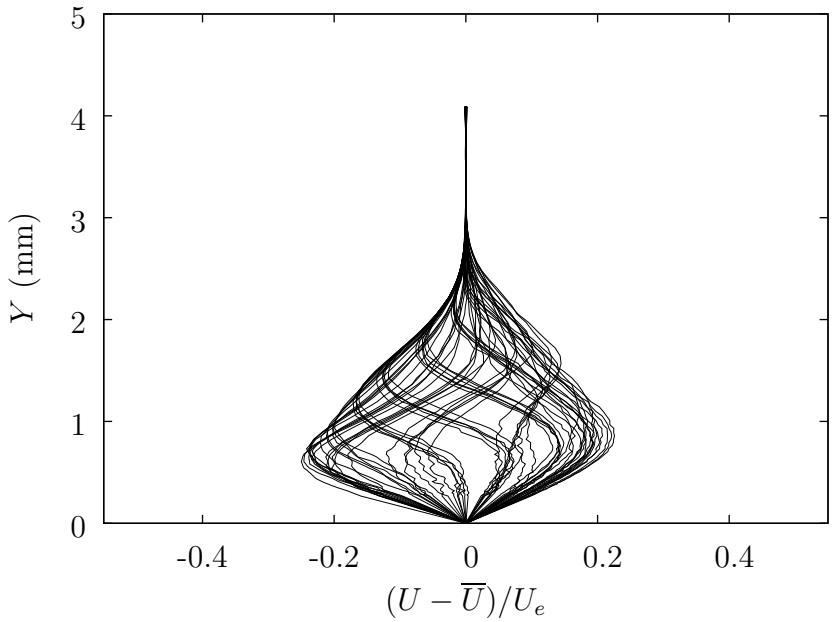

Figure C.13: Steady disturbance profiles at $x/c = 0.30$, $Re_c = 2.8 \times 10^6$, $Tu = 0.02\%$, [12|12|3] roughness.

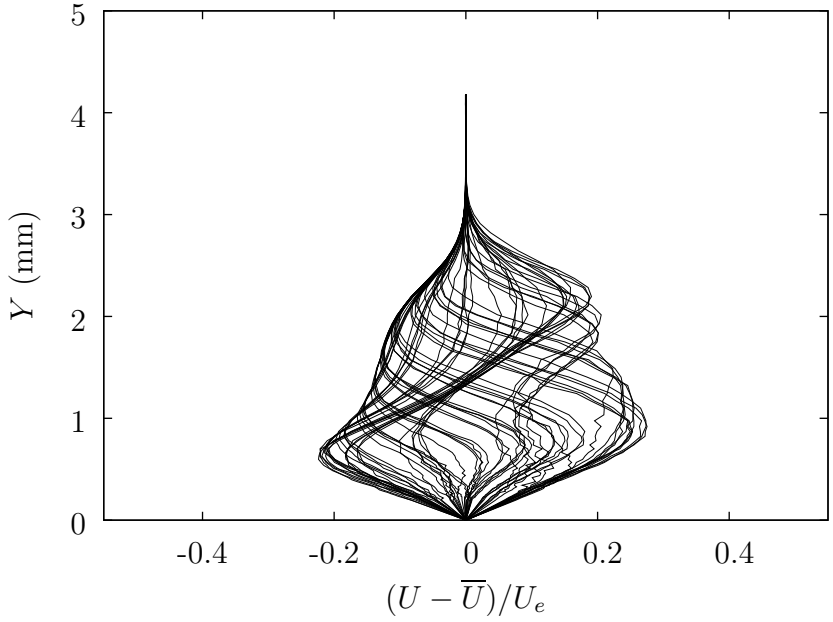

Figure C.14: Steady disturbance profiles at $x/c = 0.35$, $Re_c = 2.8 \times 10^6$, $Tu = 0.02\%$, [12|12|3] roughness.

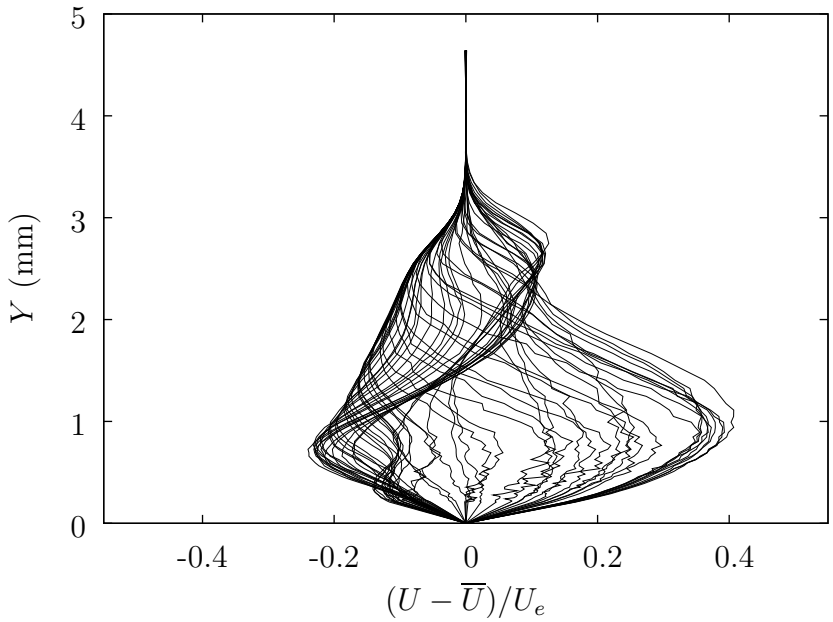

Figure C.15: Steady disturbance profiles at $x/c = 0.40$, $Re_c = 2.8 \times 10^6$, $Tu = 0.02\%$, [12|12|3] roughness.

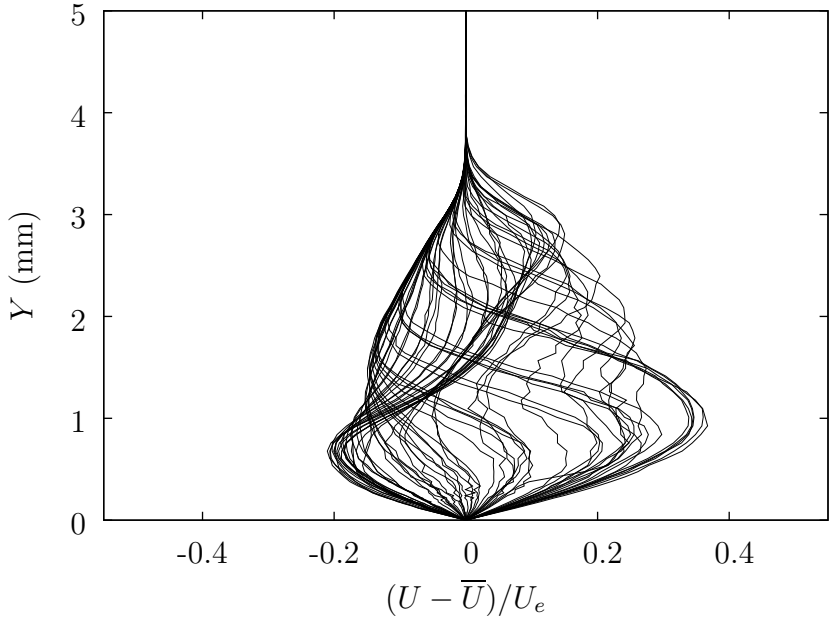

Figure C.16: Steady disturbance profiles at $x/c = 0.425$, $Re_c = 2.8 \times 10^6$, $Tu = 0.02\%$, [12|12|3] roughness.

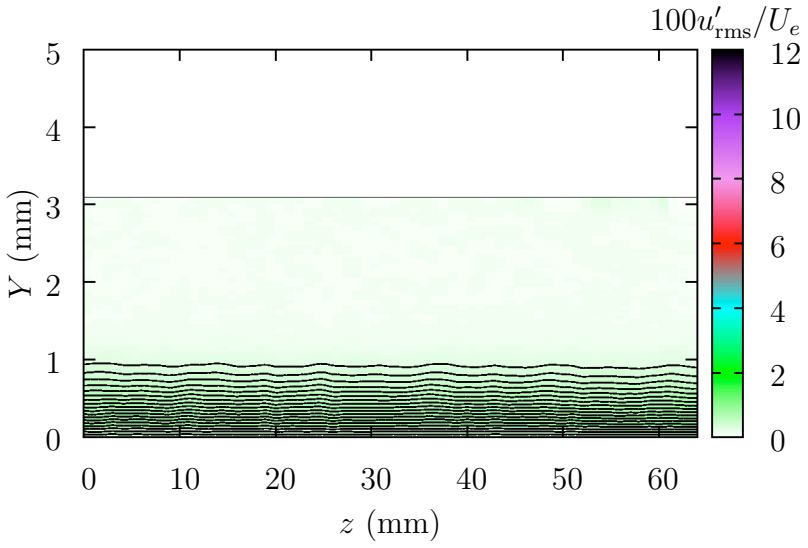

Figure C.17: U and u'_{rms} contours at $x/c = 0.10$, $Re_c = 2.8 \times 10^6$, $Tu = 0.02\%$, [12|12|3] roughness.

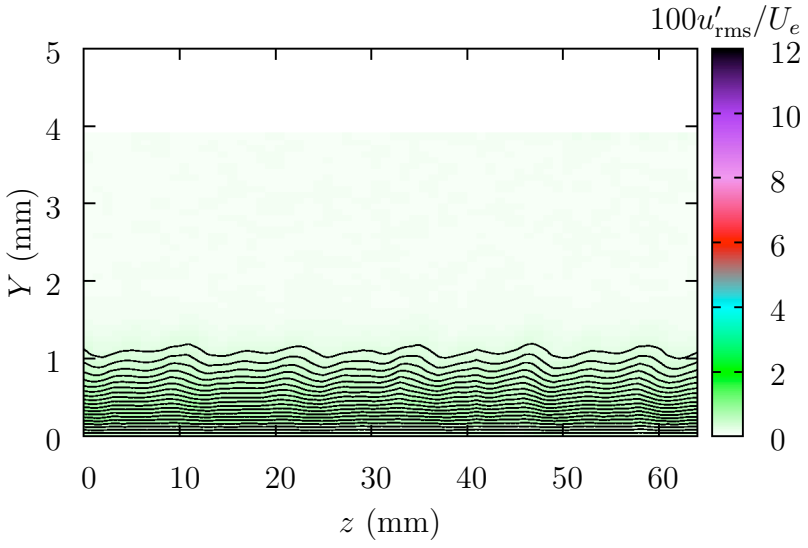

Figure C.18: U and u'_{rms} contours at $x/c = 0.15$, $Re_c = 2.8 \times 10^6$, $Tu = 0.02\%$, [12|12|3] roughness.

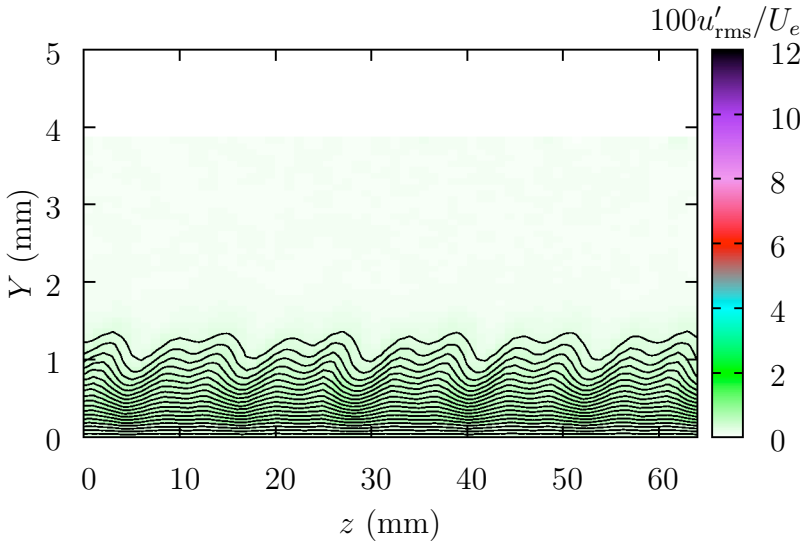

Figure C.19: U and u'_{rms} contours at $x/c = 0.20$, $Re_c = 2.8 \times 10^6$, $Tu = 0.02\%$, [12|12|3] roughness.

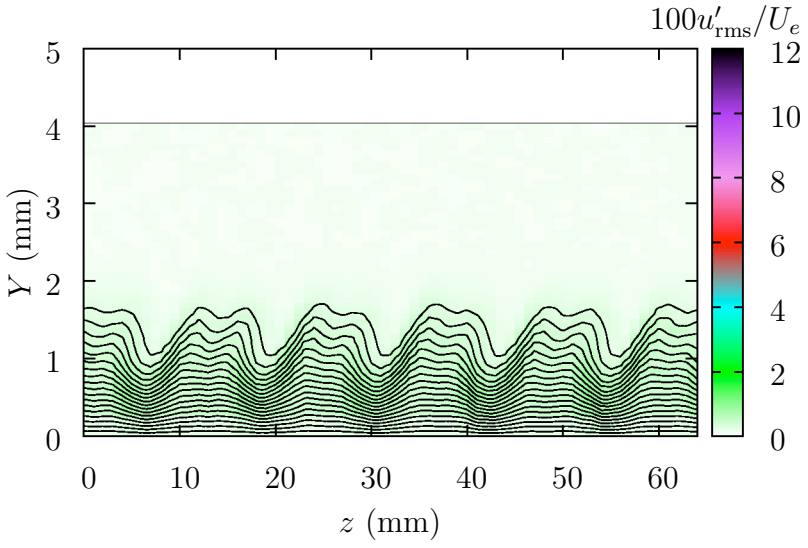

Figure C.20: U and u'_{rms} contours at $x/c = 0.25$, $Re_c = 2.8 \times 10^6$, $Tu = 0.02\%$, [12|12|3] roughness.

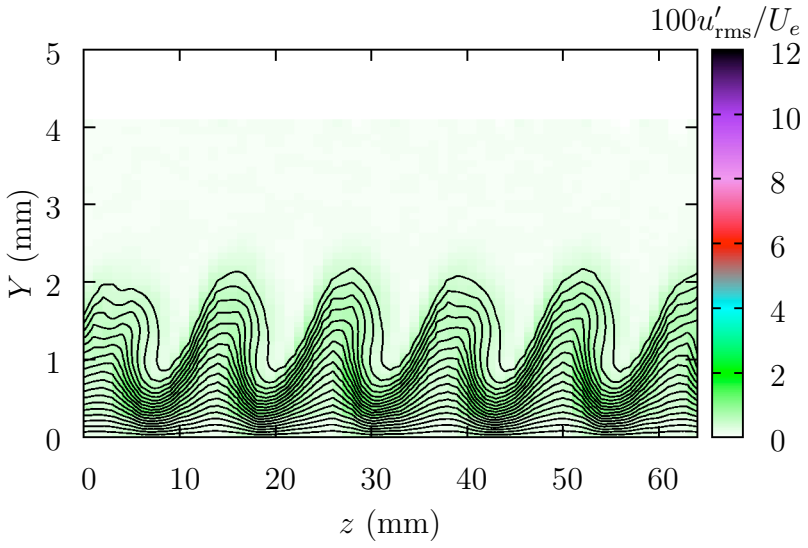

Figure C.21: U and u'_{rms} contours at $x/c = 0.30$, $Re_c = 2.8 \times 10^6$, $Tu = 0.02\%$, [12|12|3] roughness.

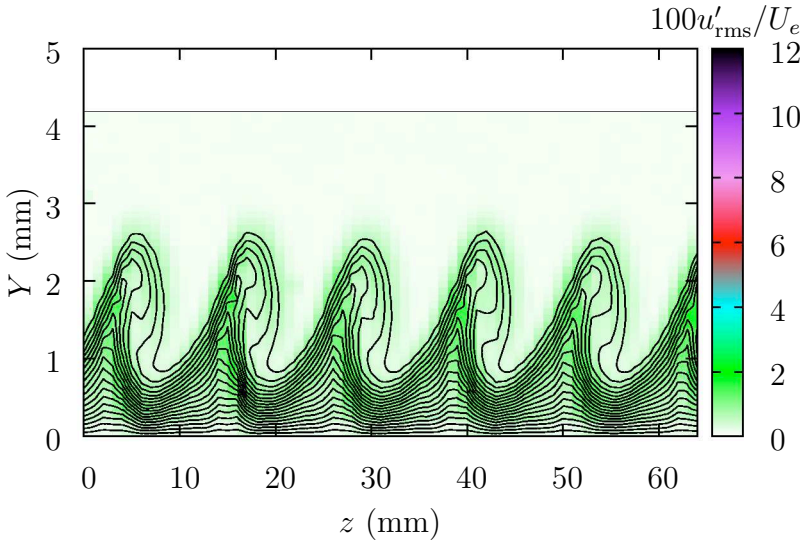

Figure C.22: U and u'_{rms} contours at $x/c = 0.35$, $Re_c = 2.8 \times 10^6$, $Tu = 0.02\%$, [12|12|3] roughness.

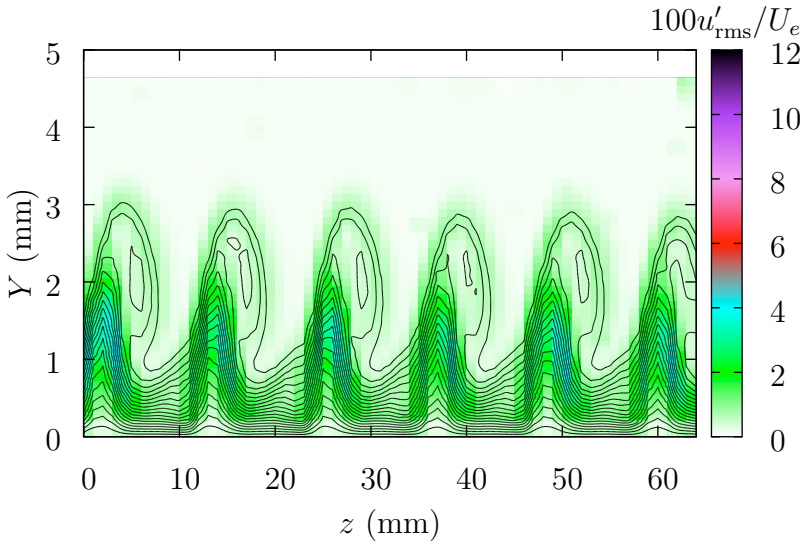

Figure C.23: U and u'_{rms} contours at $x/c = 0.40$, $Re_c = 2.8 \times 10^6$, $Tu = 0.02\%$, [12|12|3] roughness.

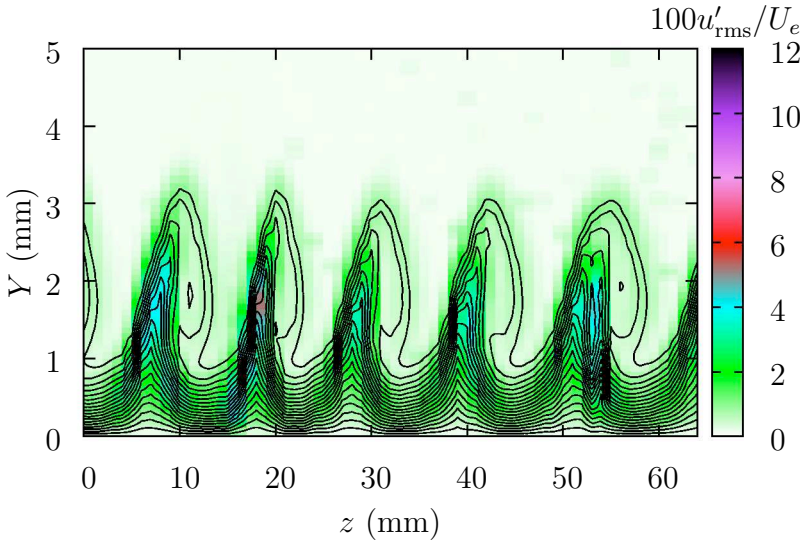

Figure C.24: U and u'_{rms} contours at $x/c = 0.425$, $Re_c = 2.8 \times 10^6$, $Tu = 0.02\%$, [12|12|3] roughness.

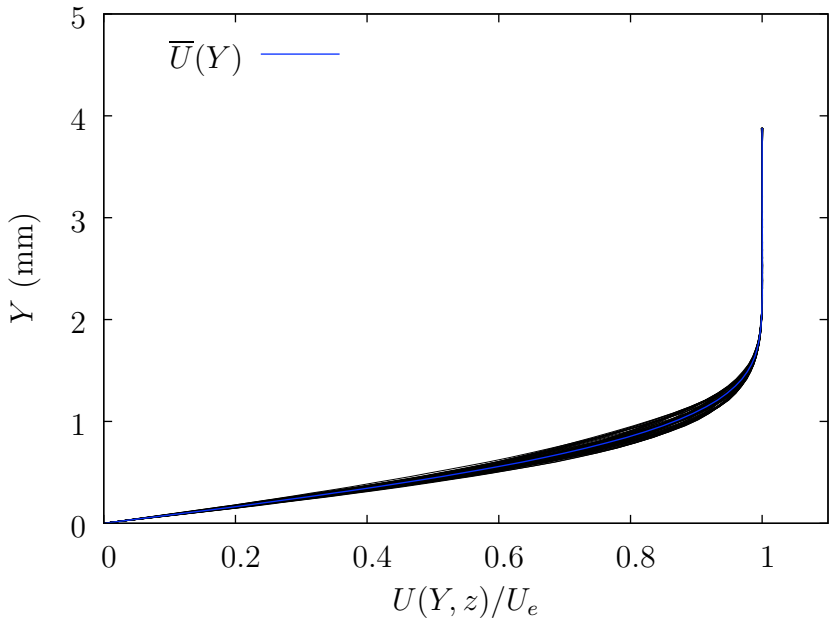

Figure C.25: Boundary-layer profiles at $x/c = 0.15$, $Re_c = 2.8 \times 10^6$, $Tu = 0.03\%$, [12|12|3] roughness.

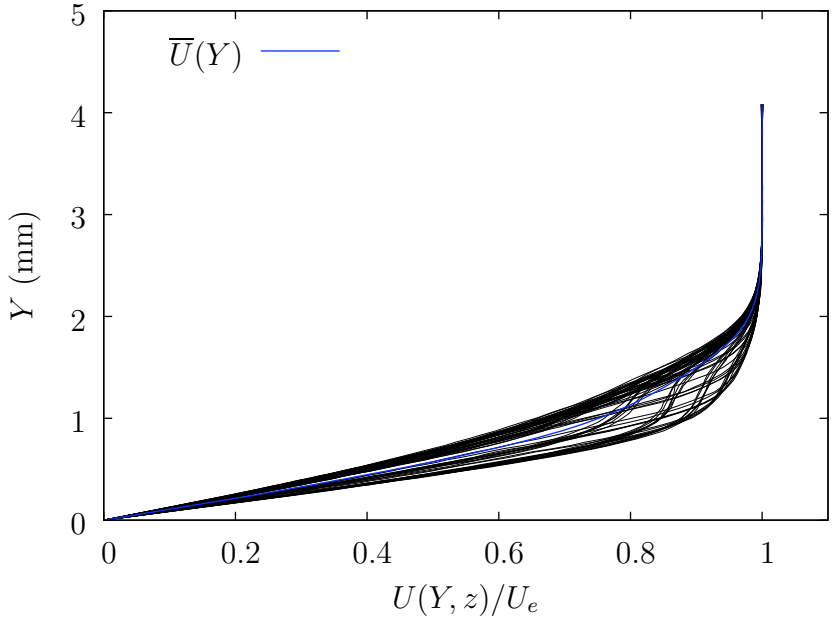

Figure C.26: Boundary-layer profiles at $x/c = 0.25$, $Re_c = 2.8 \times 10^6$, $Tu = 0.03\%$, [12|12|3] roughness.

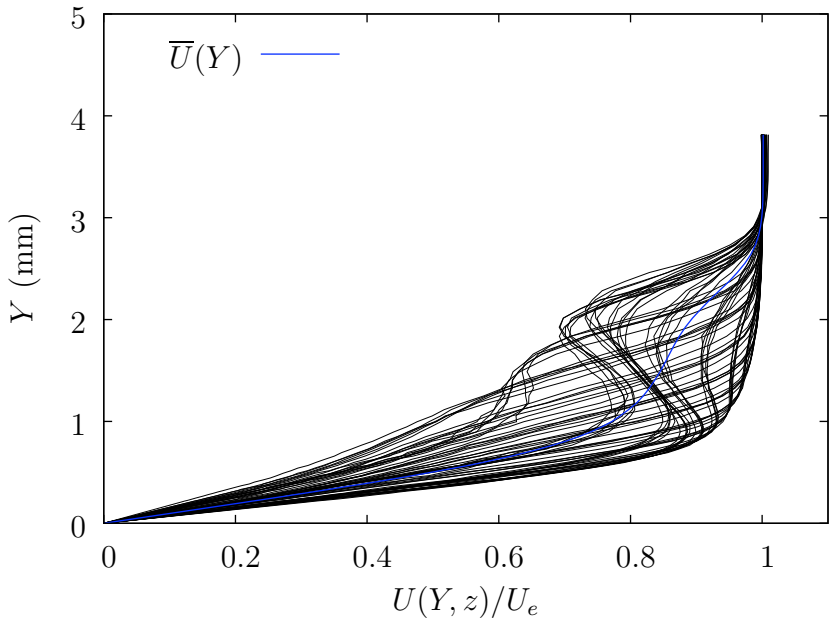

Figure C.27: Boundary-layer profiles at $x/c = 0.35$, $Re_c = 2.8 \times 10^6$, $Tu = 0.03\%$, [12|12|3] roughness.

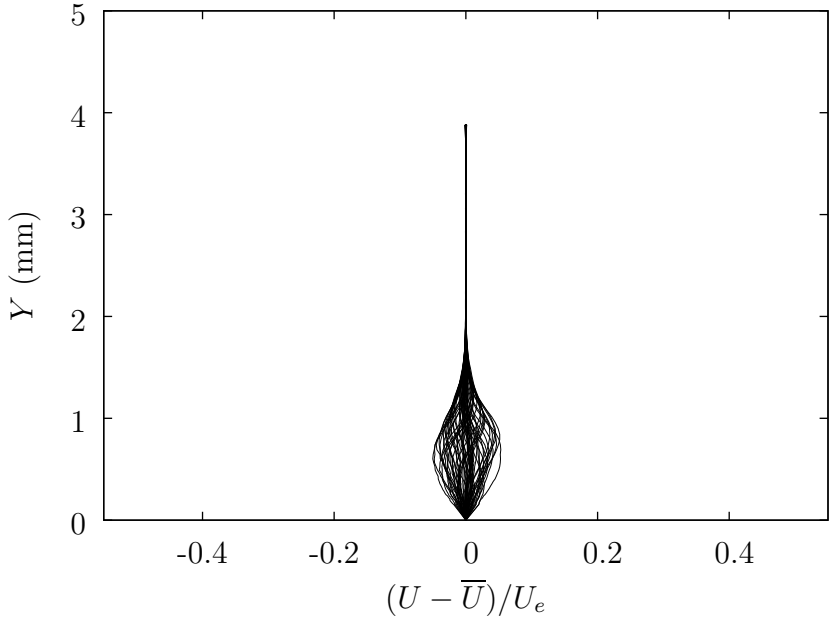

Figure C.28: Steady disturbance profiles at $x/c = 0.15$, $Re_c = 2.8 \times 10^6$, $Tu = 0.03\%$, [12|12|3] roughness.

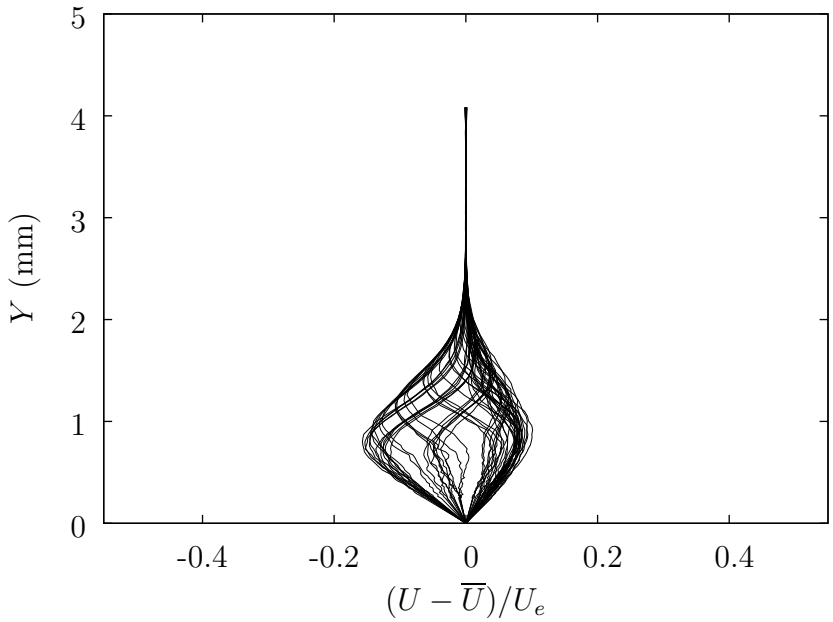

Figure C.29: Steady disturbance profiles at $x/c = 0.25$, $Re_c = 2.8 \times 10^6$, $Tu = 0.03\%$, [12|12|3] roughness.

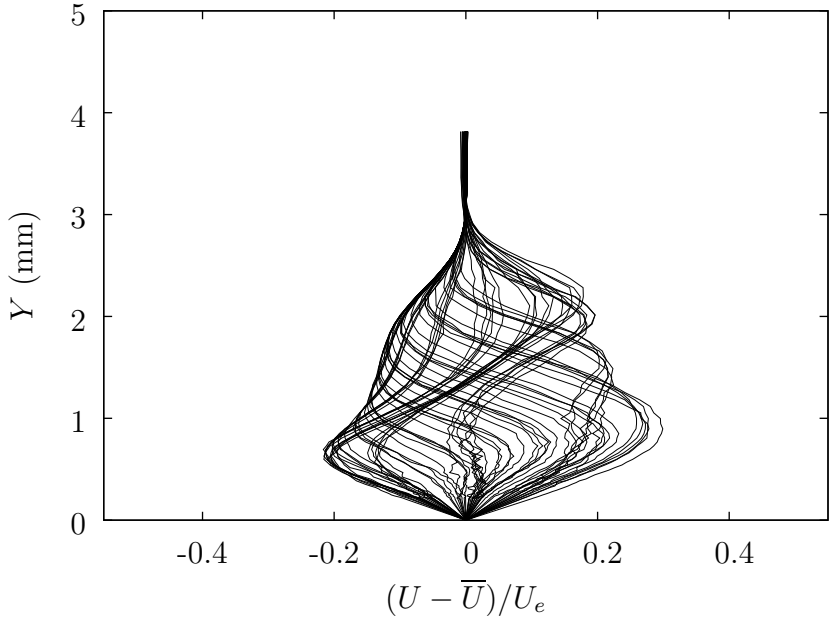

Figure C.30: Steady disturbance profiles at $x/c = 0.35$, $Re_c = 2.8 \times 10^6$, $Tu = 0.03\%$, [12|12|3] roughness.

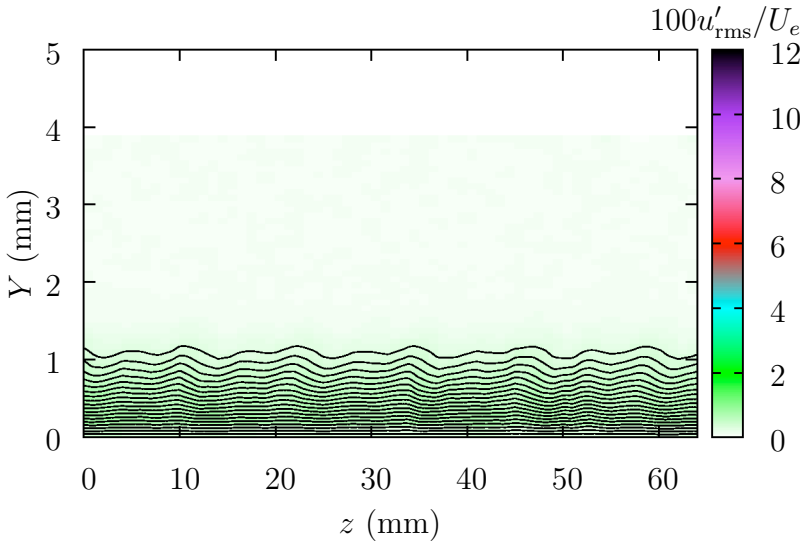

Figure C.31: U and u'_{rms} contours at $x/c = 0.15$, $Re_c = 2.8 \times 10^6$, $Tu = 0.03\%$, [12|12|3] roughness.

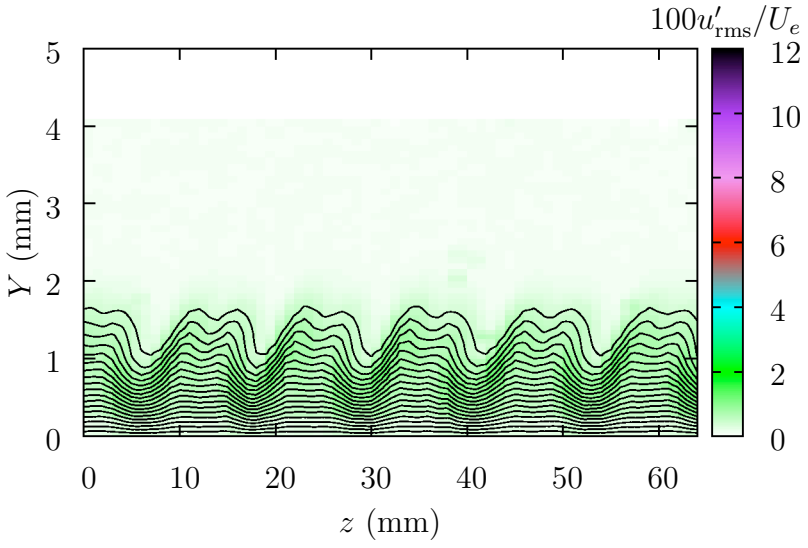

Figure C.32: U and u'_{rms} contours at $x/c = 0.25$, $Re_c = 2.8 \times 10^6$, $Tu = 0.03\%$, [12|12|3] roughness.

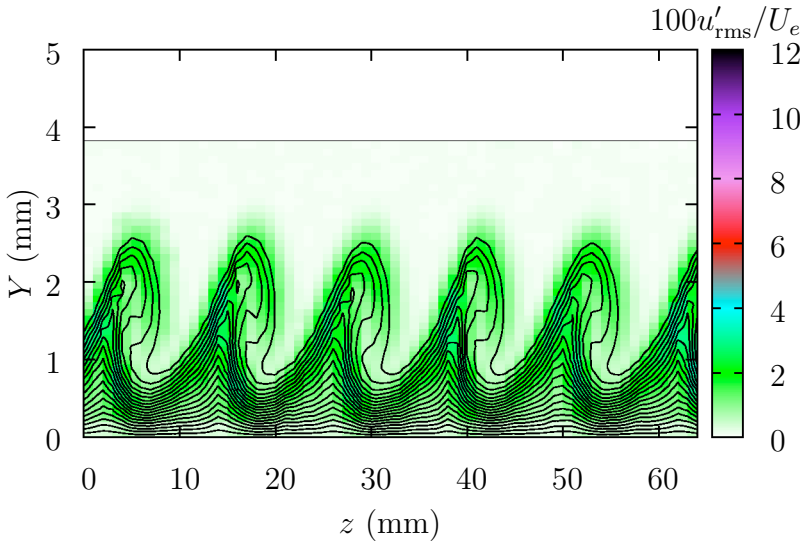

Figure C.33: U and u'_{rms} contours at $x/c = 0.35$, $Re_c = 2.8 \times 10^6$, $Tu = 0.03\%$, [12|12|3] roughness.

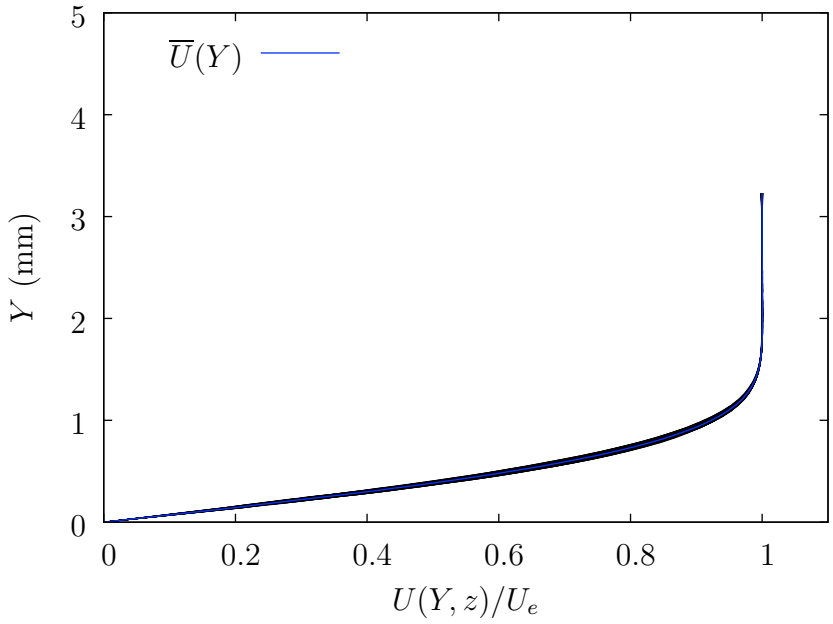

Figure C.34: Boundary-layer profiles at $x/c = 0.10$, $Re_c = 2.8 \times 10^6$, $Tu = 0.05\%$, [12|12|3] roughness.

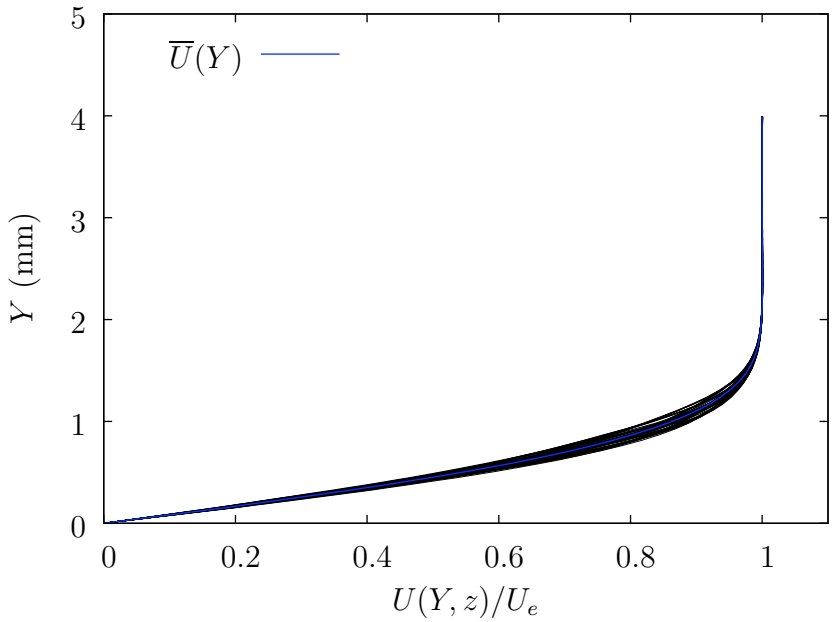

Figure C.35: Boundary-layer profiles at $x/c = 0.15$, $Re_c = 2.8 \times 10^6$, $Tu = 0.05\%$, [12|12|3] roughness.

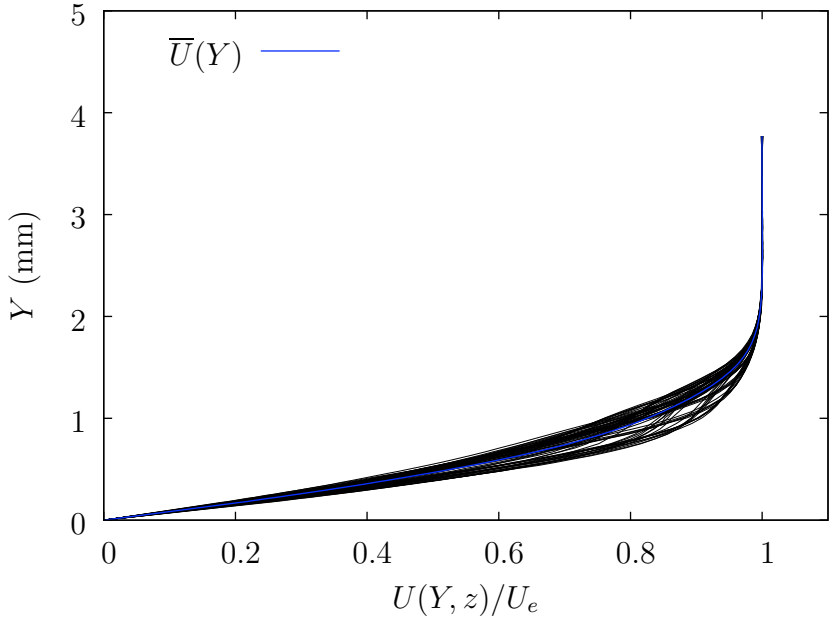

Figure C.36: Boundary-layer profiles at $x/c = 0.20$, $Re_c = 2.8 \times 10^6$, $Tu = 0.05\%$, [12|12|3] roughness.

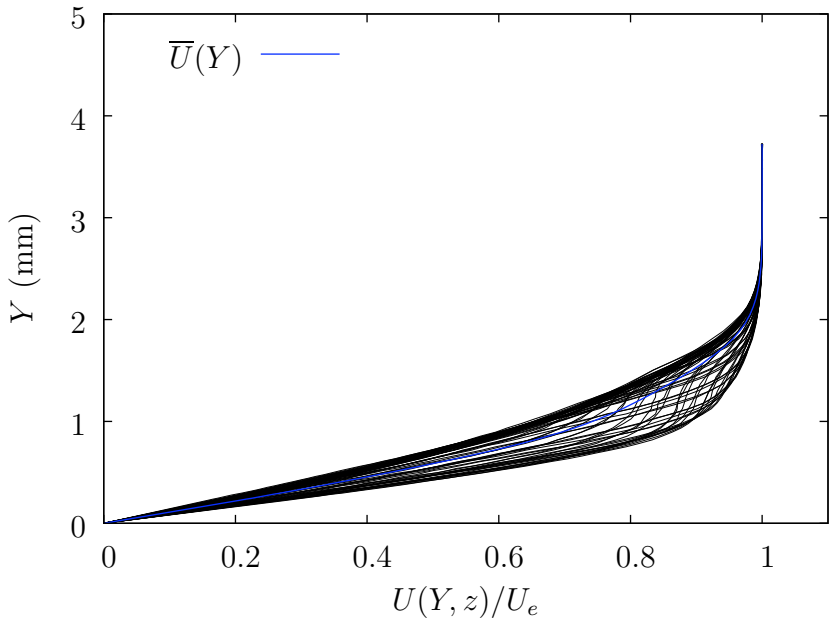

Figure C.37: Boundary-layer profiles at $x/c = 0.25$, $Re_c = 2.8 \times 10^6$, $Tu = 0.05\%$, [12|12|3] roughness.

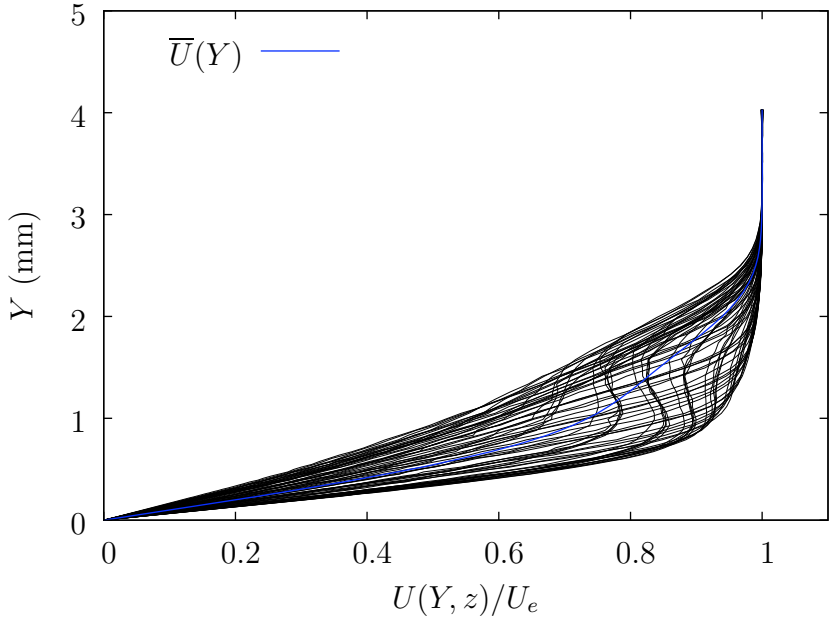

Figure C.38: Boundary-layer profiles at $x/c = 0.30$, $Re_c = 2.8 \times 10^6$, $Tu = 0.05\%$, [12|12|3] roughness.

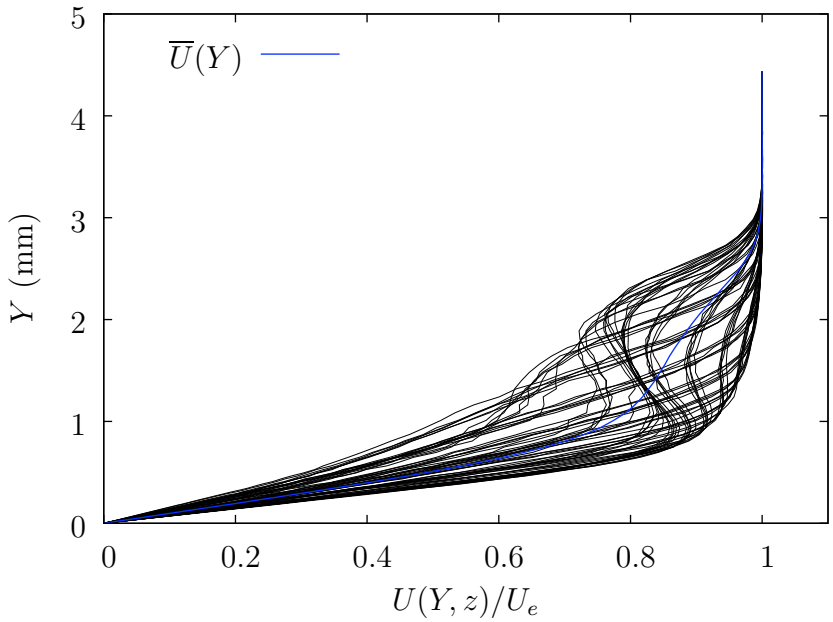

Figure C.39: Boundary-layer profiles at $x/c = 0.35$, $Re_c = 2.8 \times 10^6$, $Tu = 0.05\%$, [12|12|3] roughness.

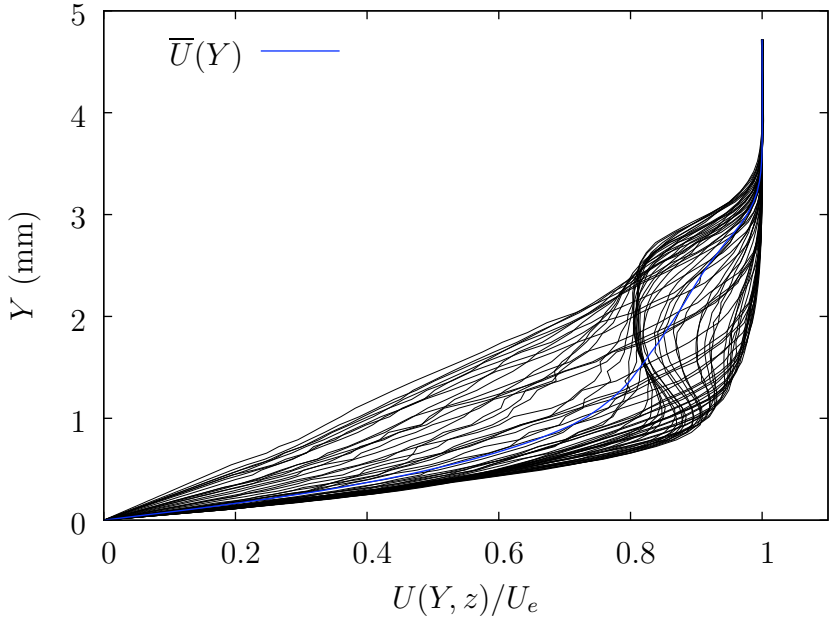

Figure C.40: Boundary-layer profiles at $x/c = 0.40$, $Re_c = 2.8 \times 10^6$, $Tu = 0.05\%$, [12|12|3] roughness.

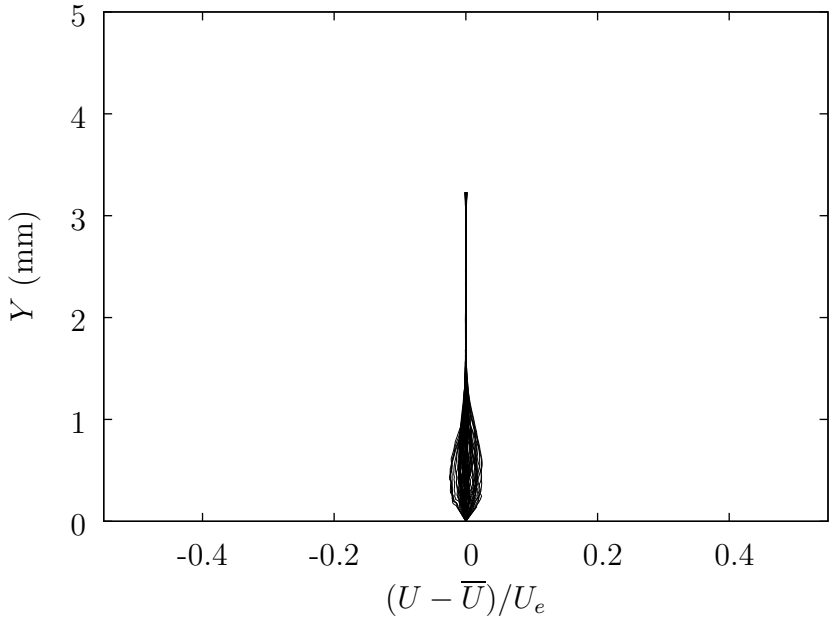

Figure C.41: Steady disturbance profiles at $x/c = 0.10$, $Re_c = 2.8 \times 10^6$, $Tu = 0.05\%$, [12|12|3] roughness.

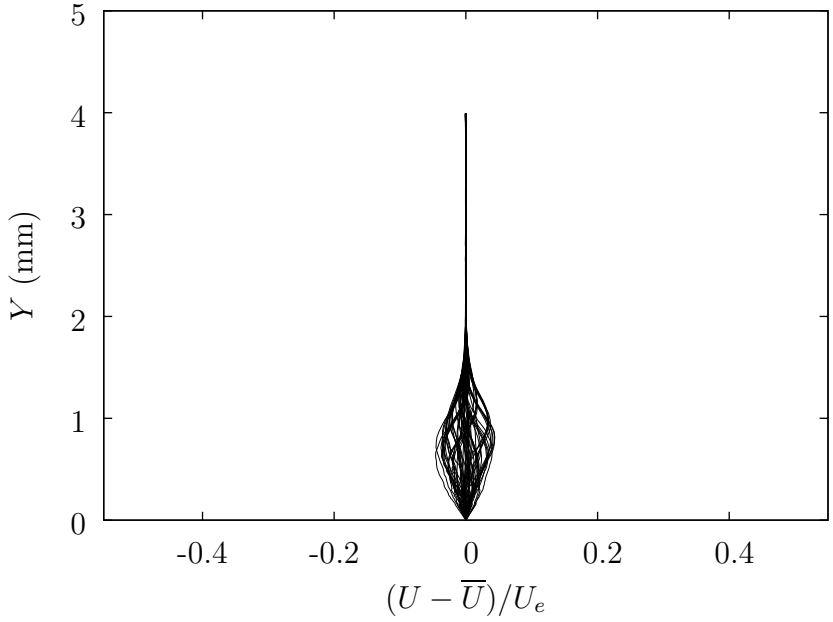

Figure C.42: Steady disturbance profiles at $x/c = 0.15$, $Re_c = 2.8 \times 10^6$, $Tu = 0.05\%$, [12|12|3] roughness.

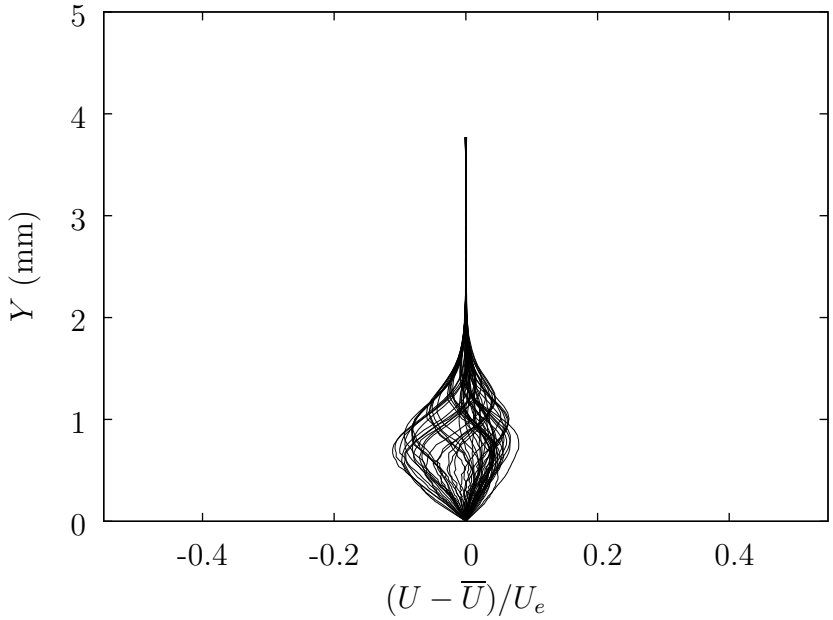

Figure C.43: Steady disturbance profiles at $x/c = 0.20$, $Re_c = 2.8 \times 10^6$, $Tu = 0.05\%$, [12|12|3] roughness.

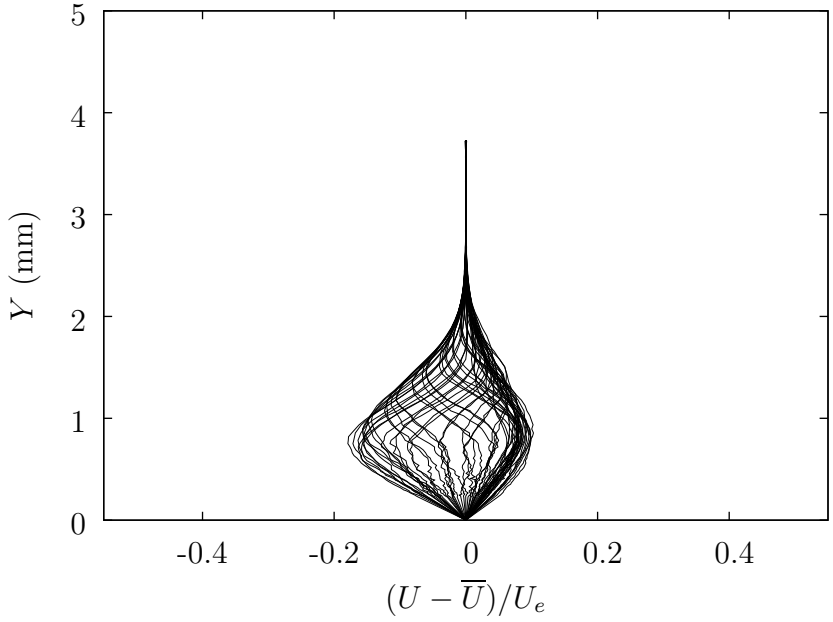

Figure C.44: Steady disturbance profiles at $x/c = 0.25$, $Re_c = 2.8 \times 10^6$, $Tu = 0.05\%$, [12|12|3] roughness.

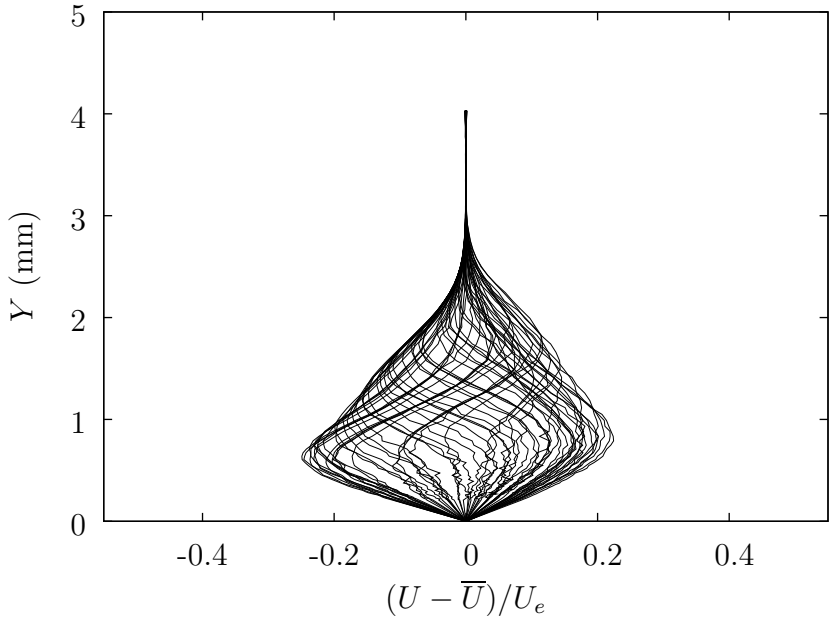

Figure C.45: Steady disturbance profiles at $x/c = 0.30$, $Re_c = 2.8 \times 10^6$, $Tu = 0.05\%$, [12|12|3] roughness.

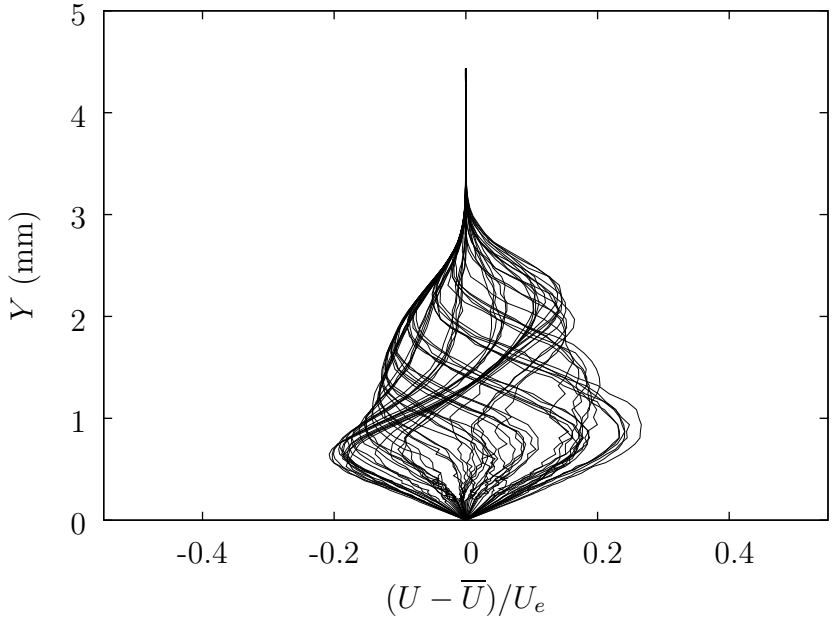

Figure C.46: Steady disturbance profiles at $x/c = 0.35$, $Re_c = 2.8 \times 10^6$, $Tu = 0.05\%$, [12|12|3] roughness.

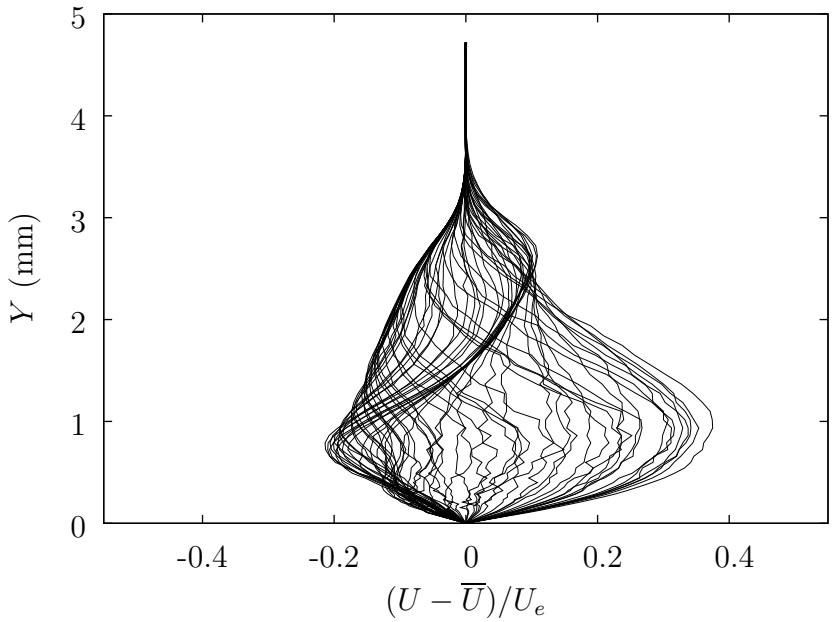

Figure C.47: Steady disturbance profiles at $x/c = 0.40$, $Re_c = 2.8 \times 10^6$, $Tu = 0.05\%$, [12|12|3] roughness.

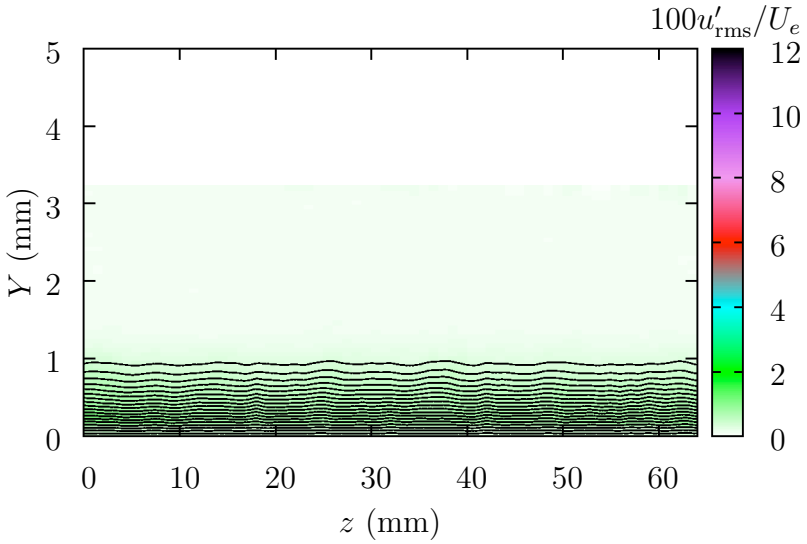

Figure C.48: U and u'_{rms} contours at $x/c = 0.10$, $Re_c = 2.8 \times 10^6$, $Tu = 0.05\%$, [12|12|3] roughness.

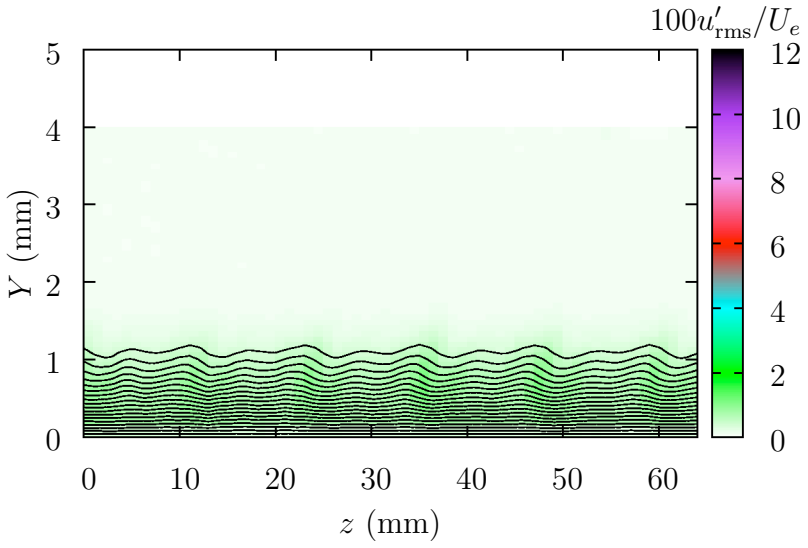

Figure C.49: U and u'_{rms} contours at $x/c = 0.15$, $Re_c = 2.8 \times 10^6$, $Tu = 0.05\%$, [12|12|3] roughness.

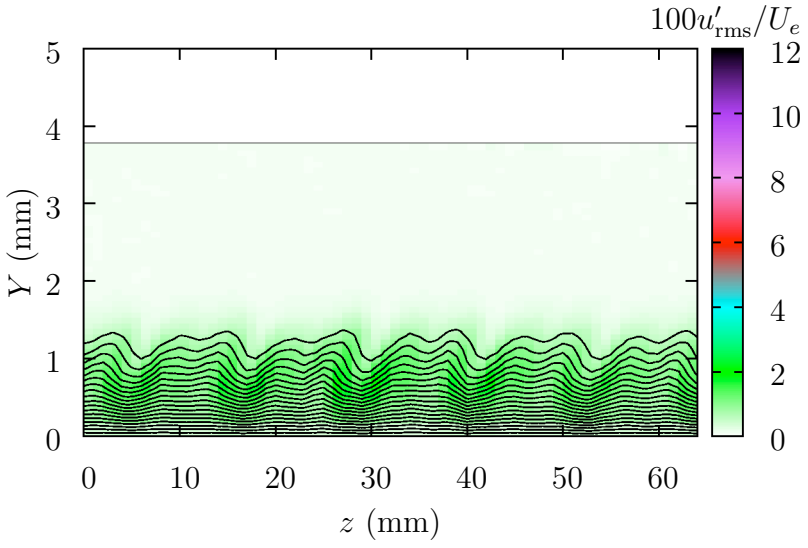

Figure C.50: U and u'_{rms} contours at $x/c = 0.20$, $Re_c = 2.8 \times 10^6$, $Tu = 0.05\%$, [12|12|3] roughness.

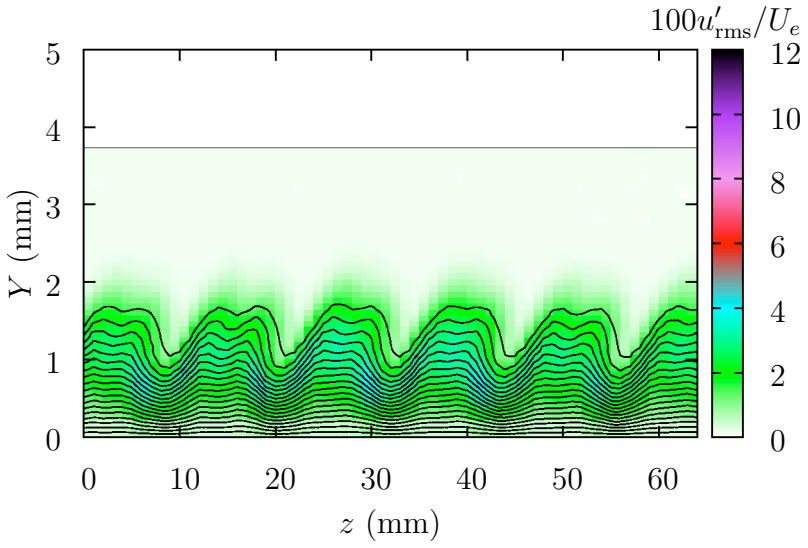

Figure C.51: U and u'_{rms} contours at $x/c = 0.25$, $Re_c = 2.8 \times 10^6$, $Tu = 0.05\%$, [12|12|3] roughness.

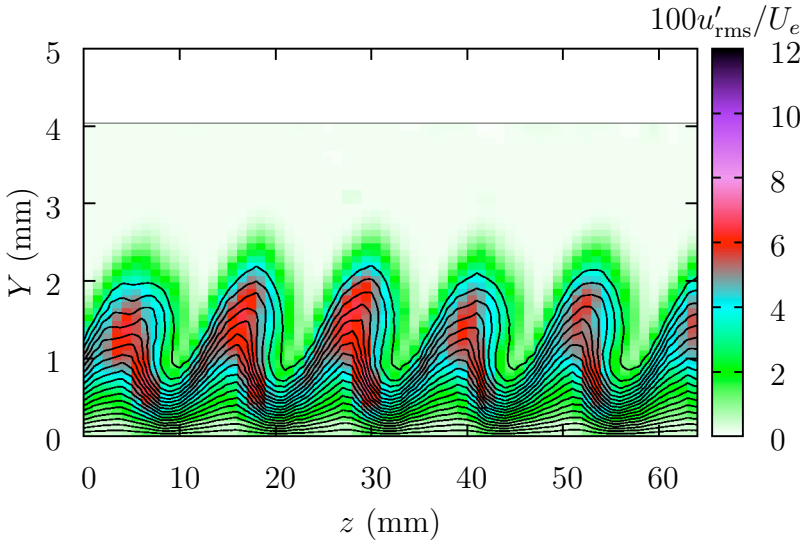

Figure C.52: U and u'_{rms} contours at $x/c = 0.30$, $Re_c = 2.8 \times 10^6$, $Tu = 0.05\%$, [12|12|3] roughness.

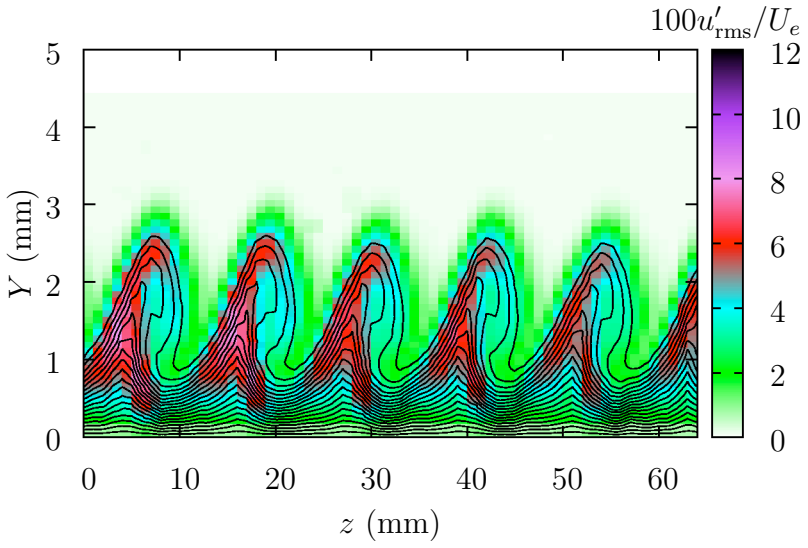

Figure C.53: U and u'_{rms} contours at $x/c = 0.35$, $Re_c = 2.8 \times 10^6$, $Tu = 0.05\%$, [12|12|3] roughness.

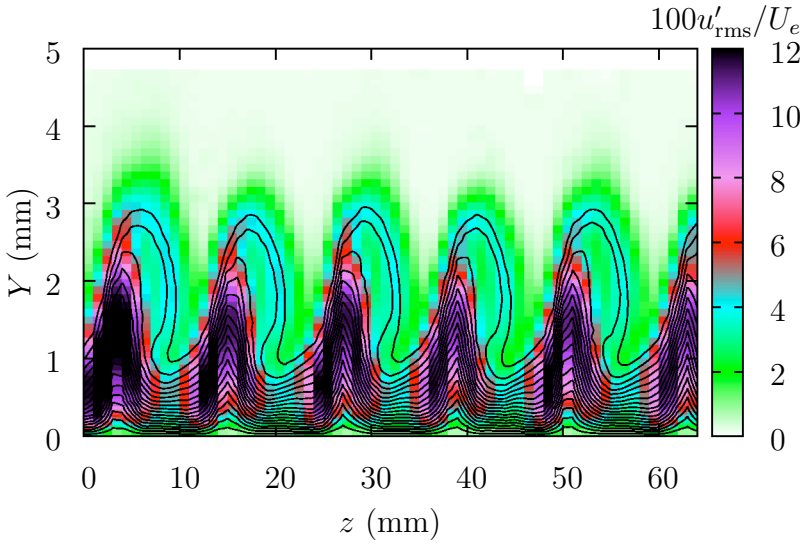

Figure C.54: U and u'_{rms} contours at $x/c = 0.40$, $Re_c = 2.8 \times 10^6$, $Tu = 0.05\%$, [12|12|3] roughness.

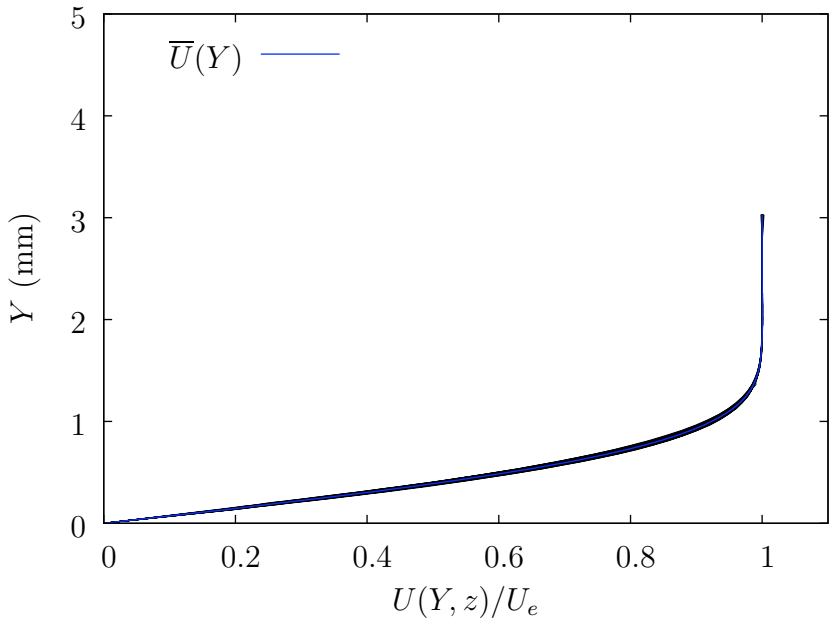

Figure C.55: Boundary-layer profiles at $x/c = 0.10$, $Re_c = 2.8 \times 10^6$, $Tu = 0.19\%$, [12|12|3] roughness.

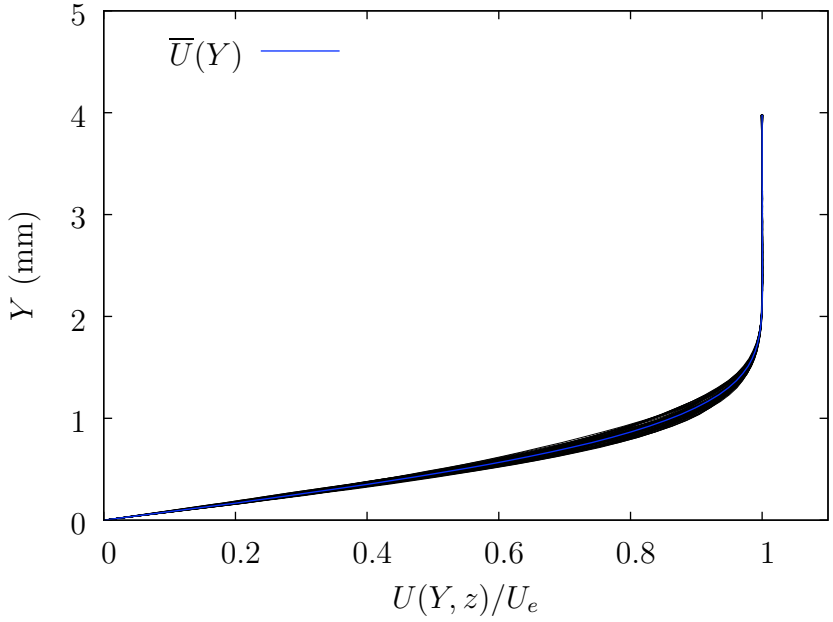

Figure C.56: Boundary-layer profiles at $x/c = 0.15$, $Re_c = 2.8 \times 10^6$, $Tu = 0.19\%$, [12|12|3] roughness.

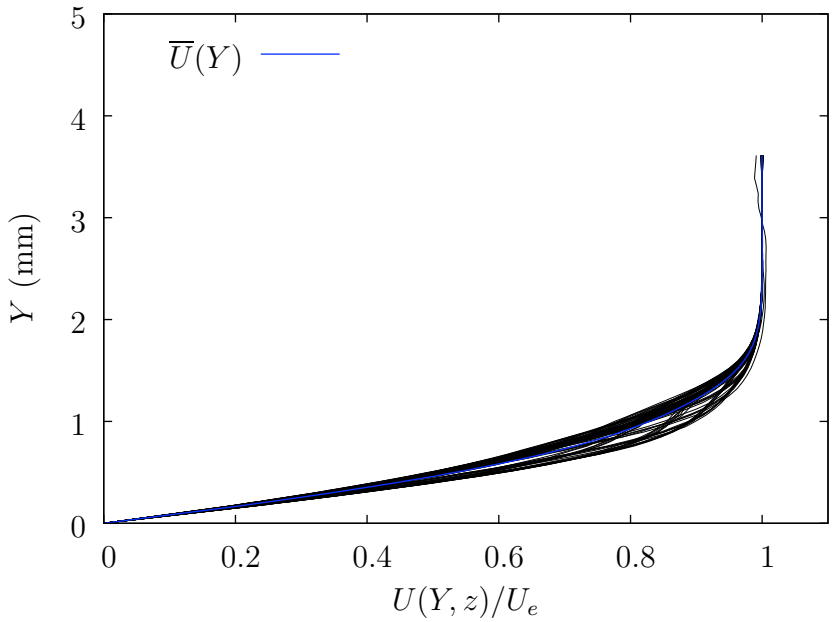

Figure C.57: Boundary-layer profiles at $x/c = 0.20$, $Re_c = 2.8 \times 10^6$, $Tu = 0.19\%$, [12|12|3] roughness.

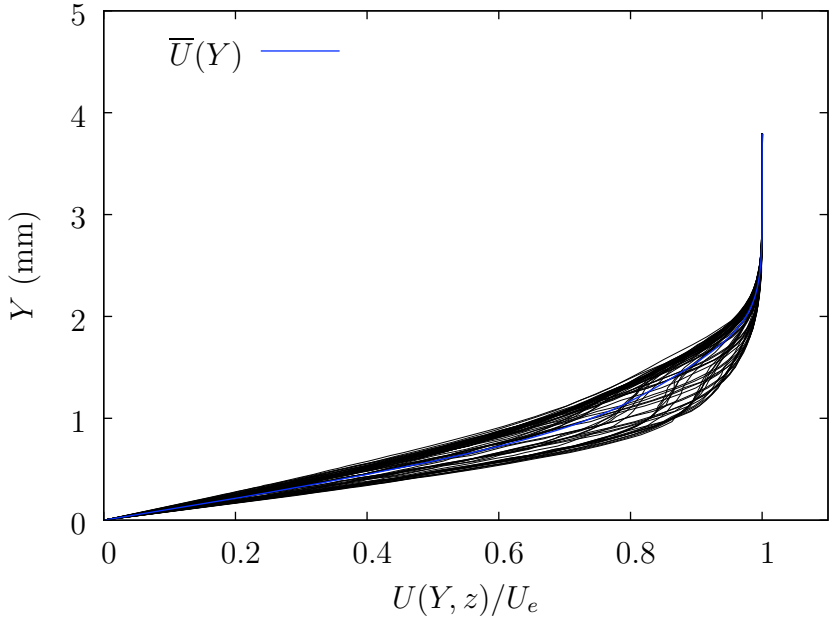

Figure C.58: Boundary-layer profiles at $x/c = 0.25$, $Re_c = 2.8 \times 10^6$, $Tu = 0.19\%$, [12|12|3] roughness.

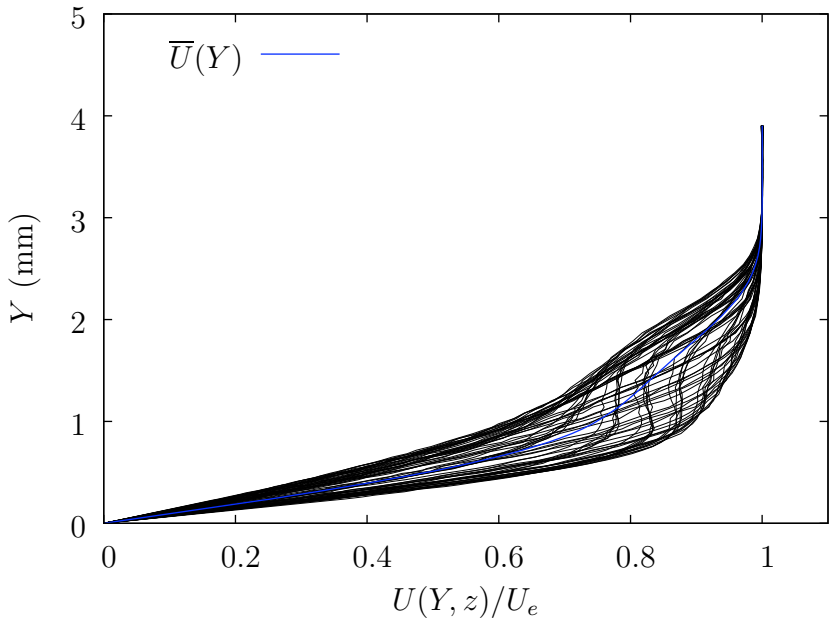

Figure C.59: Boundary-layer profiles at $x/c = 0.30$, $Re_c = 2.8 \times 10^6$, $Tu = 0.19\%$, [12|12|3] roughness.

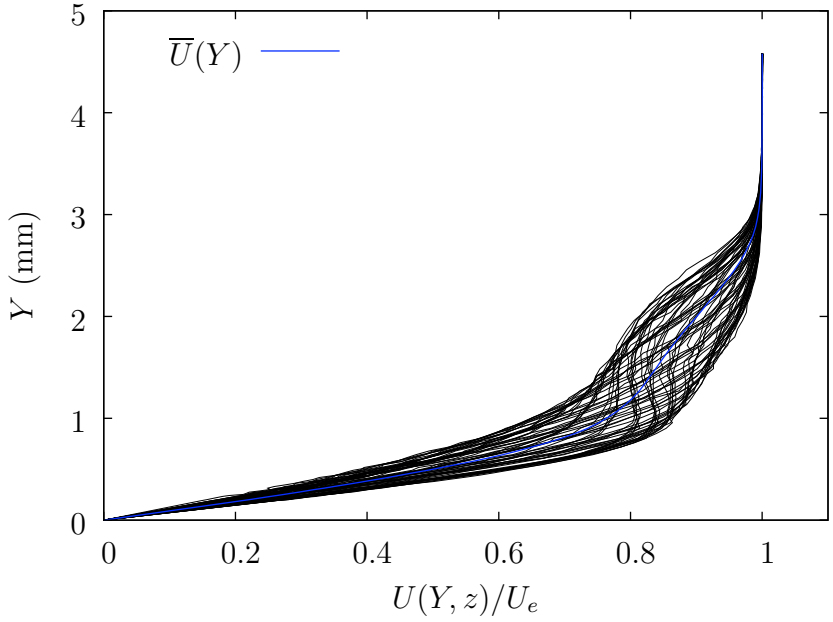

Figure C.60: Boundary-layer profiles at $x/c = 0.35$, $Re_c = 2.8 \times 10^6$, $Tu = 0.19\%$, [12|12|3] roughness.

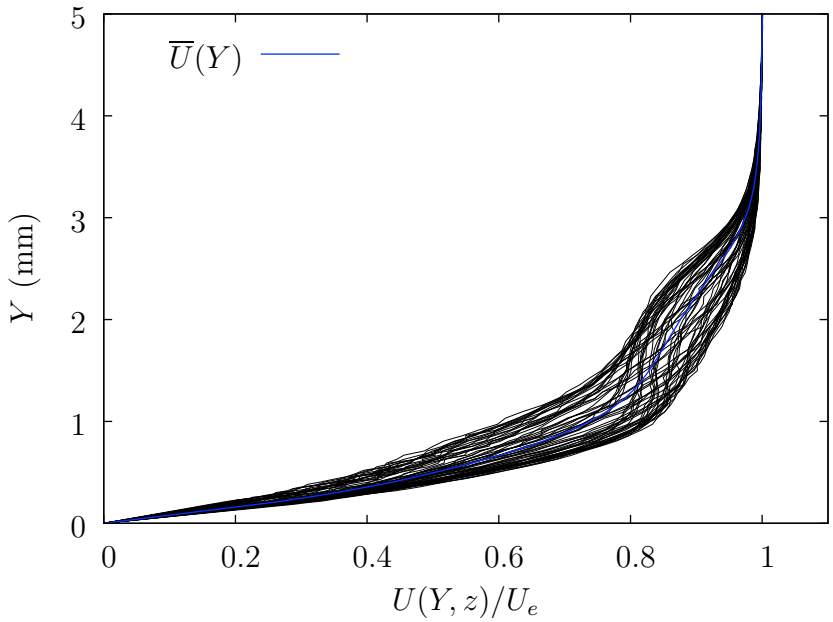

Figure C.61: Boundary-layer profiles at $x/c = 0.375$, $Re_c = 2.8 \times 10^6$, $Tu = 0.19\%$, [12|12|3] roughness.

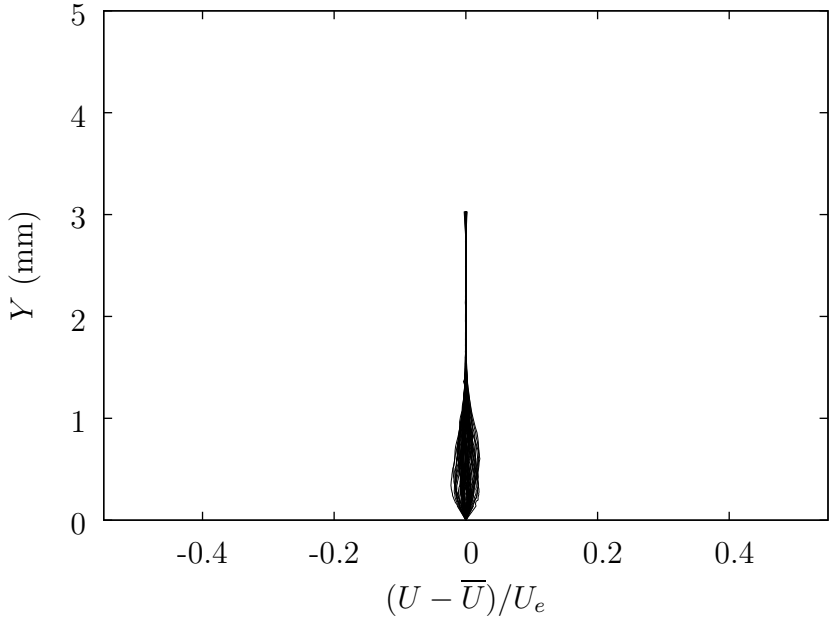

Figure C.62: Steady disturbance profiles at $x/c = 0.10$, $Re_c = 2.8 \times 10^6$, $Tu = 0.19\%$, [12|12|3] roughness.

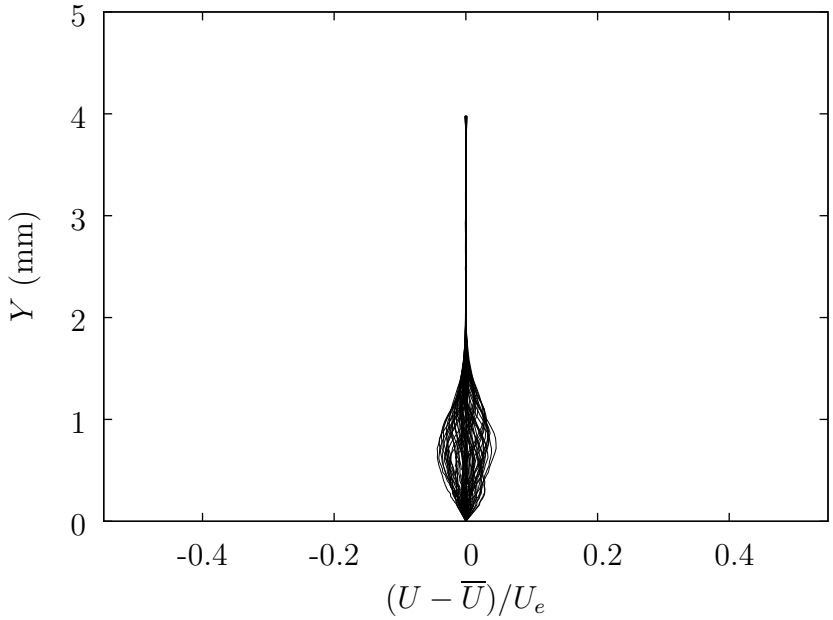

Figure C.63: Steady disturbance profiles at $x/c = 0.15$, $Re_c = 2.8 \times 10^6$, $Tu = 0.19\%$, [12|12|3] roughness.

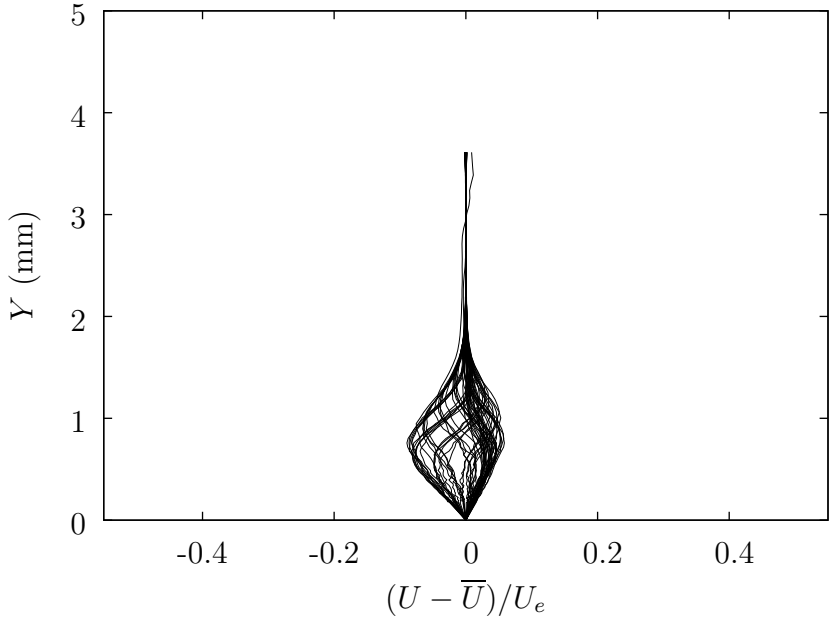

Figure C.64: Steady disturbance profiles at $x/c = 0.20$, $Re_c = 2.8 \times 10^6$, $Tu = 0.19\%$, [12|12|3] roughness.

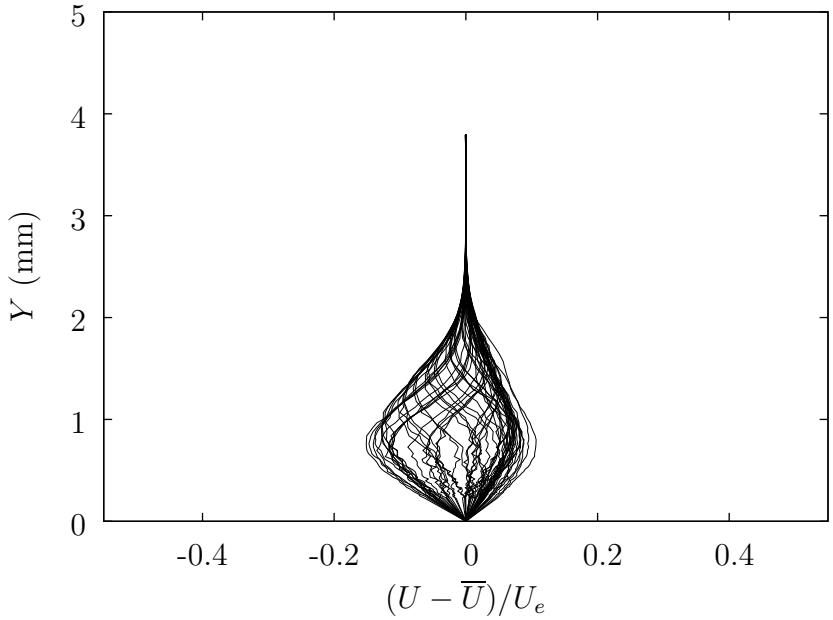

Figure C.65: Steady disturbance profiles at $x/c = 0.25$, $Re_c = 2.8 \times 10^6$, $Tu = 0.19\%$, [12|12|3] roughness.

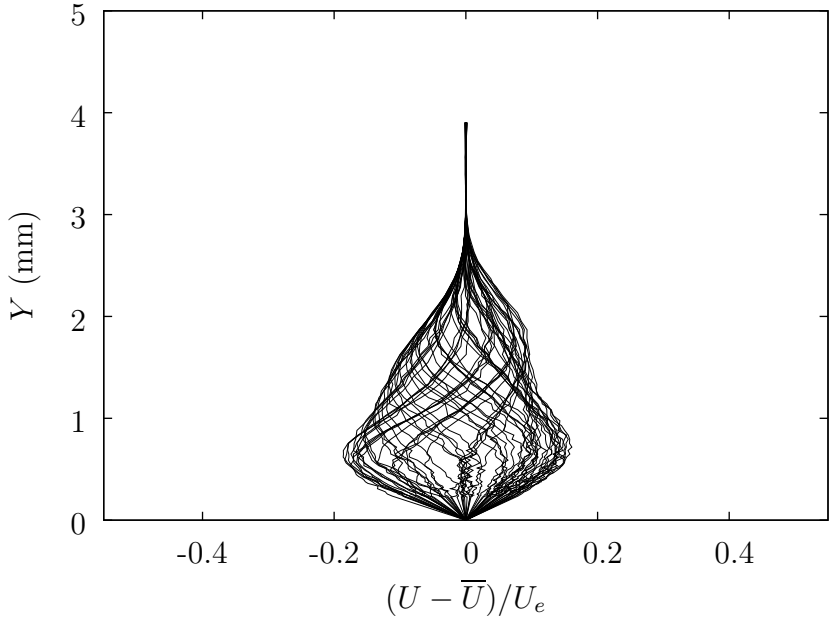

Figure C.66: Steady disturbance profiles at $x/c = 0.30$, $Re_c = 2.8 \times 10^6$, $Tu = 0.19\%$, [12|12|3] roughness.

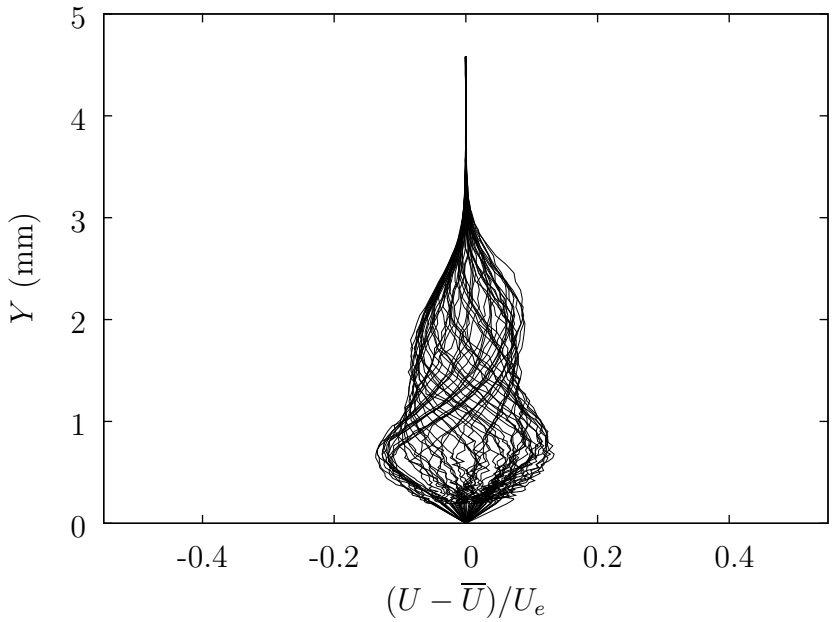

Figure C.67: Steady disturbance profiles at $x/c = 0.35$, $Re_c = 2.8 \times 10^6$, $Tu = 0.19\%$, [12|12|3] roughness.

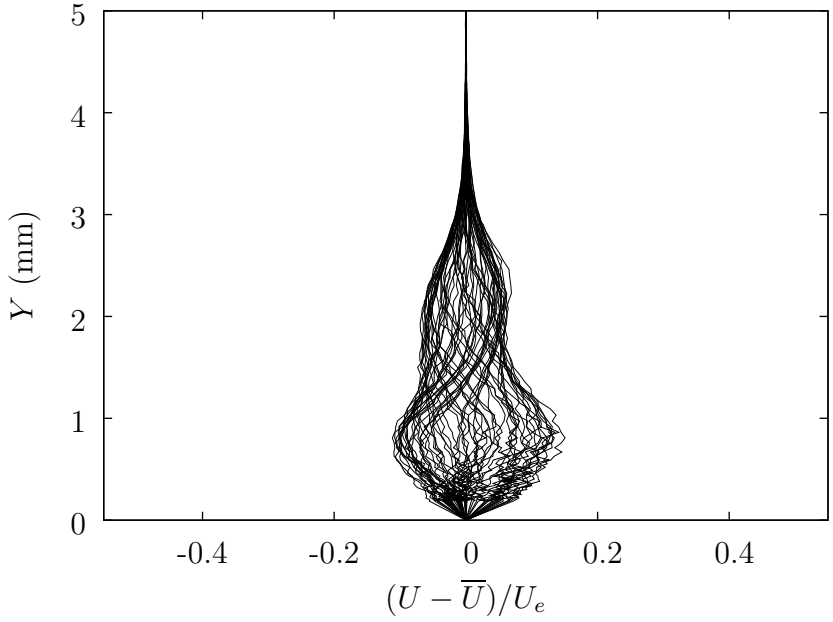

Figure C.68: Steady disturbance profiles at $x/c = 0.375$, $Re_c = 2.8 \times 10^6$, $Tu = 0.19\%$, [12|12|3] roughness.

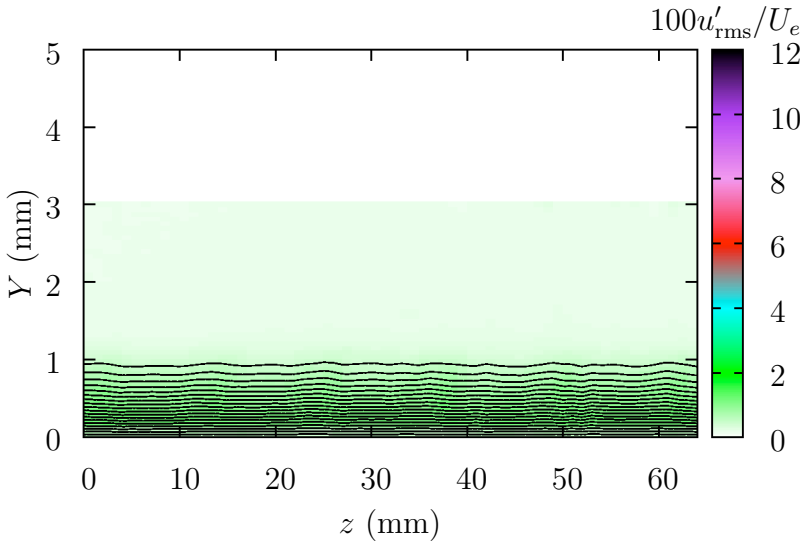

Figure C.69: U and u'_{rms} contours at $x/c = 0.10$, $Re_c = 2.8 \times 10^6$, $Tu = 0.19\%$, [12|12|3] roughness.

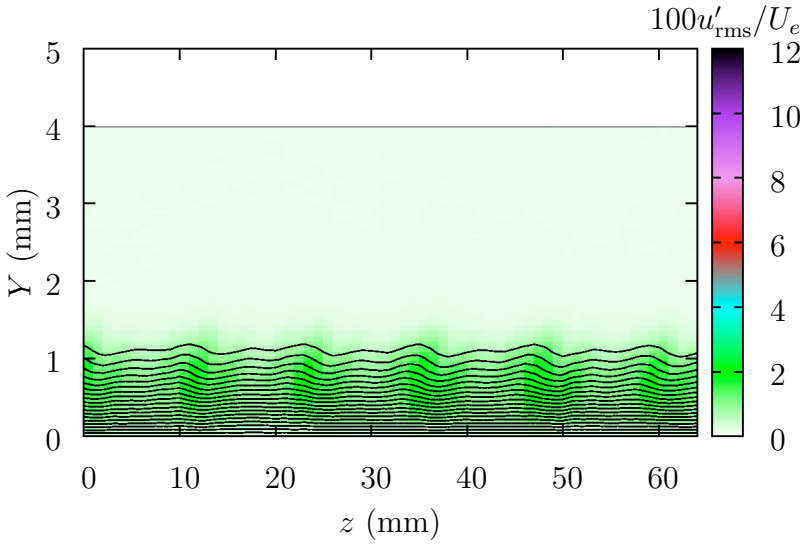

Figure C.70: U and u'_{rms} contours at $x/c = 0.15$, $Re_c = 2.8 \times 10^6$, $Tu = 0.19\%$, [12|12|3] roughness.

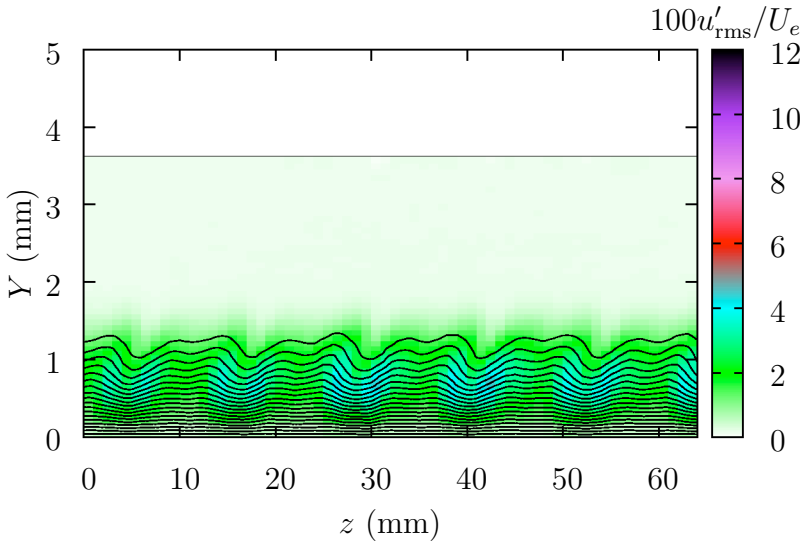

Figure C.71: U and u'_{rms} contours at $x/c = 0.20$, $Re_c = 2.8 \times 10^6$, $Tu = 0.19\%$, [12|12|3] roughness.

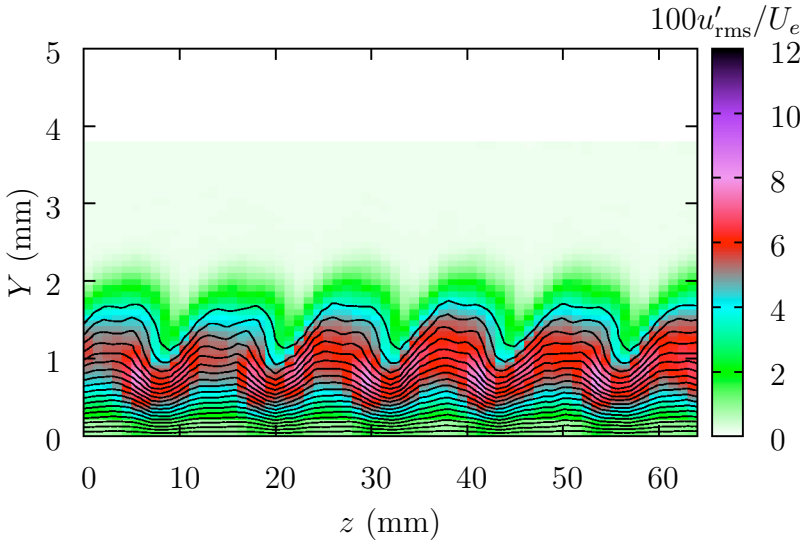

Figure C.72: U and u'_{rms} contours at $x/c = 0.25$, $Re_c = 2.8 \times 10^6$, $Tu = 0.19\%$, [12|12|3] roughness.

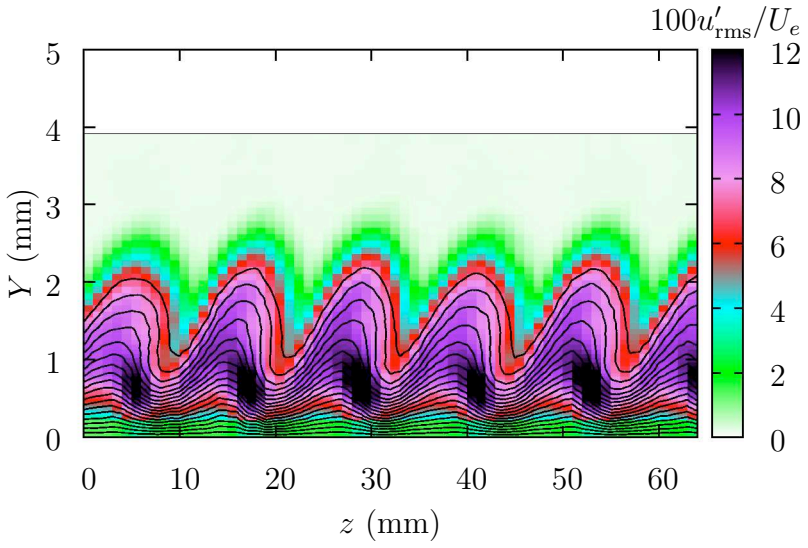

Figure C.73: U and u'_{rms} contours at $x/c = 0.30$, $Re_c = 2.8 \times 10^6$, $Tu = 0.19\%$, [12|12|3] roughness.

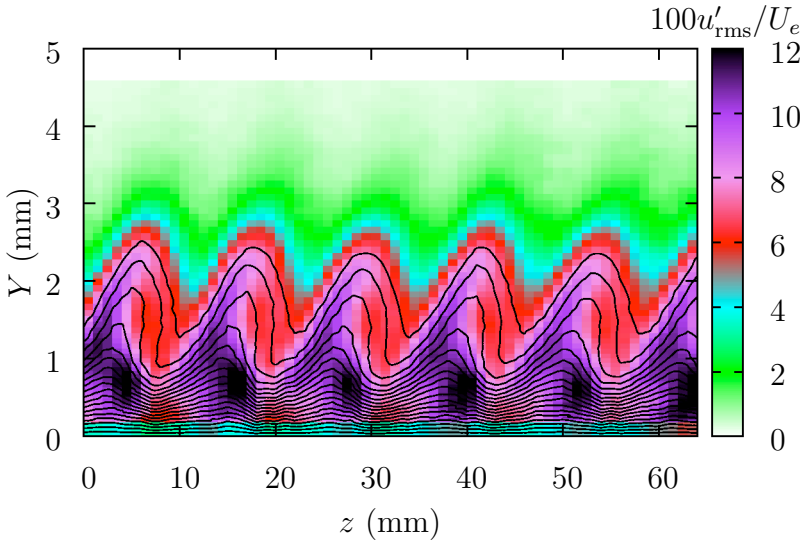

Figure C.74: U and u'_{rms} contours at $x/c = 0.35$, $Re_c = 2.8 \times 10^6$, $Tu = 0.19\%$, [12|12|3] roughness.

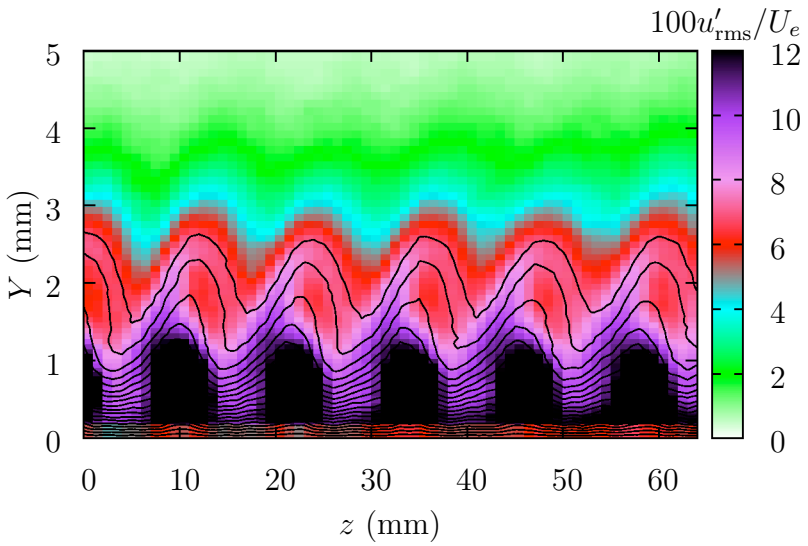

Figure C.75: U and u'_{rms} contours at $x/c = 0.375$, $Re_c = 2.8 \times 10^6$, $Tu = 0.19\%$, [12|12|3] roughness.